International Journal of Aerospace Engineering

Design, Analysis and Measurement of Space Deployable Structures

Lead Guest Editor: Tuanjie Li
Guest Editors: Xiao-Fei Ma, Sichen Yuan, Zuowei Wang, and Yaqiong Tang

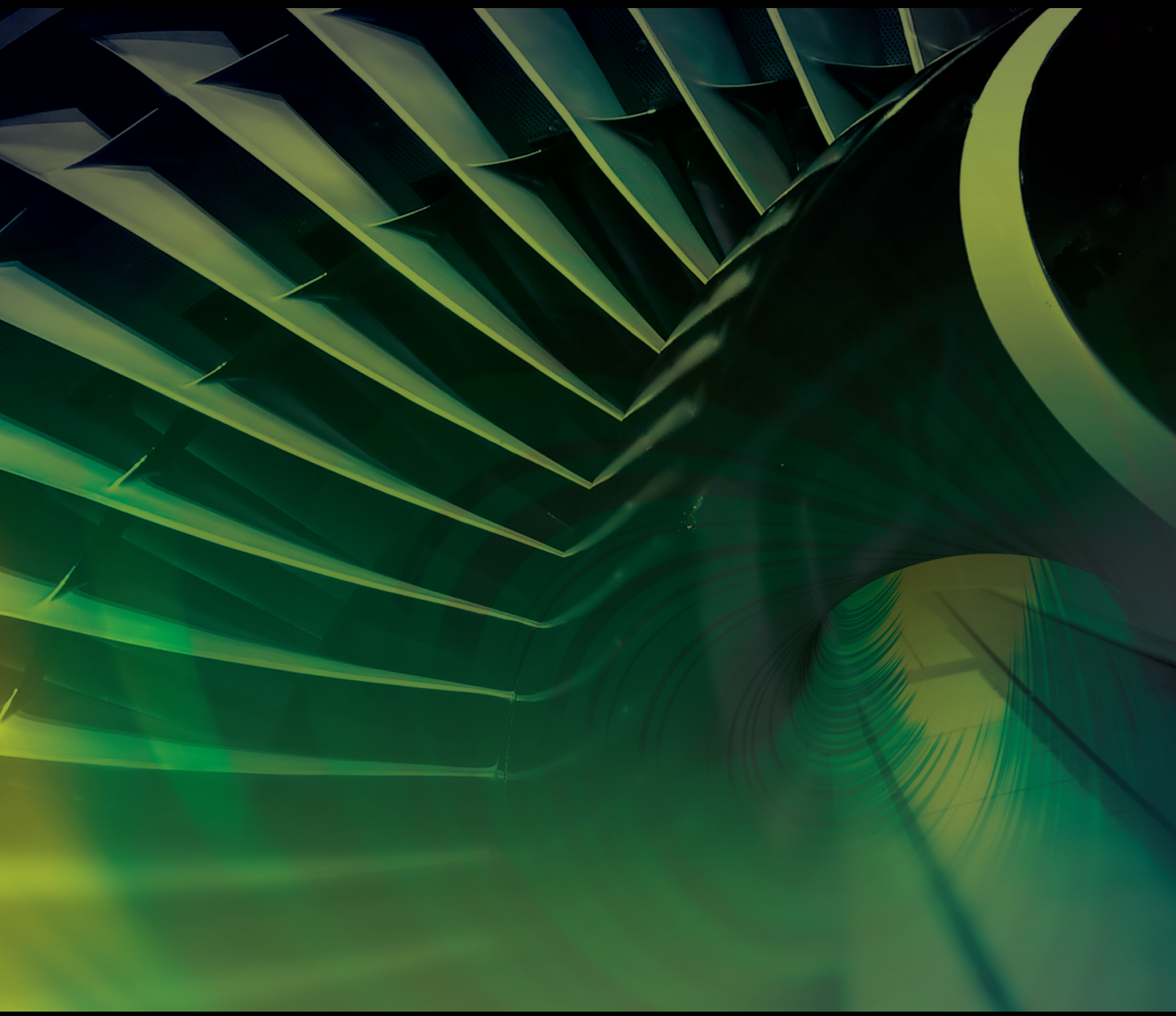

Design, Analysis and Measurement of Space Deployable Structures

International Journal of Aerospace Engineering

Design, Analysis and Measurement of Space Deployable Structures

Lead Guest Editor: Tuanjie Li
Guest Editors: Xiao-Fei Ma, Sichen Yuan, Zuowei Wang, and Yaqiong Tang

Contents

Hindawi
International Journal of Aerospace Engineering
Volume 2024, Article ID 3503468, 13 pages
https://doi.org/10.1155/2024/3503468

Research Article

An Iterative Determination Method of an Axial Deployment Force of a Lanyard-Deployed Coilable Mast in Local Coil Mode

Yu Liu[1], **Liang Sun**[1], **Hai Huang**[1], **Xurui Zhao**[2], **Jiahao Liu**[1] and **Yishi Qiao**[3]

[1]*School of Astronautics, Beihang University, 37 Xueyuan Rd., Beijing 100191, China*
[2]*Institute of Remote Sensing Satellite, China Academy of Space Technology, 104 Youyi Rd., Beijing 100094, China*
[3]*Satellite Engineering Department, China Siwei Surveying and Mapping Technology Co. Ltd., 65 Zhichun Rd., Beijing 100190, China*

Correspondence should be addressed to Liang Sun; sunliang@buaa.edu.cn

Received 7 May 2022; Revised 26 September 2023; Accepted 27 January 2024; Published 26 March 2024

Academic Editor: Antonio Concilio

The axial deployment force is an indispensable parameter of a lanyard-deployed coilable mast, which reflects its load capacity in practical applications. However, research on the axial deployment force in the literature is very limited, and there are no mature numerical methods to determine this parameter in the design stage of coilable masts. In this paper, a numerical method for determining the axial deployment force of a lanyard-deployed coilable mast in the local coil mode is presented. Through this method, the designer can quickly obtain the estimated value of the axial deployment force in the design stage, which is convenient for the quantitative design of parameters. To verify the correctness of the proposed method, a dynamic simulation of the coilable mast is carried out, and a microgravity test is performed. The comparison results show that the error between the numerical method and the simulation and experimental results is less than 5%, which proves the correctness of the proposed method. In addition, the coilable mast studied in this paper has been verified by an actual microsatellite deployment in orbit.

1. Introduction

Compared with traditional large satellites, microsatellite technology has been rapidly developed in recent years because of its advantages of light weight, small size, and low cost. However, the small size limits the application of microsatellites. A feasible way to solve this problem is to change the structure of the microsatellites. Then, high-precision space exploration is achieved by removing the payload away from the microsatellite platform [1–3]. A deployable mechanism [4–6], such as a coilable mast, is usually used. A coilable mast is a one-dimensional deployable mechanism consisting of three consecutive longerons and a series of transverse battens and diagonal cables. It possesses the merits of a high packing factor, light weight, and simple structure.

The coilable mast can be deployed in three ways, including free deployment, lanyard deployment, and nut deployment. Lanyard deployment is a passive deployment mode in which a lanyard is used to control the deployment speed and stability. At the same time, lanyard deployment consists of two methods: the helix mode and local coil mode. In most cases, the local coil mode is preferable because the coilable mast has a higher stiffness against lateral forces during deployment. Therefore, the lanyard-deployed coilable mast in the local coil mode is the most suitable for microsatellite applications.

The axial deployment force is an indispensable parameter of a lanyard-deployed coilable mast, which reflects the load capacity of the coilable mast and has guiding significance for the design of dampers or motors controlling the deployment process. At present, it is inevitable to determine the axial deployment force through complex simulations and prototype tests. Therefore, establishing a numerical method that can accurately estimate this parameter is convenient for developing designs. However, research on the determination of the axial deployment force is limited. Natori et al. listed three types of simplex masts and observed and compared the longeron deformation under different axial deployment forces [7]; however, they only performed

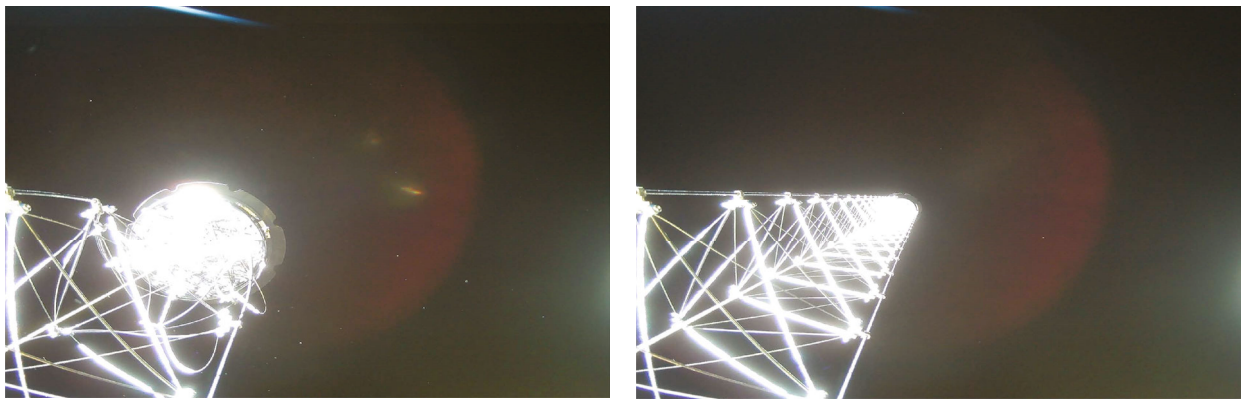

(a) (b)

Figure 1: Images of coilable mast in space: (a) during deployment; (b) after deployment.

a qualitative analysis and did not quantitatively determine the value of the axial development force. Kitamura et al. studied a Y-section hingeless mast and determined an empirical formula for the axial deployment force of the coilable mast in local coil mode [8]. Although they found that the axial deployment force was affected by the stiffness and structure of the coilable mast, it is difficult to obtain the stiffness of the coilable mast through complex simulations and tests at the design stage due to the strong nonlinearity and rigid-flexible coupling characteristics.

In this paper, a numerical method for determining the axial deployment force of a lanyard-deployed coilable mast in the local mode is presented. With this method, the axial deployment force can be quantified without knowing the stiffness of the coilable mast in advance, thus avoiding complicated simulation and testing. The aim of the numerical calculation method proposed in this paper is to determine the axial deployment force of a coilable mast through the longeron deformation of the transition zone. The "standard shape" of the longeron deformation in the transition zone is defined. The three continuous longerons are simplified into thin elastic rods that satisfy the cylindrical constraint hypothesis [9, 10]. Then, the force and deformation of the thin elastic rods are analysed by using Kirchhoff dynamic analogy theory [11]. The axial deployment force of the coilable mast conforming to the "standard shape" of the longeron deformation of the transition zone can be obtained.

In Section 2, the numerical method to determine the axial deployment force of a lanyard-deployed coilable mast in the local coil mode is described in detail. In Section 3, dynamic simulations of the deployment and microgravity deployment test are carried out. In Section 4, the correctness of the proposed method is verified, and the results are verified and discussed.

It is worth emphasizing that the research object of this paper has been applied in practice. On October 14, 2021, the SSS-1 satellite (30 kg) developed by Beihang University was successfully launched into space. The coilable mast studied in this paper was installed and deployed on October 16, 2021. A space camera is installed at the bottom to record the deployment process, as shown in Figure 1. The length of the coilable mast is approximately 2 metres, and its weight is 0.8 kg. In addition, the packing factor can reach 20/1. Undoubtedly, it lays a solid foundation for the subsequent in-orbit application of coilable masts.

2. Numerical Determination Method of the Axial Deployment Force

Under lanyard control, the deployment speed of a lanyard-deployed coilable mast is approximately constant. In this way, the axial deployment force and the lanyard tension can be considered balanced. The method proposed in this paper can be used to obtain the axial deployment force by solving the lanyard tension of the coilable mast. By analysing the deformation of the longeron in the transition zone, the lanyard tension can be determined.

As shown in Figure 2, in the local coil mode, the transition zone is located between the deployed zone and the coiled zone of the lanyard-deployed coilable mast. During deployment, the shape in the transition zone changes periodically within a small range, which results in small periodic fluctuations in the lanyard tension. To obtain the estimated value of the lanyard tension, the "standard shape" in the transition zone is defined in this paper according to the experiment, and the lanyard tension corresponding to this shape is what we need to solve. The actual lanyard tension and axial deployment force will fluctuate in a small range around this value.

2.1. Definition of the "Standard Shape" in the Transition Zone. According to previous research and development tests of coilable masts, the number of segments in the transition zone is approximately 4. As shown in Figure 3, the segments are defined as segments 1 to 4, the corresponding longerons are defined as rods 1 to 4, and the battens are defined as battens 1 to 5.

To quantitatively define the "standard shape" in the transition zone, the helical angle θ of the longeron, which is defined as the angle between the normal direction of the longeron cross section and the deployment direction of the coilable mast, is introduced as shown in Figure 4. In the deployed zone, the longeron is in a state of full deployment, and the helical angle is $\theta_{\text{deploy}} = 0^{\circ}$. In the coiled zone, the

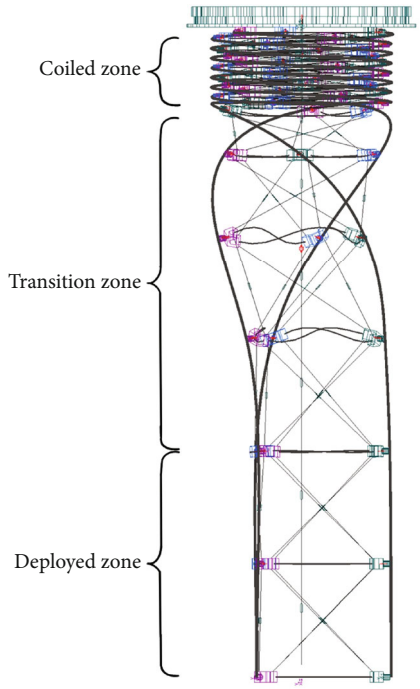

Figure 2: Coilable mast in local coil mode.

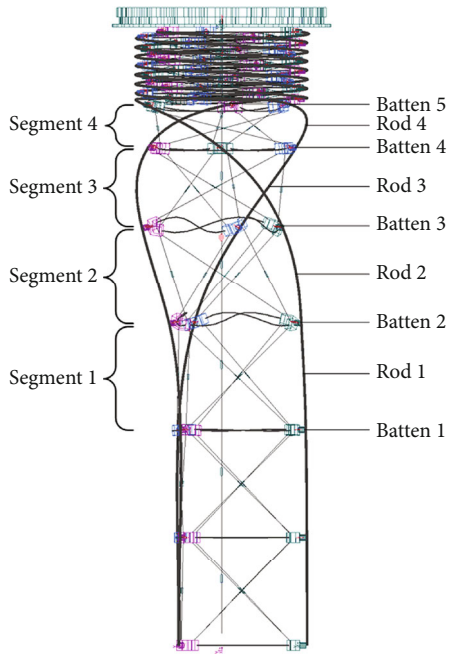

Figure 3: "Standard shape" of transition zone.

longeron is in a uniform helical state, satisfying the cylindrical constraint, as shown in Figure 5, and points A and B represent two adjacent hinges in one longeron. In cylindrical triangle ABC, the helical angle is $\theta_{coil} = \arccos(h_1/t)$, where t and h_1 are the pitch length and the height between two adjacent hinges, respectively. Combined with the definition of the helical angle, the "standard shape" in the transition zone can be quantitatively defined such that the helical angle

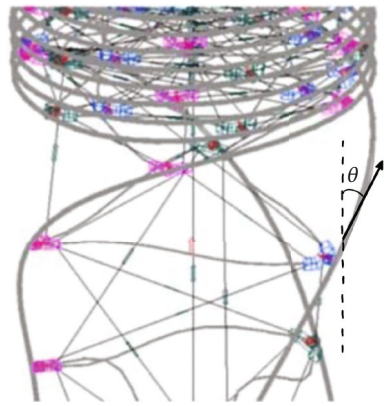

Figure 4: Definition of helical angle θ.

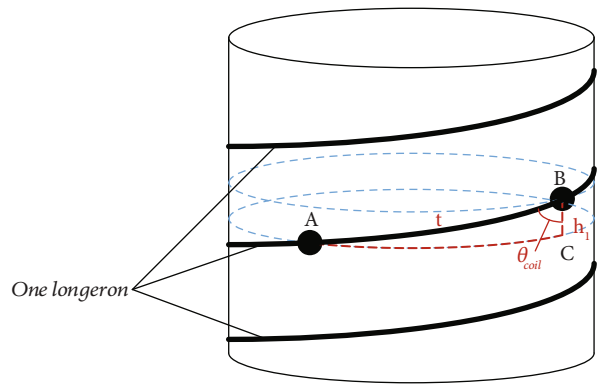

Figure 5: Helical angle in coiled zone θ_{coil}.

of the longeron increases from θ_{deploy} to θ_{coil} in 4 segments. The selection of the helical angle θ to describe longeron deformation is based on three considerations. The first is that the helical angle θ is an intuitive physical parameter that visualizes the deformation shape. The second is that this parameter can be solved quantitatively by the deformation equation extended from Kirchhoff's kinetic analogy theory, which will be introduced in detail in the following sections. The third is that when the helical angle θ is determined, the remaining geometric parameters are properly known based on geometric constraints, so as to completely describe longeron deformation.

It should be noted that in the transition zone of the coilable mast, the battens buckle under pressure, resulting in a slight reduction in the coiled radius of the longerons in the transition zone. However, this reduction can be ignored because it is small relative to the coiled radius. Therefore, it can be assumed that the longeron of the coilable mast deforms along the cylinder in the transition zone, and the cylindrical radius is the coiled radius [12].

2.2. Equations of the Longeron Deformation. In this section, based on Kirchhoff dynamic analogy theory, a deformation equation is introduced to describe the relationship between the deformation of a longeron and the external load. This equation is the basis of the deformation analysis of longerons in the transition zone.

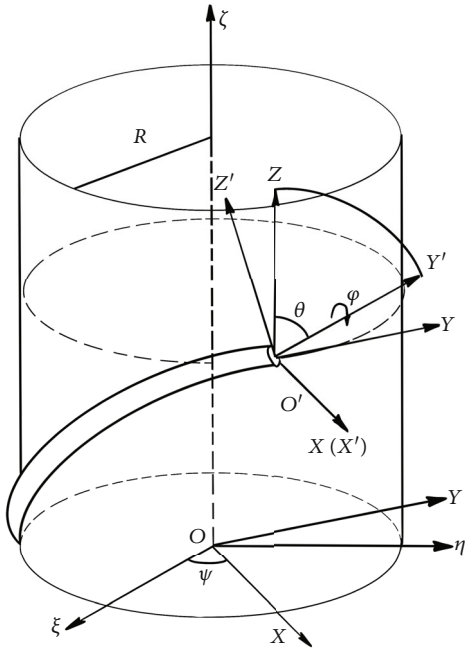

Figure 6: Definition of coordinate systems.

First, we need to establish a series of coordinate systems. As shown in Figure 6, in the rectangular coordinate system, $O\zeta$ is the central axis of the cylinder, and $O\xi$ is randomly defined along the cross section of the cylinder. The coordinate system $O\xi\eta\zeta$ is rotated about the $O\zeta$ axis by ψ to obtain the coordinate system $OXYZ$. Then, $OXYZ$ is translated from O to the center point of the rod cross section O'. Finally, the coordinate system $O'XYZ$ around $O'X$ is rotated by $(\pi/2) - \theta$ to obtain the coordinate system $O'X'Y'Z'$.

φ is taken as the angle around the axis $O'Y'$, representing the rotation between two adjacent cross sections of the rod. The angles ψ, θ, and φ are selected to describe the position and orientation of the rod cross section. All are functions of the arc length s. $d\psi/ds$, $d\theta/ds$, and $d\varphi/ds$ along the arc length describe the deformation of the rod. $d\psi/ds$ and $d\theta/ds$ define the changes in the rotating angles around the $O'Z$ and $O'X$ axes, respectively, between the adjacent cross sections, and $d\varphi/ds$ describes the change in the torsion angle between the adjacent cross sections. Under the cylindrical constraint assumption, $\psi(s)$ and $\theta(s)$ satisfy

$$d\psi = \frac{ds \cdot \sin\theta}{R}. \tag{1}$$

Then, according to Kirchhoff's kinetic analogy theory, the longeron with an external load on both ends satisfies the following deformation equation when the dynamic effect of the mass deployment and the reduction of the coiling diameter in the transition zone are ignored.

$$\frac{d^2\theta}{ds^2} = -\frac{1}{R}(l_0 \cos\theta - m\cos 2\theta) + \left(\frac{p}{2} + \frac{2\cos\theta \sin^2\theta}{R^2}\right)\sin\theta. \tag{2}$$

In Equation (2), R is the coiling radius, s is the arc length of the thin elastic rod, and θ is the helical angle of the thin elastic rod at the current cross section. p, l_0, and m are integral constants. Here, p is proportional to the force acting axially on the rod cross section along the $O'Z$ axis. l_0 is proportional to the torque on the $O\zeta$ axis; and m is related to the torsional deformation. The specific equations are as follows:

$$\begin{cases} l_0 = \dfrac{M_0}{A} = \dfrac{F_Y R + M_Z}{A} = \left(\dfrac{R}{A}\right)F_Y + m\cos\theta + \dfrac{\sin^3\theta}{R}, \\ m = \dfrac{C}{A}\omega, \\ \omega = \dfrac{d\psi}{ds}\cos\theta + \dfrac{d\varphi}{ds}, \\ p = \dfrac{2F_Z}{A}. \end{cases} \tag{3}$$

In Equation (3), A and C are the bending and torsional stiffness of the cross section, respectively, which are related to the material properties of the longeron. M_0 and M_Z are the external torques of the cross section along the $O\zeta$ axis and the $O'Z$ axis, respectively. F_Y and F_Z are the external forces of the cross section along the $O'Y$ axis and the $O'Z$ axis, respectively. ω is the torsional curvature of the longeron, which remains constant along the arc length, while the rod is constrained only at both ends [11]. Then, Equation (4) can be obtained as follows:

$$\int_0^t \omega ds = \int_0^t \left(\frac{d\psi}{ds}\cos\theta + \frac{d\varphi}{ds}\right)ds = \omega t. \tag{4}$$

According to the actual assembly conditions of the longeron of the coilable mast, the torsion of the longeron between the adjacent hinges is limited. Thus, in the interval $[0, t]$, $d\varphi/ds$ is equal to 0. Combined with Equation (1), the relationship between the helical angle and torsion ratio can be obtained as follows:

$$\begin{aligned} \omega t &= \int_0^t \left(\frac{d\psi}{ds}\cos\theta + \frac{d\varphi}{ds}\right)ds = \int_0^t \left(\frac{d\psi}{ds}\cos\theta\right)ds + \int_0^t \frac{d\varphi}{ds}ds \\ &= \int_0^t \frac{\sin\theta\cos\theta}{R}ds. \end{aligned} \tag{5}$$

2.3. Deformation Analysis of the Longeron in the Transition Zone. In this section, the method of solving the deformation equation in Section 2.2 will be introduced in detail, and the deformation analysis of the longeron in the transition zone will be carried out. Due to the internal load caused by transverse battens and diagonals, the equation established in the above section cannot be directly used to solve the entire

deformation in the transition zone. One feasible approach is to discretize the transition zone into several parts, as shown in Figure 4. In this way, each discrete rod satisfies the conditions of the previous deformation equation, and the deformation in the transition zone can be obtained by solving the deformation from rod 4 to rod 1 in turn. The upper end of each rod is where the arc length is $s = 0$, and the lower end is where $s = t$.

To solve Equation (2) for each rod, it is necessary to determine the integral initial values $\theta_i(0)$ and $d\theta_i(0)/ds$ and the integral constants p_i, l_{0i}, and m_i $(i = 1,2,3,4)$, which are related to the boundary conditions and external forces of each rod.

First, we need to determine the initial value of the integral. According to the definition of the "standard shape", the initial value of $\theta_4(0)$ is equal to θ_{coil}. To simplify the calculation, a reasonable assumption is made on the longeron deformation in transition zone based on the results of simulations and tests. It is considered that the helical angle of the longeron in segment 1 is maintained as $\theta_{\text{deploy}} = 0°$, and the helical angle of the longeron in segments 2-4 presents a linear change relationship, which is expressed by Equation (6) [13]. The purpose of this assumption is only to estimate the initial integral values $\theta_4(0)$ and $d\theta_4/ds_{s=0}$ of segment 4 to make the deformation equation solvable, and it will not affect the solution of the nonlinear state regions of the helical angle.

$$\begin{cases} \theta_4(0) = \theta_{\text{coil}}, \\ \left.\dfrac{d\theta_4}{ds}\right|_{s=0} = \dfrac{\theta_{\text{deploy}} - \theta_{\text{coil}}}{3t}. \end{cases} \tag{6}$$

Since the deformation of the longeron in the transition zone is continuous, in segment 3 to segment 1, according to Liu's research [11], the helical angle and its rate satisfy Equation (7). Combined with Equations (6) and (7), the initial integral value required for each rod can be obtained.

$$\begin{cases} \theta_i(0) = \theta_{i+1}(t), \\ \left.\dfrac{d\theta_i}{ds}\right|_{s=0}\left(m_i - \dfrac{3}{2R}\sin 2\theta_i(0)\right) = \left.\dfrac{d\theta_{i+1}}{ds}\right|_{s=t}\left(m_{i+1} - \dfrac{3}{2R}\sin 2\theta_{i+1}(t)\right). \end{cases} \tag{7}$$

The second step is to determine the integral constant of each rod. According to Equation (3), to determine the integral constants p_i, l_{0i}, and m_i, we need to identify F_{Zi}, M_{0i}, and F_{Yi}. These forces and torques can be determined by boundary force analysis. As shown in Figure 6, considering the segments and the coiled zone on rod i as a whole T, T is in an equilibrium state with the lanyard tension F_L, the rod reaction force and torque, and the diagonal cable tension. F_{ri}, F_{vi}, and F_{hi} are three components of the diagonal cable tension. Thus, the forces and torques are balanced along the $O\zeta$ axis to satisfy Equation (8). It should be noted that the coilable mast is a spatially axisymmetric structure, so the force analysis of only one longeron is shown in Figure 7, and the forces and torques of the other two longerons on T are the same.

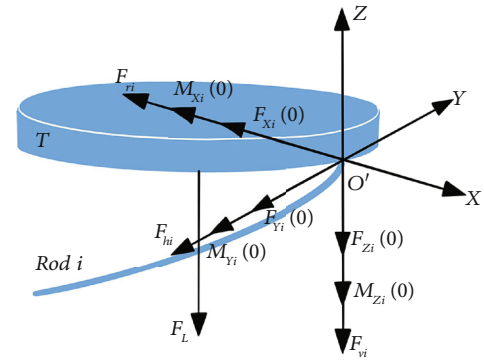

Figure 7: Equilibrium analysis of the unity T.

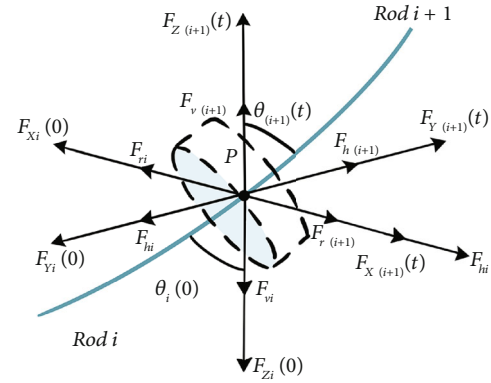

Figure 8: Infinitesimal balance analysis.

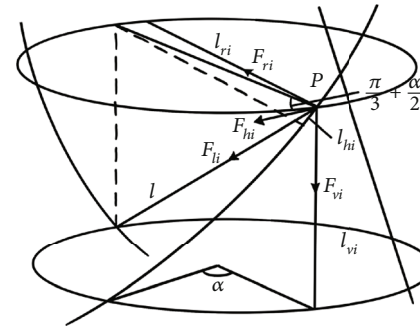

Figure 9: Section deformation analysis.

$$\begin{cases} F_L + 3F_{Zi}(0) + 3F_{vi} = 0, \\ 3(F_{Yi}(0)R + M_{Zi}(0) + F_{hi}R) = 0. \end{cases} \tag{8}$$

The infinitesimal at the connection point between the adjacent rods is considered the object of analysis, as shown in Figure 8. Ignoring dynamic effects, the force is balanced

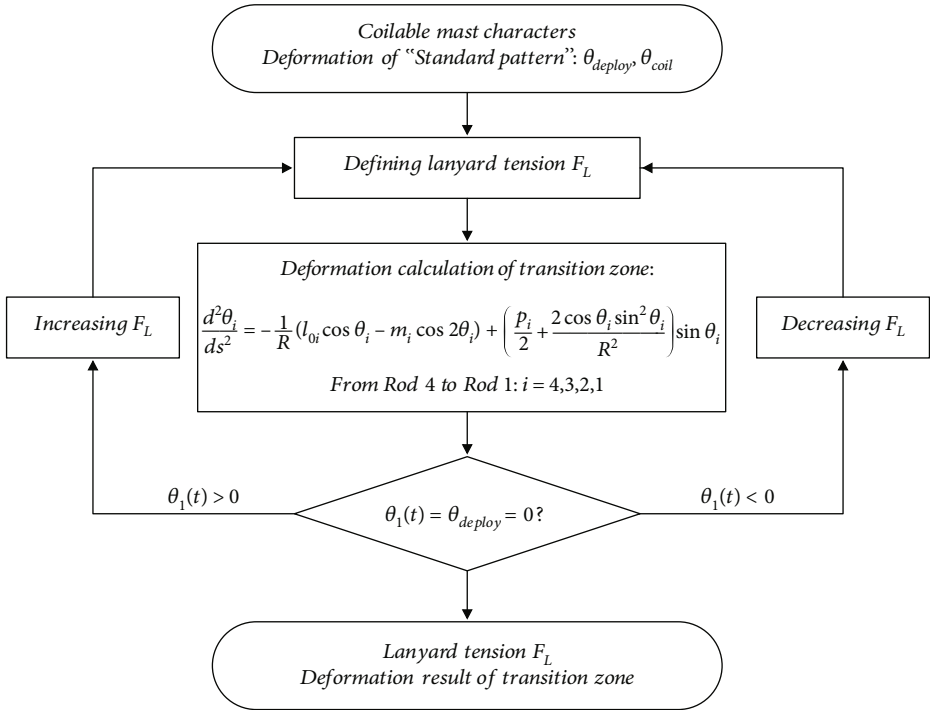

Figure 10: Deformation analysis process for calculating the lanyard tension.

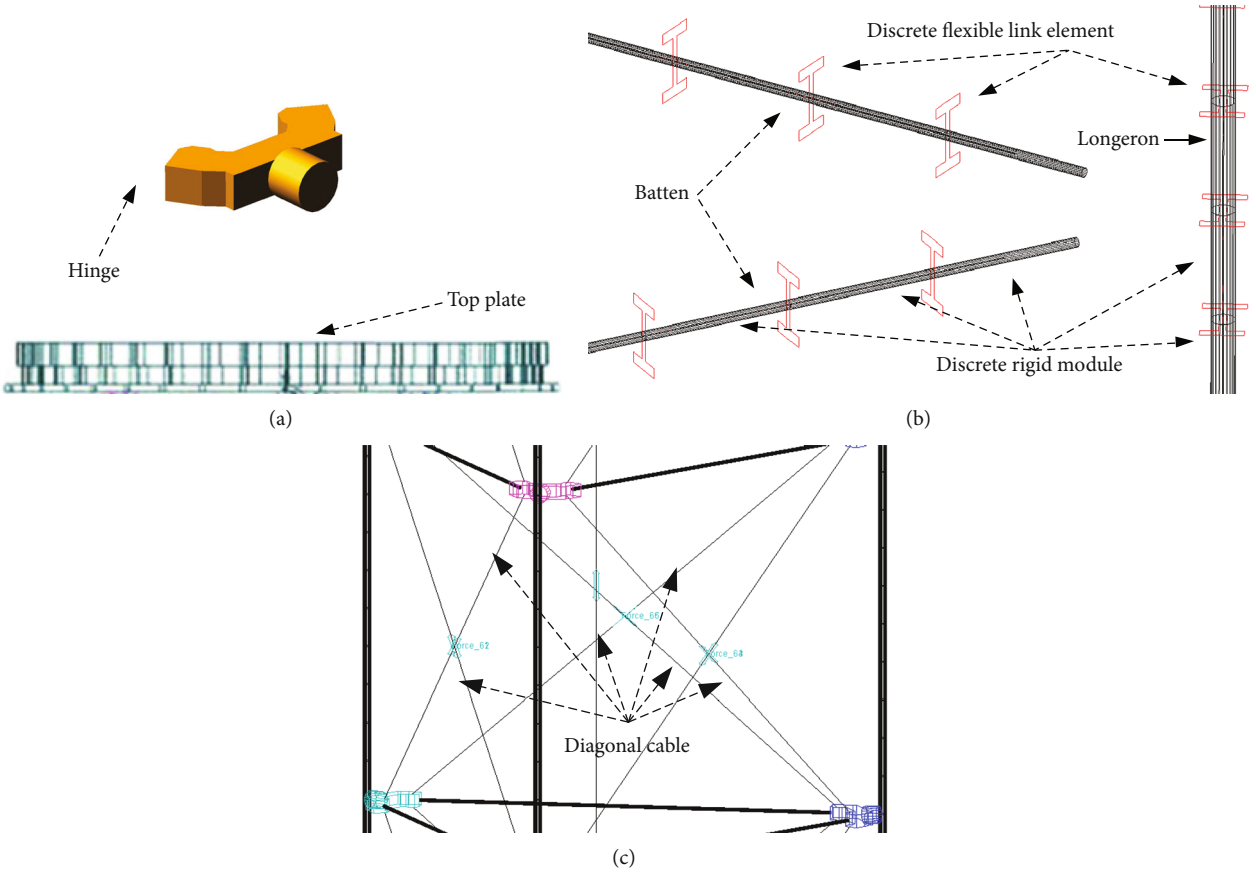

Figure 11: Model of different components: (a) rigid body; (b) flexible body; (c) force.

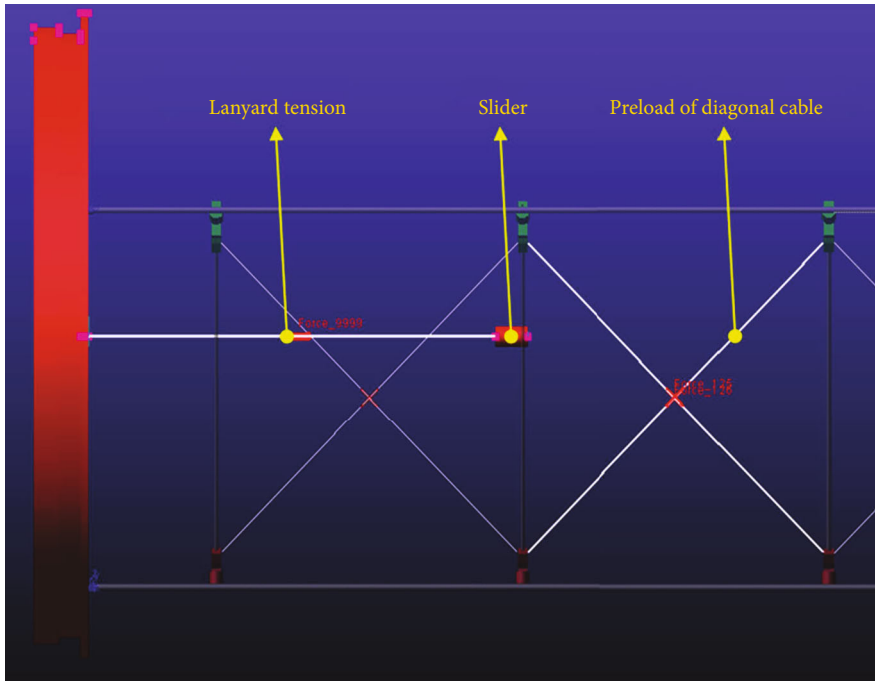

Figure 12: Lanyard tension and diagonal cables in the simulated model.

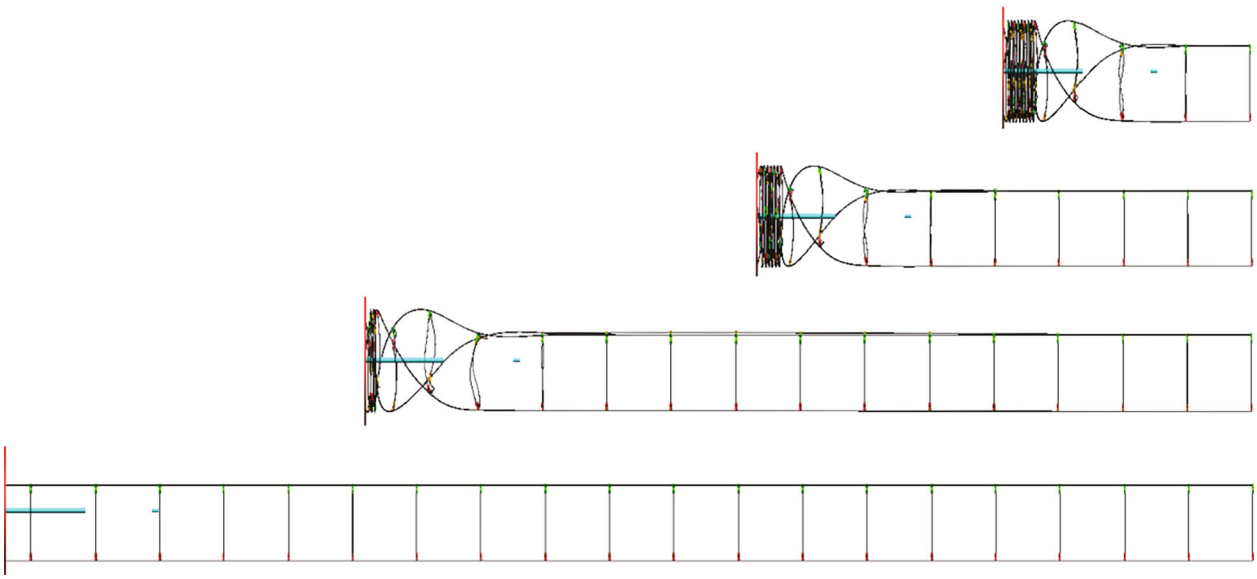

Figure 13: Virtual prototype model of coilable mast.

along the $O'Y$ and $O'Z$ axes, satisfying Equation (9). $F_{Z(i+1)}(t)$ and $F_{Y(i+1)}(t)$ can be solved by p_{i+1} and l_{0i+1}.

$$\begin{cases} F_{Yi}(0) + F_{hi} = F_{Y(i+1)}(t) + F_{h(i+1)}, \\ F_{Zi}(0) + F_{vi} = F_{Z(i+1)}(t) + F_{v(i+1)}. \end{cases} \tag{9}$$

In the experiment, it was observed that the diagonal cables of segments 4 and 3 in the transition zone of the coilable mast were not tensioned. Equations (8) and (9) can be simplified because F_{hi} and F_{vi} are equal to 0. F_{Zi}, M_{0i}, and F_{Yi} can be calculated easily. However, for segments 2 and 1, the function of the diagonal cable tension must be considered. Therefore, more equations need to be added to calculate the diagonal cable tension. According to the segment deformation analysis shown in Figure 9, the tension component of the diagonal cable can be obtained. Assuming the length of the diagonal cable is l, the three components in $O'XYZ$ are l_{ri}, l_{hi}, and l_{vi}. Since diagonal cables only withstand tension, the diagonal cable tension components F_{ri},

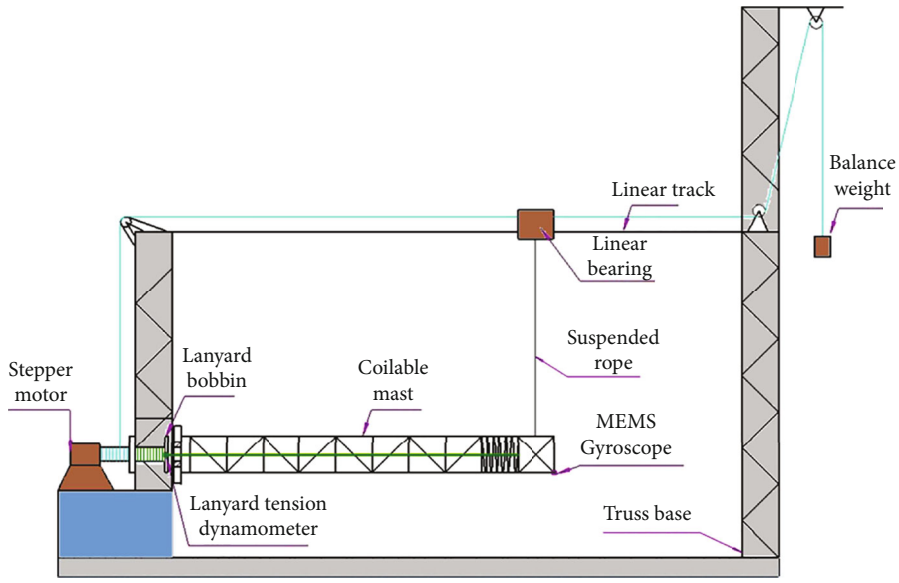

Figure 14: Microgravity deployment test system.

F_{hi}, and F_{vi} have the same geometric relationship to the diagonal cable length. Therefore, the diagonal cable tension can be calculated from Equation (10).

$$\begin{cases} \dfrac{F_{li}}{l} = \dfrac{F_{hi}}{l_{hi}} = \dfrac{F_{vi}}{l_{vi}} = \dfrac{F_{ri}}{l_{ri}}, \\ l_{vi} = \displaystyle\int_t \cos\theta_i ds, \\ \alpha_i = \displaystyle\int_t \frac{\sin\theta_i}{R} ds, \\ l_{hi} = 2R\cos\left(\dfrac{\pi}{3} + \dfrac{\alpha_i}{2}\right)\sin\left(\dfrac{\pi}{3} + \dfrac{\alpha_i}{2}\right), \\ l_{ri} = 2R\sin^2\left(\dfrac{\pi}{3} + \dfrac{\alpha_i}{2}\right), \\ l = \sqrt{\left(l_{vi}^2 + l_{hi}^2 + l_{ri}^2\right)}. \end{cases} \tag{10}$$

Combined with Equations (6)–(10), all the initial values of the integral and the integral constants p_i, l_{0i}, and m_i for any rod i can be determined. When the characteristics of the coilable mast, including geometric dimensions and material properties, are given, the only unknown parameter in the deformation equation (Equation (2)) is the lanyard tension F_L. Therefore, as long as the lanyard tension F_L is given, the deformation equation from rod 4 to rod 1 can be solved in turn, and the deformation in the transition zone corresponding to the lanyard tension can be obtained.

Due to the strong nonlinearity of the deformation equation, the equation cannot be solved directly by the analytical solution, so the iterative calculation approach is a simple and effective method. The iterative solving process is shown in Figure 10. In the iterative solution process, the input parameters of the solution process mainly include two types: one is the characteristics of the coilable mast, including geometric dimensions and material properties, and the other is the parameters of the "standard shape" in the transition zone, θ_{deploy} to θ_{coil}. Then, the initial value of the lanyard tension F_{L0} is given, and the deformation in the transition zone is solved according to the deformation equation in Section 2.2. Then, the helical angle at the bottom of the transition zone $\theta_1(t)$ is compared with θ_{deploy}. If they are equal, it indicates that the transition zone has formed a "standard shape" and that the current lanyard tension is what we need. Then, the axial deployment force is obtained. If they are not equal, the deformation analysis will be repeated after adjusting the lanyard tension value until the transition zone forms a "standard shape."

Moreover, according to formula analysis and accumulated rich data of deployment simulations and tests of coilable masts with different configurations and dimensions, the relationship between the helical angle in the bottom of transition zone $\theta_1(t)$ and the lanyard tension is deeply explored, and they are found to be monotonic over a wide range. In other words, the system has strong stability to the initial value. More than that, the rich data of deployment simulations and tests can guide the selection of the initial value of the lanyard tension closer to the real value, which is conducive to improve the convergence speed of the system.

Remark 1. It should be noted that there are many kinds of uncertainties in application, including internal or external, parametric or nonparametric, constant, characteristic, or random. In a coilable mast, the uncertainties relate to geometric dimensions and material properties. For geometric dimensions, the uncertainties of the coiling radius and the batten pitch length are mainly caused by the assembly error of the coilable mast. For material properties, the uncertainties are mainly caused by material defects and degradation under large deformation. A comparison between the tests and simulations shows that the uncertainties do not cause large deviations in real-time applications.

(a) (b)

Figure 15: Test platform: (a) front view; (b) side view.

Remark 2. It should be noted that in real engineering problems, there are complex systems whose structures, uncertain properties, and all the parameters are unknown. In this case, advanced system identification and signal processing approaches can be developed and optimized with sophisticated approaches [14]. This should be the focus of further research in this paper.

3. Deployment Dynamic Simulation and Microgravity Deployment Test

Through dynamic simulation and microgravity testing of the deployment process, the correctness of the numerical method is verified in Section 2.

3.1. Deployment Dynamic Simulation. The deployment simulation was carried out using MSC.ADAMS and based on the finite element method (FEM). The FEM is a general numerical method for solving partial differential equations in two or three space variables, which is a well-known and widely applied approach in almost every part of such engineering problems. To solve a problem, the FEM subdivides a large system into smaller, simpler finite elements which is achieved by a particular discretization in the space dimension. The simple equations that model these finite elements are then assembled into a larger system of equations that models the entire problem. The FEM approximates the unknown analytical equations over the domain and improves the approximation accuracy by minimizing an associated error function via the calculus of variations. As a complex rigid-flexible hybrid mechanism, the coilable mast is composed of components with different characteristics which will be introduced in the following paragraph, and the deployment process of the mast is strongly nonlinear due to the existence of mechanism clearance and large deformation of flexible components. So it is almost impossible to establish analytical equations of the problem and solve it accurately. Therefore, the FEM is an effective and necessary method for deployment simulation of the coilable mast [5, 15].

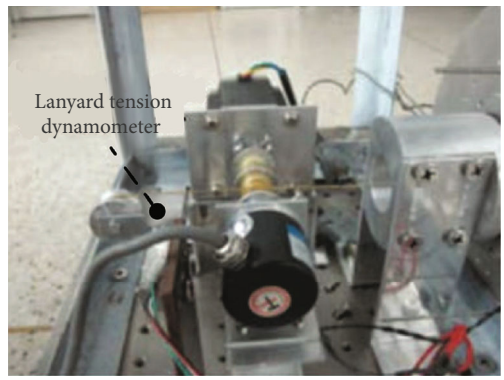

Figure 16: Lanyard tension dynamometer.

Table 1: Technical parameters of the coilable mast.

Parameter	Value
Coiling radius (R)	75 mm
Radius of longeron	1 mm
Radius of batten	0.65 mm
Batten pitch length (t)	95 mm
Height between hinges (coiled zone) (h_1)	3 mm
Material of hinge	Aluminum alloy Young's modulus: 70.6 GPa; Poisson's ratio: 0.33
Material of longeron and batten	Ti-Ni alloy Young's modulus: 83 GPa; Poisson's ratio: 0.31

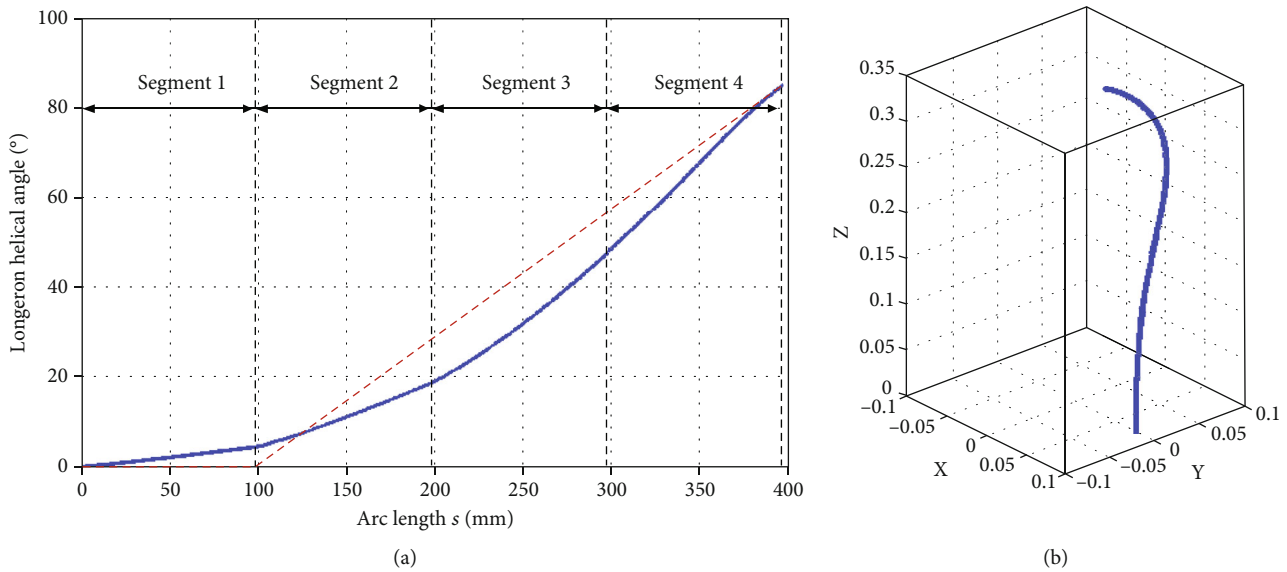

Figure 17: Longeron deformation in the transition zone: (a) helical angle; (b) longeron deformation.

As described in the previous paragraph, different components of the coilable mast exhibit different physical characteristics under applied loads. In this case, four modelling methods are used to reflect its deployment motion characteristics: (1) rigid body: the hinge and top plate of the coilable mast have little deformation during the process and can be simplified into rigid units; (2) flexible body: for longerons and battens, because they are thin rods with elasticity, they will undergo large deformation during the deployment process and are considered flexible bodies. In particular, the longerons and battens are discretized into a series of rigid modules, and discrete flexible link elements are used to connect the adjacent rigid modules to simulate their deformation characteristics; (3) force: since the diagonal cable can only be tensioned but not compressed, a pair of actions and reactions is used to complete the modelling work. The direction of the force is along the central axis of the diagonal cable, and its value is related to the distance between the two ends; and (4) kinematic pair: the components in the simulation model are connected to each other, and the motion relationship is limited by several kinematic pairs, such as the rotating pair between the longeron and the top plate and the fixed pair between the hinge and the longeron. The modelling relationships of the different components are shown in Figure 11. In addition, a slider is set to control the deployment speed of the coilable mast, and the force between the top plate and the slider is the lanyard tension, as shown in Figure 12.

The simulation model of the coilable mast during the deployment process is shown in Figure 13. The deployment process takes place at a constant speed of 30 mm/s. The deformation in the transition zone is basically unchanged, consistent with the defined "standard shape."

3.2. Microgravity Deployment Test. To simulate the weightless environment in space, a microgravity deployment test system for a coilable mast was developed, as shown in Figure 14. The truss base is fixed to the ground to provide mounting space for the coilable mast and support for all other equipment. The coilable mast is placed horizontally, and the top plate is connected to a sliding linear bearing by suspension rope. The linear bearing is located directly above the top plate, so the tension of the rope counteracts the gravity of the coilable mast, creating a microgravity environment. During the development process, as the top plate moves forward, the linear bearing must move synchronously along the linear trajectory to confirm that the suspension rope is in the direction of the plumb line. The lanyard bobbin and balancing weight are especially introduced. When the coilable mast is released by the stepper motor, the presence of the lanyard bobbin ensures that the deployment length of the coilable mast is equal to the movement length of the linear bearing, and in this process, the friction can be overcome by a balancing weight. The physical test platform is shown in Figure 15.

During the coilable mast deployment test, a tension dynamometer mounted on the bottom plate was used to measure the lanyard force with a sampling frequency of 5 Hz, as shown in Figure 16. In addition, the stepped motor is started to release the coilable mast at a speed of 30 mm/s, maintaining consistency with the dynamic simulation.

4. Result Validation and Discussion

4.1. Numerical Calculation Result of Axial Deployment Force. The coilable mast verified on the SSS-1 satellite is taken as the object. The characteristics of the coilable mast are shown in Table 1. According to the numerical method presented in Section 2, the axial deployment force of the coilable mast is calculated as 11.808 N. The helical angle change and longeron deformation in the transition zone are shown in Figure 17. The red-dotted line in Figure 17(a) is the assumption we made of helical angle to obtain the initial integral values, which is described in Section 2.3. This assumption

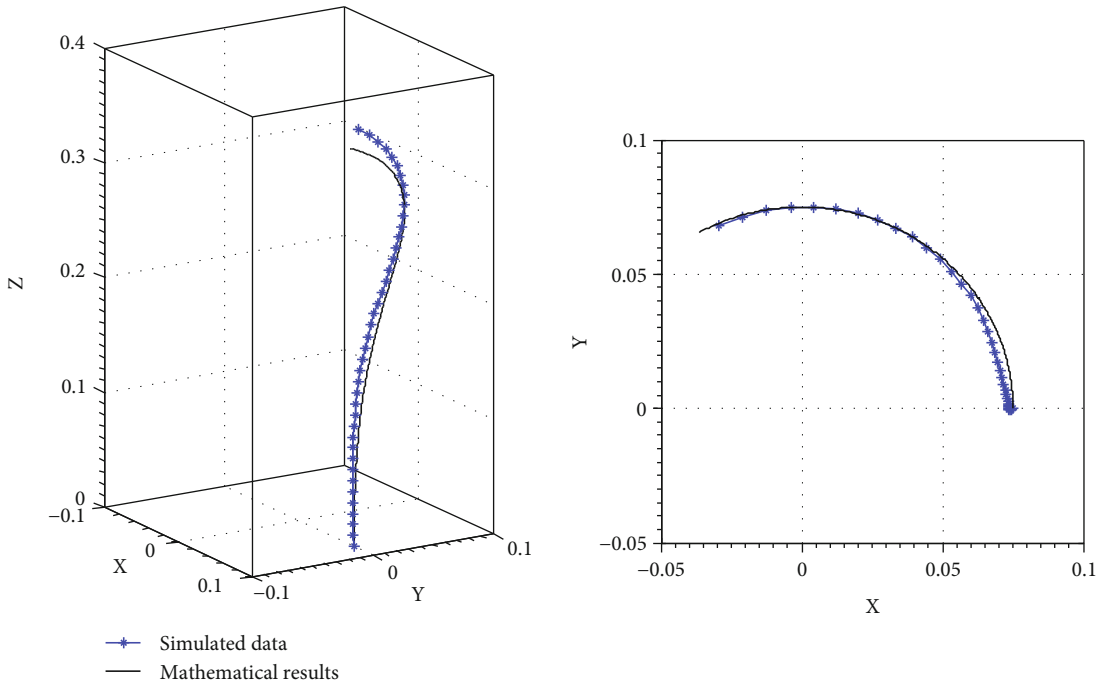

Figure 18: Deformation comparison between mathematical results and simulated data.

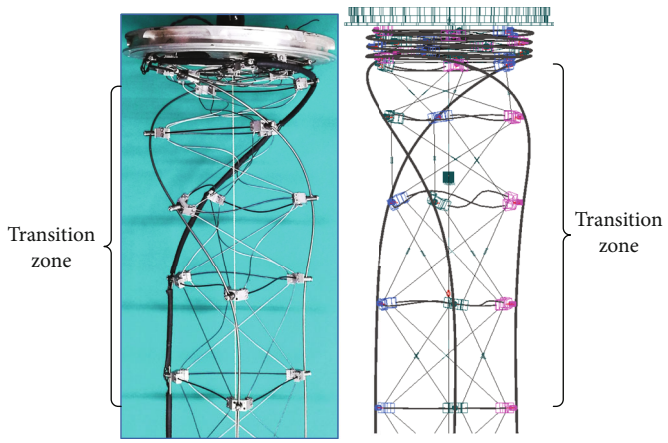

Figure 19: Longeron deformation comparison between tested results and simulated data.

can be considered to be a linear simplification of the actual helical angle. And the assumption does not affect the solution of the actual nonlinear regions of helical angle of the longeron.

In the transition zone, from bottom to top, the helical angle of the longeron changes from 0 to θ_{coil}. The change rate of the longeron helical angle of segment 3 and segment 4 along the arc length s is greater than that of segment 1 and segment 2. Due to the limitation of the diagonal cable, the torsional stiffness of segment 1 and segment 2 is greater than that of segment 3 and segment 4. Therefore, the longeron bearings of segment 1 and segment 2 are subjected to greater torsional stress, and the helical angle changes more slowly.

4.2. Validation of the Longeron Deformation. The longeron deformation can be used to determine the mechanical properties of the coilable mast, so it has been verified for the first time. The longeron deformation in the simulation has similar characteristics to the mathematical results, as shown in Figure 18. It is worth noting that the coiling radius near the bottom of the transition zone is slightly reduced in the simulation. This phenomenon is reasonable because the battens bend under the action of diagonal forces during the development process. Furthermore, the transition zone of the simulation model and the actual test model was compared, as shown in Figure 19. The simulation model can well reflect the actual deployment state of the coilable mast.

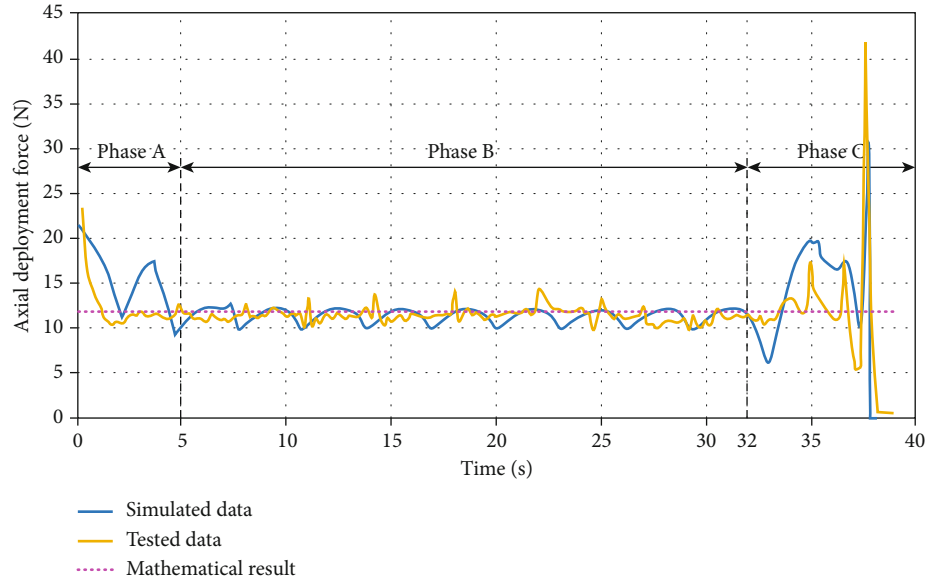

Figure 20: Axial deployment force variation during deployment process.

From the above comparison, it can be seen that the deformation analysis of the numerical method accords with the actual situation of the coilable mast.

4.3. Validation of Axial Deployment Force. According to the above numerical calculation method, the axial deployment force is 11.808 N. The corresponding microgravity test and dynamic simulation results are given. The comparison of the axial deployment force of the three methods is shown in Figure 20.

The development process of the coilable mast is divided into three phases. Phases A and C represent the beginning and end of the development, respectively, where the axial development force changes irregularly because the transition zone of the coilable mast has not yet fully formed or gradually disappeared. Phase B is the stable development phase, and the axial development force presents periodic fluctuations. By comparing the three results in phase B, it can be found that the numerical result is a constant value because it is obtained while ignoring the mast deployment dynamic effects, and both simulation and test results fluctuate periodically near the numerical results. The main reason for the periodic fluctuation of the axial development force is the reflection of energy conversion when a section is unrolled in the local coil mode, which can be called "snap through" [16]. At this moment, the deformation energy of longerons and battens is quickly transformed into the kinetic energy of the top plate, resulting in a sudden increase in the axial development force. Compared with the simulation results, the fluctuation of the test results is relatively irregular, which is mainly due to the influence of measurement noise and actual friction between the hinges of the coilable mast.

The quantitative comparison results of the axial deployment force in phase B are shown in Table 2. Because the axial deployment force in the simulation and test results fluctuates periodically in a small range, the average value is solved to compare with the numerical results. The average value of the simulation result and test results is slightly smaller than that of the numerical results. The reason is that the mathematical result is based on an idealized model, and many factors that affect the axial deployment force have been ignored, such as the friction between hinges and the assembly error of the actual coilable mast. Even so, the results are still close, with absolute values of relative errors less than 5%, as shown in Equation (11).

Table 2: Axial deployment force results in phase B.

Method	Value range (N)	Average value (N)
Numerical	—	11.808
Simulation	9.606~12.554	11.28
Test	9.592~14.351	11.336

$$\text{Simulatation result}: \frac{11.280 - 11.808}{11.808} \times 100\% = -4.5\%,$$
$$\text{Test result}: \frac{11.336 - 11.808}{11.808} \times 100\% = -4.0\%. \quad (11)$$

5. Conclusion

In this paper, a numerical method for determining the axial deployment force of a coilable mast in practice is presented. According to the "standard shape" in the transition zone of the coilable mast in the local coil mode, the calculation process of the complex axial deployment force is transformed into the solution of the lanyard tension, which is obtained by analysing the deformation of the longeron in the transition zone. To verify the correctness and applicability of the proposed numerical method, dynamic simulation and

microgravity deployment tests are carried out. The results show that the maximum relative error is less than 5%. The verified method can be used to easily obtain the estimated axial deployment force of the coilable mast in the local coil mode without complicated simulations and testing, which provides convenience for the design of the coilable mast.

Data Availability

The data used to support the findings of this study are included within the article.

Disclosure

The manuscript is new, neither the entire paper nor any part of its content has been published or accepted elsewhere, and it is not currently under consideration or review by any other journal.

Conflicts of Interest

There is no conflict of interest in the manuscript.

References

[1] L. Puig, A. Barton, and N. Rando, "A review on large deployable structures for astrophysics missions," *Acta Astronautica*, vol. 67, pp. 12–26, 2010.

[2] F. A. Harrison, W. W. Craig, F. E. Christensen et al., "The nuclear spectroscopic telescope array (NuSTAR) high-energy X-ray mission," *The Astrophysical Journal*, vol. 770, no. 2, p. 103, 2013.

[3] Y. Sato, S. K. Kim, Y. Kusakawa et al., "Extensible flexible optical system for nano-scale remote sensing satellite "PRISM"," *Transactions of the Japan Society for Aeronautical and Space Sciences, Space Technology Japan*, vol. 7, no. 26, pp. 13–18, 2008.

[4] L. Johnson, L. Alexander, L. Fabisinski et al., "Multiple NEO rendezvous using solar sail propulsion," in *Global Space Exploration Conference*, Washington, DC, 2012.

[5] M. E. McEachen, "Validation of SAILMAST technology and modeling by ground testing of a full-scale flight article," in *The 48th AIAA Aerospace Sciences Meeting Including the New Horizons Forum and Aerospace Exposition*, Orlando, Florida, 2010.

[6] D. M. Murphy, M. E. McEachen, and B. D. Macy, "Demonstration of a 20-m solar sail system," in *The 46th AIAA/ASME/ASCE/AHS/ASC Structures, Structural Dynamics and Materials Conference*, Austin, Texas, 2005.

[7] M. Natori, K. Okazaki, M. Sakamaki, M. Tabata, and K. Miura, "Model study of simplex masts," in *Proceedings of International Symposium on Space Technology and Science*, pp. 489–496, Tokyo, Japan, 1986.

[8] T. Kitamura, K. Okazaki, M. Natori, K. Miura, S. Sato, and A. Obata, "Development of a "hingeless mast" and its applications," *Acta Astronautica*, vol. 17, pp. 341–346, 1998.

[9] W. Seemann, "Deformation of an elastic helix in contact with a rigid cylinder," *Archive of Applied Mechanics*, vol. 67, pp. 117–139, 1996.

[10] G. H. M. Van Der Heijden, "The static deformation of a twisted elastic rod constrained to lie on a cylinder," *Proceedings of the Royal Society A*, vol. 457, pp. 695–715, 2001.

[11] L. Yanzhu, *Nonlinear Mechanics of Thin Elastic Rod: Theoretical Basis of Mechanical Model of DNA*, Tsinghua University Press, 2006.

[12] H. Jianbin, X. Wang, and H. Ma, "Mechanical principle of the deploying mode for coilable mast," *Journal of Beijing University of Aeronautics and Astronautics*, vol. 39, pp. 1168–1173, 2013.

[13] M. Haibo, H. Hai, H. Jianbing, Z. Wei, and W. Xinsheng, "Study on the criterion to determine the bottom deployment modes of a coilable mast," *Acta Astronautica*, vol. 141, pp. 89–97, 2017.

[14] O. Tutsoy, K. Balikci, and N. F. Ozdil, "Unknown uncertainties in the COVID-19 pandemic: multi-dimensional identification and mathematical modelling for the analysis and estimation of the casualties," *Digital Signal Processing*, vol. 114, article 103058, 2021.

[15] H. Ma, "Triangle-section coilable mast development for BUAA-SAT," in *65th International Astronautical Congress*, Toronto, Canada, 2014.

[16] M. Eiden, O. Brunner, and C. Stavrinidis, "Deployment analysis of the Olympus Astromast and comparison with test measurements," *Journal of Spacecraft and Rockets*, vol. 24, pp. 63–68, 1987.

Hindawi
International Journal of Aerospace Engineering
Volume 2022, Article ID 6125831, 8 pages
https://doi.org/10.1155/2022/6125831

Research Article

Multiobjective Optimization Design of Truss Antenna

Di Wu,[1,2] **Xiaofei Ma**,[1,2] **Jinbao Chen**,[1] **Chuanzhi Chen**,[1] **Jiang Zhao**,[2] **and Kunyang Lin**[2]

[1]*College of Astronautics, Nanjing University of Aeronautics and Astronautics, Nanjing 210016, China*
[2]*Xi'an Institute of Space Radio Technology, Xi'an 710100, China*

Correspondence should be addressed to Xiaofei Ma; maxf504@126.com

Received 15 July 2022; Revised 15 September 2022; Accepted 3 October 2022; Published 5 December 2022

Academic Editor: Zuowei Wang

During the design and manufacturing process of the truss antenna, the surface accuracy of the truss antenna is inherently affected by tolerance. An appropriate optimal design of the truss antenna structure is important to improve surface accuracy. In order to receive the optimal design of the truss structure, this paper adopts the multiobjective optimization algorithm based on an approximate model to optimize the tolerance model with random error. Firstly, considering the influence of the processing and assembly errors of the members on the surface accuracy of the structure, the equilibrium state equation of the truss is established by the principle of minimum potential energy. Then, the relationship between the tolerance and the surface accuracy is obtained by the Monte Carlo method. For improving the computing efficiency of the Monte Carlo method, an approximate model of the truss antenna unit is established, where the rod length tolerance is set as the design variable, and the truss surface accuracy and processing cost are set as the objective functions. Finally, tolerance optimization is carried out by using the multiobjective genetic algorithm. The results indicate that the Pareto solution is obtained with an error less than 10%. Moreover, a set of solutions of the tolerance are obtained which can meet different antenna design requirements. And the results show that the influence of the web rod is significantly greater than that of the bottom rod on the surface accuracy of the structure.

1. Introduction

With the development of aerospace technology, the truss antenna has been successfully used in many aerospace missions due to its high storage ratio, high stiffness, and good deployment stability [1–3], for example, the "Mir" space station, the HJ-1-C satellite, and the Beidou navigation satellite. The truss antenna is composed of several essential truss elements, such as tetrahedron [4], quadrangular pyramid [5], hexagonal prism [6], and hexagonal pyramid [7]. Since the truss element is directly connected to the reflective surface, the surface accuracy is closely related to the truss accuracy. Due to the large number of truss rods, the cumulative error caused by the processing and assembly error has a significant impact on the accuracy. Many scholars have conducted in-depth research on the influence of processing and assembly error, especially random errors, on the surface accuracy of the truss based on the traditional empirical method and analogy method [8–11]. And the Monte Carlo method is also widely used for random error analysis on the surface accuracy analysis [12–16].

Sun et al. [17] analyzed the influence of the cable net manufacturing error and other factors on surface accuracy and used the Monte Carlo method to calculate the variable range of surface accuracy. Forouraghi [18] introduced a new method based on GAs, which addresses both the worst-case tolerance analysis of mechanical assemblies and robust design. Yang et al. [19] established the precision analysis model of the planar four-closed-loop deployment mechanism, which reflects the relationship between the deformation of the mechanism and the deviation of the single rod. Lin et al. [20] employed the Monte Carlo method to simulate the machining error and the multi-closed-loop mechanism clearance and analyzed the deployment error of the antenna module, without optimizing tolerances further. Deng et al. [21] employed the back propagation neural

network algorithm to establish the prediction model of the truss antenna which can analyze the truss surface accuracy, repeatability, and critical node error. Wu et al. [16] derived the sensitivity relationship between node coordinate deviation, cable force deviation, and cable length error for Astro-Mesh reflectors, which is utilized to carry out the Monte Carlo simulations quickly. The method can predict the worst surface accuracy as precisely as the traditional method but with less time consumption. Singh et al. [22] optimized the cost-tolerance design of mechanical components based on the genetic algorithm and verified two example problems with interrelated dimensional chains. Sanz et al. [23] proposed a kind of Lagrange multiplier method to optimize the total manufacturing cost bearing in mind the cost functions based on the process and summarized several cost-tolerance relation models to get comparable results. Koziel and Ogurtsov [24] and Easum et al. [25] applied the multiobjective optimization method to antenna design, which improved the efficiency of the overall optimization analysis and opened up new ideas. Li et al. [26] built a flatness-oriented model for the Highly Stowed Deployable Antenna (HSDA), and Monte Carlo simulations are implemented to obtain the sensitivity for the parameters. Yuan et al. [27–30] put forward the concept of direct root mean square (DRMS) to describe the performance of antenna reflectors and carried out the related analysis on the large deployable mesh reflectors.

The Monte Carlo method is widely used for the analysis and calculation of tolerances in the above studies. However, due to the high time consumption and low efficiency of the Monte Carlo method, it is difficult to build an efficient optimization model, making it challenging to optimize further and analyze the tolerance design. To improve the accuracy of the reflective surface of the truss antenna, it is necessary to carry out an overall optimization design for the tolerance of the truss rods to reduce the influence of random errors on the accuracy.

This paper calculates the equilibrium position based on the minimum potential energy principle for a tetrahedral truss antenna class, considering the customarily distributed errors. The surface accuracy distribution probability of the structure within the tolerance range is obtained by the Monte Carlo method, and an explicit model based on the radial basis function (RBF) approximation model is constructed to replace the calculation process of the Monte Carlo method. Finally, combined with the genetic algorithm to optimize its objective value, the Pareto solution set is obtained.

2. Truss Antenna Analysis

As shown in Figure 1, a type of truss antenna structure is composed of a plurality of tetrahedral elements, and each element contains four disc chucks, three base rods, and three web rods.

The truss rod deforms slightly due to tolerance-induced strains under ideal size assembly. Since the disc chuck size is small, it can be approximated as a rigid body. Due to the rods connected by the disc chuck and the included angle between the rods being fixed by the disc chuck, it is considered that the included angle remains unchanged. In the analysis, rod bending and compression deformation in the balance state should be fully considered.

2.1. Rod Model. Figure 2 shows the diagram of the deformation of the connection between the truss antenna rod and the disc chuck. As the disc chuck is connected with 6 bottom rods and 3 web rods, the geometric center of the disc chuck is the stitching point with the metal mesh surface. Connect the points to get a simple model of the disc chuck, which is a rigid body with 9 connection points and 1 center point.

In the local coordinate system, the rod has compression deformation and bending deformation, without considering torsional deformation. Due to the force on both ends of the rod, the bending deformation of the rod can be approximated as a bending model with one end fixed and the other free. At the same time, in order to meet the assembly requirements, it is assumed that the rod is suitable for the ideal rod length, resulting in axial deformations, and the deformation is the tolerance value. Under this initial deformation, the rod has the initial axial strain energy. When the member system is in equilibrium, the strain energy of the rod is expressed as

$$U = U_t + U_b. \tag{1}$$

The tensile and compressive strain energy is given by

$$U_t = \frac{1}{2} F\Delta l = \frac{F\Delta x}{2} = \frac{EA\Delta x^2}{2l}. \tag{2}$$

And the bending strain energy can be computed by

$$U_b = \frac{1}{2} M\theta = \frac{EI}{2l} y^2 = \frac{EI}{2l} \int_0^l \left(\frac{\pi \Delta z}{2l} \sin\left(\frac{\pi x}{2l}\right) \right)^2 dx = \frac{(\pi \Delta z)^2 EI}{16 l^2}, \tag{3}$$

where E is the elastic modulus and A is the cross-sectional area of the rod. I is the moment of inertia of the cross-section while l is the length of the rod. F and M are the force and the bending moment of the rod, respectively, while y is the bending curve derivative of the rod, that is, the end bend angle. Δx, Δz are the deformation of the rod end in the X and Z directions in the local coordinate system, respectively. Therefore, the matrix representation of strain energy is as follows:

$$U = \begin{bmatrix} \frac{EA}{2} & \frac{\pi^2 EI}{16} \end{bmatrix} \cdot \begin{bmatrix} \frac{\Delta x^2}{l} \\ \frac{\Delta z^2}{l^2} \end{bmatrix}. \tag{4}$$

2.2. Overall Model of the Truss. For the truss structure shown in Figure 3, a constraint equation needs to be established.

There are two types of geometric constraints, one is the angle constraint between the end of the rod and the disc chuck, and the other is the distance constraint of the connection point. In order to ensure the geometric constraints between the rod and the connecting feet of the disc chuck,

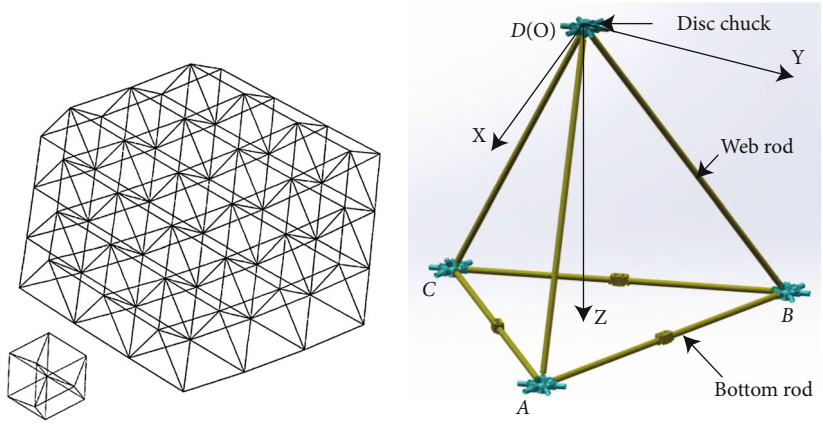

Figure 1: Antenna truss diagram: (a) truss antenna; (b) tetrahedral element.

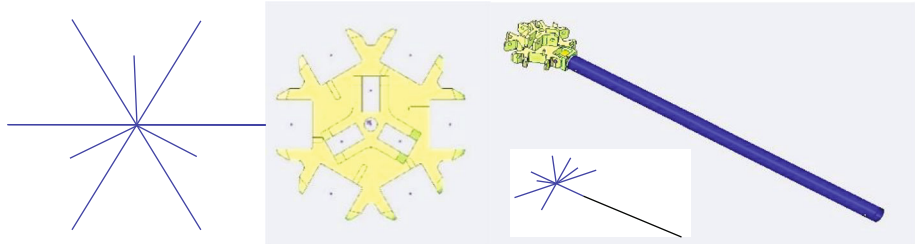

Figure 2: Rod deformation and disc chuck.

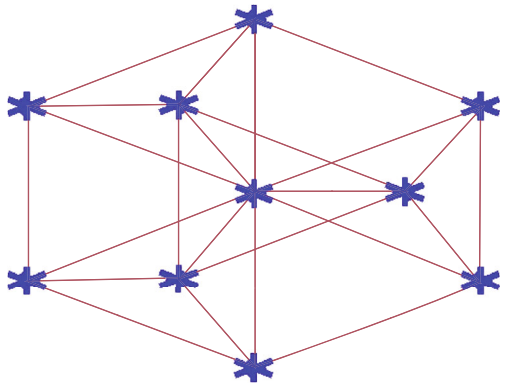

Figure 3: Rod deformation diagram.

there is a vector perpendicular relationship between the end normal of the bending rod and the direct line of the connecting feet of the disc chuck. The constraints are as follows:

$$\begin{aligned} g_1 &= i \cdot fx, \\ g_2 &= \|N - L\|, \end{aligned} \tag{5}$$

where i is the direction vector of the disc chuck connecting foot pointing to the geometric center of the disc chuck, fx is the normal vector of the end of the rod, $\|N - L\|$ is the distance between the disc chuck connecting foot and the end point of the member, N is the coordinate of the disc chuck connecting foot, and L is the end coordinate of the member.

Hence, the construction of the mechanical model of the truss has been completed, and the equilibrium state can be obtained by solving the minimum value of the energy expression of the truss system.

2.3. Surface Accuracy Solution. According to the mechanical model of the truss antenna established above, we can solve the equilibrium position of the disc chuck. Since the reflection net is directly connected to the disc chuck, the position change of the disc chuck is used to measure the accuracy of the reflector, and the root mean square (RMS) of the disc chuck displacement in the normal direction of the reflector is used as the surface accuracy. Therefore, the expression is as follows:

$$\mathrm{RMS} = \sqrt{\frac{1}{n}\sum_{i=1}^{n} \Delta_i^2}, \tag{6}$$

where Δ is the radial deviation between the actual position of the disc chuck node and the ideal position and n is the number of disc chucks that constitute the reflective surface. By solving Equation (4), the obtained result is substituted into Equation (6) to solve the accuracy. Thus, the calculation of the surface accuracy of any tolerance value is completed. Considering the uncertainty of the actual length of the rod, the surface accuracy distribution model of the antenna under the tolerance is further constructed by the Monte Carlo method.

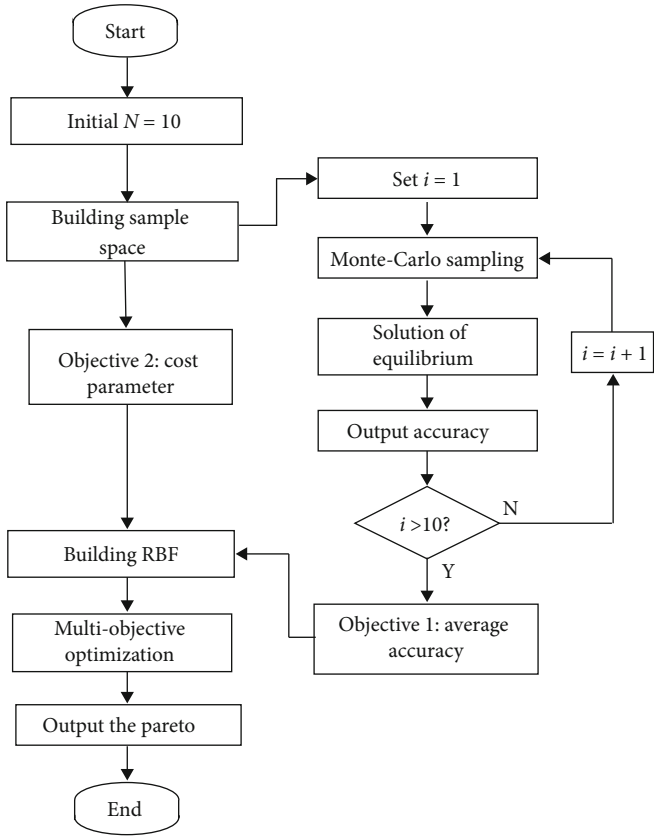

Figure 4: Calculation flow chart of the optimal design.

3. Optimization Model

The multiobjective optimization problem (MOP) consists of multiple objective functions that have constraints and contradict each other. Because there is no unified measurement standard between those objectives, it is challenging to assign weights. In recent years, intelligent algorithms have been commonly used to solve such problems. This paper employs a multiobjective genetic algorithm to solve the problem.

3.1. Design Variable. As shown in Figure 1, the members of the truss include two types of web rods and bottom rods. Tolerance ranges are set for two types, assuming that their tolerance ranges are symmetrically distributed. Referring to the actual processing experience, in general, the tolerances are symmetrically distributed in both directions and do not exceed 0.4 mm. The bottom rod tolerance value and the web rod tolerance value need to be set as design variable 1 and design variable 2, respectively, as shown in the following formula:

$$x_1 \in [0, 0.4] x_2 \in [0, 0.4]. \tag{7}$$

These variables are in millimeters.

3.2. Objective Function. The surface accuracy and cost are set as the optimization objective. Since the surface accuracy is affected by random errors, which lead to the floated accuracy, the average accuracy value is taken as objective 1. This value is calculated by the Monte Carlo method. The smaller the average value, the higher the antenna accuracy. Considering that the size of the rods obeys the normal distribution within the tolerance range, the standard deviation is set to one-third of the tolerance value, and the mean value is 0. The normal distribution parameter is $(0, x/3)$, where x is the tolerance value. Objective 1 is expressed as follows:

$$f_1 = 100 \times \text{ave}(\text{RMS}), \tag{8}$$

where ave(RMS) means to calculate the average value of the RMS from the Monte Carlo result.

The cost of the product is affected by different processing personnel and different processing techniques. In order to obtain a more accurate cost-tolerance model, it is necessary to obtain the relevant parameters to fit the actual statistical sample data. Scholars [31, 32] have proposed a variety of fitting methods based on different elementary functions. Currently, the commonly used fitting model curves include the exponential model and negative square model. In this paper, the relationship between processing cost and tolerance is fitted with a negative square model. Considering the confidentiality and uncertainty of the specific cost value, and to simplify the calculation, the relevant parameters in the model are set to 1. The total processing cost cb is expressed as follows:

$$cb = \left(a(X_i)^{-2} + b\right), \tag{9}$$

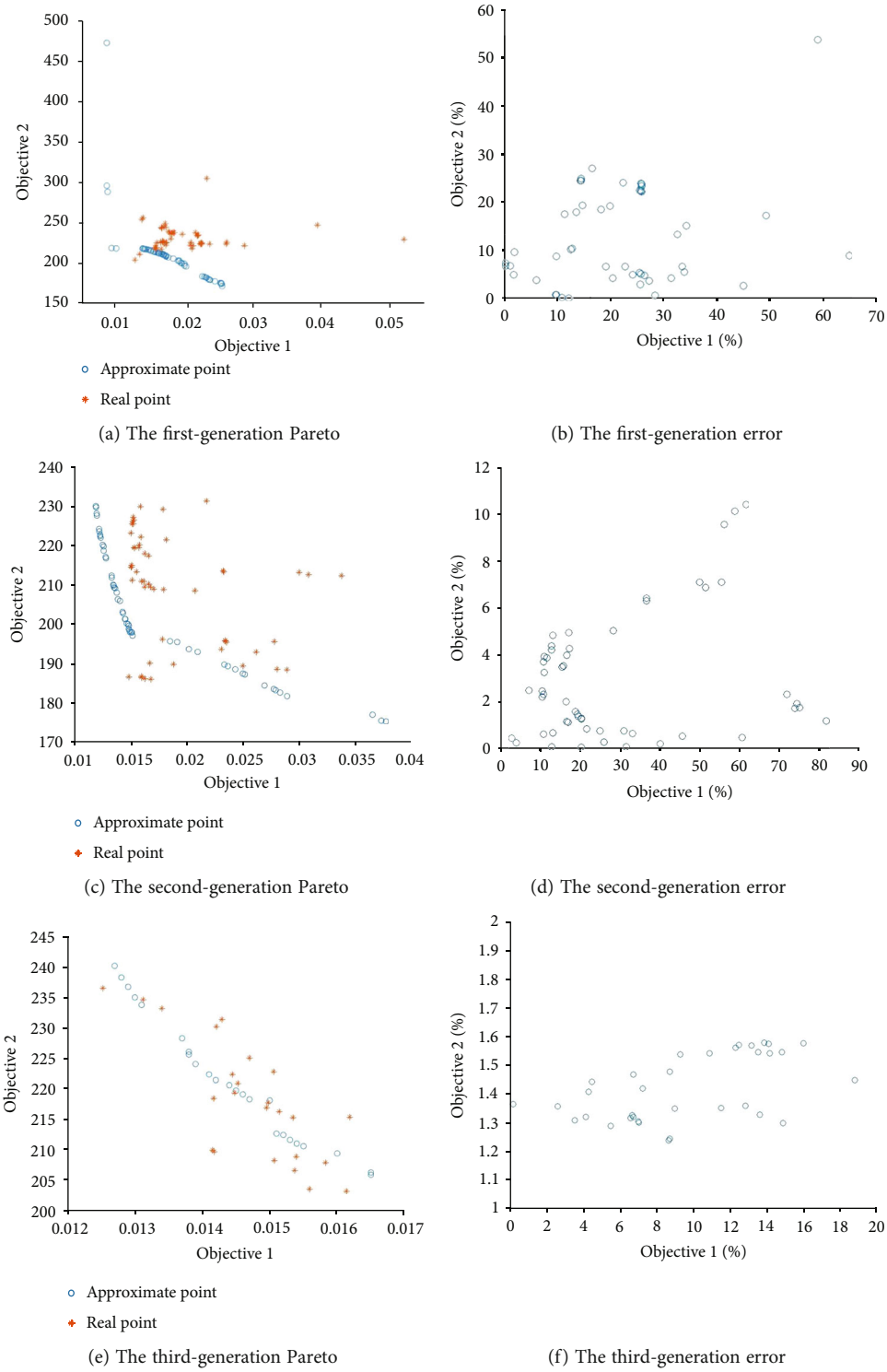

(a) The first-generation Pareto

(b) The first-generation error

(c) The second-generation Pareto

(d) The second-generation error

(e) The third-generation Pareto

(f) The third-generation error

Figure 5: Continued.

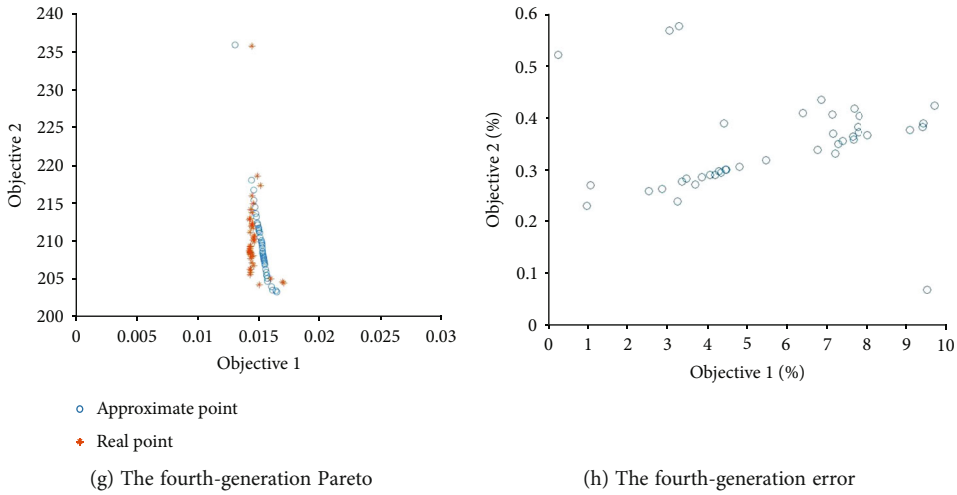

(g) The fourth-generation Pareto

(h) The fourth-generation error

Figure 5: Pareto result.

where b is the fixed cost during machining, which is not affected by changes in business volume during a certain period of time. a is the cost variation coefficient caused by the tolerance change of the machined part, and X is the rod tolerance. In order to improve the computational efficiency of the objective, an approximate model is constructed for the above objectives. The approximate model is a method to complete the construction of an explicit function model based on the mapping relationship of the implicit function. The radial basis function approximation model is selected, and its expression is as follows:

$$\tilde{f}(X) = \sum_{i=1}^{N} h_i(\|X - X_i\|)w_i, \tag{10}$$

where N is the number of overall sample points, $i = 1, 2, \cdots, N$, X_i is the sample point matrix, $\tilde{f}(X)$ is the approximation value corresponding to X, $h_i(\|X - X_i\|)$ is the kernel function, and w_i is the linear weighting coefficient.

3.3. Optimization Model. Considering the above factors, the optimization model of the truss structure can be described as

$$\begin{aligned} &\text{Minimize} \quad \left\{\tilde{f}_1(\mathbf{X}_1, \mathbf{X}_2), \tilde{f}_2(\mathbf{X}_1, \mathbf{X}_2)\right\} \\ &\text{subjected to} \quad 0 \le \mathbf{X}_1 \le 0.4, 0 \le \mathbf{X}_2 \le 0.4 \end{aligned} \tag{11}$$

$\tilde{f}_1(\mathbf{X}_1, \mathbf{X}_2), \tilde{f}_2(\mathbf{X}_1, \mathbf{X}_2)$ is an approximation of the real function. $\mathbf{X}_1, \mathbf{X}_2$ is the design variable. The process of the optimization algorithm is shown in Figure 4.

4. Optimization Results

4.1. Initial Settings. To simplify the calculation of the antenna truss, the length of the rod is set as 500 mm, and the total samples of the approximate model are set to 20. First, in the feasible domain of the design variables, the sample is obtained by the optimal Latin hypercube sampling method. Then, the calculation of the objective value is completed by the Monte Carlo method for each sample point. Finally, the initial construction of the optimization model is completed.

4.2. Analysis of Optimization Results. The multiobjective optimization genetic algorithm is set 600 times, and the model accuracy is further improved through the interpolation method. The results obtained by each generation of interpolation are shown in Figures 5(a), 5(c), 5(e), and 5(g). At the same time, the approximate value of the Pareto solution is compared with the real value. The error is shown in Figures 5(b), 5(d), 5(f), and 5(h). The interpolation method is used to update each generation, and the interpolation is four times in total.

Figures 5(a), 5(c), 5(e), and 5(g) are the distribution diagrams of the Pareto, and the horizontal axis is objective 1. Its value indicates the size of the average error, that is, the antenna surface accuracy. The vertical axis is objective 2, and its value indicates the level of the tolerance of the rod, that is, the cost of processing. Figures 5(b), 5(d), 5(f), and 5(h) are the percentage error between the approximate value and the real value, where the horizontal axis is the error of objective 1, and the vertical axis is the error of objective 2. Finally, we calculated the relationship between objective and tolerance, with accuracy and cost as the objective. In the overall truss antenna, the surface accuracy is usually between 1 mm and 3 mm. Since only one antenna unit is analyzed in this paper, the accuracy is relatively high. The above results are updated between generations by interpolation, and the points inserted in each generation are listed in Table 1.

Table 1 and Figure 5 show that the accuracy of the optimization results is improved by 2 interpolations effectively, and the final error is within 10%, of which the error of objective 2 is within 1%, which meets the initial design requirements. Figure 5(g) shows that the approximate point fits well with the real point, which can reflect the mathematical relationship between the variable and the objective. Therefore, it can obtain several sets of design points. Due to the

Table 1: Interpolation points.

No.	Design variable		Objective	
1	0.3546	0.2795	0.0153	258.4548
2	0.3756	0.3283	0.0148	213.8136
3	0.3367	0.3314	0.0209	238.2558
4	0.3367	0.3280	0.0195	239.9791
5	0.3375	0.3283	0.0194	239.1903
6	0.3981	0.3649	0.0168	186.2326
7	0.4000	0.3085	0.0338	212.3154
8	0.3687	0.3272	0.0142	218.3945

Table 2: Optimization results.

No.	×1 bottom rod tolerance	×2 web rod tolerance	f1 average precision	f2 cost
1	0.3870	0.3375	0.01613	203.15525
2	0.3672	0.3272	0.01448	219.31574
3	0.3794	0.3341	0.01540	208.85426
4	0.3680	0.3199	0.01506	222.69887
5	0.3558	0.3097	0.01253	236.36700

large number of obtained solutions, some points are selected and listed in Table 2.

Table 2 shows that if attention is paid to the high precision of the antenna regardless of the cost, the second set of design data can be selected, which has a high average accuracy of 0.01448 mm. If more emphasis is placed on cost, the first and third sets of design data can be selected, on the basis of sacrificing certain accuracy. If the accuracy and cost are considered comprehensively, there are several other sets of design data for selection, which can be further discussed according to other design requirements to meet different needs.

From the relationship between design variables and accuracy, one can conclude that the value of the web rod tolerance is often smaller than the bottom rod tolerance. In other words, the web rod tolerance has a more critical impact on the surface accuracy, so it is necessary to pay more attention to the web rod during manufacturing.

5. Conclusion

This paper analyzes the influence of uncertainty on the surface accuracy caused by the processing and assembly error in the space deployable antenna structure. First, the mechanical model is established based on the principle of minimum potential energy, and the precision distribution of its equilibrium state is solved by the Monte Carlo method. Then, a mathematical model between tolerance and accuracy is constructed by the radial basis function approximation model, which effectively saves the computational cost. Finally, a multiobjective optimization model is established, and the multiobjective genetic optimization algorithm is adopted to optimize and solve multiple sets of Pareto solutions that meet different production requirements. The conclusion is as follows:

(1) Under the premise of the processing and assembly error set in this paper, when the tolerances of the bottom rod and the web rod are designed as (±0.3558 mm, ±0.3097 mm), they have the best average accuracy value of 0.01253 mm, which can be considered the minimum accuracy of the structure

(2) From the relationship between design variables and accuracy, it can be concluded that the value of the web rod tolerance is often smaller than the bottom rod tolerance. That is, the influence of the web rod tolerance on the accuracy is more critical. Hence, more attention needs to be paid to the web rod accuracy during designing

(3) The calculation process of the accuracy probability distribution based on the Monte Carlo method is simplified by the radial basis function approximation model. As a result, through the multiobjective genetic optimization method and the local interpolation method, a solution set with an average error of less than 10% is obtained, which provides a more efficient and comprehensive design scheme for the antenna tolerance design

Data Availability

The raw/processed data required to reproduce these findings cannot be shared at this time as the data also forms part of an ongoing study.

Conflicts of Interest

The authors declare that they have no conflicts of interest.

Acknowledgments

This work was supported in part by the National Natural Science Foundation of China under Grant No. U20B2033.

References

[1] C. Z. Chen, J. Y. Dong, J. B. Chen, F. Lin, S. Jiang, and T. M. Liu, "Research progress of large spaceborne parabolic antennas," *Acta Aeronautica Sinica*, vol. 42, no. 1, pp. 133–153, 2021.

[2] B. Y. Duan, "Large spaceborne deployable antennas (LSDAs)—a comprehensive summary," *Chinese Journal of Electronics*, vol. 29, no. 1, pp. 1–15, 2020.

[3] X. F. Ma, Y. Li, Y. Xiao, S. K. Zheng, Z. R. Huang, and T. Feng, "Research status and prospects of large-scale space deployable antenna reflectors," *Space Electronics Technology*, vol. 15, no. 2, pp. 16–26, 2018.

[4] Y. Xu and F. L. Guan, "Structure-electronic synthesis design of deployable truss antenna," *Aerospace Science and Technology*, vol. 26, no. 1, pp. 259–267, 2013.

[5] Y. Yi and X. L. Ding, "Kinematic analysis of a plane deployable mechanism assembled by four pyramid cells," *Acta Aeronautica et Astronautica Sinica*, vol. 31, no. 6, pp. 1257–1265, 2010.

[6] T. Seki, K. Uehara, N. Ohmuro, M. Hirabe, and R. Kuzuya, *A 6-Sector Terminal Antenna Placed on the Face of a Hexagonal Prism for ATM Wireless Access System. Proceedings of the IEICE General Conference*, The Institute of Electronics, Information and Communication Engineers, 1998.

[7] K. Yonezawa, "Outline of engineering test satellite-VIII (ETS-VIII)," *21th International Symposium on Space Technology and Science*, pp. 24–31, 1998.

[8] T. Takano, K. Miura, M. Natori et al., "Deployable antenna with 10-m maximum diameter for space use," *Antennas & Propagation IEEE Transactions*, vol. 52, no. 1, pp. 2–11, 2004.

[9] D. K. Tian, R. Q. Liu, and X. L. Yang, "Deployment accuracy measurement and analysis of truss structure for modular space deployable truss antenna," *Journal of Mechanical Engineering*, vol. 56, no. 5, pp. 63–71, 2020.

[10] H. Xiao, L. Y. U. Shengnan, and X. L. Ding, "Optimizing accuracy of a parabolic cylindrical deployable antenna mechanism based on stiffness analysis," *Chinese Journal of Aeronautics*, vol. 33, no. 5, pp. 1562–1572, 2020.

[11] M. Mobrem, "Methods of analyzing surface accuracy of large antenna structures due to manufacturing tolerances," in *44th AIAA/ASME/ASCE/AHS/ASC Structures, Structural Dynamics, and Materials Conference*, 2003.

[12] C. Yang, X. B. Hou, and L. Wang, "Uncertain surface accuracy evaluation based on non-probabilistic approach for large spacecraft," *Acta Astronautica*, vol. 151, pp. 95–102, 2018.

[13] J. Zhang and F. Guo, "Statistical modification analysis of helical planetary gears based on response surface method and Monte Carlo simulation," *Chinese Journal of Mechanical Engineering*, vol. 28, no. 6, pp. 1194–1203, 2015.

[14] Y. Cao, T. Liu, and J. Yang, "A comprehensive review of tolerance analysis models," *International Journal of Advanced Manufacturing Technology*, vol. 97, no. 2, pp. 1–31, 2018.

[15] A. Ghaderi, H. Hassani, and S. Khodaygan, "A Bayesian-reliability based multi-objective optimization for tolerance design of mechanical assemblies," *Reliability Engineering and System Safety*, vol. 213, p. 107748, 2021.

[16] X. Wu, R. Cheng, T. Chan, G. Liu, and J. Xia, "Algorithm for rapidly predicting the worst surface accuracy of deployable mesh reflectors," *Applied Mathematical Modelling*, vol. 98, no. 4, pp. 229–244, 2021.

[17] S. U. Zihan, D. U. Baoyan, Y. Zhang, and Y. A. Dongwu, "Influence and experiment of cable-net manufacturing errors on surface accuracy of mesh reflector antennas," *Chinese Journal of Aeronautics*, 2021.

[18] B. Forouraghi, "Worst-case tolerance design and quality assurance via genetic algorithms," *Journal of Optimization Theory and Applications*, vol. 113, no. 2, pp. 251–268, 2002.

[19] Y. Yang, J. Luo, W. Zhang, S. Xie, Y. Sun, and H. Li, "Accuracy analysis of a multi-closed-loop deployable mechanism," *Proceedings of the Institution of Mechanical Engineers, Part C. Journal of mechanical engineering science*, vol. 230, no. 4, pp. 611–621, 2015.

[20] F. Lin, C. Z. Chen, J. B. Chen, and M. Chen, "Accuracy analysis of spatial multi-loop mechanism effected by paired bearings support joint clearance," *Journal of Mechanical Science and Technology*, vol. 34, no. 3, pp. 987–1003, 2020.

[21] Z. Q. Deng, D. K. Tian, R. Q. Liu, and H. W. Guo, "Prediction model for optimization parameters of framed space deployable antenna structure," *Journal of Harbin Institute of Technology*, vol. 43, no. 11, pp. 39–43, 2011.

[22] P. K. Singh, S. C. Jain, and P. K. Jain, "Advanced optimal tolerance design of mechanical assemblies with interrelated dimension chains and process precision limits," *Computers in Industry*, vol. 56, no. 2, pp. 179–194, 2005.

[23] A. Sanz, M. Guimeráns, I. González, and J. Pérez, "Comparative analysis of tolerance allocation in mechanical assemblies based on cost-tolerance curves," in *AIP Conference Proceedings*, vol. 1431, pp. 197–206, Cadiz, Spain, September 2012.

[24] S. Koziel and S. Ogurtsov, "Multi-objective design of antennas using variable-fidelity simulations and surrogate models," *IEEE Transactions on Antennas and Propagation*, vol. 61, no. 12, pp. 5931–5939, 2013.

[25] J. A. Easum, J. Nagar, P. L. Werner, and D. H. Werner, "Efficient multiobjective antenna optimization with tolerance analysis through the use of surrogate models," *IEEE Transactions on Antennas and Propagation*, vol. 66, no. 12, pp. 6706–6715, 2018.

[26] M. Li, Q. Cui, M. Wu, X. Zhou, F. Shi, and G. Meng, "Flatness-oriented parameters allocation of multi-panel deployable antenna based on Monte-Carlo simulation," in *2019 9th International Conference on Recent Advances in Space Technologies (RAST)*, vol. 22, pp. 497–502, Istanbul, Turkey, June 2019.

[27] S. Yuan, B. Yang, and H. Fang, "Self-standing truss with hard-point-enhanced large deployable mesh reflectors," *AIAA Journal*, vol. 57, no. 11, pp. 5014–5026, 2019.

[28] S. Yuan and M. J. Wu, "Optimal shape adjustment of large high-precision cable network structures," *AIAA Journal*, vol. 59, no. 4, pp. 1441–1456, 2021.

[29] S. Yuan, B. Yang, and H. Fang, "Direct root-mean-square error for surface accuracy evaluation of large deployable mesh reflectors," in *AIAA Scitech 2020 Forum*, Orlando, FL, USA, January, 2020.

[30] S. Yuan, "Review of root-mean-square error calculation methods for large deployable mesh reflectors," *International Journal of Aerospace Engineering*, vol. 2022, Article ID 5352146, 18 pages, 2022.

[31] Q. S. Chen, B. Q. Xin, S. Q. Bie, Z. J. Men, and Y. B. Sun, "Study on mathematical model of multi-objective tolerance distribution of press quality and cost," *China Metalforming Equipment & Manufacturing Technology.*, vol. 54, no. 1, pp. 78–83, 2019.

[32] X. B. Hu, W. Zhang, B. C. Lu, L. Z. Huang, S. Wang, and M. Q. Wang, "Multi-objective optimization design of tolerance based on discretized cost-tolerance model," *Computer Integrated Manufacturing Systems*, vol. 25, no. 1, pp. 182–189, 2019.

Hindawi
International Journal of Aerospace Engineering
Volume 2022, Article ID 5424839, 7 pages
https://doi.org/10.1155/2022/5424839

Research Article

Electrical Property of 3D Printed Continuous Fiber Reinforced Thermoplastic Composite Mesh Reflecting Surfaces

Kunyang Lin,[1,2] **Xiaofei Ma**,[2] **Zhen Cui**,[2] **Youwei Kang**,[3] **Pengfei Huang**,[2] **Huanxiao Li**,[2] **Di Wu**,[2,4] **Guanlong Su**,[2] **and Xiaoyong Tian**[3]

[1]*School of Mechanical Engineering, Xi'an Jiaotong University, Xi'an, 710049 Shaanxi, China*
[2]*Xi'an Institute of Space Radio Technology, Xi'an, 710100 Shaanxi, China*
[3]*State Key Laboratory for Manufacturing Systems Engineering, Xi'an Jiaotong University, Xi'an, 710049 Shaanxi, China*
[4]*College of Astronautics, Nanjing University of Aeronautics and Astronautics, Nanjing, 210016 Jiangsu, China*

Correspondence should be addressed to Xiaofei Ma; maxf041600@sina.com

Received 26 July 2022; Revised 21 September 2022; Accepted 24 September 2022; Published 11 October 2022

Academic Editor: Sichen Yuan

Continuous fiber reinforced thermoplastic composites have been widely used in modern aerospace and other high-end manufacturing fields because of their light weight, high strength, fatigue resistance, and corrosion resistance properties. Due to the reinforcement of carbon fiber strands, continuous fiber reinforced thermoplastic composites have good conductivity which makes it a potential material for the preparation of space-borne antennas reflecting surfaces. The reflecting surfaces of common mesh antennas are usually prepared by gold-plated molybdenum wire which is expensive and hard to produce. In this study, the continuous fiber reinforced thermoplastic composites mesh reflecting surfaces are prepared by 3D printing technology. The effect of different mesh shape and mesh size on the electrical properties are investigated systematically. The electrical property of the reflecting surface were tested by waveguide method at the S band with the frequency of 1.9 ~ 2.3GHz. The results show that the reflection loss of the 3D printed continuous fiber reinforced thermoplastic composite mesh reflecting surfaces are lower than 0.25 dB, which can well meet the requirement of space-borne antennas in the S waveband. The reflection loss of the 3D printed continuous fiber reinforced thermoplastic composite mesh reflecting surfaces increases with the increase of mesh size accordingly for both the quadrangular and the triangular mesh reflecting surface. The reflecting property of the mesh reflecting surface tends to be better with a higher surface mass density. The results foresee that the continuous fiber reinforced thermoplastic composites can be used to develop the reflector of large mesh antenna in the future work.

1. Introduction

Space-borne antennas are one of the most important payloads on the satellite used for communication, deep space exploration, remote sensing, navigation radio astronomy, and earth observation. In order to meet the demand of increased resolution or sensitivity for multiple functions, the size of space-borne antennas tends to be larger and larger during the past decades [1–5]. Considering the constraints of the current launch vehicle, traditional space-borne antennas are designed as deployable structures which folded in the fairing during launch stage and unfolded independently in space. The size of deployable space-borne antenna is always restrained by the fairing size and weight requirements of the launch vehicle with a limit of one hundred meter level [6–8].

In order to construct super large space antennas in the kilometer scale, the deployable antenna cannot meet the requirements. The focus now on in-space construction technology is becoming very noticeable due to the capacity of constructing large space structure on the orbit, the moon, the mars, and another planet [9–11]. Nowadays, agencies like National Aeronautics and Space Administration (NASA) and European Space Agency (ESA) have been conducting research in how to use additive manufacturing in a variety of space-related applications, from using it to print CubeSat propulsion systems, to printing ceramics,

and to printing large spacecraft in space [12]. NASA released a national initiative in 2020 to accelerate "in-orbit space assembly and maintenance". The Defense Advanced Research Projects Agency (DARPA) also listed "in-orbit manufacturing of large antennas" in its top 10 aerospace frontier technologies. The European Union released the "Space Factory" project in 2021, which aims at building a manufacturing platform for spacecraft such as satellites and large antennas in space orbit. In the 2020 China Space Conference, "on-orbit additive manufacturing technology for space ultra-large antenna structure" was listed as the "top ten scientific and technical problems" in the field of aerospace.

As the most vital part of space-borne antenna, the reflecting surface is the most likely component to be constructed in space by additive manufacturing technology. The performance of deployable space-borne antennas depends primarily on the properties of reflecting surfaces which is always made of knitted wire mesh with different kind waves to reduce weight and volume [13–15]. However, considering the complexity technology of wire mesh, it is hard to produce the wire mesh surface in space. An alternative is to consider continuous fiber reinforced thermoplastic composites as the raw material of reflecting surface to printing the reflecting surface in space by additive manufacturing technology.

Benefit from the superior conductivity of carbon fiber, continuous fiber reinforced thermoplastic composites tends to be a good electrical conductor which makes it a potential candidate material for the reflecting surface of space-borne antenna [16, 17]. Fused deposition modeling (FDM) is one of the most commonly used additive manufacturing technologies (also known as 3D printing) [18, 19]. Tian et al. proposed a novel FDM process to print continuous fiber reinforced thermoplastic composites using fiber and plastic filament as the raw materials [20]. The FDM process is used to print the reflecting surface in this study. In a typical process, a filament of material is fed into a machine via a pinch roller mechanism. The feedstock is melted in a heated liquefier with the solid portion of the filament acting as a piston to push the melt through a print nozzle. A gantry moves the print nozzle in the horizontal x–y plane as the material is deposited on a build surface that can be moved in the vertical z direction. The extruded material rapidly solidifies and adheres with the surrounding material to accumulate the required complex plastic parts. The 3D printed continuous fiber reinforced thermoplastic composites with a fiber content of 27% achieve the maximum flexural strength of 335 MPa and flexural modulus of 30GPa. The technology has been tested in space by Chinese Changzheng-5B rocket, which has shown high application value in in-space manufacturing field. Markforged Company also developed a 3D printer for continuous fiber reinforced thermoplastic composites process using pre-preg filament with continuous fiber and thermal plastic matrix.

For the continuous fiber reinforced thermoplastic composites, most of the researches focus on the material preparation process and properties [21]. There are few researches have been done for the continuous fiber reinforced thermoplastic composites as a reflecting mesh surface of antenna. The performance of space-borne antenna mainly depends on the electrical property of the reflecting surface at designated frequency. Li and Su developed a method to predict the electrical performances of the mesh reflector structures with complex weave patterns [22]. However, the electrical property of continuous fiber reinforced thermoplastic composites reflecting surface has not been studied yet, which will restrict the application of continuous fiber reinforced thermoplastic composites in the field of space-borne antenna.

In this research, the continuous fiber reinforced thermoplastic composites reflecting surfaces with different shape and mesh were prepared by the FDM process. The electrical property of 3D printed continuous fiber reinforced thermoplastic composites reflecting surfaces were systematically studied. Electrical property of the reflecting surface was tested by waveguide method. The effect of mesh shape, mesh size, and surface mass density on the electrical property was discussed in this paper. The structure of this paper is organized as below. In Section 2, the experimental platform, specimens and electrical property test method are presented. In Section 3, the effect of different parameters on the electrical property of the continuous fiber reinforced thermoplastic composites reflecting surfaces are discussed. Finally, the conclusions are given in Section 4.

2. Experimental Procedures

2.1. Experimental Platform. In this work, the FDM based 3D printing method was utilized to print the continuous fiber reinforced thermoplastic composites reflecting surfaces. The 3D printer was developed by Xi'an Jiaotong University, which was consisted of extrusion head, control system, building platform, X-Y motion mechanism etc., as shown in Figure 1. Detailed parameters and components of the 3D printer were introduced in the reference [20]. The printing process is called continuous fiber reinforced thermoplastic composite 3D printing technology. The scheme of printing head and process parameters are shown in Figure 2. During the 3D printing process, thermoplastic polymers filaments and continuous fibers were fed into the heated printer head simultaneously. As the action of high temperature, polymers filaments melted and formed a melting pool. Continuous carbon fibers were impregnated with molten polymers while passed through the printer head. Under the pressure in the printer head, impregnated continuous fibers were extruded. The carbon fibers and polymers solidified and bonded on the workbench with the preplanned print routes. The continuous fiber reinforced thermoplastic composite components were fabricated with layer by layers upon the deposited components.

2.2. Material and Specimens. The thermoplastic matrix material was polyamides wire produced by Flashforge Corp in China. 1 K carbon fiber tows from TENAX-J Corp in Japan was used as the reinforcement. In order to investigate the effect of mesh shape and mesh size on the electric property of the continuous fiber reinforced thermoplastic composite mesh reflecting surface, two kinds of mesh shape with four kinds of fiber interval were prepared in this experiment as shown in Table 1. The mesh shape included

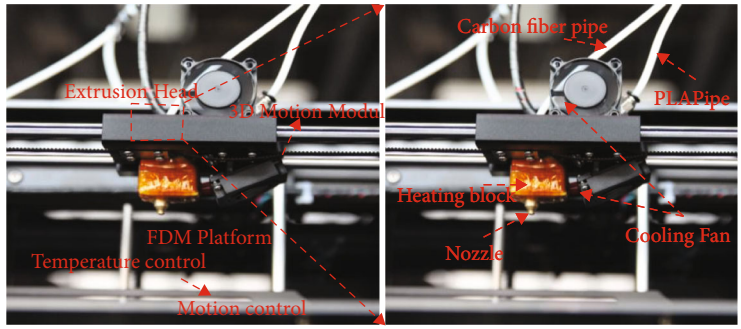

Figure 1: 3D printer used to prepare the continuous fiber reinforced thermoplastic composites.

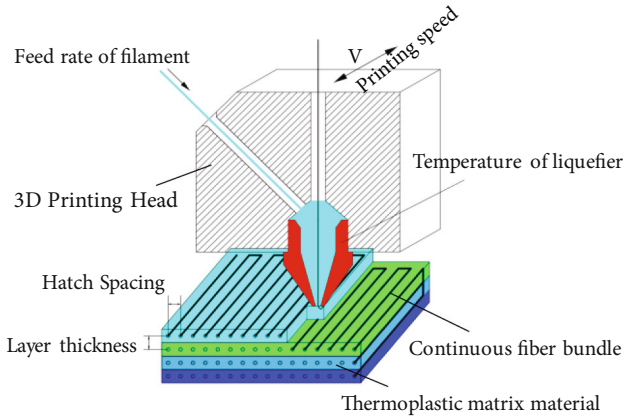

Figure 2: Scheme of 3D printing for the continuous fiber reinforced thermoplastic composites.

triangle and quadrangle mesh. The dimension of specimens was all 200 mm ×200 mm. The fiber interval of different mesh size was set as 2 mm, 3 mm 4 mm, and 5 mm, respectively. All of the specimens were prepared by the aforementioned FDM 3D printer with the same printing parameters. The specimens are shown in Figure 3.

2.3. Electrical Property Test. Waveguide method was utilized to test the electrical property of the continuous fiber reinforced thermoplastic composites mesh reflecting surface. The electrical property test schematic is shown in Figure 4. The electromagnetic wave energy was measured by the vector network analyzer which was produced by Agilent Technologies Inc. The recycling mesh was placed at one end of the waveguide and fixed by four bolts as shown in Figure 5. Before each test, a 5 mm aluminum plate was utilized for zero setting.

3. Results and Discussion

It is well known that the performance of mesh reflector antennas depended on how well the reflecting surface performs at the designed frequencies. The reflection loss is one of the main factors of reflecting surfaces due to the microwave leakage loss through the mesh gap. The mesh material, mesh structure, mesh shape and mesh size, and wire diameter are related to the reflection loss. In order to test the reflecting properties of 3D printed continuous fiber reinforced thermoplastic composite reflecting surfaces, the reflection losses of the reflecting surfaces with different mesh size and shape are get by the vector network analyzer at the S waveband with the frequency of 1.9 ~ 2.3GHz.

3.1. Effect of Mesh Shape on the Electrical Property. Triangle and quadrangle mesh surface are the most widely used reflecting surface of space-borne antennas, which can be well produced by the 3D printing technology layer by layers. In this experiment, the reflecting properties of different mesh shape surfaces are tested. Figure 6 shows the effect of triangle and quadrangle mesh surfaces on the reflection loss. In general, the reflection loss of the 3D printed continuous fiber reinforced thermoplastic composite reflecting surface is lower than 0.25 dB. It seems that the continuous fiber reinforced thermoplastic composite reflecting surface can well meet the requirement of space-borne antennas in the S waveband. When the mesh size is 3 ~ 5 mm, the reflection loss of triangle mesh reflecting surface is lower than the quadrangle mesh surface. It seems that the reflecting property of triangle mesh reflecting surface performs better than the quadrangle mesh reflecting surface at a larger mesh size. When the mesh size is 2 mm, the reflection loss of triangle mesh reflecting surface is larger than the quadrangle mesh reflecting surface with the reflecting loss of 0.06 dB and 0.10 dB, respectively. This is due to the reason that the surface mass density increases with the decrease of mesh size. For the smaller size mesh, the surface mass density is higher. The higher mass density means higher resin matrix content, which may have a significant effect on the reflection loss due to the poor reflection properties of resin matrix.

3.2. Effect of Mesh Size on the Electrical Property. The effect of mesh size on the electrical property of the continuous fiber reinforced thermoplastic composites reflecting surfaces with different shape is shown in Figure 7. It can be seen that the reflection loss increases with the increase of mesh size accordingly no matter for the quadrangular or triangular mesh reflecting surface. For the quadrangular mesh reflecting surface in Figure 7(a), the reflection loss almost linear increases with the mesh size smaller than 4 mm. When the quadrangular mesh is larger than 4 mm, the effect of mesh size on the electrical property tend to decrease. For the triangular mesh reflecting surface in Figure 7(b), when the

Table 1: The continuous fiber reinforced thermoplastic composites reflecting surface with different mesh shape and mesh size.

Mesh shape of reflecting surface	Dimension of specimen (mm)	Mesh size L (mm)	Scheme
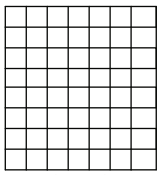 Quadrangle	200 × 200	2, 3, 4, 5	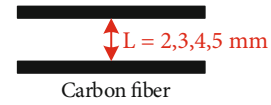
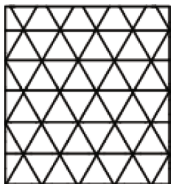 Triangle	200 × 200	2, 3, 4, 5	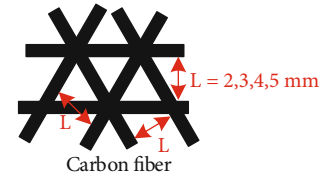

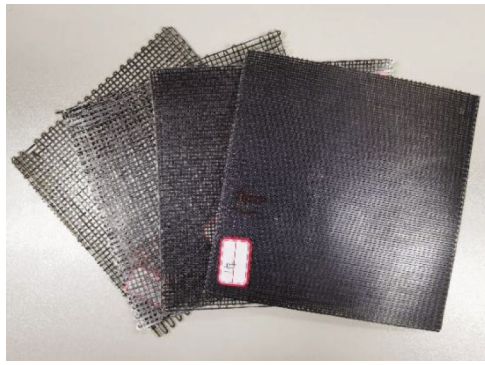

Figure 3: Continuous fiber reinforced thermoplastic composite mesh reflector specimen based on additive manufacturing technology.

triangular mesh size is smaller than 4 mm, the effect of mesh size on the reflection loss in not significant when the triangular mesh size is larger than 4 mm, a larger mesh size results in a higher reflection loss.

In order to express the electrical properties of reflecting surface clearly, the mean reflection coefficient Γ is calculated by the Equation (1), where L is reflection loss.

$$\Gamma = 10^{-L/20} \times 100\%. \quad (1)$$

The reflection wave, transmission wave, and loss are formed while the incident electromagnetic wave is reflected through the continuous fiber reinforced thermoplastic composites reflecting surfaces. Higher reflection coefficient corresponds to more reflection wave which means better reflection properties of the reflection mesh surface. The reflection coefficient of continuous fiber reinforced thermoplastic composites is generally greater than 97% which shows a perfect reflecting performance. Compared with the knitted wire mesh reflecting surface, the nonuniform mesh size and the imperfect electrical contact between the wires will cause unwanted clutter and power loss due to passive intermodulation. Passive intermodulation, also known as intermodulation distortion, represents the intermodulation products generated when two or more signals are transmitted through a passive device with nonlinear characteristics. Passive intermodulation may affect the transceiver characteristics of antennas and must be minimized for the antenna during the development stage. The continuous fiber reinforced thermoplastic composites reflecting surfaces produced by 3D printing technology layer by layer continuously results in a better interlayer bonding performance which may reduce the passive intermodulation properties. The excellent reflecting performance of the continuous fiber reinforced thermoplastic composites also makes it potential candidate materials for the in-orbit constructed larger antenna reflecting surface.

3.3. Effect of Surface Mass Density on the Electrical Property. For the mesh reflector antenna, the surface mass density is always related with the reflection performance of the mesh reflecting surface. In order to investigate the relationship between the surfaces mass density and reflecting properties of the continuous fiber reinforced thermoplastic composites. The mass and area of every specimen are measured by the electronic balance and ruler. The surface mass density D is calculated as follows:

$$D = \frac{m}{S}, \quad (2)$$

where m and S are the mass and area of the continuous fiber reinforced thermoplastic composites reflecting surface specimen, respectively.

In Figure 8, the reflection coefficient of the continuous fiber reinforced thermoplastic composites reflecting surfaces is plotted versus the increase of surface mass density. The short dash lines in the figure, which is the linear fitting curves for the experimental results, have no exact physical meaning and just show the approximate changing trends of the data. The surface mass density seems to play an important role in the reflecting properties. For the quadrangular mesh reflecting surface, the reflection coefficient increases with the increase of surface mass density. On the other hand, the relationship between reflection coefficients

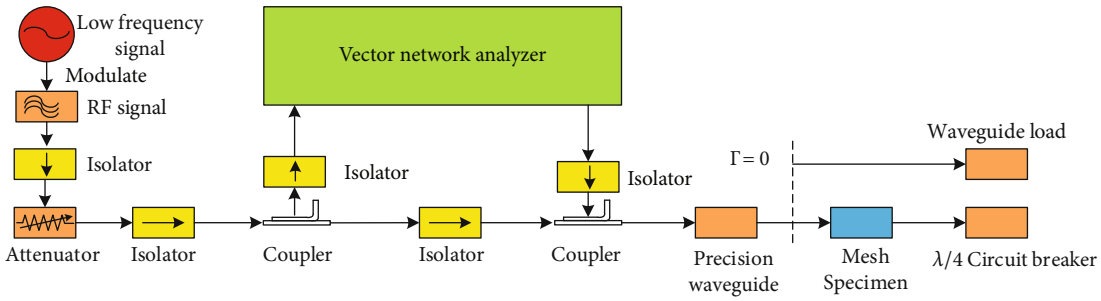

Figure 4: Electrical property test scheme by waveguide method.

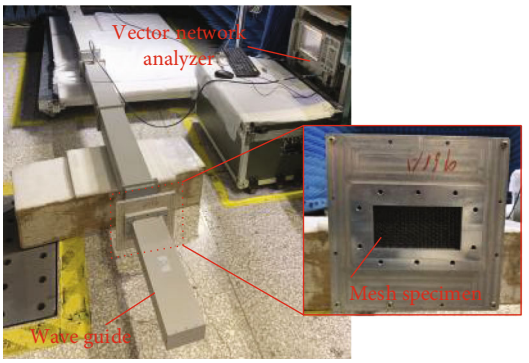

Figure 5: Electrical property test experiment.

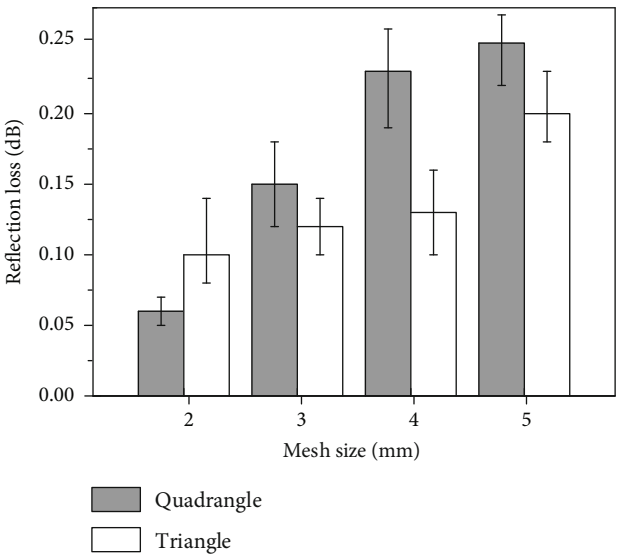

Figure 6: Effect of mesh shape on the reflection loss of the continuous fiber reinforced thermoplastic composites reflecting surfaces.

and surface mass density is not monotonic for the triangular mesh reflecting surface. The reflection coefficient tends to increase with a larger surface mass density of the triangular mesh reflecting surface while the surface mass density is lower than 0.03 g/cm^2. However, the reflection coefficient of the triangular mesh reflecting surface is not significant while the surface mass density is larger than 0.03 g/cm^2.

The shape of mesh surface has an important effect on the surface reflecting properties. For the mesh reflecting surface with the same mesh size and different mesh shape, the surface mass density is different. The surface mass density of triangular mesh reflecting surface is higher than the quadrangular mesh reflecting surface with the same mesh size. For this reason, the triangular mesh reflecting surface seems to have better electrical properties with smaller mesh size. As the surface mass density increases further, the quadrangular mesh reflecting surface shows a greater reflecting performance than the triangular mesh reflecting surface. The larger surface mass density means more raw material and higher cost. The quadrangular mesh reflecting surface with

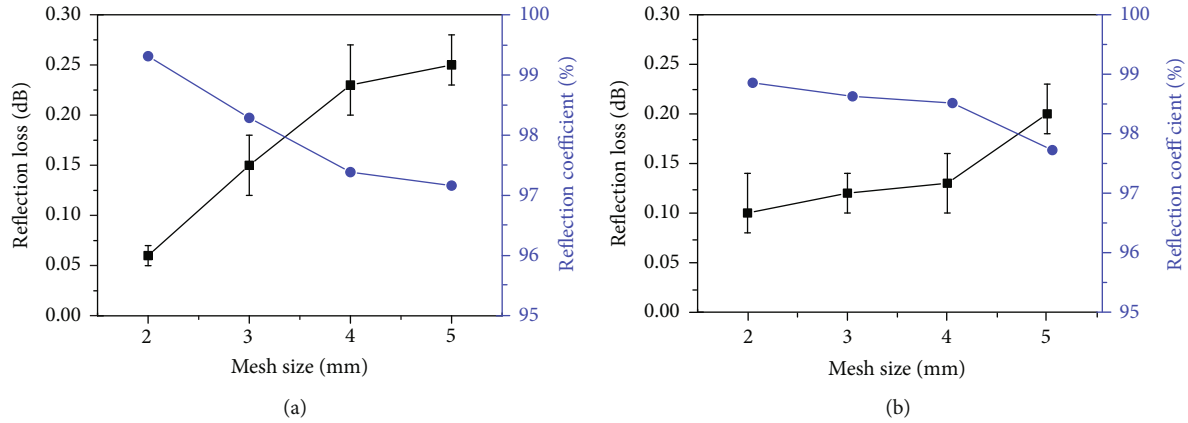

FIGURE 7: Effect of mesh size on the electrical property of the continuous fiber reinforced thermoplastic composites reflecting surfaces: (a) quadrangular mesh reflecting surface; (b) triangular mesh reflecting surface.

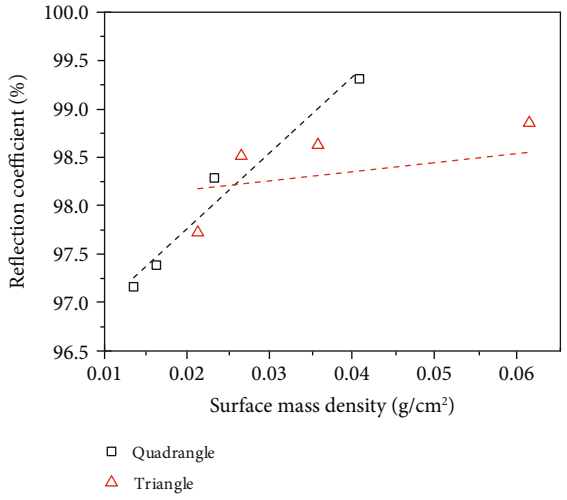

FIGURE 8: Effect of surface mass density on the reflection coefficient of the continuous fiber reinforced thermoplastic composites reflecting surfaces.

smaller mesh size is preferred for the antenna desired greater reflecting performance.

4. Conclusions

The electrical properties of 3D printed continuous fiber reinforced thermoplastic composite mesh reflecting surfaces with different mesh shape and mesh size have been investigated experimentally in this study. The reflecting properties of the mesh surface were obtained using waveguide method at the S waveband with the frequency of 1.9 ~ 2.3GHz. The main conclusions can be drawn as follows:

(1) The reflection loss of the 3D printed continuous fiber reinforced thermoplastic composite mesh reflecting surfaces are lower than 0.25 dB, which can well meet the requirement of space-borne antennas in the S waveband

(2) The electrical property of the 3D printed continuous fiber reinforced thermoplastic composite mesh reflecting surfaces is related with the surface mesh shape. The triangular mesh reflecting surface performs a better electrical property when the mesh size is larger than 3 mm

(3) The reflection loss of the 3D printed continuous fiber reinforced thermoplastic composite mesh reflecting surfaces increases with the increase of mesh size accordingly for both the quadrangular and the triangular mesh reflecting surface

(4) The surface mass density of the 3D printed continuous fiber reinforced thermoplastic composite mesh reflecting surfaces with 2 ~ 5 mm mesh size is found around 0.01~0.06 g/cm^2. The reflecting property of the mesh reflecting surface tends to be better with a higher surface mass density

Data Availability

The data used to support the findings of this study are available from the corresponding author upon request.

Conflicts of Interest

The authors declare that there is no conflict of interest regarding the publication of this paper.

Acknowledgments

This work is sponsored by the Project founded by China Postdoctoral Science Foundation (Grant No. 2021 M703492).

References

[1] X. F. Ma, T. J. Li, J. Y. Ma et al., "Recent advances in space-deployable structures in China," *Engineering*, 2022.

[2] Z. Sun, D. Yang, B. Duan, L. Kong, and Y. Zhang, "Structural design, dynamic analysis, and verification test of a novel

double-ring deployable truss for mesh antennas," *Mechanism and Machine Theory*, vol. 165, article 104416, 2021.

[3] B. Siriguleng, W. Zhang, T. Liu, and Y. Z. Liu, "Vibration modal experiments and modal interactions of a large space deployable antenna with carbon fiber material and ring-truss structure," *Engineering Structures*, vol. 207, article 109932, 2020.

[4] M. J. Li, M. Li, Y. F. Liu, X. Y. Geng, and Y. Y. Li, "A review on the development of Spaceborne membrane antennas," *Space: Science & Technology*, vol. 2022, article 9803603, 12 pages, 2022.

[5] L. Puig, A. Barton, and N. Rando, "A review on large deployable structures for astrophysics missions," *Acta Astronautica*, vol. 67, no. 1-2, pp. 12–26, 2010.

[6] G. Su, X. Ma, Y. Li, Y. Fan, and H. Wang, "Pretension design and analysis of deployable mesh antenna considering the effect of gravity," *International Journal of Aerospace Engineering*, vol. 2022, Article ID 4676944, 11 pages, 2022.

[7] S. Yuan and W. Jing, "Optimal shape adjustment of large high-precision cable network structures," *AIAA Journal*, vol. 59, no. 4, pp. 1441–1456, 2021.

[8] S. Yuan, B. Yang, and H. Fang, "Self-standing truss with hard-point-enhanced large deployable mesh reflectors," *AIAA Journal*, vol. 57, no. 11, pp. 5014–5026, 2019.

[9] E. Sacco and S. K. Moon, "Additive manufacturing for space: status and promises," *The International Journal of Advanced Manufacturing Technology*, vol. 105, no. 10, pp. 4123–4146, 2019.

[10] T. Prater, N. Werkheiser, F. Ledbetter, D. Timucin, K. Wheeler, and M. Snyder, "3D printing in zero G technology demonstration mission: complete experimental results and summary of related material modeling efforts," *The International Journal of Advanced Manufacturing Technology*, vol. 101, no. 1-4, pp. 391–417, 2019.

[11] B. Blakey-Milner, P. Gradl, G. Snedden et al., "Metal additive manufacturing in aerospace: a review," *Materials & Design*, vol. 209, article 110008, 2021.

[12] K. Ishfaq, M. Asad, M. A. Mahmood, M. Abdullah, and C. I. Pruncu, "Opportunities and challenges in additive manufacturing used in space sector: a comprehensive review," *Rapid Prototyping Journal*, 2022.

[13] T. Li, J. Jiang, T. Shen, and Z. Wang, "Analysis of mechanical properties of wire mesh for mesh reflectors by fractal mechanics," *International Journal of Mechanical Sciences*, vol. 92, pp. 90–97, 2015.

[14] S. Yuan and B. Yang, "A New strategy for form finding and optimal design of space cable network structures," in *Nonlinear Approaches in Engineering Application: Design Engineering Problems*, L. Dai and R. N. Jazar, Eds., pp. 245–285, Springer, Cham, 2022.

[15] S. Yuan, B. Yang, and H. Fang, "The projecting surface method for improvement of surface accuracy of large deployable mesh reflectors," *Acta Astronautica*, vol. 151, pp. 678–690, 2018.

[16] Q. Chen, P. Boisse, C. H. Park, A. Saouab, and J. Bréard, "Intra/inter-ply shear behaviors of continuous fiber reinforced thermoplastic composites in thermoforming processes," *Composite Structures*, vol. 93, no. 7, pp. 1692–1703, 2011.

[17] Q. Jia, N. An, X. Ma, and J. Zhou, "Exploring the design space for nonlinear buckling of composite thin-walled lenticular tubes under pure bending," *International Journal of Mechanical Sciences*, vol. 207, article 106661, 2021.

[18] B. N. Turner, R. J. Strong, and S. A. Gold, "A review of melt extrusion additive manufacturing processes: i. process design and modeling," *Rapid Prototyping Journal*, vol. 20, no. 3, pp. 192–204, 2014.

[19] B. N. Turner and S. A. Gold, "A review of melt extrusion additive manufacturing processes: ii. materials, dimensional accuracy, and surface roughness," *Rapid Prototyping Journal*, vol. 21, no. 3, pp. 250–261, 2015.

[20] X. Tian, T. Liu, C. Yang, Q. Wang, and D. Li, "Interface and performance of 3D printed continuous carbon fiber reinforced PLA composites," *Composites Part A: Applied Science and Manufacturing*, vol. 88, pp. 198–205, 2016.

[21] X. L. Ma, L.-h. Wen, S. Y. Wang, J. Y. Xiao, W. H. Li, and X. Hou, "Inherent relationship between process parameters, crystallization and mechanical properties of continuous carbon fiber reinforced PEEK composites," *Defence Technology*, 2022.

[22] T. Li and J. Su, "Electrical properties analysis of wire mesh for mesh reflectors," *Acta Astronautica*, vol. 69, no. 1-2, pp. 109–117, 2011.

Hindawi
International Journal of Aerospace Engineering
Volume 2022, Article ID 1862392, 17 pages
https://doi.org/10.1155/2022/1862392

Research Article

A Passive Vibration Control Method of Modular Space Structures Based on Band Gap Optimization

Juntao Zhu, Tuanjie Li, Bo Li, Yaqiong Tang, Zuowei Wang, and Qingjuan Duan

School of Mechano-Electronic Engineering, Xidian University, Xi'an 710071, China

Correspondence should be addressed to Tuanjie Li; tjli@mail.xidian.edu.cn

Received 17 July 2022; Revised 5 August 2022; Accepted 26 August 2022; Published 9 September 2022

Academic Editor: Jinchao Chen

Modular space structure has become a research hotspot in the aerospace field. In the microgravity and weak damping space environment, modular space structures may continuously vibrate due to the transient excitation caused by satellite attitude adjustment or space debris impact, which will make the structure unstable. Therefore, a passive vibration control method based on band gap design is proposed for the modular space structures. Firstly, a modular spectral element model based on the super element is established, and the modular spectral element model is expanded into modular space structures. Then, band gap characteristics of the modular space structure are analyzed and optimized to improve the wave isolation ability. The numerical simulation shows that the elastic wave in the band gap can be effectively isolated and the band gap is significantly improved by optimizing structural parameters.

1. Introduction

Deployable space structures have been widely used in aerospace due to the advantages of lightweight and large ratio of deployed and folded volumes. With the development toward large-scale, high-precision, and on-orbit assembling [1], the modularization structure has become a popular structural form for deployable space structures. Modular space structures belong to a class of dynamical systems with weak damping and large flexibility. It is well known that this type of system will continuously vibrate under complex space environments, such as the transient excitation caused by satellite attitude adjustment or space debris impact. Therefore, control methods [2–5] must be considered to eliminate the vibration.

For space structures, the vibration control method can be divided into two categories: active and passive control. Active control [6–8] introduces an automatic control system with an additional power supply to dampen the vibration amplitude. It can provide optimal vibration control effect under some specific conditions, but the control system is complex, and it is hard to obtain enough power in space. Passive control, in contrast, needs no additional power supply, and it has the advantages of low cost, high reliability, broadband vibration reduction, and so on.

So far, some scholars have investigated the passive control methods for space structures. Bishop and Striz [9] studied an optimal configuration method of viscous dampers for a modular frame structure based on the genetic algorithm. Xu et al. [10] proposed a hybrid optimization model combining the evolutionary algorithm with the simulated annealing algorithm to solve the configuration problem of viscoelastic dampers. Kim et al. [11] investigated a magnetorheological (MR) damper-based intelligent passive control system for mitigating the vibration of stay cables. It was found that the vibration reduction effect was slightly better than conventional MR dampers. Tong and Zhao [12] investigated the optimization of multiple tuned mass dampers (TMDs) to reduce vibrations of flexible structures. Preumont et al. [13] studied the vibration reduction analysis of the modular frame structure based on the piezoelectric vibration absorber. It can be found that the damping vibration reduction with surface damping layers [14], discrete dampers, and vibration absorbers [15] has been widely used in space structures. However, the damping vibration reduction needs to be equipped with many dampers to achieve a

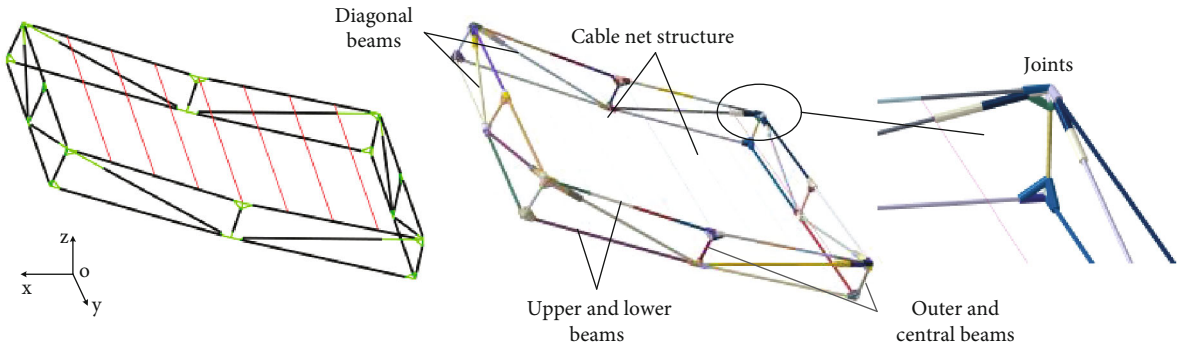

Figure 1: Basic unit structure of modular space structures.

better control effect, which will increase the additional mass of the system.

It is noted that modular space structures have the property of periodic arrays, that is, band gaps. That is to say, we can optimize the structure material and geometric parameters to tune the position and width of the band gaps so that the self-vibration-suppression capability can be improved [16]. Inspired by this, we take the basic unit of modular space structures as a super element composed of various materials so that we can improve the elastic wave isolation ability by artificially optimizing the band gap.

At present, the band gap of periodic structures can be analyzed by the finite element method (FEM) [17, 18], the finite difference method [19], the plane wave expansion method [20], the traveling wave method [21], the transfer matrix method [22], the spectral element method (SEM) [23–26], etc. Thereinto, SEM is proposed and applied to truss-type space structures by U. Lee and J. Lee [27]. Dutkiewicz and Machado [28] analyzed vibrations of an overhead transmission line in a damping environment. Jeong et al. [29] investigated the vibration analysis of a multispan beam subjected to a moving point force by SEM. The SEM has the advantages of low computational cost and accurate calculation results. So, the SEM is used to build the dynamic model for the gap band analysis of modular space structures.

However, in the optimization iteration process, a large number of frequencies need to be calculated over and over again, which results in a huge amount of computation. What is worse, there are too many structural parameters to optimize the gap band effectively. Therefore, a super element model is first established and grouped for modular structures to obtain a fast and accurate calculation. Then, sensitivity analysis is carried out to select sensitive parameters and eliminate invalid design variables for the band gap optimization model. Compared with traditional damping vibration reduction methods, the proposed method realizes the vibration control without additional mass and cost. This paper provides a new idea for the vibration control of the modular space structure.

The remainder of this paper is organized as follows. Section 2 introduces the basic unit of modular space structures. In Section 3, the basic unit is taken as a super element, and its dynamic spectral element model is established. Section 4 reveals band gap characteristics of modular space structures. In Section 5, the band gap is optimized to improve the wave isolation ability of modular space structures. Some conclusions are summarized in Section 6.

2. Problem Statement

As shown in Figure 1, the basic unit structure of modular space structures is mainly composed of upper beams, lower beams, outer and central beams, diagonal beams, joints, and the cable net structure. The modular space structure is formed by a basic module structure through the periodic array, which is a form of the periodic structure. Periodic structures have band gap characteristics [26], and the propagation of elastic waves is prohibited within a certain frequency band. The band gap characteristic of the periodic structure is related to the structure's material and geometry properties and the number of periods. So, the modular space structure can exhibit different characteristics of band gaps of elastic wave propagation, by adjusting the magnitude of cross-section, structure dimension, and pretensions of the element. To effectively reveal the characteristics of elastic wave propagation of this complex structure, we derive the spectral element matrixes of the 3D cable and beam elements and the dynamic spectral element model of the basic unit based on SEM. The basic unit structure is the smallest repeating unit in the modular space structure, as shown in Figure 1. Then, to reduce the calculation, the super element of the basic unit structure can be obtained by the dimension reduction process. Finally, the spectral element model of the modular space structure can be obtained by periodically expanding the super element according to the topological connection relationship.

3. Spectral Element Method

3.1. Spectral Element Matrix for 3D Beams. In this paper, the spectral element matrix of the beam element is derived based on the Euler-Bernoulli beam assumptions. The assumption is that the additional deflection changes caused by shear deformation are not considered. According to the theoretical analysis of the Euler-Bernoulli beam and the force-displacement relationship [20], the spectral finite element equation for the flexural motion of the beam can be

obtained as

$$\begin{Bmatrix} Q_i \\ M_i \\ Q_j \\ M_j \end{Bmatrix} = \frac{EI_y}{L^3} \begin{bmatrix} S_{B11} & S_{B12} & S_{B13} & S_{B14} \\ S_{B21} & S_{B22} & S_{B23} & S_{B24} \\ S_{B31} & S_{B32} & S_{B33} & S_{B34} \\ S_{B41} & S_{B42} & S_{B43} & S_{B44} \end{bmatrix} \begin{Bmatrix} W_i \\ \Phi_i \\ W_j \\ \Phi_j \end{Bmatrix} = \frac{EI_y}{L^3} S_B(k_F, L)^T d = S_B(\omega) d, \tag{1}$$

where $\{Q_i\, M_i\, Q_j\, M_j\}^T$ is the generalized force vector, Q_i and Q_j are cross forces of nodes, and M_i and M_j are moments of the beam element. $\{W_i\, \Phi_i\, W_j\, \Phi_j\}^T$ is the displacement vector, W_i and W_j are spectral node displacements, and Φ_i and Φ_j are cross-section corner of the beam element. E is the elastic modulus, I_y is the sectional area moment of inertia about the neutral axis, L is the length of the beam element, and $S_B(\omega)$ is the spectral element stiffness matrix of the flexural wave of 3D beams, which characterizes the relationship of the flexural wave between displacement and force in the frequency domain. The subitems of $S_B(\omega)^T$ are

$$\begin{aligned} S_{B11} &= S_{B33} = \Delta_B \bar{L}^3 \left(\cos \bar{L} \bullet \sinh \bar{L} + \sin \bar{L} \bullet \cosh \bar{L}\right), \\ S_{B22} &= S_{B44} = \Delta_B \bar{L}^3 k_F^{-2} \left(\sin \bar{L} \bullet \cosh \bar{L} - \cos \bar{L} \bullet \sinh \bar{L}\right), \\ S_{B12} &= -S_{B34} = \Delta_B \bar{L}^3 k_F^{-1} \sin \bar{L} \bullet \sinh \bar{L}, \\ S_{B13} &= -\Delta_B \bar{L}^3 \left(\sin \bar{L} + \sinh \bar{L}\right), \\ S_{B14} &= -S_{B23} = \Delta_B \bar{L}^3 k_F^{-1} \left(-\cos \bar{L} + \cosh \bar{L}\right), \\ S_{B24} &= \Delta_B \bar{L}^3 k_F^{-2} \left(-\sin \bar{L} + \sinh \bar{L}\right), \\ \Delta_B &= \frac{1}{\left(1 - \cos \bar{L} \bullet \cosh \bar{L}\right)}, \\ \bar{L} &= k_F L, \end{aligned} \tag{2}$$

where $k_F = \sqrt[4]{\omega^2 \rho A / EI_z}$ is the wave number of the flexural motion of the beam.

The longitudinal motion can be obtained as

$$\begin{Bmatrix} N_i \\ N_j \end{Bmatrix} = \frac{EA}{L} \begin{bmatrix} k_L L \cot(k_L L) & -k_L L \csc(k_L L) \\ -k_L L \csc(k_L L) & k_L L \cot(k_L L) \end{bmatrix} \begin{bmatrix} U_i \\ U_j \end{bmatrix} = \frac{EA}{L} S_R(k_L, L)^T d = S_R(\omega) d, \tag{3}$$

where N_i and N_j are the nodal longitudinal forces. U_i and U_j are the nodal longitudinal displacements. $k_L = \sqrt{\omega^2 \rho A / EA}$ is the wave number for the longitudinal motion, ρ is the mass density, A is the sectional area, and $S_R(\omega)$ is the spectral element stiffness matrix of the longitudinal wave of 3D beams, which characterizes the relationship of the longitudinal wave between displacement and force in the frequency domain.

The torsional motion can be obtained as

$$\begin{Bmatrix} T_i \\ T_j \end{Bmatrix} = \frac{GI_P}{L} \begin{bmatrix} k_T L \cot(k_T L) & -k_T L \csc(k_T L) \\ -k_T L \csc(k_T L) & k_T L \cot(k_T L) \end{bmatrix} \begin{bmatrix} \Phi_i \\ \Phi_j \end{bmatrix} = \frac{GI_P}{L} S_T(k_T, L)^T d = S_T(\omega) d, \tag{4}$$

where T_i and T_j are the nodal torsional moments. Φ_i and Φ_j are the nodal torsional angles, and $G = E/(2(1+\mu))$ is the shear modulus, μ is the Poisson's ratio, I_P is the polar moment of inertia, and $k_T = \sqrt{\omega^2 \rho I_P / GI_P}$ is the wave number for the torsional motion, and $S_T(\omega)$ is the spectral element stiffness matrix of the torsional wave of 3D beams, which characterizes the relationship of the torsional wave between displacement and force in the frequency domain.

The spectral element matrix of 3D beam elements can be obtained by assembling longitudinal, torsional, and flexural spectral element matrixes of the Euler-Bernoulli beam as

$$S_B^L(\omega) d_B^L = F_B^L, \tag{5}$$

where $S_B^L(\omega)$ is the spectral element stiffness matrix of the 3D beams in the element coordinate system, and it can also be written as

$$S_B^L(\omega) = \begin{bmatrix} S_{B11}^L & S_{B12}^L \\ \text{sym} & S_{B22}^L \end{bmatrix}, \tag{6}$$

where S_{B11}^L, S_{B12}^L, and S_{B22}^L can be expressed as

$$S_{B11}^L = \begin{bmatrix} S_{R11} & 0 & 0 & 0 & 0 & 0 \\ 0 & S_{B11} & 0 & 0 & 0 & S_{B12} \\ 0 & 0 & S_{B11} & 0 & -S_{B12} & 0 \\ 0 & 0 & 0 & S_{T11} & 0 & 0 \\ 0 & 0 & -S_{B12} & 0 & S_{B22} & 0 \\ 0 & S_{B21} & 0 & 0 & 0 & S_{B22} \end{bmatrix}, \tag{7}$$

$$S_{B12}^{L} = \begin{bmatrix} S_{R12} & 0 & 0 & 0 & 0 & 0 \\ 0 & S_{B13} & 0 & 0 & 0 & S_{B14} \\ 0 & 0 & S_{B13} & 0 & -S_{B14} & 0 \\ 0 & 0 & 0 & S_{T12} & 0 & 0 \\ 0 & 0 & -S_{B23} & 0 & S_{B24} & 0 \\ 0 & S_{B23} & 0 & 0 & 0 & S_{B24} \end{bmatrix}, \quad (8)$$

$$S_{B22}^{L} = \begin{bmatrix} S_{R22} & 0 & 0 & 0 & 0 & 0 \\ 0 & S_{B33} & 0 & 0 & 0 & S_{B34} \\ 0 & 0 & S_{B33} & 0 & -S_{B34} & 0 \\ 0 & 0 & 0 & S_{T22} & 0 & 0 \\ 0 & 0 & -S_{B43} & 0 & S_{B44} & 0 \\ 0 & S_{B43} & 0 & 0 & 0 & S_{B44} \end{bmatrix}, \quad (9)$$

where S_{Rij} and $S_{Tij}(i, j = 1, 2)$ are the subitems of the spectral element stiffness matrixes of longitudinal and torsional motion of the Euler-Bernoulli beam, respectively, and S_{Bij} $(i, j = 1, 2, 3, 4)$ is the subitems of the spectral element stiffness matrix of flexural motion of the Euler-Bernoulli beam.

The spectral element matrix of the 3D beams in the global coordinate system can be obtained by transformation of coordinates as

$$S_B^G(\omega) = T_r^T S_B^L(\omega) T_r, \quad (10)$$

where T_r is the coordinate transformation matrix and $S_B^G(\omega)$ is the total spectral element stiffness matrix of 3D beams in global coordinate system.

3.2. Spectral Element Matrix for 3D Cables. Cables involved in the cable net structure are simulated by strings of which the longitudinal vibration equation of the tension cable is consistent with the Bernoulli-Euler beam. The spectral element equation of the transverse vibration of the tension cable can be given as follows.

$$\begin{Bmatrix} H_i \\ H_j \end{Bmatrix} = \frac{T}{L} \begin{bmatrix} k_{CT}L \cot(k_{CT}L) & -k_{CT}L \csc(k_{CT}L) \\ -k_{CT}L \csc(k_{CT}L) & k_L L \cot(k_{CT}L) \end{bmatrix} \begin{bmatrix} W_i \\ W_j \end{bmatrix} = \frac{T}{L} S_{CT}(k_{CT}, L)^T d = S_{CT}(\omega) d, \quad (11)$$

where H_i and H_j are the nodal transverse forces. W_i and W_j are the nodal transverse displacements. $k_{CT} = \sqrt{\omega^2 \rho A / T}$ is the wave number of the transverse motion. T is the pretension, which provides the transverse stiffness of the tension cable. $S_{CT}(\omega)$ is the spectral element stiffness matrix of the transverse wave of 3D cables, which characterizes the transverse motion relationship of 3D cables between displacement and force in the frequency domain. The subitems of $S_{CT}(\omega)^T$ are

$$\begin{aligned} S_{CT11} &= S_{CT22} = (k_{CT}L) \cot(k_{CT}L), \\ S_{CT12} &= S_{CT21} = -(k_{CT}L) \csc(k_{CT}L). \end{aligned} \quad (12)$$

The spectral element stiffness matrix of 3D cables can be obtained by assembling the transverse and longitudinal spectral element matrixes as

$$S_C^L(\omega) d_C^L = F_C^L, \quad (13)$$

where $S_C^L(\omega)$ is the spectral element stiffness matrix of the 3D cables, and it can also be written as

$$S_C^L(\omega) = \begin{bmatrix} S_{C11}^L & S_{C12}^L \\ \text{sym} & S_{C22}^L \end{bmatrix}, \quad (14)$$

where S_{C11}^L, S_{C12}^L, and S_{C22}^L can be expressed as

$$S_{C11}^L = \begin{bmatrix} S_{R11} & 0 & 0 \\ 0 & S_{CT11} & 0 \\ 0 & 0 & S_{CT11} \end{bmatrix}, \quad S_{C12}^L = \begin{bmatrix} S_{R12} & 0 & 0 \\ 0 & S_{CT12} & 0 \\ 0 & 0 & S_{CT12} \end{bmatrix}, \quad S_{C22}^L = \begin{bmatrix} S_{R22} & 0 & 0 \\ 0 & S_{CT22} & 0 \\ 0 & 0 & S_{CT22} \end{bmatrix}, \quad (15)$$

where S_{Rij} and $S_{CTij}(i, j = 1, 2)$ are the subitems of the spectral element matrixes of longitudinal and transverse motion of the tension cable, respectively.

The spectral element matrix of the 3D cables in the global coordinate system can be obtained by transformation of coordinates as

$$S_C^G(\omega) = T_r^T S_C^L(\omega) T_r, \quad (16)$$

where T_r^T is the coordinate transformation matrix and $S_C^G(\omega)$ is the total spectral element stiffness matrix of 3D cables in global coordinate system.

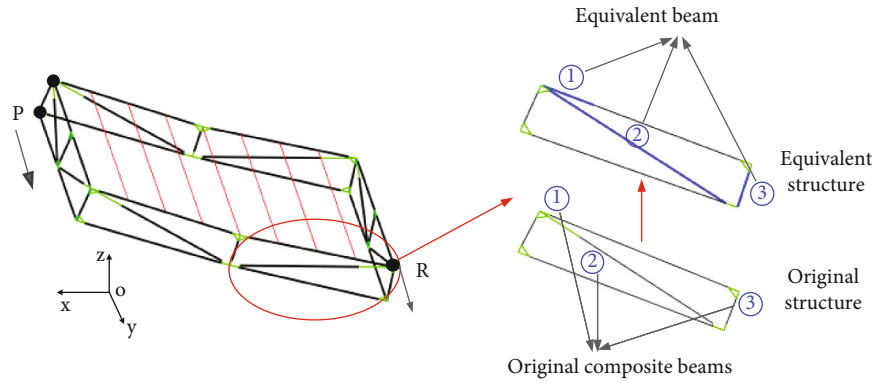

Figure 2: Equivalent super element.

Table 1: Material parameters.

Properties	Frame	Joints	Cable net
Material type	Carbon fiber	Aluminum alloy	Aramid fiber
Section type	Hollow circle section	Solid circle section	Solid circle section
Radius (m)	Outer diameter 0.015 Inside diameter 0.0135	0.03	0.001
Elastic modulus (GPa)	370	72	20
Poisson's ratio	0.3	0.33	0.3
Density (kg/m^3)	1800	2730	1450
Pretension (N)	0	0	1

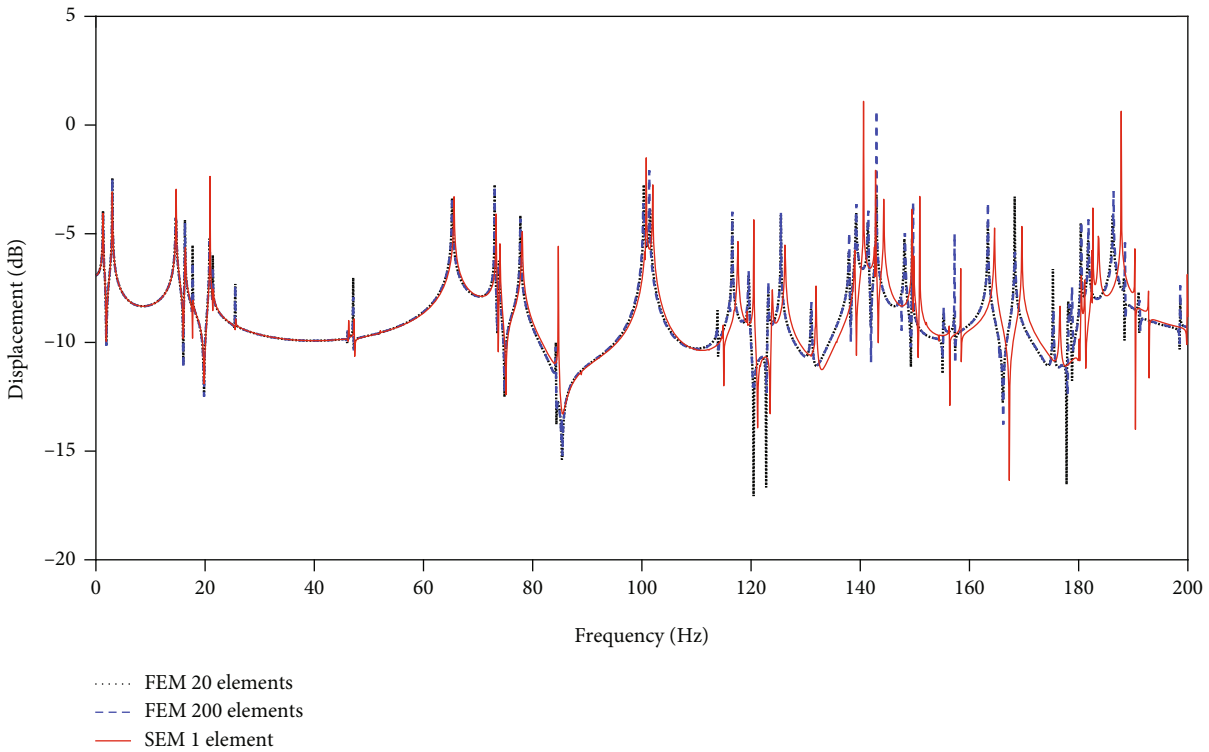

Figure 3: Frequency response comparison between FEM and SEM.

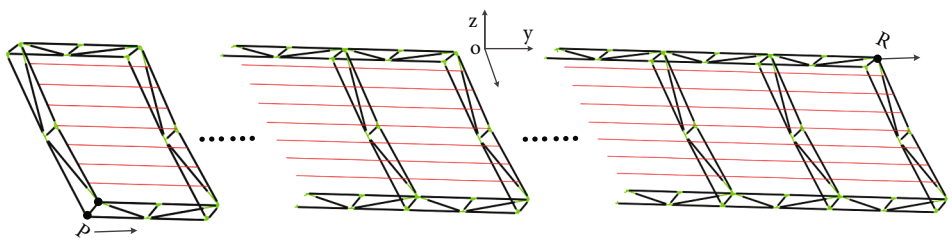

Figure 4: Modular space structure.

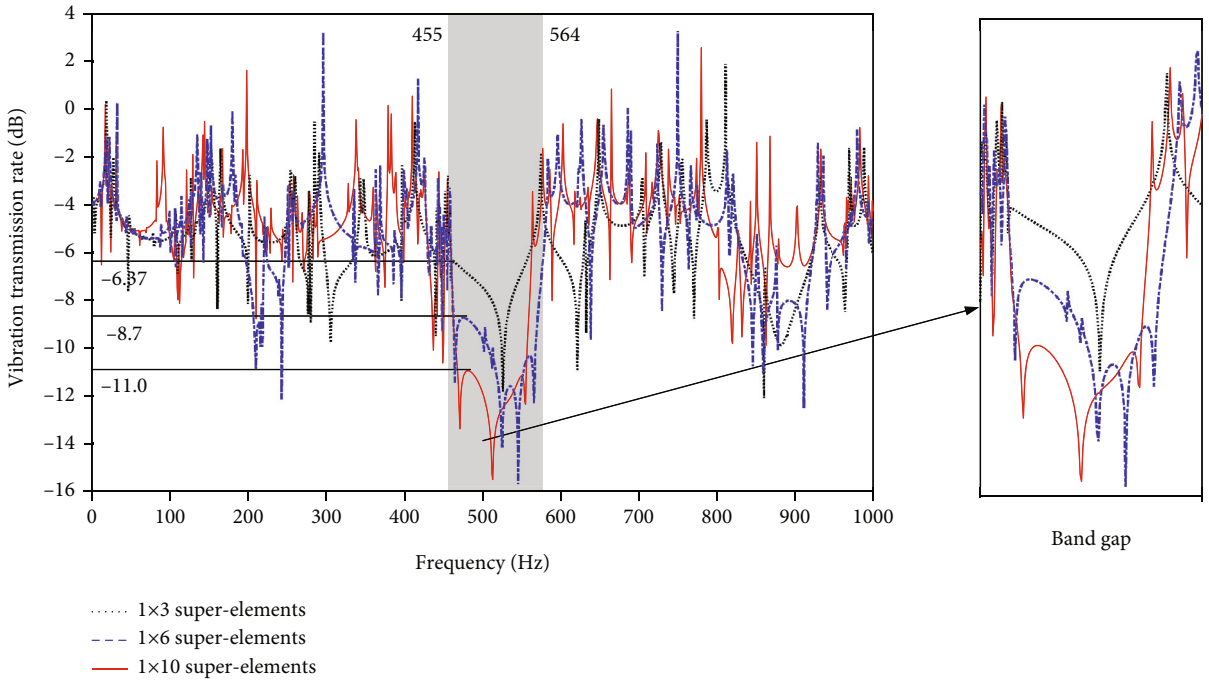

Figure 5: Vibration transmission rate of node R of the modular space structure.

3.3. Spectral Element Matrix of the Super Element. In order to improve computational efficiency, a degree reduction method is used to reduce the dimensionality of the spectral element matrix. As shown in Figure 2, the internal nodes of original composite beams ② can be presented by two end nodes. The spectral element equation of original composite beams ② in the global coordinate system can be written as

$$\begin{bmatrix} \bar{S}_{B2ii} & \bar{S}_{B2ij} \\ \bar{S}_{B2ji} & \bar{S}_{B2jj} \end{bmatrix} \begin{Bmatrix} \bar{d}_i \\ \bar{d}_j \end{Bmatrix} = \begin{Bmatrix} \bar{f}_i \\ 0 \end{Bmatrix}, \tag{17}$$

where $\bar{d}_i$ and $\bar{d}_j$ are the boundary and internal nodal displacements of original composite beams ②, respectively, and $\bar{f}_i$ is the boundary force vector.

According to the principle of condensation, the equivalent beam ② can be deduced as

$$\bar{S}^G_{B2}(\omega)\bar{d} = \bar{f}, \tag{18}$$

where the spectral element matrix of equivalent beam ② is

$$\bar{S}^G_{B2}(\omega) = \bar{S}_{B2ii} - \bar{S}_{B2ij}\left(\bar{S}_{B2jj}\right)^{-1}\bar{S}_{B2ji}. \tag{19}$$

The spectral element matrixes of equivalent beams ① and ③ are similar to that of the equivalent beam ② and can be shown as

$$\bar{S}^G_{Bn}(\omega) = \bar{S}_{Bnii} - \bar{S}_{Bnij}\left(\bar{S}_{Bnjj}\right)^{-1}\bar{S}_{Bnji}\ (n = 1, 3). \tag{20}$$

Specifying material parameters of the super element shown in Table 1 and applying the displacement excitation

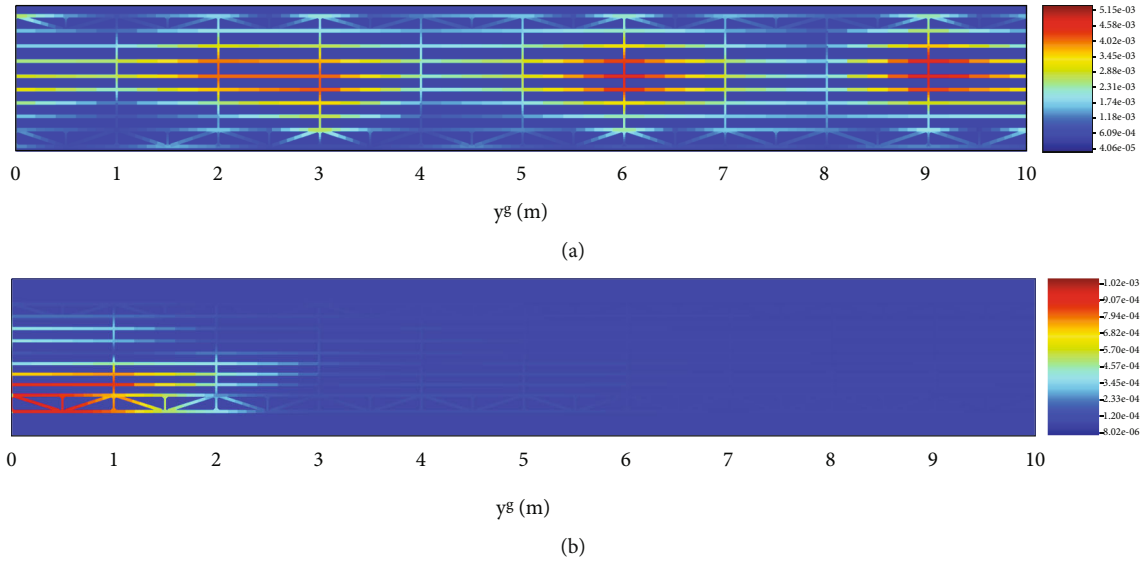

Figure 6: Vibration distributions of the modular space structure: (a) $f = 400$ Hz; (b) $f = 500$ Hz.

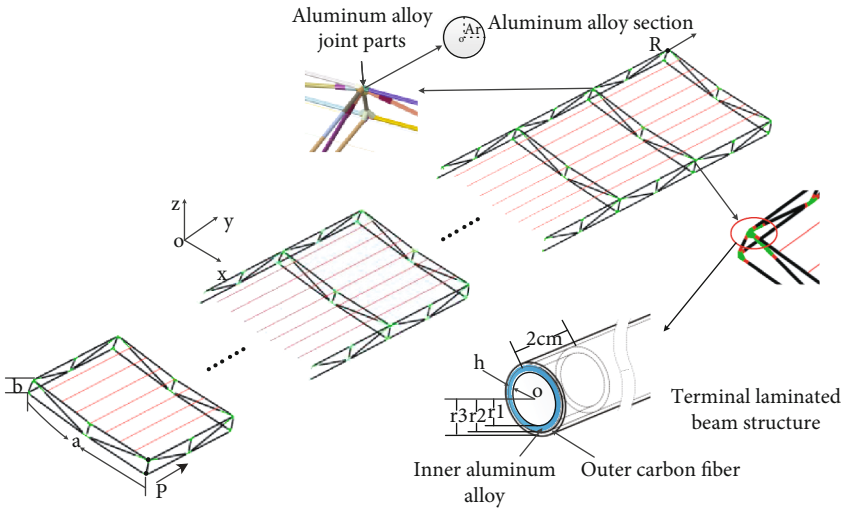

Figure 7: Structural details of the modular space structure.

$d = 0.001e^{i\omega t}$ m at node P, we can obtain the frequency response at node R by solving the spectral element model. The comparisons of the results obtained by the finite element simulation with our numerical results are shown in Figure 3.

It is found that the results of FEM are almost consistent with SEM from 0 to 100 Hz, while they gradually deviate from 100 Hz to 200 Hz. The reason for this difference is that FEM has truncation errors if the refined mesh number is insufficient, while SEM uses the precise wave solution in the frequency domain. Compared with FEM, SEM has no truncation error, so it can obtain accurate calculation results with a smaller number of elements, thereby reducing the amount of calculation and improving the calculation efficiency.

4. Band Gap Analysis of Modular Space Structure

The super element can be used as the basic element to expand into a periodic structure. The vibration transmission rate is defined as Equation (21) and used to evaluate the attenuation characteristics of the periodic structure.

$$T = \lg\left(\frac{w_0}{w_i}\right), \tag{21}$$

where w_0 and w_i are the output and input displacements, respectively.

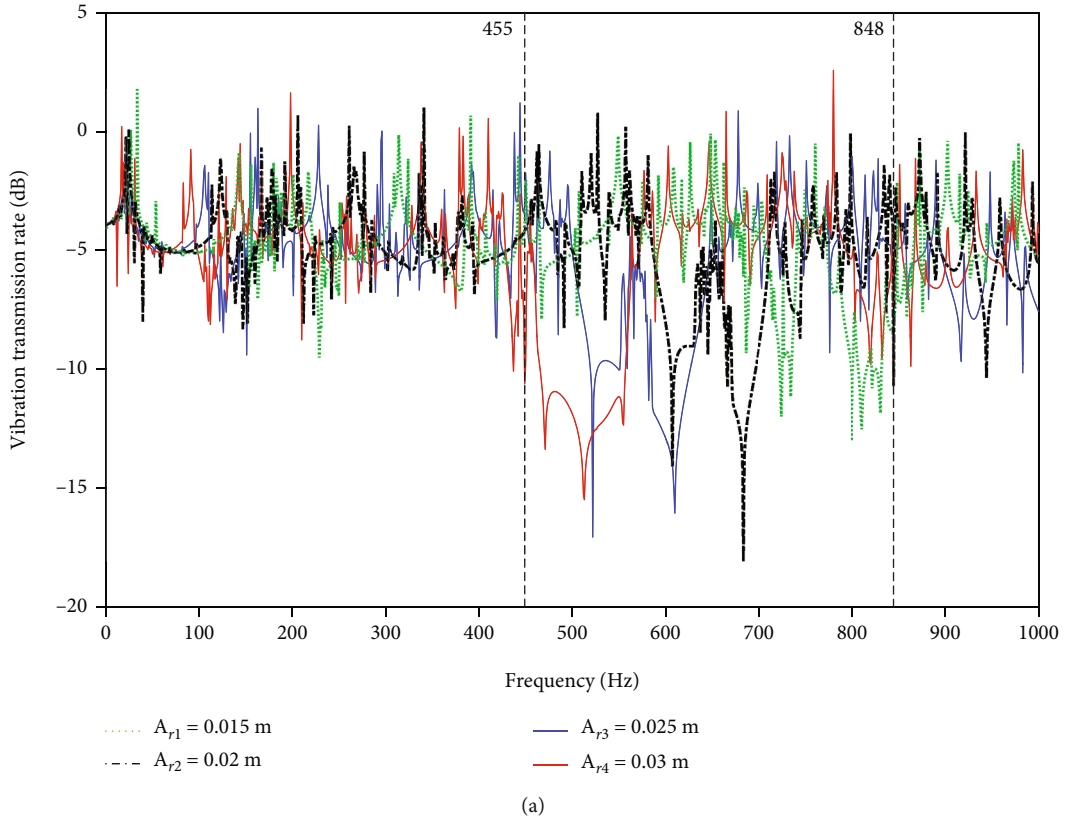

Figure 8: Corresponding to the change of the aluminum alloy section radius: (a) vibration transmission rate of node R; (b) the first band gap.

The structure formed by extending the super element along one dimension is shown in Figure 4. The displacement excitation is applied at node P along the positive y-axis. The y-axis vibration transmission rate of node R is solved and shown in Figure 5.

It can be seen that the vibration transmission rate of node R is attenuated sharply from 455 Hz to 564 Hz, and this frequency range is called as a band gap. The depth of band gap is the value at which the vibration transmission rate within the band gap is the largest, as shown in Figure 5. As

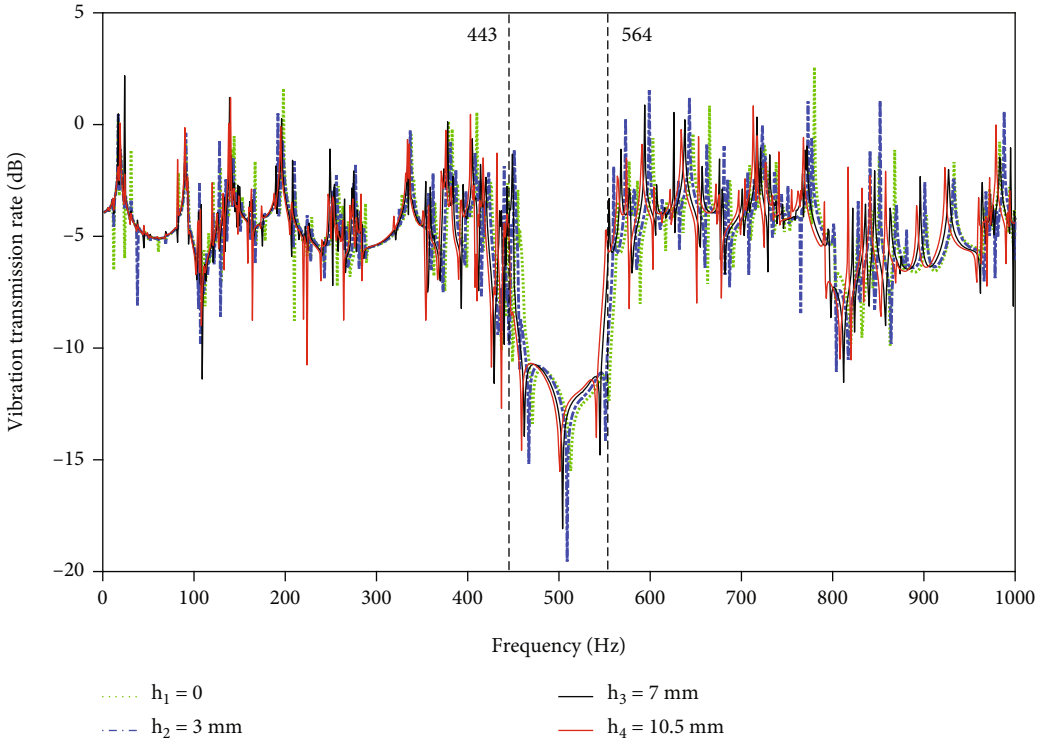

Figure 9: Vibration transmission rate of node R corresponding to the changes in the thickness of the embedded part.

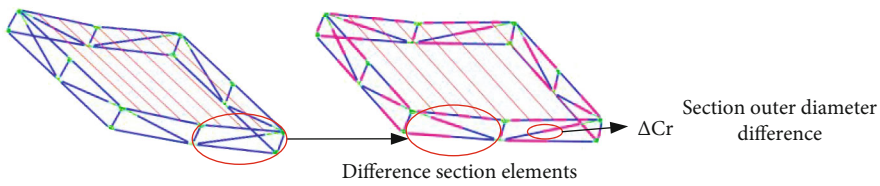

Figure 10: The super element composed of two different sections of carbon fiber tube elements.

the number of super elements is increased from 3 to 6 and 10, the depth is increased by 36.69% and 72.9%, respectively, but the position and width of the band gap are basically the same.

The vibration distributions of the modular space structure at 400 Hz and 500 Hz are shown in Figure 6. It can be seen that the whole structure vibrates at 400 Hz, which means that the elastic wave can move to the far end. However, the vibration at 500 Hz is limited near the excitation source that means the elastic wave can be effectively isolated at the band gap.

5. Optimal Design of the Band Gap of Modular Space Structure

5.1. Sensitivity Analysis. The band gap of the structure may be affected by structural parameters such as element cross-sections, structure size, and cable forces, as shown in Figure 7. The material parameters of the structures in this section are the same as those in Table 1.

At first, the influence of aluminum alloy section radius on the band gap is studied. It can be seen from Figure 8 that when increasing the aluminum alloy section radius Ar by 33.3%, 66.7%, and 100%, the lower limit frequency of the first band gap is decreased by 24.55%, 35.71%, and 40.91%, and the width of the band gap is increased by 69.23%, 97.44%, and 39.74%, respectively. It can be found that with the increase of the aluminum alloy section radius, the band gap shifts towards low frequency, the width of the band gap first increases and then decreases, but the depth is almost not changed. Changes in structural parameters may cause little vibration attenuation between specific frequencies in the band gap, which is called surface localization as shown Figure 8(b). It means the vibration is transmitted with a low attenuation rate in the frequencies.

Then, the aluminum alloy joints are embedded in the carbon fiber beams to form a terminal laminated beam structure. As shown in Figure 9, when the thickness h of the embedded part is set as 0 mm, 3 mm, 7 mm, and

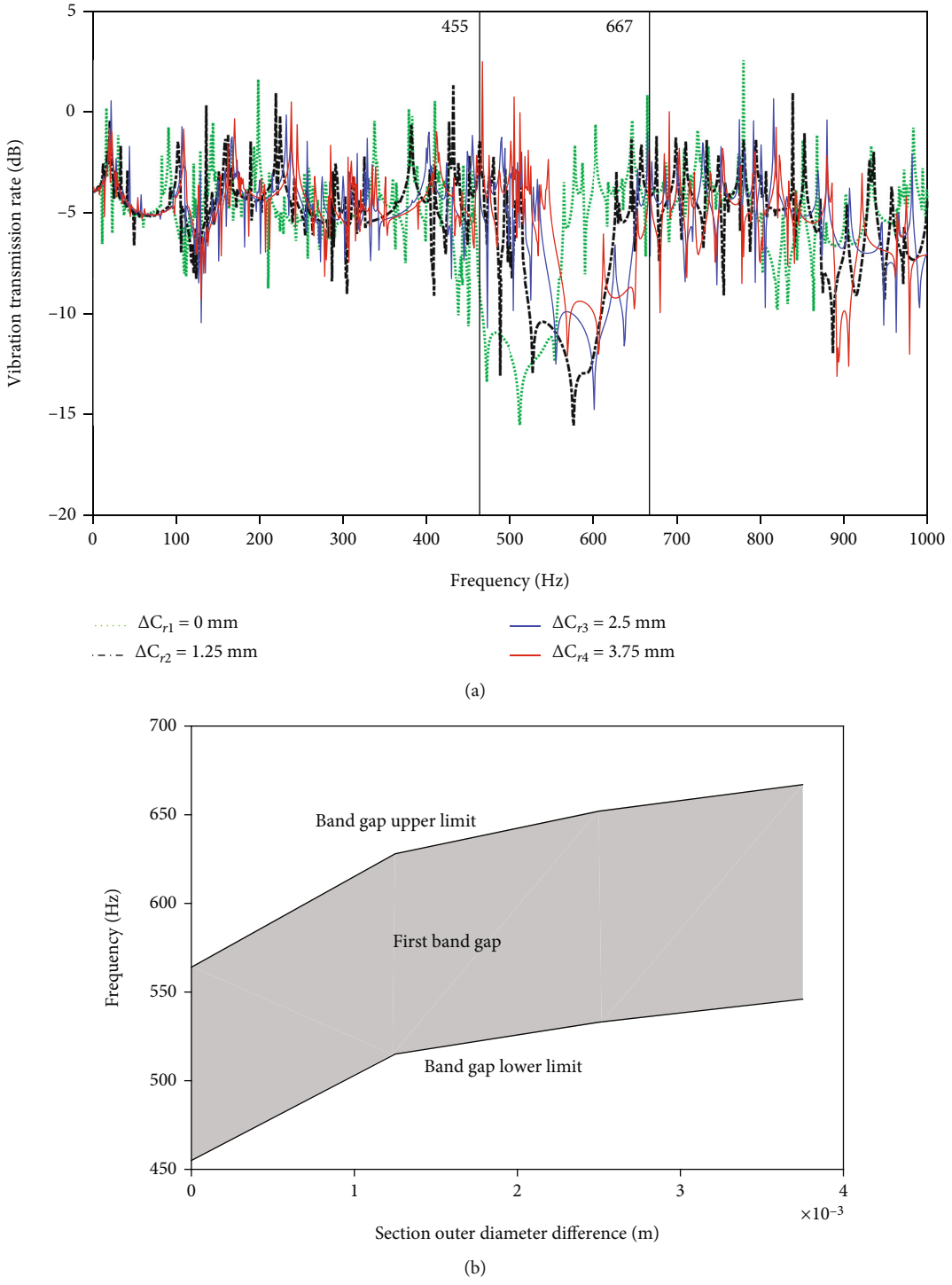

Figure 11: Corresponding to the change of the section outer diameter difference: (a) vibration transmission rate of node R; (b) the first band gap.

10.5 mm, respectively, the band gap will slightly shift towards low frequency, but the width and the depth of the band gap are not changed. The phenomenon may be that the equivalent stiffness of the embedded part is much more minor than the stiffness of the aluminum alloy joint, which has little effect on the band gap.

As shown in Figure 10, the carbon fiber tube is designed as two different section elements. As shown in Figure 11, when the mean value of the outer diameters is set as 0.015 m, 0.0156 m, and 0.0169 m, the difference ΔC_r is set as 0 mm, 1.25 mm, 2.5 mm, and 3.75 mm, respectively. The lower limit frequency of the first band gap is increased by

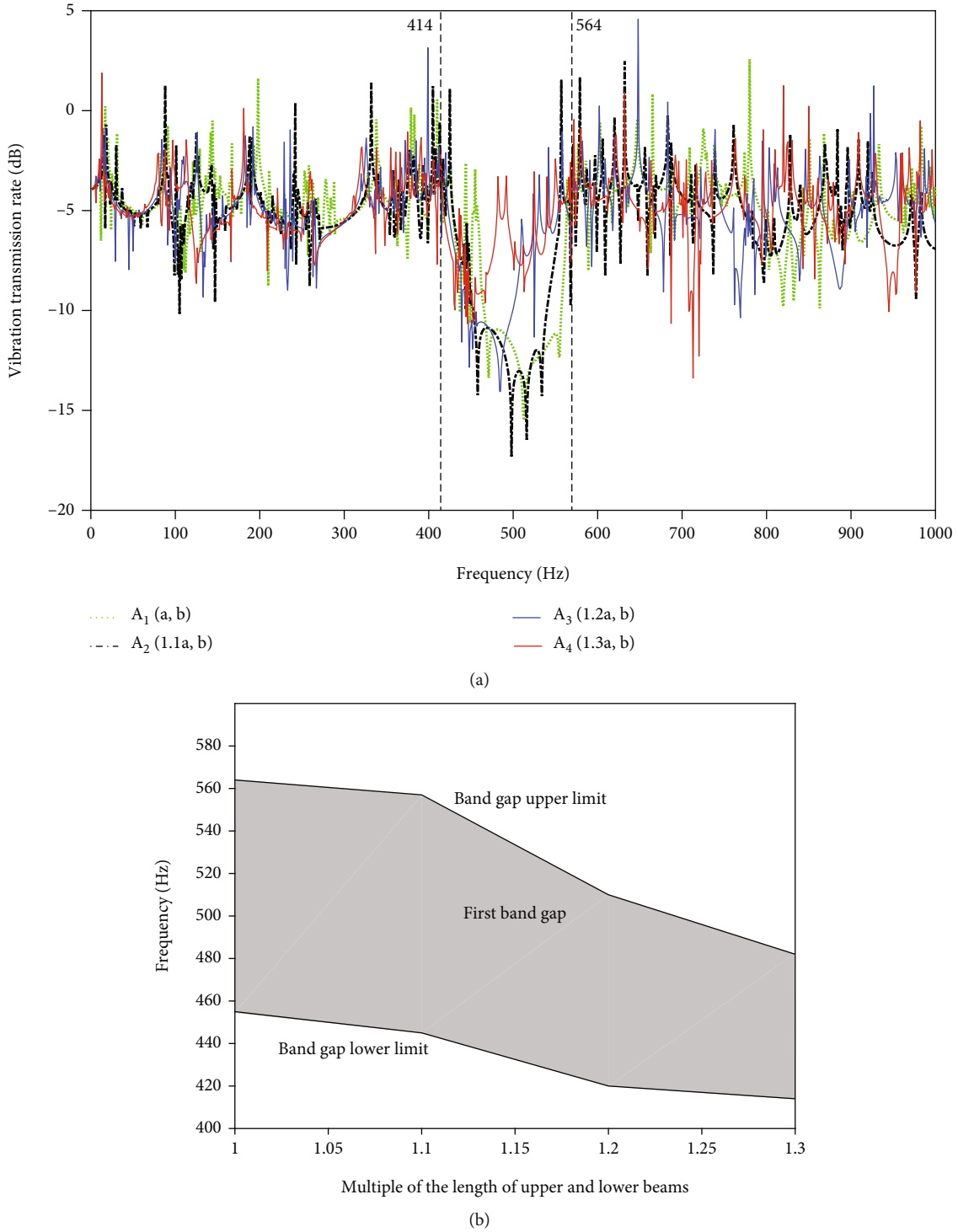

Figure 12: Corresponding to the change of the length of upper and lower chord beams: (a) vibration transmission rate of node R; (b) the first band gap.

13.19%, 17.14%, and 20.00%, and the width of the band gap is increased by 3.67%, 9.17%, and 11.01%, respectively. It can be found that with the increase of the difference ΔC_r, the band gap will gradually shift towards high frequency, the first band gap width increases, and the depth steadily decreases.

As shown in Figure 12, when the length of the upper beams and the lower beams is synchronously increased by 10%, 20%, and 30%, respectively, the lower limit frequency of the first band gap is decreased by 2.20%, 7.69%, and 9.01%, respectively, and the width of the band gap is increased by 2.75%, -19.43%, and -38.53%, respectively. It

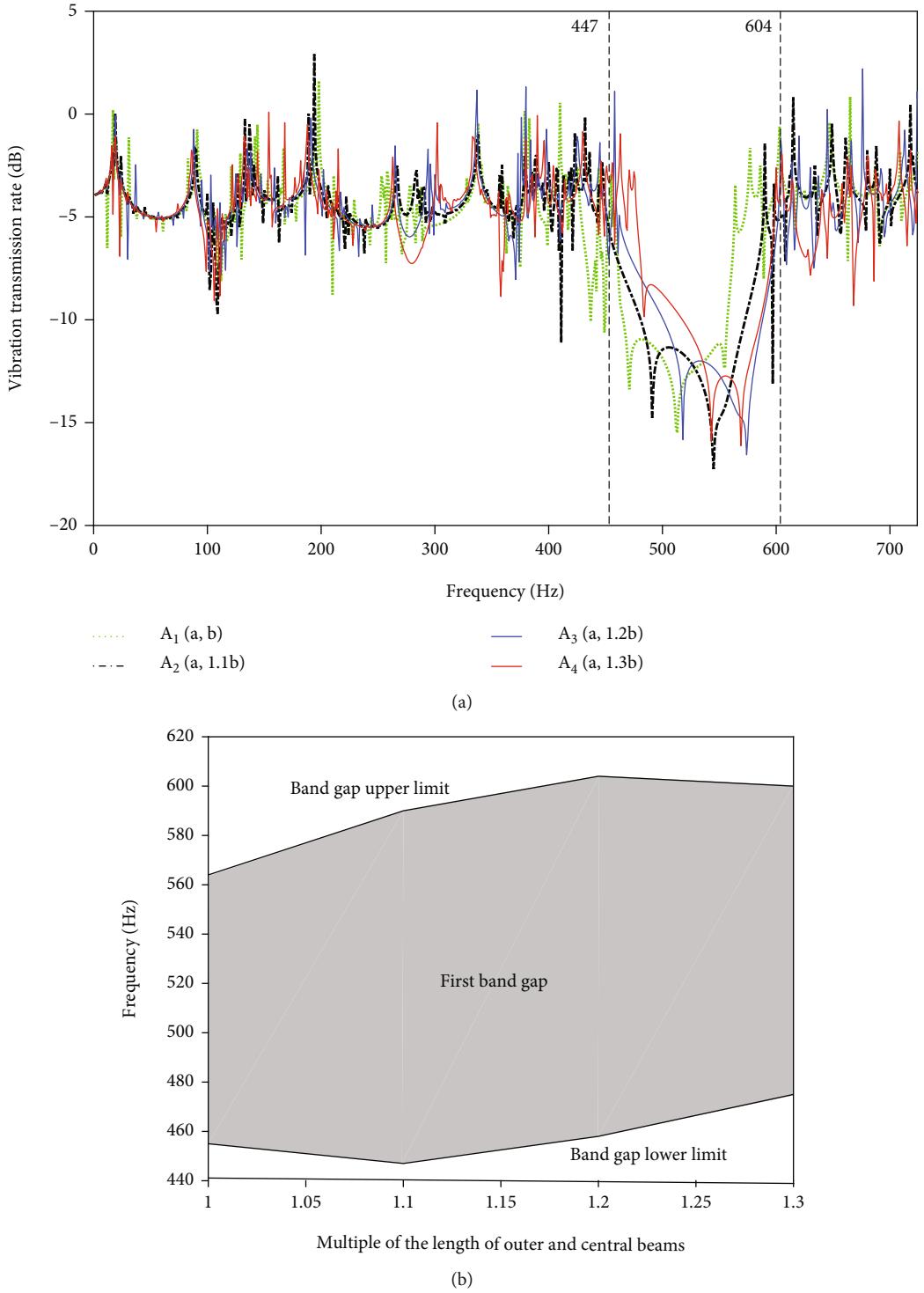

Figure 13: Corresponding to the change of the length of outer beams and center beams: (a) vibration transmission rate of node *R*; (b) the first band gap.

can be found that with the increase of the length of the upper beams and the lower beams, the band gap will shift towards low frequency, the first band gap width first increases and then decreases, and the depth is gradually decreased.

As shown in Figure 13, when the lengths of the outer beams and center beams are synchronously increased by 10%, 20%, and 30%, respectively, the lower limit frequency of the first band gap is decreased by 1.76%, -0.66%, and -4.40%, respectively, and the width of the band gap is

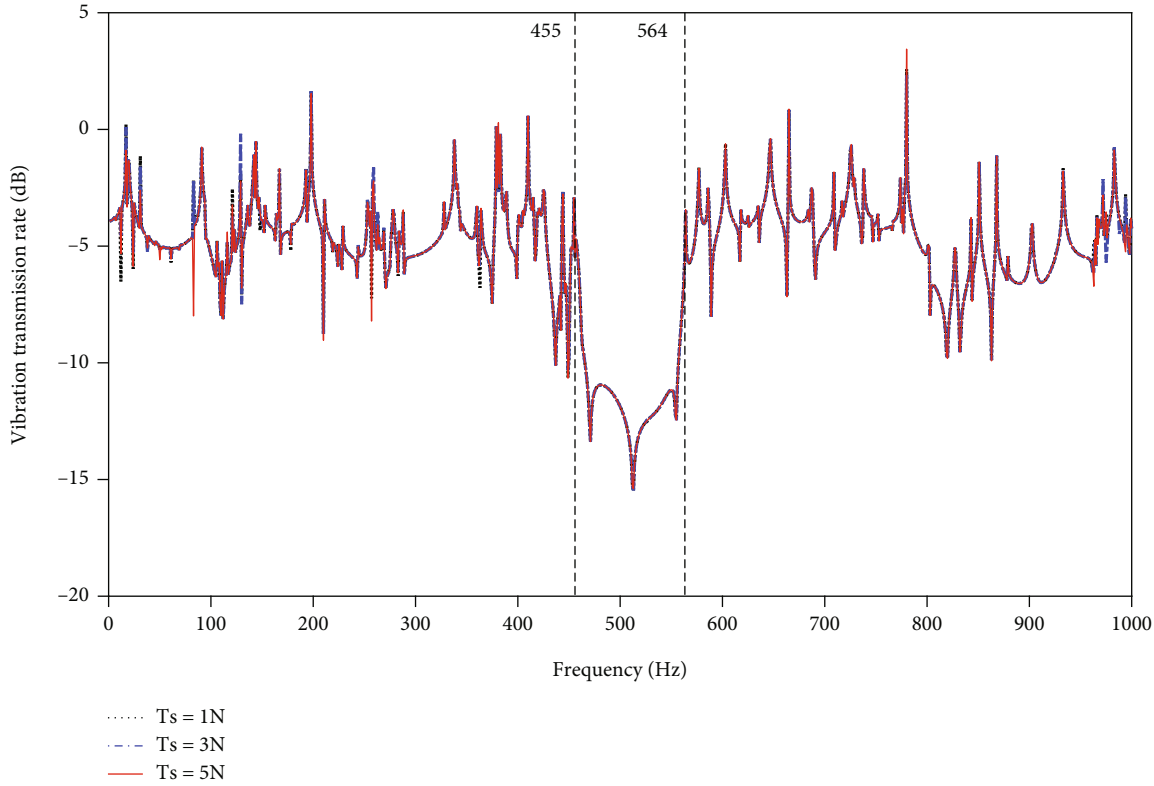

Figure 14: The vibration transmission rate of node R corresponding to the change of cable pretension.

increased by 31.19%, 33.94%, and 14.68%, respectively. It can be found that with the increase of the lengths of the outer beams and center beams, the band gap does not move substantially, the width of the band gap has a significant change, and its value first increases and then decreases, and the depth is gradually increased.

As shown in Figure 14, when the cable pretensions Ts are set as 1 N, 3 N, and 5 N, respectively, the vibration amplitudes of the modular space structure at low frequencies are changed slightly. However, the position, the width, and the depth of the band gap are not changed. The reason is as follows. According to Bloch's theorem, the band gap of the structure is mainly related to the wave number k (i.e., the material parameter of the structure) and the effective length. The cable pretension can affect the structural parameters to a certain extent, thus affecting the wave number k. So, it was considered a factor in the sensitivity analysis. However, it has little effect on the band gap due to the low pretension of the cable in the deployable space structure.

5.2. Optimization Design. The above analysis illustrates that we can optimize the aluminum alloy section radius, the lengths of the upper and lower beams, and the lengths of the central and outer beams to change the position and the width of the band gap. In order to improve the wave isolation characteristics of the modular space structure, we comprehensively consider the influence of these parameters and establish the following band gap optimization model with the ratio of the lower limit of the band gap to the width as the objective function. In addition, to ensure that the change of component size has little effect on the structure's overall size change, the beam length's value range is selected to be between 1 and 1.1 of the original length. The value range of the joint radius is between 1 and 1.5 of the original size.

$$\begin{aligned} &\text{Find } L = \{(1+a)L_1\ (1+b)L_2\ r\}, \\ &\min \quad RB = \frac{f_1}{f_2 - f_1} \\ &\text{s.t.} \begin{cases} a \in [0,0.1] \\ b \in [0,0.1] \\ L_1 = 0.126\,\text{m} \\ L_2 = 1.114\,\text{m} \\ r \in [0.03,0.045]. \end{cases} \end{aligned} \tag{22}$$

where L_1 represents the length of the upper and lower chord beams, L_2 represents the length of the outer and central beams, r is the section radius of the aluminum alloy joints, f_1 is the lower limit of the band gap, and f_2 is the upper limit of the band gap.

The calculation process of the optimization algorithm is shown in Figure 15. Firstly, the optimization variables

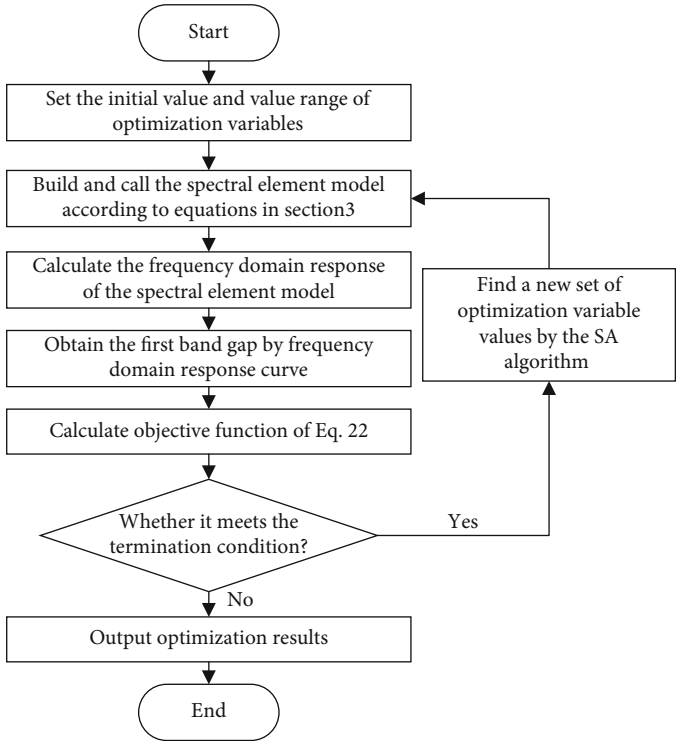

Figure 15: Optimization algorithm flow chart.

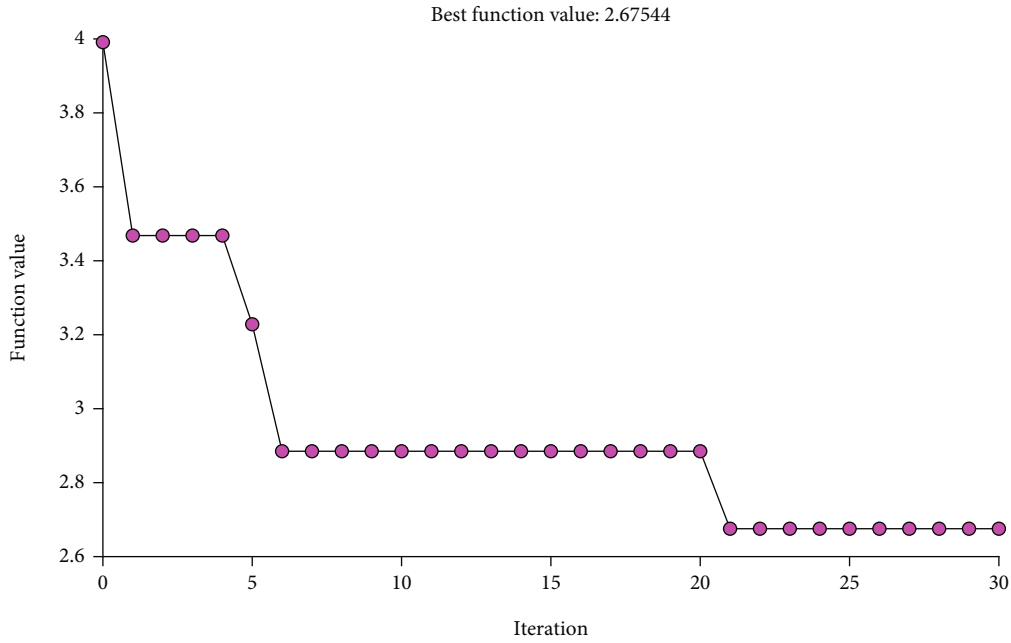

Figure 16: Relative bandwidth optimization iterative process.

are brought into the spectral element model in Section 3, and the frequency-domain response curve of the model is calculated. Then, the first band gap information of the structure is obtained through the frequency domain response curve, including the bandwidth and the lower limit frequency of the band gap. Next, the objective function is calculated by Equation (22) and returned to the SA algorithm to obtain a new set of optimization variable values. Repeat the above process until it satisfies the optimization termination condition and outputs the result.

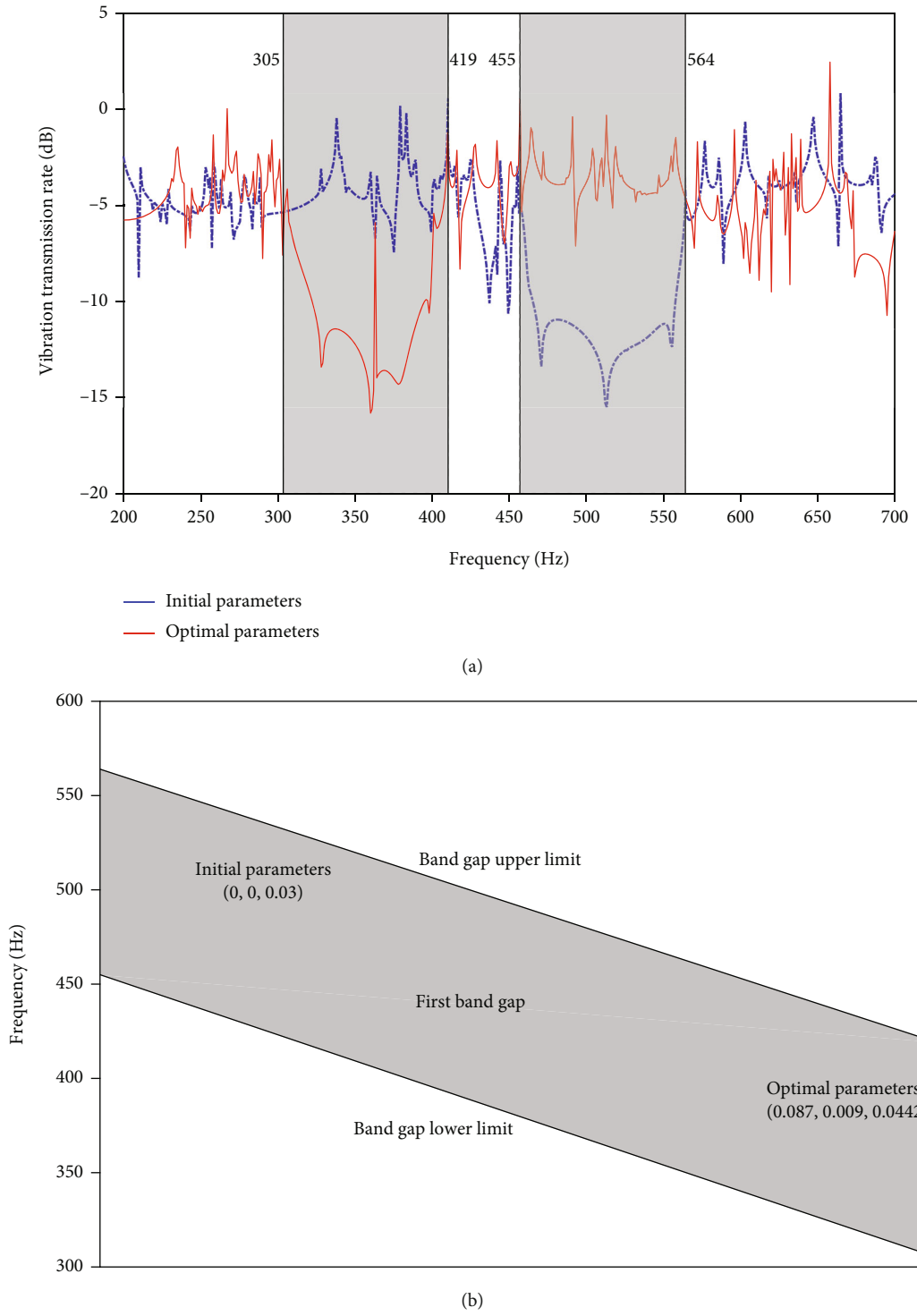

Figure 17: Corresponding to initial parameters and optimal parameters: (a) vibration transmission rate of node R; (b) the first band gap.

For the optimization model of Equation (22), obtaining the optimal global solution is considered at first. In addition, the computational efficiency of the algorithm is considered. The simulated annealing algorithm can obtain the optimal global solution of the optimization model without falling into the optimal local solution. The method also has high computational efficiency. Therefore, the optimization model is solved by the simulated annealing algorithm. The initial parameters are set as [0,0,0.03]. Figure 16 shows that the optimal result can be obtained after 30 iterations. At this time, the optimal length of the upper and lower beams and the central and outer beams and the optimal radius of the aluminum alloy joint are $1.087L_1$, $1.009L_2$, and 0.0442 m, respectively. In this case, the band gap is shifted to the low frequency as shown in Figure 17. It is illustrated that optimization of the

structural parameters can significantly change the position of the band gap.

6. Conclusions

This paper studies a passive vibration control analysis of the modular space structure based on band gap design. Through the band-gap sensitivity analysis of the modular space structure, some key influence factors on the band gap are firstly illustrated. And then, a band gap optimization model is established to improve the wave isolation characteristics of the modular space structure. According to the simulation results, some conclusions can be summarized as follows:

(a) The band gap exists in modular space structures. As the number of basic units increases, the vibration transmission rate of the modular space structure will be decreased

(b) The position and the width of the band gap are greatly influenced by structural parameters, including the aluminum alloy section radius, the length of the upper and lower beams, and the length of the central and outer beams

(c) The elastic wave in the band gap can be effectively isolated, and manual optimization of the structural parameters can significantly change the position of the band gap. That is to say, wave isolation characteristics of the modular space structure can be improved by optimizing the structural parameters

Data Availability

The data used to support the findings of this study are available from the corresponding author upon request.

Conflicts of Interest

The authors declare that they have no conflicts of interest.

Acknowledgments

The project is supported by the National Natural Science Foundation of China (Grant Nos. 51775403 and 51905401), the Fundamental Research Funds of Xidian University (Grant No. JB210415), and the Key Research and Development Program of Shaanxi (Program No. 2022GY-314).

References

[1] F. Hu, Y. P. Song, Y. D. Xu, and H. Wen, "Synthesis and optimization of modular deployable truss antenna reflector," *Aircraft Engineering and Aerospace Technology*, vol. 90, no. 8, pp. 1288–1294, 2018.

[2] J. C. Chen, Y. Zhang, L. W. Wu, T. You, and X. Ning, "An adaptive clustering-based algorithm for automatic path planning of heterogeneous UAVs," *IEEE Transactions on Intelligent Transportation Systems*, pp. 1–12, 2021.

[3] J. Chen, C. Du, Y. Zhang, P. Han, and W. Wei, "A clustering-based coverage path planning method for autonomous heterogeneous UAVs," *IEEE Transactions on Intelligent Transportation Systems*, pp. 1–11, 2021.

[4] J. C. Chen, Y. He, Y. Zhang, P. Han, and C. Du, "Energy-aware scheduling for dependent tasks in heterogeneous multiprocessor systems," *Journal of Systems Architecture*, vol. 129, article 102598, 2022.

[5] J. C. Chen, F. Y. Ling, Y. Zhang, T. You, Y. Liu, and X. Du, "Coverage path planning of heterogeneous unmanned aerial vehicles based on ant colony system," *Swarm and Evolutionary Computation*, vol. 69, article 101005, 2022.

[6] Y. Liu, K. Zhang, W. Z. Zhang, and X. Y. Meng, "Wave-based vibration control of large cable net structures," *Wave Motion*, vol. 77, pp. 139–155, 2018.

[7] Y. Zhao, Y. Y. Wang, and W. L. Ma, "Active control of power flow transmission in complex space truss structures based on the advanced Timoshenko theory," *Journal of Vibration and Control*, vol. 21, no. 8, pp. 1594–1607, 2015.

[8] Y. Q. Tang, T. J. Li, Q. Lv, and X. Wang, "A self-vibration-control tensegrity structure for space large-scale construction," *Mechanical Systems and Signal Processing*, vol. 177, article 109241, 2022.

[9] J. A. Bishop and A. G. Striz, "On using genetic algorithms for optimum damper placement in space trusses," *Structural and Multidisciplinary Optimization*, vol. 28, no. 2, pp. 136–145, 2004.

[10] R. Xu, D. X. Li, Q. Luo, W. Liu, and J. Jiang, "Microvibration suppression of space truss structures using viscoelastic dampers with design parameter optimization," *Proceedings of the Institution of Mechanical Engineers Part G-Journal of Aerospace Engineering*, vol. 230, no. 3, pp. 539–553, 2016.

[11] I. H. Kim, H. J. Jung, and J. T. Kim, "Numerical investigation of an MR damper-based smart passive control system for mitigating vibration of stay cables," *Structural Engineering and Mechanics*, vol. 37, no. 4, pp. 443–458, 2011.

[12] X. Tong and X. W. Zhao, "Passive vibration control of the SCOLE beam system," *Structural Control and Health Monitoring*, vol. 25, no. 8, article e2204, 2018.

[13] A. Preumont, B. de Marneffe, A. Deraemaeker, and F. Bossens, "The damping of a truss structure with a piezoelectric transducer," *Computers and Structures*, vol. 86, no. 3-5, pp. 227–239, 2008.

[14] Y. R. Teo and A. J. Fleming, "Optimal integral force feedback for active vibration control," *Journal of Sound and Vibration*, vol. 356, pp. 20–33, 2015.

[15] B. Agrawal, "Jitter control for imaging spacecraft," in *2009 4th International Conference on Recent Advances in Space Technologies*, pp. 615–620, Istanbul, Turkey, 2009.

[16] V. S. Sorokin and J. J. Thomsen, "Effects of weak nonlinearity on the dispersion relation and frequency band gaps of a periodic Bernoulli-Euler beam," *Mechanical Systems and Signal Processing*, vol. 472, no. 2186, article 20150751, 2016.

[17] X. Zhaowang, X. Xiangxi, J. Fuyu, W. Zongyao, L. Zhiwei, and C. Rui, "Study on vibration characteristics of periodic truss structure of offshore platform," *Advances in Mechanical Engineering*, vol. 12, no. 11, Article ID 168781402097288, 2020.

[18] J. Q. Li and H. J. Shen, "Analysis of longitudinal vibration band gaps in periodic carbon nanotube intramolecular junctions using finite element method," *AIP Advances*, vol. 5, no. 12, 2015.

[19] X. Q. Zhou, D. Y. Yu, X. Y. Shao, S. Wang, and Y. H. Tian, "Band gap characteristics of periodically stiffened-thin-plate based on center- finite-difference-method," *Thin-Walled Structures*, vol. 82, pp. 115–123, 2014.

[20] Y. Z. Wang, F. M. Li, K. Kishimoto, Y. S. Wang, and W. H. Huang, "Wave band gaps in three-dimensional periodic piezoelectric structures," *Mechanics Research Communications*, vol. 36, no. 4, pp. 461–468, 2009.

[21] T. Li, X. Ma, Q. Zhang, and Z. Wang, "Band gap properties of periodic tapered beam structure using traveling wave method," *Journal of Theoretical and Applied Mechanics*, vol. 54, no. 4, pp. 1297–1308, 2016.

[22] V. Ferrando, J. C. Castro-Palacio, B. Marí, and J. A. Monsoriu, "Study on band gap structure of Fibonacci quantum superlattices by using the transfer matrix method," *Modern Physics Letters B*, vol. 28, article 1450053, no. 7, 2014.

[23] Z. J. Wu, Y. Z. Wang, and F. M. Li, "Analysis on band gap properties of periodic structures of bar system using the spectral element method," *Waves in Random and Complex Media*, vol. 23, no. 4, pp. 349–372, 2013.

[24] Y. Tang, X. Wang, X. Zhou, and T. Liu, "A simple wave/power flow analysis method for vibration control of large cable-frame structures," *Journal of Vibration and Control, online*, vol. 28, no. 17-18, pp. 2319–2332, 2022.

[25] Z. J. Wu, F. M. Li, and C. Z. Zhang, "Vibration band-gap properties of three-dimensional Kagome lattices using the spectral element method," *Journal of Sound and Vibration*, vol. 341, pp. 162–173, 2015.

[26] Z. Zhang, T. J. Li, Z. W. Wang, and Y. Tang, "Band gap characteristics of flexural wave of two-dimensional periodic frame structure composed of locally resonant composite beam," *Mechanical Systems and Signal Processing*, vol. 131, pp. 364–380, 2019.

[27] U. Lee and J. Lee, "Dynamic continuum modeling of truss-type space structures using spectral elements," *Journal of Spacecraft and Rockets*, vol. 33, no. 3, pp. 404–409, 1996.

[28] M. Dutkiewicz and M. Machado, "Spectral element method in the analysis of vibrations of overhead transmission line in damping environment," *Structural Engineering and Mechanics*, vol. 71, no. 3, pp. 291–303, 2019.

[29] B. Jeong, T. Kim, and U. Lee, "Vibration analysis of a multi-span beam subjected to a moving point force using spectral element method," *Structural Engineering and Mechanics*, vol. 65, no. 3, pp. 263–274, 2018.

Hindawi
International Journal of Aerospace Engineering
Volume 2022, Article ID 4725423, 9 pages
https://doi.org/10.1155/2022/4725423

Research Article

Deployment Strategy and Dynamic Analysis of Large Ring Truss Antenna

Jiang Zhao, Jungang Yang, Yong Xiao, and Xiaofei Ma

Xi'an Institute of Space Radio Technology, Xi'an 710100, China

Correspondence should be addressed to Jiang Zhao; 344041630@qq.com

Received 25 April 2022; Revised 17 July 2022; Accepted 1 August 2022; Published 25 August 2022

Academic Editor: Adel Ghenaiet

The deployment strategy and dynamic analysis of the AM-2 AstroMesh ring truss antenna reflector are studied in this paper. The rigid multibody dynamic models of the truss structures with alterable and fixed diagonal length are established, respectively, by using the natural coordinate formulation (NCF). The driving scheme and the synchronous constraint scheme are proposed for two types of truss structure, respectively. The degree of freedom (DOF) analysis of the truss structure is carried out according to the redundant constraint processing method. The deployment strategies of the two different types of truss structures are discussed. The dynamic simulation of the deployment of a 30-side AM-2 AstroMesh reflector truss structure with fixed diagonal length without gravity is carried out. The deployment characteristics of the truss structure are obtained. The driving forces are predicted according to the dynamic simulation.

1. Introduction

With the rapid development of the aerospace technology, many kinds of large-scale space structures are widely used, such as deployable solar panels, deployable satellite antennas, and the large-scale deployable solar sails [1–4]. Due to the limits of space and weight of the vehicles, these large space structures must be folded up during the launch stage, and the structures deploy to the work state by the driving system after the spacecraft is in orbit. To meet the increasing space telecommunication requirements, more and more large deployable mesh antennas have been developed and applied for the aerospace missions in recent decades [5, 6].

Compared to the other structure types, the ring truss antenna has the advantage of light weight and high storage ratio. The mass of the ring truss antenna does not increase proportionally with the increase of the aperture, as shown in Figure 1. Therefore, the ring truss deployable antenna has been widely concerned by various research institutions [1, 2, 7–11].

The AstroMesh reflector, developed by the Northrop Grumman Corporation, is one of the most famous ring truss deployable antenna reflectors and has gained wide acceptance in the world of commercial satellites [8, 9]. In order to meet the requirements of the smaller fold size and the lower weight, several classes of AstroMesh reflectors such as AM-1, AM-Lite, and AM-2 have been designed and developed by Northrop Grumman Corporation based on the first generation of the AstroMesh reflector AM [12]. The AM-1 class has a reduced stowed diameter versus the first-generation AM. The AM-Lite class is also developed by optimized mass design with 50% reduction in mass from AM-1. In order to reduce the storage volume, the Northrop Grumman Corporation developed an improved mesh reflector, called AM-2, which can reduce the stowed height of the ring truss by 40% from AM-1, as shown in Figure 2 [12].

The success of deployment in orbit plays a critical role in the success of the entire space mission. Therefore, researchers have paid enough attention to the dynamic characteristics of deployment process of the ring truss antenna. Base on the second kind of Lagrange equations, Li [13] studied the deployment dynamics of a rigid ring truss structure. A five-order polynomial was used to describe the angular velocity of the deployment of the truss structure. Zhang et al. [14] studied the deployment dynamics of a simplified ring truss structure of the AstroMesh reflector by using the assumption

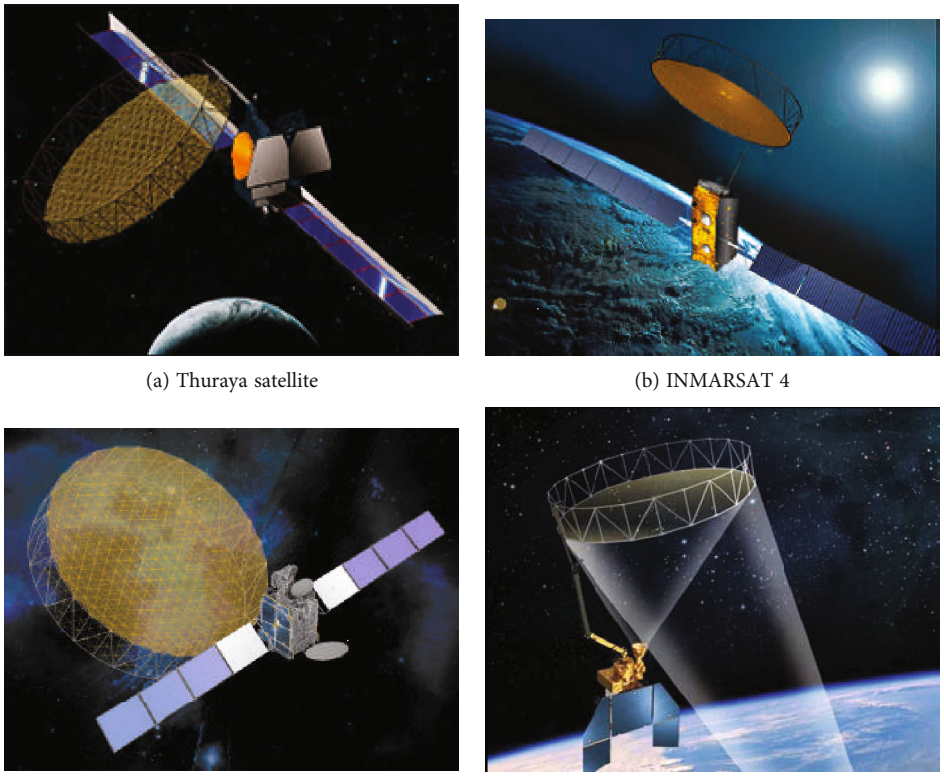

(a) Thuraya satellite

(b) INMARSAT 4

(c) MBSAT

(d) SMAP spacecraft

Figure 1: Satellite with ring truss antenna.

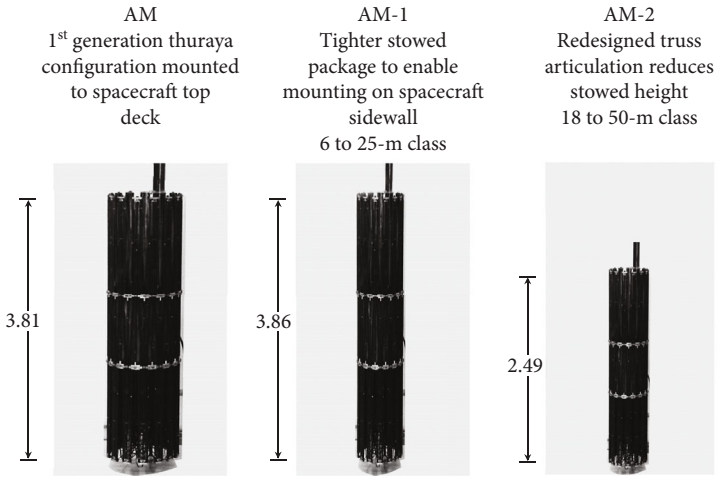

Figure 2: AstroMesh reflectors with 12-meter deployed aperture.

of small deformations and without considering the coupling effects between the rigid motion and the elastic deformation. Li et al. [15] proposed an effective form-finding methodology that combines the iterative force density method and the minimum norm method. The form-finding analysis of the reflector with the standard configuration, the central hub configuration, and the circular configuration is performed to validate the proposed methodology. Based on the initial configuration, the deployment dynamics of a complex AstroMesh reflector was studied by using the parallel computation [16]. Peng et al. [17] proposed a new cable element of ALE formulation to simulate the cable pulley system with friction and carried out the deployment simulation of a full-scale flexible multibody model of the AstroMesh. The variations of the kinetics of the structure, the bending moments of the truss members, and the motor driving forces in the deployment process are discussed.

However, most scholars focused on the AM class of AstroMesh reflectors in the dynamic characteristics research of the ring truss deployable reflector; the dynamic analysis of the AM-2 class has seldom been investigated. In this paper, the natural coordinate formulation (NCF) [16] is applied to model

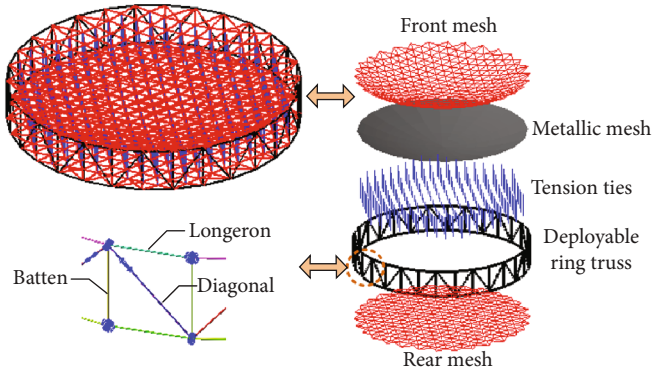

Figure 3: Components of AstroMesh reflector truss.

the ring truss deployable antenna structure. Combining the analysis of degrees of freedom (DOFs) and the dynamic simulation, the deployment strategy and dynamic analysis of the AM-2 class of AstroMesh reflectors are analyzed.

2. AstroMesh Truss Structure

The AstroMesh reflector is mainly composed of a deployable ring truss, the front net, the rear net, and tension ties. The metal mesh is attached to the front net for the reflective surface. When the deployment of the reflector is completed, the front net, the near net, and ties are all in tension. The AstroMesh reflector truss is comprised of longeron, diagonal, and batten rods, as shown in Figure 3 [15].

The AM-class of the AstroMesh truss is composed of several parallelogram elements. The diagonal in the parallelogram element is extensible mechanism. The length of the diagonal is maximum when the structure is in the folded state, and that is minimum when the structure is in the deployment state. The ring truss structure is deployed by driving the cable embedded in the diagonals of each parallelogram of the structure, as shown in Figure 4.

The AM-2 of the AstroMesh ring truss reflector is also composed of several parallelogram elements as AM. However, unlike AM, the hinge connecting the batten rod and the other rods is not fixed that can slide freely on the batten rod. The hinge slides from the bottom of the batten rod to the top during the deploying process of ring truss structure, and the hinge slides from the top of the batten rod to the bottom during the stowing process of the ring truss structure, as shown in Figure 5.

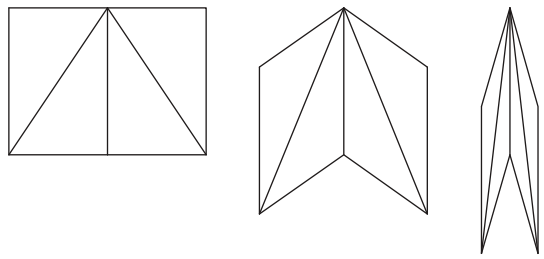

Figure 4: Parallelogram element of AM ring truss structure.

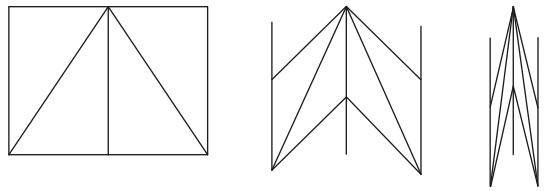

Figure 5: Parallelogram element of AM-2 ring truss structure.

3. Modeling of Truss Structure

3.1. Natural Coordinate Formulation. In the natural coordinate formulation (NCF), the Cartesian coordinates in the global inertial coordinate system are applied to define the motion of the rigid body [18]. The mass matrices in the dynamic formulations are constant. Therefore, it can greatly improve the computational efficiency in the dynamic simulation by using NCF. In this paper, two fixed points and two non-coplanar unit vectors are used as the generalized coordinates, as shown in Figure 6.

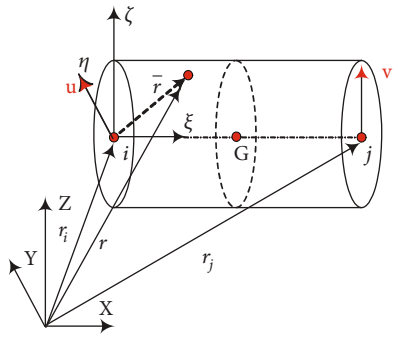

Figure 6: Rigid body described by NCF.

The rigid body has 12 generalized coordinates in the global coordinate system

$$\mathbf{q} = \left[\mathbf{r}_i^T \; \mathbf{r}_j^T \; \mathbf{u}^T \; \mathbf{v}^T\right]^T, \tag{1}$$

where $\mathbf{r}_i$ and $\mathbf{r}_j$ are the position vectors of the node i and j, respectively. The vectors $\mathbf{u}$ and $\mathbf{v}$ are two non-coplanar unit

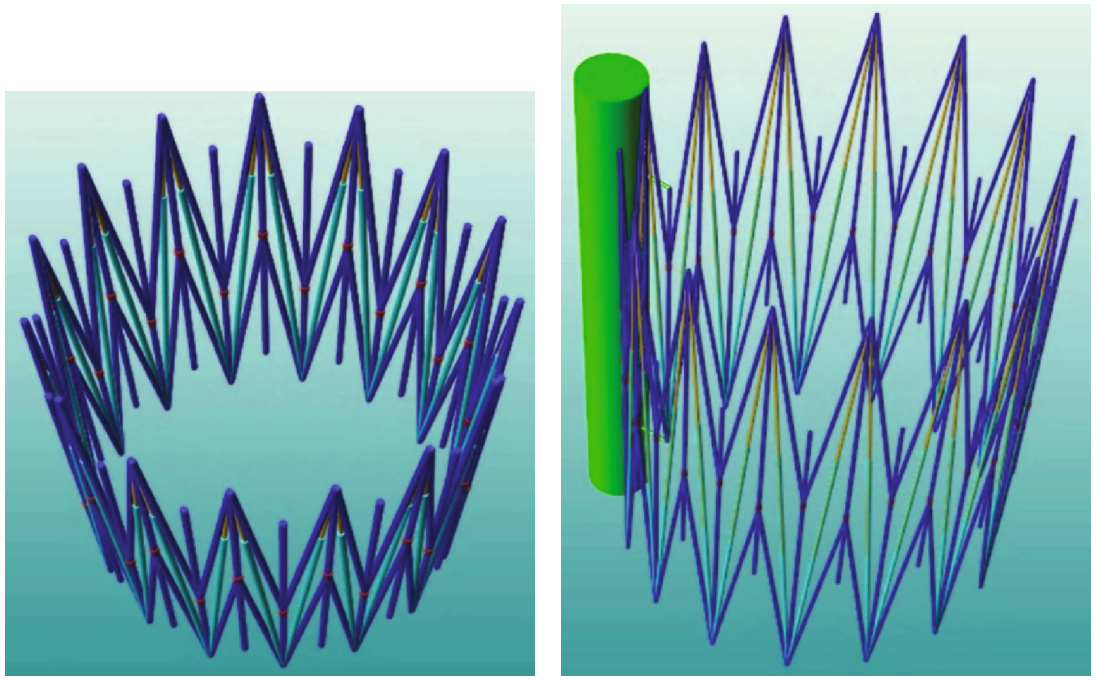

(a) Space free case (b) One batten fixed case

Figure 7: Two different cases of the ring truss structure.

Table 1: DOFs of truss structure in two cases.

Case of structure	Space free	One batten fixed
Degrees of freedom	61	55

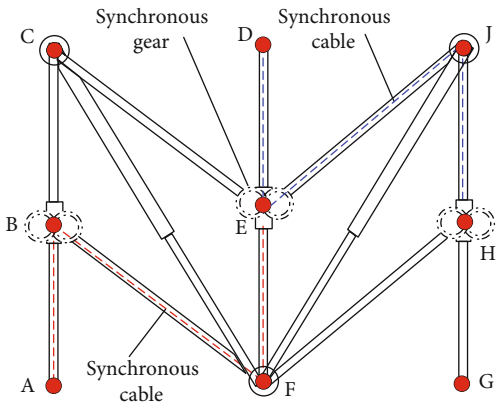

Figure 8: Truss element with synchronous constraints.

vectors. The vectors $\mathbf{r}_j - \mathbf{r}_i$, $\mathbf{u}$, and $\mathbf{v}$ are perpendicular to each other. The global position of an arbitrary point P in the rigid body can be described as

$$\mathbf{r} = [(1 - c_1)\mathbf{I}_3 \; c_1\mathbf{I}_3 \; c_2\mathbf{I}_3 \; c_3\mathbf{I}_3] \begin{Bmatrix} \mathbf{r}_i \\ \mathbf{r}_j \\ \mathbf{u} \\ \mathbf{v} \end{Bmatrix} = \mathbf{Cq}, \tag{2}$$

Table 2: DOFs of truss structure in different cases.

Case of structure	Synchronous cables	Synchronous gears	Synchronous cables and synchronous gears
Space free	34	33	8
One batten fixed	28	27	2

Table 3: DOFs of truss structure with fixed length of diagonal.

Case of structure	Without synchronous constraint	Synchronous cables
Space free	32	7
One batten fixed	26	1

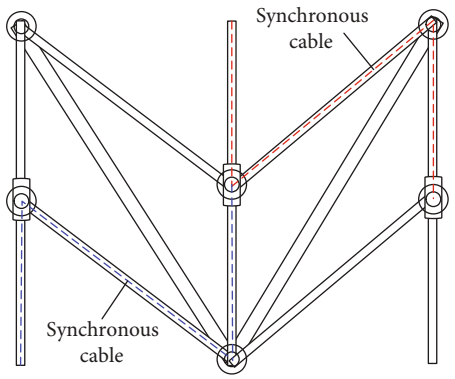

Figure 9: Truss element with synchronous cables constraints.

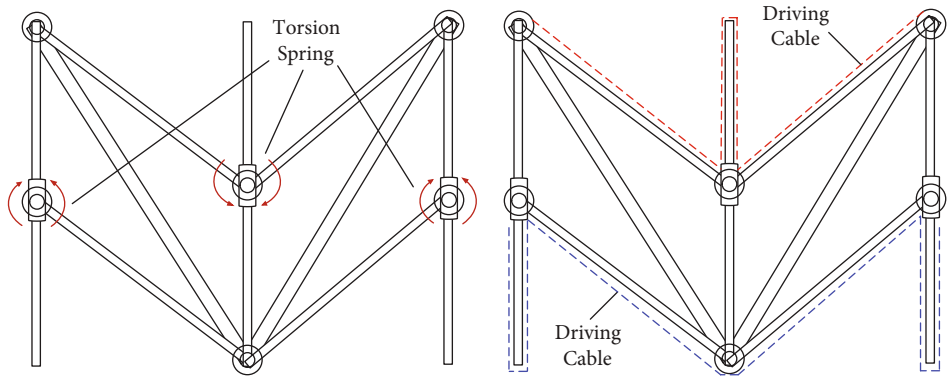

(a) Torsion spring (b) Driving cable

Figure 10: Driving scheme for the deployment of the ring truss structure.

where $\mathbf{C}$ is the shape function matrix which depends on the local coordinate of point P. $\mathbf{I}_3$ is the 3×3 identity matrix.

It is known that the rigid body has 6 degrees of freedom (DOFs) in the space. The rigid body described by NCF has 12 generalized coordinates. There are 6 inherent constraints for one rigid body, and the constraint functions can be written as

$$\begin{cases} |\mathbf{r}_i - \mathbf{r}_j| = L, \quad |\mathbf{u}| = 1, \quad |\mathbf{v}| = 1, \\ (\mathbf{r}_i - \mathbf{r}_j) \perp \mathbf{u}, \quad (\mathbf{r}_i - \mathbf{r}_j) \perp \mathbf{v}, \quad \mathbf{u} \perp \mathbf{v}. \end{cases} \tag{3}$$

3.2. Dynamic Equation of the Truss Structure. Based on the first Lagrange equation, considering the constraints, the governing equation of motion for a multibody system can be expressed in a compact form as a set of differential and algebraic equations (DAEs) with constant mass matrix

$$\begin{cases} \mathbf{M}\ddot{\mathbf{q}} + \boldsymbol{\Phi}_{\mathbf{q}}^{\mathrm{T}} \boldsymbol{\lambda} = \mathbf{Q}(\mathbf{q}, t), \\ \boldsymbol{\Phi}(\mathbf{q}, t) = \mathbf{0}, \end{cases} \tag{4}$$

where $\mathbf{M}$ represents a system constant mass matrix of the system, $\mathbf{q}$ represents the generalized coordinates of the whole multibody system, and $\boldsymbol{\Phi}(\mathbf{q}, t)$ represents the constraint vector of the system. The Jacobian matrix $\boldsymbol{\Phi}_{\mathbf{q}}$ is the derivative matrix of the constraint vector with respect to the generalized coordinates $\mathbf{q}$, $\boldsymbol{\lambda}$ is the Lagrange multiplier vector, and $\mathbf{Q}(\mathbf{q}, t)$ is the generalized external forces vector of the system.

It should be pointed out that redundant constraints are usually generated inevitably when describing the constraint equations for the complex multibody system, especially the closed-loop deployable structure. Therefore, the redundant constraints should be removed by eliminating the dependent constraint equations in the degree of freedom analysis and the dynamic analysis of the system.

The total constraint equations of a multibody system are usually composed of the inherent constraint equations such as Equation (3) and the constraint equations for the connections between the components of the structure. The Gaussian elimination method is adopted to eliminate the principal elements in the Jacobian matrix $\boldsymbol{\Phi}_{\mathbf{q}}$, and then, the independent constraint equations would be obtained after removing the corresponding redundant constraint equations. The degrees of freedom of the system can be obtained by subtracting the number of the independent constraint equations from the number of generalized coordinates.

4. DOF Analysis and Constraint Scheme

Based on this configuration with sliding hinges on the batten rods, the deployment strategy of the ring truss structure with alterable diagonal length and with fixed diagonal length is discussed, respectively, in this section.

4.1. Truss with Alterable Diagonal Length. The AM-2 type of ring truss structure with variable length of the diagonal is considered in this section. The rigid dynamic model of the ring truss structure with 30 sides in two different cases are established by using NCF introduced in Section 3.1, respectively. The rigid parts in the dynamic model include 60 longeron rods, 30 batten rods, 60 diagonal rods, and 30 sliding hinges on the batten rods. The constraint equations include the rotation joints between the longeron and the batten rods, the rotation joints between the diagonal and the batten rods, the sliding joints between the hinges and the batten rods, and the sliding joints between the diagonal rods in the same parallelogram elements.

The first case is that the truss structure is completely free in the space without any external constraint, and the second case is that one batten rod of the truss structure is fixed in the space, as shown in Figure 7. The degree of freedom of the ring truss structure is analyzed by the rigid dynamic model.

The DOFs of the truss structure are shown in Table 1. As shown in this table, the DOFs of the structure in space free case are 6 more than the DOFs of the structure in one batten fixed case as expected. It is obvious that the structure is not reliable with such numbers of DOFs as shown in the table.

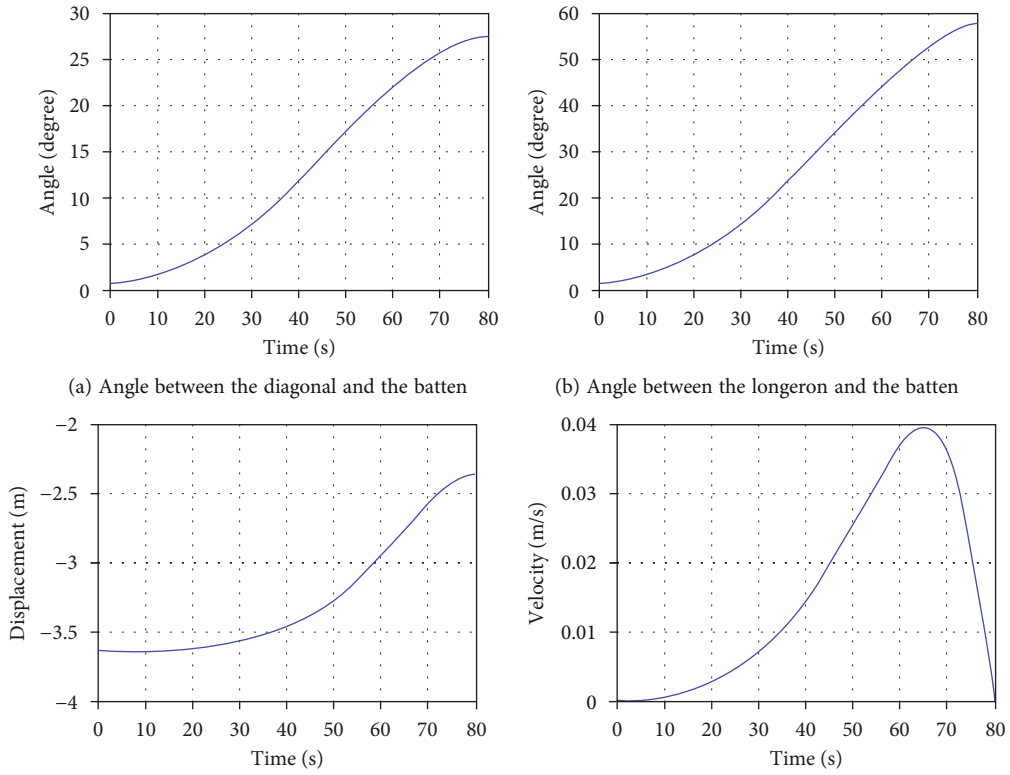

(a) Angle between the diagonal and the batten

(b) Angle between the longeron and the batten

(c) Displacement of sliding joint from the tip of the batten

(d) Velocity of sliding joint from the batten

Figure 11: Simulation results of the truss deployment in the first stage.

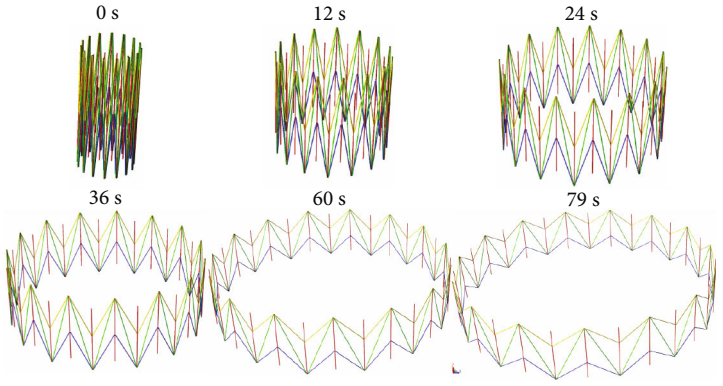

Figure 12: Deployment configurations in the first stage.

In order to reduce the DOFs of the structure and improve the deployment reliability of the truss structure, the synchronous constraints are needed for the structure which can be achieved by using the synchronous cables and the synchronous gears, as shown in Figure 8.

The synchronous cable has a constant length which is the sum of the length of the batten and the longeron rod. It can be used to control the sliding motions of two hinges in the same truss unit, and the truss units remain parallelograms in the deployment progress due to the synchronous cables. The constraint equations for the synchronous cables in Figure 8 can be described as follows:

$$\begin{cases} |\mathbf{r}_A - \mathbf{r}_B| - |\mathbf{r}_D - \mathbf{r}_E| = 0, \\ |\mathbf{r}_D - \mathbf{r}_E| - |\mathbf{r}_G - \mathbf{r}_H| = 0, \end{cases} \tag{5}$$

where $\mathbf{r}_A$, $\mathbf{r}_B$, $\mathbf{r}_D$, $\mathbf{r}_E$, $\mathbf{r}_G$, and $\mathbf{r}_H$ represent the position vectors of points A, B, D, E, G, and H in the global coordinate, respectively.

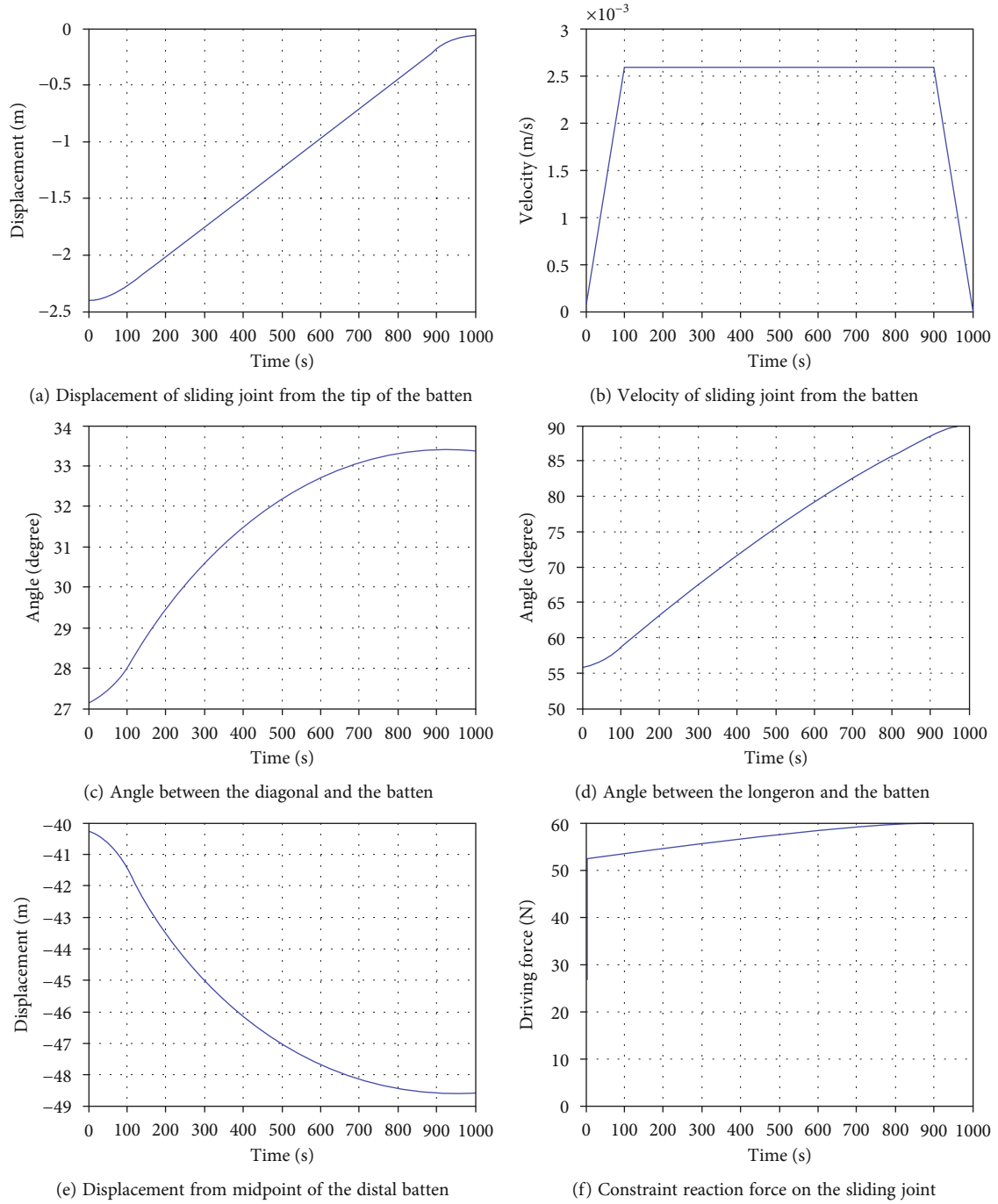

(a) Displacement of sliding joint from the tip of the batten

(b) Velocity of sliding joint from the batten

(c) Angle between the diagonal and the batten

(d) Angle between the longeron and the batten

(e) Displacement from midpoint of the distal batten

(f) Constraint reaction force on the sliding joint

Figure 13: Simulation results of the truss deployment in the second stage.

The synchronous gear is installed in the sliding hinge connecting one batten and two longeron rods, as shown in Figure 8. It can be used to control the motion of the adjacent truss units. The rotation angles of two adjacent longeron rods connecting the sliding hinge with respect to the batten rod keep consistent due to the synchronous gears. The constraint equations for the synchronous gears in Figure 8 can be described as follows:

$$\frac{(\mathbf{r}_D - \mathbf{r}_E)\cdot(\mathbf{r}_C - \mathbf{r}_E)}{|\mathbf{r}_D - \mathbf{r}_E||\mathbf{r}_C - \mathbf{r}_E|} - \frac{(\mathbf{r}_D - \mathbf{r}_E)\cdot(\mathbf{r}_J - \mathbf{r}_E)}{|\mathbf{r}_D - \mathbf{r}_E||\mathbf{r}_J - \mathbf{r}_E|} = 0, \quad (6)$$

where $\mathbf{r}_C$ and $\mathbf{r}_J$ represent the position vectors of points C and J in the global coordinate, respectively.

The rigid dynamic model of the 30-side ring truss structure with synchronous cables and synchronous gears is established by using NCF. DOF analysis of the truss structure in different cases is performed, as shown in Table 2.

It is shown from the table that the DOFs of the ring truss structure can be reduced significantly by using the synchronous constraints. If the synchronous cables and synchronous gears are applied simultaneously, the DOFs of the structure

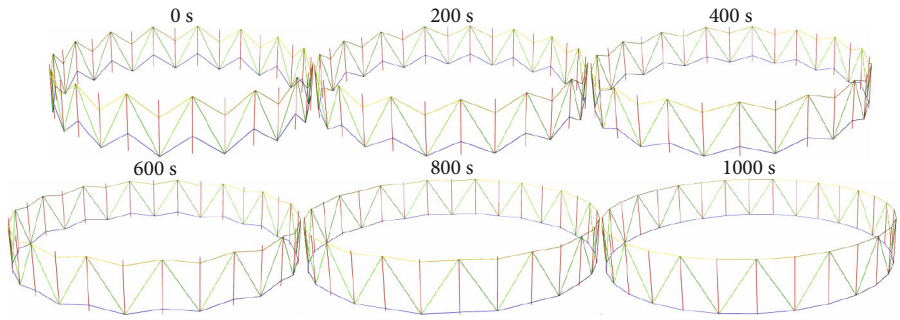

Figure 14: Deployment configurations in the second stage.

are reduced to 2 which means that the deployment reliability of the truss structure is significantly improved.

4.2. Truss with Fixed Diagonal Length. The AM-2 type of ring truss structure with fixed length of the diagonal is considered in this section. The rigid dynamic model of the ring truss structure with 30 sides in the case of space free and in the case of one batten fixed is established by using NCF, respectively. Compared with the rigid dynamic model of the truss with alterable diagonal length, this kind of rigid dynamic model has 30 fewer diagonal rods, and the constraint equations do not contain the sliding joints between the diagonal rods in the same parallelogram elements.

The degrees of freedom of the ring truss structure are analyzed by using the rigid dynamic model.

It can be seen that the DOFs of the structure with the fixed diagonal length are much less than the structure with the alterable diagonal length by comparing Tables 2 and 3. Since the length of the diagonal rods keep constant, it eliminates some of the DOFs from the truss structure. The DOFs of the truss structure with the fixed diagonal length reduce to 1 when the synchronous cables constraints are applied, as shown in Figure 9. It is obvious that this type of AM-2 truss structure has higher stability and reliability.

5. Dynamic Simulation of AM-2 Truss Structure

The dynamic simulation of the deployment of a 30-side AM-2 AstroMesh reflector truss with the fixed diagonal length without gravity is carried out in this section by using the rigid dynamic model established before. As with the AM class of AstroMesh reflectors, the deployment of the AM-2 AstroMesh reflector truss can be divided into two stages. In the first stage, the truss deploys to a semi-unfolding configuration under the action of the moments between the longeron rod and the batten rod which can be achieved by torsion springs. In the second stage, the truss deploys to the final unfolding configuration under the action of the driving forces between the hinge and the batten rod which can be achieved by the driving cables, as shown in Figure 10.

The aperture of the truss structure is 50 m. The length of the longeron and the batten rods are 5.1 m and 7.8 m, respectively. The outer diameter of the rods is 30 mm, and the thickness is 1.2 mm. The density of the material is 1600 kg/m^3. The initial rotational torque of the torsion spring is set as 3.0 Nm, and it would reduce to zero when the rotation angle reaches to 33 degrees.

As shown in Figure 11, in the first deployment stage, the deployment speed of the truss decreases to zero when the angle between the longeron and the batten rods is 56.8 degrees and the angle between the diagonal and the batten rods is 27.3 degrees. The deployment time is 79.8 s. The deployment configurations of the truss structure at different times in the first stage are shown in Figure 12.

In the second stage, in order to ensure the stability of the deployment process, the dynamic simulation of the deployment is carried out according to the constraint planning method [19]. The total time for the deployment process is set as 1000 s. The displacement and the velocity of the sliding joint on the batten rod are planned as shown in Figures 13(a) and 13(b). As shown in Figures 13(c)–13(e), the truss is gradually deployed to the final state configuration under the action of driving force. It can also be seen from the constraint reaction curves in Figure 13(f) that the maximum driving force required for truss deployment is about 60 N. The deployment configurations of the truss structure at different times in the second stage are shown in Figure 14.

6. Conclusion

According to the concept of AM-2 AstroMesh reflector truss structure, the rigid multibody system of two different types of AM-2 ring truss structure is established in this work. The system is described by using the natural coordinate formulation (NCF). The synchronous constraint schemes are proposed for the two types of truss structure, respectively. The deployment strategy of the truss structures is studied by using the degree of freedom (DOF) analysis. The results show that the DOFs of the truss structure can be reduced effectively by applying the synchronous constraints. It also can be shown from the results that the truss structure with fixed diagonal length has higher stability and reliability than the truss structure with alterable diagonal length. The dynamic simulation of the deployment of a 30-side AM-2 AstroMesh reflector truss structure with fixed diagonal length without gravity is carried out. The truss is deployed by the torsion springs and the driving cables in the first and second deployment stage, respectively. The driving forces are predicted according to the dynamic simulation. The dynamic characteristics of the deployment of the truss structure are obtained. Based on this work, the flexible

multibody dynamic model of the reflector truss would be developed for the truss structure. The mesh and tension ties can also be considered in the deployment simulation in the future work. The dynamic characteristics of the deployment of the reflector would be simulated more accurately.

Data Availability

The raw/processed data required to reproduce these findings cannot be shared at this time as the data also forms part of an ongoing study.

Conflicts of Interest

The authors declare that they have no conflicts of interest.

Acknowledgments

This work was supported in part by the National Natural Science Foundation of China under Grant Nos. 11402196 and 11290154.

References

[1] W. Thomson, "The AstroMesh deployable reflector," *IEEE Antennas and Propagation Society*, vol. 3, pp. 1516–1519, 1999.

[2] A. Meguro, S. Harada, and M. Watanabe, "Key technologies for high-accuracy large mesh antenna reflectors," *Acta Astronautica*, vol. 53, no. 11, pp. 899–908, 2003.

[3] M. A. Neto, J. A. C. Ambrosio, and R. P. Leal, "Composite materials in flexible multibody systems," *ComputerMethods in Applied Mechanics and Engineering*, vol. 195, pp. 6860–6873, 2006.

[4] Y. Miyazaki, Y. Shirasawa, O. Mori, and H. Sawada, "Finite element analysis of deployment of gossamer space structure," in *Multibody Dynamics ECCOMAS Thematic Conference*, p. 2011, Brussels, Belgium, 2011.

[5] J. M. Hedgepeth, "Accuracy potentials for large space antenna reflectors with passive structure," *Journal of Spacecraft and Rockets*, vol. 19, no. 3, pp. 211–217, 1982.

[6] S. J. Wang and J. M. Cameron, "Dynamics and control of a large space antenna," *Journal of Guidance, Control, and Dynamics*, vol. 7, no. 1, pp. 69–76, 1984.

[7] Z. You and S. Pellegrino, "Cable-stiffened pantographic deployable structures part 2: mesh reflector," *AIAA Journal*, vol. 35, no. 8, pp. 1348–1355, 1997.

[8] M. W. Thomson, "Astromesh deployable reflectors for Ku- and Ka-band commercial satellites," in *20th AIAA International Communication Satellite Systems Conference and Exhibit*, Montreal, Quebec, Canada, 2002.

[9] M. Mobrem, S. Kuehn, C. Spier, and E. Slimko, "Design and performance of AstroMesh reflector onboard soil moisture active passive spacecraft," in *Proceedings of the Aerospace Conference*, pp. 1–10, Piscataway, NJ, 2012.

[10] X. Qi, H. Huang, B. Li, and Z. Deng, "A large ring deployable mechanism for space satellite antenna," *Aerospace Science and Technology*, vol. 58, pp. 498–510, 2016.

[11] B. Li, X. Qi, H. Huang, and W. Xu, "Modeling and analysis of deployment dynamics for a novel ring mechanism," *Acta Astronautica*, vol. 120, pp. 59–74, 2016.

[12] Northrop Grumman, *AstroMesh™ Reflector Parametrics*, Northrop Grumman Corporation, 2016.

[13] T. Li, "Deployment analysis and control of deployable space antenna," *Aerospace Science and Technology*, vol. 18, no. 1, pp. 42–47, 2012.

[14] Y. Zhang, B. Duan, and T. Li, "A controlled deployment method for flexible deployable space antennas," *Acta Astronautica*, vol. 81, no. 1, pp. 19–29, 2012.

[15] P. Li, C. Liu, Q. Tian, H. Hu, and Y. Song, "Dynamics of a deployable mesh reflector of satellite antenna: form-finding and modal analysis," *Journal of Computational and Nonlinear Dynamics*, vol. 11, no. 4, article 041017, 2016.

[16] P. Li, C. Liu, Q. Tian, H. Hu, and Y. Song, "Dynamics of a deployable mesh reflector of satellite antenna: parallel computation and deployment simulation," *Journal of Computational and Nonlinear Dynamics*, vol. 11, no. 6, p. 61005, 2016.

[17] Y. Peng, Z. Zhao, J. He, J. Yang, and Y. Xiao, "Flexible multibody model and the dynamics of the deployment of mesh antennas," *Journal of Guidance, Control, and Dynamics*, vol. 40, no. 6, pp. 1499–1510, 2017.

[18] J. Garcia De Jalon and E. Bayo, *Kinematic and Dynamic Simulation of Multibody Systems the Real-Time Challenge*, Springer, New York, 1994.

[19] C. Liu, Q. Tian, and H. Hu, "Dynamics and control of a spatial rigid-flexible multibody system with multiple cylindrical clearance joints," *Mechanism and Machine Theory*, vol. 52, pp. 106–129, 2012.

Hindawi
International Journal of Aerospace Engineering
Volume 2022, Article ID 5352146, 18 pages
https://doi.org/10.1155/2022/5352146

Review Article

Review of Root-Mean-Square Error Calculation Methods for Large Deployable Mesh Reflectors

Sichen Yuan

A. Leon Linton Department of Mechanical, Robotics and Industrial Engineering, Lawrence Technological University, MI 48075-1058, USA

Correspondence should be addressed to Sichen Yuan; syuan@ltu.edu

Received 26 March 2022; Revised 24 May 2022; Accepted 8 July 2022; Published 4 August 2022

Academic Editor: Adel Ghenaiet

In the design of a large deployable mesh reflector, high surface accuracy is one of ultimate goals since it directly determines overall performance of the reflector. Therefore, evaluation of surface accuracy is needed in many cases of design and analysis of large deployable mesh reflectors. The surface accuracy is usually specified as root-mean-square error, which measures deviation of a mesh geometry from a desired working surface. In this paper, methods of root-mean-square error calculation for large deployable mesh reflectors are reviewed. Concept of reflector gain, which describes reflector performance, and its relationship with the root-mean-square error is presented. Approaches to prediction or estimation of root-mean-square error in preliminary design of a large deployable mesh reflector are shown. Three methods of root-mean-square error calculation for large deployable mesh reflectors, namely, the nodal deviation root-mean-square error, the best-fit surface root-mean-square error, and the direct root-mean-square error, are presented. Concept of effective region is introduced. An adjusted calculation of root-mean-square error is suggested when the concept of effective region is involved. Finally, these reviewed methods of root-mean-square error calculation are applied to surface accuracy evaluation of a two-facet mesh geometry, a center-feed mesh reflector, and an offset-feed mesh reflector for demonstration and comparison.

1. Introduction

Large deployable mesh reflectors (DMRs), due to their important space applications, have experienced continued research and development interest in the past several decades [1–4]. A deployable mesh reflector uses a spherical or parabolic surface as a working shape (a required radiofrequency surface), which is formed by a network or mesh of tensioned facets.

A DMR in consideration is illustrated in Figure 1, which, after full deployment, is supported by a stiff and stable flat frame. Although there are some variations, a typical DMR is composed of a front cable net, a rear cable net, tension ties, and a supporting structure. The front net (working surface) in the figure, as well as the rear net, is constructed by a mesh of flat triangular facets. Edges of the facets are elastic cable elements interconnected at facet nodes. The nodes of the front and rear nets are also connected by tension ties of adjustable lengths. In setting up the DMR, folded nets are deployed into highly stretched elastic meshes, with lengths of the tension ties being properly adjusted such that the facets of the front net eventually form a working surface that is approximate to the desired radiofrequency surface.

In the design of a large DMR, high surface accuracy is one of the ultimate goals since it directly determines overall performance of the reflector. Therefore, evaluation of surface accuracy is needed in many cases of design and analysis of large DMRs. For example, surface accuracy can be either roughly estimated in preliminary design of a DMR to determine topology, member materials, and facet sizes [1, 5] or accurately evaluated for analysis of generated mesh geometry [1, 6]. The surface accuracy is usually specified as root-mean-square (RMS) error, which measures deviation of the mesh geometry from the desired working surface.

In this paper, commonly used state-of-the-art methods of RMS error calculation for large DMRs shall be reviewed. Methods to be reviewed include approaches to both rough

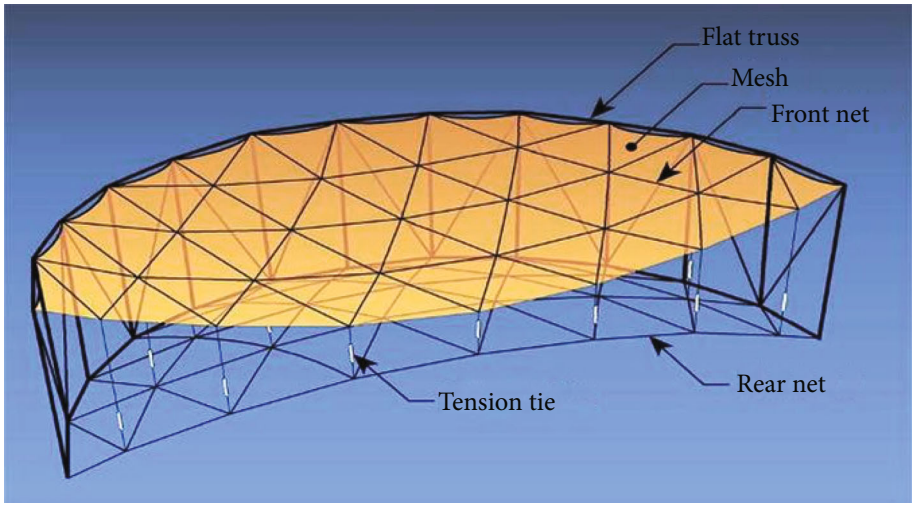

Figure 1: A typical DMR with deployed working surface.

estimation of RMS error for preliminary design and accurate calculation of RMS error for performance evaluation of large DMRs. Concepts of reflector gain and effective region, and their relationship with RMS error calculation shall also be reviewed. A comprehensive mathematical description shall be given for each method introduced. The reviewed methods shall be implemented both in a simple example for illustrative purpose and in practical examples for validation of engineering applicability.

The remainder of this paper is organized as follows: concept of reflector gain, which is a factor that describes reflector performance, and its relationship with RMS error calculation will be presented in Section 2. Methods of RMS error prediction in preliminary DMR design will be introduced in Section 3. Method of RMS error calculation for generated mesh geometries of DMRs will be described in Section 4. Concept of effective region and the corresponding incorporation in RMS error calculation will be shown in Section 5. Reviewed methods of RMS error calculation will be applied to evaluate surface accuracies of several mesh geometries for demonstration and comparison in Section 6. Conclusions of the reviewed methods of RMS error calculation will be given in Section 7.

2. Reflector Gain and RMS Effective Surface Error

Gain of a reflector is a factor that describes reflector performance. It is essential to obtain a reflector with high gain since loss of gain will seriously reduce efficiency in signal transmission. An axial gain of a circular aperture may be written as [7]

$$G = G_0 e^{-\bar{\delta}^2}, \quad \bar{\delta} = \frac{4\pi\varepsilon}{\lambda}. \tag{1}$$

where G_0 is the gain of no-error reflecting surface with the value being $\eta_{\text{eff}} (\pi D/\lambda)^2$. η_{eff} is the aperture efficiency. D is the aperture diameter. λ is the wavelength. $\bar{\delta}$ is the illumination weighted mean phase error. ε is called half-path-length error [8] or effective surface error [7] of a reflecting point on the reflecting surface with coordinate $(x_\varepsilon, y_\varepsilon, z_\varepsilon)$ (see Figure 2). In Equation (1), it is assumed that random reflector surface deformation is much smaller than the wavelength.

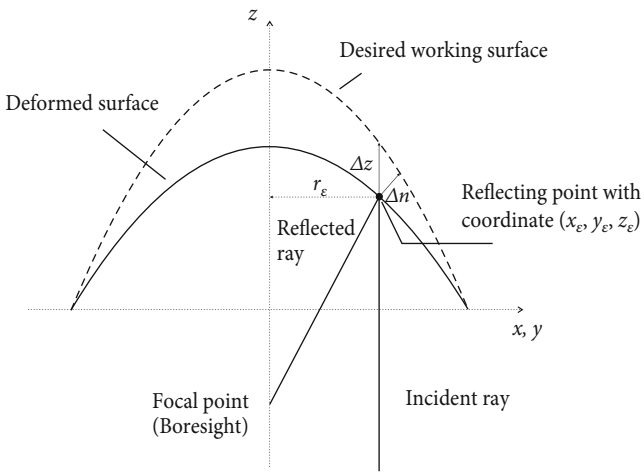

Figure 2: Geometric information of surface deviations in the z -direction and in the direction normal to the reflecting surface.

A relationship between reflector gain and half-path-length error is described in Equation (1), which indicates that large surface error significantly deteriorates gain of a reflector, which was first found out by Spencer [9]. According to Ruze [7], ε may be obtained by Equations (2a) and (2b) with a measurement of a surface deviation Δz in the z -direction or a surface deviation Δn in the direction normal to the reflecting surface (see Figure 2).

$$\varepsilon = \frac{\Delta z}{1 + (r_\varepsilon/2F)^2}, \tag{2a}$$

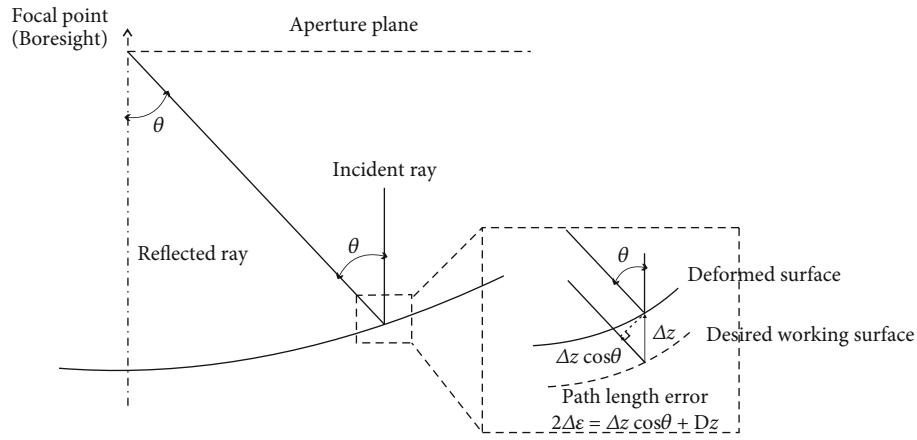

Figure 3: Geometric relation between path length error and antenna surface deformation from Ref. [8].

$$\varepsilon = \frac{\Delta n}{\sqrt{1 + (r_\varepsilon/2F)^2}}, \tag{2b}$$

where F is the focal length of a reflector and $r_\varepsilon = \sqrt{x_\varepsilon^2 + y_\varepsilon^2}$ is the distance from this given reflecting point to the center of a reflector in the xy-plane.

According to Tanaka [8], ε may also be obtained by Equation (3)

$$\varepsilon = \frac{(1 + \cos\theta)\Delta z}{2}. \tag{3}$$

Figure 3 shows the geometric information of ε. In this figure, θ is the angle between focal point direction and direction from a reflecting point on the reflector to the focal point.

Note that in Equations (2a), (2b), and (3), ε is defined as surface error of a specific reflecting point within a reflector aperture. To evaluate surface error of the whole reflector, a root-mean-square effective surface error is defined in [10, 11]

$$\varepsilon_{\text{rms}} = \sqrt{\frac{\iint_{S'} \varepsilon(x,y)^2 \psi dS'}{\iint_{S'} \psi dS'}}, \tag{4}$$

where ψ is an "illumination function" which sometimes is assumed uniform with $\psi = 1$ [11]. S' is aperture area of the reflector.

3. RMS Error Prediction in Preliminary Design of DMRs

For a large DMR whose reflecting surface is formed by facets, it is essential to predict surface accuracy of the DMR before a mesh geometry is fully generated. Facet sizes need to be known in preliminary design, such that numbers of nodes and facets can be determined. Different from the root-mean-square half-path-length error ε_{rms}, which measures deviation of a deformed reflecting surface from a desired working surface of general reflectors, the root-mean-square flat facets error δ_{rms} is used to evaluate deviation of a mesh geometry from a desired working surface. δ_{rms} is defined to have the same unit of wavelength λ. Depending on applications, different budgets for surface accuracy related to the facet geometry are suggested as follows [6, 12]:

$$\delta_{\text{rms}} \le \frac{\lambda}{N}, \tag{5}$$

where $N = 50$, 75, 100, 150, or 200. Surface deviation of a DMR may be caused by geometric difference between flat facets and desired working surface (say, a parabolic or spherical surface), variation of tension tie load, member length imperfection, ring structure distortion, and/or thermal strain.

A link between δ_{rms} and gain/loss estimation can be obtained by an approach similar to Equation (1) [13]:

$$\eta_{\text{rms}} = \exp\left[-\left(\frac{4\pi\delta_{\text{rms}}}{\lambda}\right)^2\right], \tag{6}$$

where η_{rms} is the efficiency factor of reflector gain due to the RMS error. The reflector gain estimation due to the RMS error can be obtained as

$$G = \eta_{\text{rms}} G_0. \tag{7}$$

Although Ruze's derivation in Equation (1) assumes random surface errors, it was proved that the approach in Equation (6) is also useful for estimating gain/loss from systematic error sources [14].

Agrawal et al. [1] proposed a technique to predict RMS error for a mesh reflector. RMS error $\delta_{\text{rms-pre}}$ in preliminary design is estimated in Equation (8) as

$$\delta_{\text{rms-pre}} = \frac{1}{8\sqrt{15}} \frac{L^2}{R}. \tag{8}$$

Note that this approximation is obtained under two assumptions: first, the desired working surface is a sphere with radius being R; second, all facets are equilateral triangles with the lengths of three sides being L. Then, the allowable length of facet edge is calculated as

$$\frac{L}{D} = 4\sqrt[4]{15}\sqrt{\frac{\delta_{\text{rms-pre}}}{D}\frac{F}{D}}. \tag{9}$$

Reference [1] also introduced an RMS error prediction method for equilateral square and hexagonal facets as

$$\frac{L}{D} = K\sqrt{\frac{\delta_{\text{rms-pre}}}{D}\frac{F}{D}}, \tag{10}$$

where K in Equation (10) is 6.160 for square facets and 4.046 for hexagonal facets. Equations (8) and (9) are widely used in stage of preliminary design of large DMRs to determine the maximum allowable facet size [14–16].

Meyer [17] introduced differential geometry of a mesh surface and used membrane theory to calculate RMS error for a mesh reflector. Fichter [18] extended theory in Equations (8)–(10) by considering stress of membrane within the facets. Similar with the work in Ref. [1], RMS error of a shallow reflector with equilateral triangular facets is predicted as

$$\frac{\delta_{\text{rms-pre}}}{D} = \frac{\sqrt{15}}{560}\frac{(L/D)^2}{F/D}. \tag{11}$$

For equilateral rectangular facets of length $2h$ and width $2k = 2\rho h$, with $0 < \rho \le 1$, RMS error was estimated as

$$\frac{\delta_{\text{rms-pre}}}{D} = \frac{\sqrt{5}}{120}\sqrt{1+\rho^4}\frac{(2h/D)^2}{F/D}. \tag{12}$$

Hedgepeth [19, 20] considered mesh saddling in RMS error prediction by introducing stress of membrane within the facets, which was also pointed out in Refs. [13, 21]. When effect of membrane tension is considered, mesh of a reflector is often pulled into a dish shape by auxiliary chords attached to several interior points. The lateral loading tends to curve the supporting members inward. Thus, nodal positions of the mesh were suggested to be adjusted, so as to compensate this effect. According to Refs. [13, 19], RMS error of a mesh of equilateral triangular facets is estimated as

$$\frac{\delta_{\text{rms-pre}}}{D} = 0.01614\frac{(L/D)^2}{F/D}\sqrt{1+0.660\frac{pL}{t}+0.133\left(\frac{pL}{t}\right)^2}, \tag{13}$$

where p and t are mesh tension and force in supporting elements.

Influences of member lengths imperfection and thermal strain on the surface accuracy of large DMRs were studied by many researchers in the past decades [5, 22–24]. RMS error prediction for various types of structures including tetrahedral truss, geodesic dome, radial ribs, and pretensioned truss were investigated by Hedgepeth [5]. For a geodesic dome, RMS error under member lengths imperfection is estimated as

$$\frac{\delta_{\text{rms-pre}}}{D} = \frac{2F}{D}\sigma_\varepsilon, \tag{14}$$

where σ_ε is the standard deviation of member errors.

Hedgepeth [20] and Mobrem [25] used natural frequency results from available closed form solutions to estimate surface error under member length imperfection in preliminary design of a large DMR. In this inverse frequency squared method, weighted lump masses were assigned on nodes of a mesh in the direction normal to the reflecting surface. With computed natural frequencies w_i, RMS error is estimated by

$$\delta_{\text{rms-pre}} = \sqrt{\frac{\left(EAL\sigma_\varepsilon^2\right)_{\text{ref}}}{\bar{m}}\sum_{i=1}^{n}\frac{1}{w_i^2}}, \tag{15}$$

where n is the number of modes, E and A are Young's modulus and the cross-sectional area of members, and $\bar{m}$ is the total weighted masses. $\left(EAL\sigma_\varepsilon^2\right)_{\text{ref}}$ is the reference values of these variables under the assumption of

$$EA_jL_j\sigma_{\varepsilon,j}^2 = \left(EAL\sigma_\varepsilon^2\right)_{\text{ref}}, \tag{16}$$

where A_j, L_j, and $\sigma_{\varepsilon,j}^2$ are the cross-sectional area, length, and standard deviation of error of the j-th member.

RMS error prediction for mesh reflectors considering deformation caused by thermal loads during in-orbit missions was investigated in Ref. [5]. Due to a significant temperature change when entering or leaving the Earth's shadow, the corresponding thermal strain may result in large surface distortion of a mesh reflector. The work in Ref. [5] also studied temperature difference at nodes of a reflecting surface due to their different angles to solar radiation. RMS error was predicted in Equations (17) and (18) by the average strain ε_{ave} and the maximum shear strain $\gamma_{\max}$, if the strains are expressed in terms of equivalent biaxial membrane strains.

$$\frac{\delta_{\text{rms-pre}}}{D} = 0.0180\frac{\varepsilon_{\text{ave}}}{F/D}, \tag{17}$$

$$\frac{\delta_{\text{rms-pre}}}{D} = 0.0128\frac{\gamma_{\max}}{F/D}. \tag{18}$$

The calculations of ε_{ave} and $\gamma_{\max}$ are given in Figure 13 of Ref. [5]

4. RMS Error Calculation for a Generated Mesh Geometry

Geometric surface error of a DMR can be obtained by either rough estimation (prediction) or analytical calculation. For a large DMR, rough surface error estimation (prediction), as introduced in Section 3, is only used for a preliminary design. When a mesh geometry is fully generated, evaluation

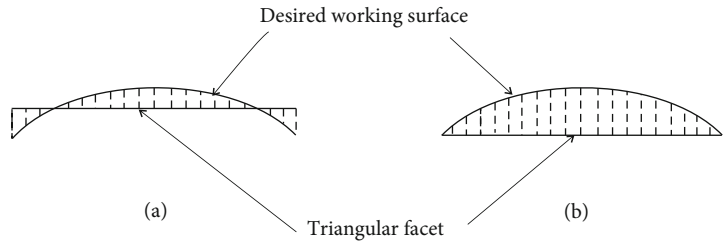

Figure 4: Triangular facet and desired working surface: (a) nodes are placed off the desired working surface and (b) nodes are placed on the desired working surface.

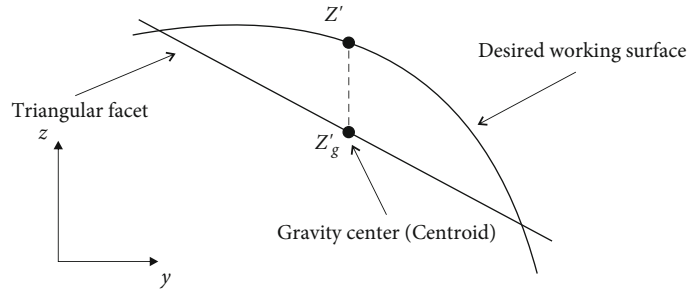

Figure 5: Geometric illustration of facet gravity center deviation RMS error.

of surface accuracy for a given topology and nodal positions are needed in complete DMR design, especially in comparing different structural design techniques [26] or form-finding methods [27, 28]. Methods of RMS error calculation for evaluating surface accuracy of a generated mesh geometry shall be introduced and compared in this section.

Surface accuracy of a generated mesh geometry in general can be evaluated by three methods: the nodal deviation RMS error, the best-fit surface RMS error, and the direct RMS error. Note that the nodal deviation RMS error and the best-fit surface RMS error do not measure a real deviation of the mesh geometry from the desired working surface. If stringent requirement on high surface accuracy in DMR design is implemented, or if nodes of a mesh geometry are placed off the desired working surface [29], the direct RMS error is necessary for a more accurate evaluation.

4.1. Nodal Deviation RMS Error. One commonly used evaluation of surface accuracy of a DMR is to calculate an RMS error due to deviation of the nodes of a mesh geometry from a desired working surface. For instance, such an RMS error $\delta_{\text{rms-n}}$ can be expressed by [30, 31]

$$\delta_{\text{rms-n}} = \sqrt{\frac{1}{n}\sum_{i=1}^{n}\left(\Delta x_i^2 + \Delta y_i^2 + \Delta z_i^2\right)}, \tag{19}$$

where Δx_i, Δy_i and Δz_i are the normal distances between the i-th node and the desired working surface in the x-, y- and z-directions and n is the total number of nodes. This method is developed under an assumption that the nodes of a reflector are moved off the desired working surface by certain predictable or unpredictable influences, such as thermal loads and fabrication errors. While being simple and easy to use, the formula in Equation (19) is not accurate enough because it fails to consider geometric difference between facet planes and curved working surface. For instance, the surface deviation of a triangular facet from the desired working surface in Figure 4(a) should be smaller than that in Figure 4(b), but the $\delta_{\text{rms-n}}$ in Equation (19) gives an opposite result simply because the facet nodes in Figure 4(a) are off the desired working surface. Furthermore, Equation (19) concludes zero surface error if all nodes of a mesh are on the desired working surface, regardless of the number of nodes, which is misleading.

Another type of nodal deviation RMS error, used in Ref. [32], is to compare values of two parameters: Z'_{g_i} and Z'_i, where Z'_{g_i} is the z-coordinate of the gravity center (centroid [1]) of the i-th computed triangular facet on the z-axis and Z'_i is the z-coordinate of the gravity center of the i-th computed triangular facet when projected vertically onto the desired working surface, shown in Figure 5. The RMS error $\delta_{\text{rms-gc}}$ is then given by

$$\delta_{\text{rms-gc}} = \left(\frac{\sum_{i=1}^{n} S'_i \left(Z'_i - Z'_{g_i}\right)^2}{\sum_{i=1}^{n} S'_i}\right)^{1/2}, \tag{20}$$

with S'_i being the projected area of the i-th triangular facet on the xy-plane. This calculation generally provides an evaluation of surface error with relatively low accuracy because only one point (gravity center) is used for each facet. This method is developed under an assumption that nodes of a triangular facet are placed on the desired working surface of a reflector. To achieve a more accurate evaluation of

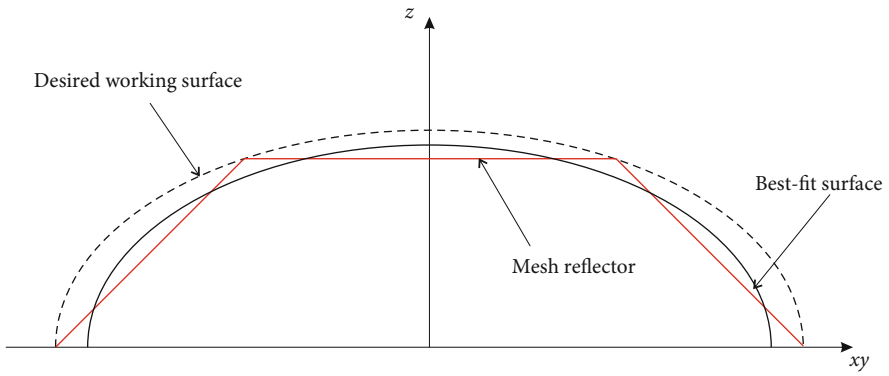

Figure 6: Schematic of the best-fit surface and desired working surface of a DMR.

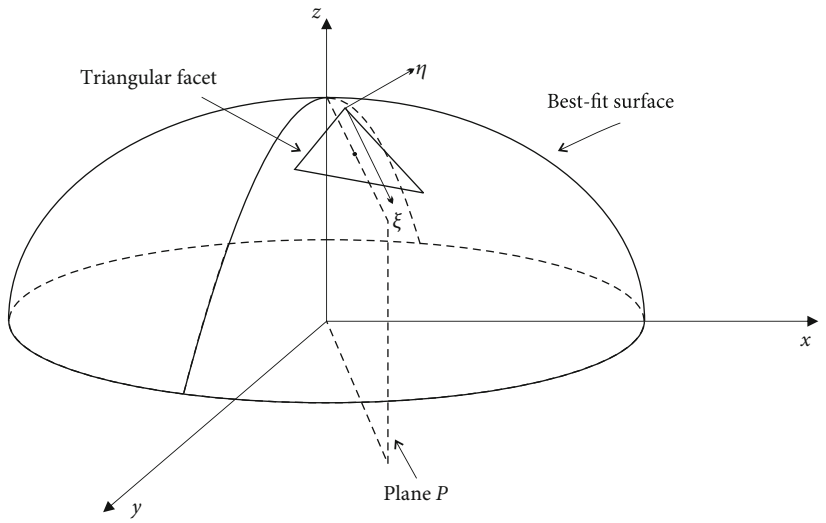

Figure 7: Local coordinate system (ξ, η) of a triangular facet in Ref. [1].

surface error, geometric difference between facet planes and desired working surface must be considered.

4.2. Best-Fit Surface RMS Error. After a mesh geometry of a DMR is generated, it is natural to find out what surface (spherical or parabolic) the mesh geometry best represents. A concept of best-fit surface is thus introduced. The best-fit surface of a DMR mesh geometry is a sphere or paraboloid, which, among all possible spherical or parabolic surfaces, has the least deviation from the mesh geometry [22, 33]. Such best-fit surface and the corresponding best-fit surface RMS error are obtained through a try and error process. To avoid confusion, the candidate of best-fit surface in each iteration is named effective surface [1]. For illustration, a schematic of a mesh geometry of a DMR, its best-fit surface, and the desired working surface is shown Figure 6.

The best-fit surface RMS error of a center-feed reflector is defined as follows. As shown in Figure 7, for a given triangular facet of the generated mesh, a plane P is defined by containing the z-axis and the centroid of the triangular facet. A local coordinate system (ξ, η) is generated by having a triangular facet node with the largest z-coordinate being the origin. The ξ-axis is parallel to the intersection between plane P and plane of the triangular facet. The η-axis is in plane of the triangular facet, perpendicular to the ξ-axis. Let (ξ_1, η_1), (ξ_2, η_2), and (ξ_3, η_3) be positions of the three nodes of the triangular facet in the local coordinate system. Denote the normal distance between a point on the facet plane and the effective surface by $\omega(\xi, \eta)$. The calculation of $\omega(\xi, \eta)$ was given in Ref. [1] with the mistakes corrected by Ref. [6] (see Equation (24)). By assuming a shallow desired working surface, an equation of ω is given as

$$\omega(\xi, \eta) = a + b\xi + c\eta + \frac{\xi^2}{2R_\xi} + \frac{\eta^2}{2R_\eta}, \tag{21}$$

where a is the normal distance from the three nodes of the triangular facet to the effective surface. Since the DMR is assumed to be shallow, the normal distances from the three nodes to the effective surface are the same in Equation (21).

In Equation (21), b and c are constants which shall be calculated later. R_ξ and R_η are radius of curvatures. For a spherical effective surface, $R_\xi = R_\eta = R$, where R is the radius of the sphere. For a parabolic effective surface,

$$R_\xi = 2F'\left[1+\left(\frac{r_c}{2F'}\right)^2\right]^{3/2},$$
$$R_\eta = r_c\sqrt{1+\left(\frac{2F'}{r_c}\right)^2}, \tag{22}$$

with $r_c = \sqrt{x_c^2 + y_c^2}$. x_c and y_c are the global coordinates of the centroid (gravity center) of the triangular facet. F' is the focal length of the effective surface. Assume the three nodes of the triangular facet are all on the effective surface (As shall be seen later in this section, it is almost impossible. This assumption is only for illustrative purpose.) and the origin of the local coordinate system (ξ, η) is at the first node of the facet, then obviously $a = 0$ and $(\xi_1, \eta_1) = (0, 0)$ and ω at the three nodes is

$$\omega(\xi_1, \eta_1) = \omega(0, 0) = 0,$$
$$\omega(\xi_2, \eta_2) = 0, \tag{23}$$
$$\omega(\xi_3, \eta_3) = 0.$$

Combining Equation (21) and Equation (23), the remaining constants are then obtained as

$$b = \frac{-(\eta_3 d_2 - \eta_2 d_3)}{4S},$$
$$c = \frac{(\xi_2 d_3 - \xi_3 d_2)}{4S},$$
$$S = \frac{1}{2}(\xi_2\eta_3 - \xi_3\eta_2), \tag{24}$$
$$d_i = \frac{\xi_i^2}{R_\xi} + \frac{\eta_i^2}{R_\eta}.$$

S is the area of the triangular facet. It should be noticed that Equation (24) is different from (A. 5) in Ref. [1], which mistakenly calculated b as $b = (\eta_3 d_2 - \eta_2 d_3)/4S$.

With Equation (21), squared deviation of the facet plane from the effective surface is calculated by integrating ω^2 over the facet area S:

$$\phi = \iint_S \omega^2 d\xi d\eta = S\left[a^2 - \frac{af}{6} + \frac{f^2}{120} - \frac{S^2}{90R_\xi R_\eta}\right], \tag{25}$$

where

$$f = \frac{\left(\xi_2^2 - \xi_2\xi_3 + \xi_3^2\right)}{R_\xi} + \frac{\left(\eta_2^2 - \eta_2\eta_3 + \eta_3^2\right)}{R_\eta}. \tag{26}$$

The effective surface RMS error $\delta_{\text{rms-eff}}$ of the entire mesh then is defined by adding up ϕ of facets of the whole reflector and divided by the summation of facet areas, given as follows:

$$\delta_{\text{rms-eff}} = \sqrt{\frac{1}{S_{\text{mesh}}}\sum_i \phi_i}, \tag{27}$$

where $S_{\text{mesh}} = \sum_i S_i$ is the total area of all facets of the mesh geometry.

The best-fit surface of a generated mesh geometry can then be found by properly determining its focal length F_{bf} and the vertex height H_{bf} through a try and error process, such that $\delta_{\text{rms-eff}}$ in Equation (27) is minimized. Therefore, the value of a in each iteration is different. The calculation of a was given in Ref. [1] and the mistake which was corrected in Ref. [6].

Geometries of a general triangular mesh facet, a desired working surface, and an effective surface are given in Figure 8. The equations of the desired working surface and the effective surface are

$$x^2 + y^2 = 4F(H - x), \tag{28}$$

$$x^2 + y^2 = 4F'(H - h - z), \tag{29}$$

where h is distance in the vertical direction between the vertices of the desired working surface and the effective surface. H is height of the desired working surface. The facet plane is defined by an equation $z = A + Bx + Cy$.

There are two assumptions in the calculation of the best-fit RMS error: first, reflector is shallow; second, the nodes are all placed on the desired working surface. Thus, under the two assumptions, a is also the normal distance between the effective surface and the desired working surface for a given mesh facet.

A line $\overline{PQ}$ is created by passing through the centroid C of the facet normal to its plane. The equation of the line in its plane created by r and z is given in (A. 10) of Ref. [1] which is represented here:

$$r^2 = x^2 + y^2,$$
$$z = z_c + \frac{r - r_c}{\sqrt{B^2 + C^2}}, \tag{30}$$

where z_c and r_c are coordinates of the centroid of the facet. The r_c is given as

$$r_c^2 = x_c^2 + y_c^2. \tag{31}$$

r_p, r_q, z_p, and z_q are shown in Figure 8, and their formulas of calculation are obtained by substituting Equation (30) into Equations (28) and (29):

$$r_q = \frac{-2F}{\sqrt{B^2 + C^2}} + 2\sqrt{\frac{F^2}{B^2 + C^2} + F\left(H - z_c + \frac{r_c}{\sqrt{B^2 + C^2}}\right)}, \tag{32}$$

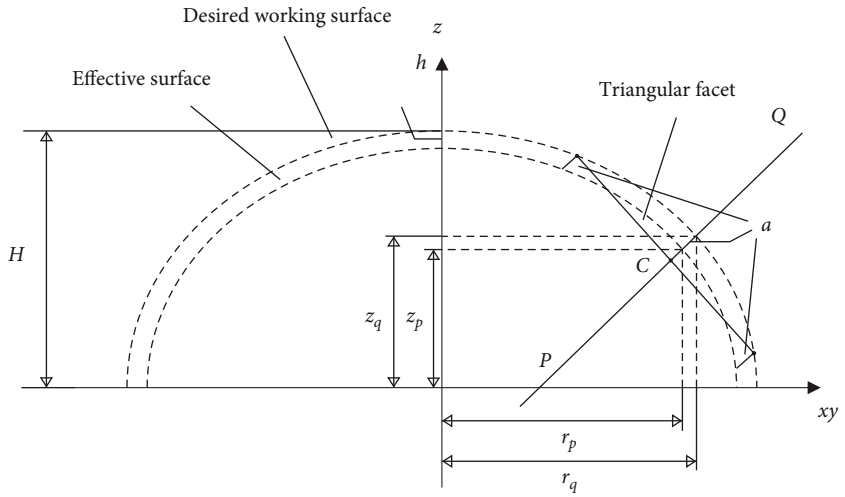

Figure 8: Geometries of desired working surface, effective surface, and a facet.

$$r_p = \frac{-2F'}{\sqrt{B^2+C^2}} + 2\sqrt{\frac{F'^2}{B^2+C^2} + F'\left(H - h - z_c + \frac{r_c}{\sqrt{B^2+C^2}}\right)}, \tag{33}$$

$$z_q = H - \frac{r_q^2}{4F}, \tag{34}$$

$$z_p = H - h - \frac{r_p^2}{4F'}, \tag{35}$$

$$a = \sqrt{\left(z_p - z_q\right)^2 + \left(r_p - r_q\right)^2}, \tag{36}$$

where Equation (35) is different from the incorrect form in (A. 12) of Ref. [1] shown in

$$z_p = H - \frac{r_q^2}{4F'}. \tag{37}$$

With the value of a, the best-fit parabolic or sphere surface is then found by adjusting F' and h to minimize the RMS error in Equation (27). The optimal result is the best-fit surface RMS error $\delta_{\text{rms–bf}}$. This can be done by a numerical optimization algorithm [34].

$$\min\left[\delta_{\text{rms}}\left(F', h\right)\right], \tag{38}$$

$$\begin{aligned} F_{bf} &= F'_{\min}, \\ H_{bf} &= H - h_{\min}. \end{aligned} \tag{39}$$

The evaluation of the best-fit surface of an offset-feed parabolic mesh geometry is different from that of a center-feed one and can be found in Ref. [6]. As shown in Figure 9, the parent paraboloid and its best-fit surface are in the global coordinates. Here, $D_{ca,bf}$ is the diameter of the circular aperture of the reflector's best-fit working surface which is the portion of the parent best-fit surface within the offset aperture; $F_{p,bf}$ and $\Delta H_{g,bf}$ are the parent best-fit focal length and the vertical deviation; and φ is the slope of the best-fit parabola at the point intersecting with the parent aperture in the $x_g z_g$-plane. From Figure 9,

$$D_{p,bf} = 4\sqrt{F_{p,bf}\left(H_g - \Delta H_{g,bf}\right)}, \tag{40}$$

$$\varphi = \sin^{-1}\left(\frac{D_{p,bf}}{2R_{s,bf}}\right), \tag{41}$$

$$\varphi_{off} = \tan^{-1}\left(\frac{H_g - e_z}{2R_c}\right). \tag{42}$$

If $\Delta H_{g,bf}$ is always sufficiently small, it can be assumed that

$$\begin{aligned} R_s &= R_{s,bf}, \\ \varphi &= \varphi'. \end{aligned} \tag{43}$$

From the geometry in Figure 9,

$$\frac{AC}{BC} = 1 - \frac{\tan\left(\varphi_{\text{off}}\right)}{\tan\left(\varphi\right)}, \tag{44}$$

where

$$\begin{aligned} AC &= \frac{1}{2}\left(D_{ca} - D_{ca,bf}\right), \\ BC &= \frac{1}{2}\left(D_p - D_{p,bf}\right). \end{aligned} \tag{45}$$

Hence,

$$D_{ca,bf} = D_{ca} - \frac{\tan\left(\varphi\right)}{\tan\left(\varphi\right) - \tan\left(\varphi_{\text{off}}\right)}\left(D_p - D_{p,bf}\right). \tag{46}$$

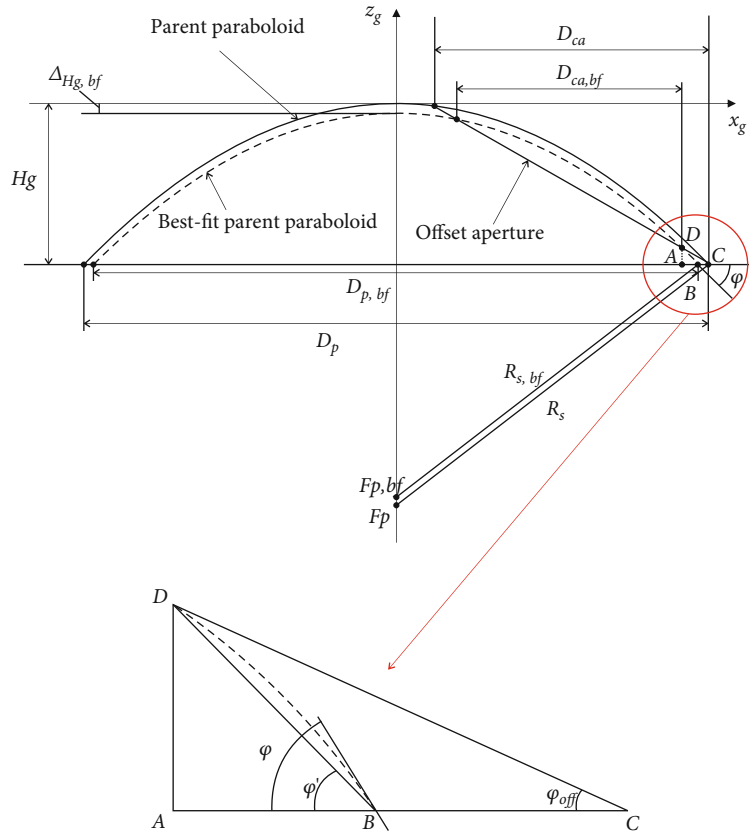

Figure 9: The best-fit surface for an offset-feed parabolic reflector in the $x_g z_g$-plane.

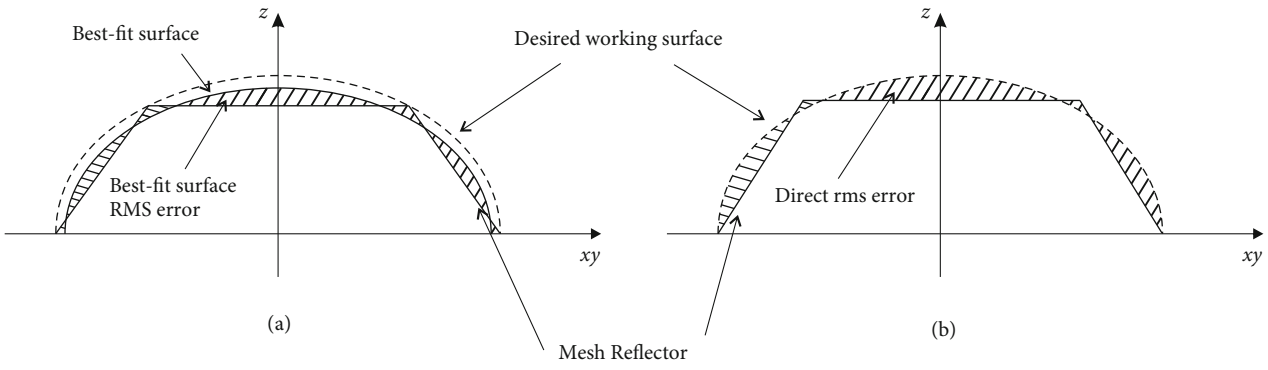

Figure 10: Comparison of two types of RMS errors: (a) the best-fit surface RMS error and (b) the direct RMS error.

4.3. Direct RMS Error. The best-fit surface RMS error described in Section 4.2 is not a true evaluation of geometric deviation of a DMR mesh geometry from its desired working surface. For design of a DMR with high surface accuracy, the direct RMS error that truly measures geometric deviation of a DMR mesh geometry from its desired working surface was proposed in Refs. [35, 36]. A comparison of these two types of RMS errors is shown in Figure 10.

Consider a typical triangular facet in Figure 11, where the desired working surface is also shown. To calculate the direct RMS error, a local coordinate system (τ, υ) is established on the facet plane; see Figure 12, where the origin can be any one of nodes of the facet. Let $\mu(\tau, \upsilon)$ be normal distance between a point on the facet plane and the desired working surface. Squared deviation of the triangular facet from the desired working surface is

$$\varphi = \iint_S \mu^2 d\tau d\upsilon. \tag{47}$$

By summing the deviations of all facets, the direct RMS error $\delta_{\text{rms-d}}$ of a DMR mesh geometry is defined as follows:

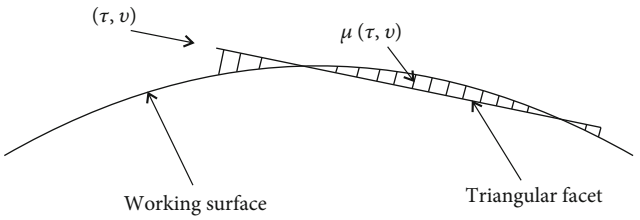

Figure 11: The desired working surface and a triangular facet for calculation of direct RMS error.

$$\delta_{\text{rms-d}} = \sqrt{\frac{1}{S_{\text{mesh}}}\sum_i \varphi_i}. \tag{48}$$

Note that the distance $\omega(\xi, \eta)$ and the distance $\mu(\tau, \upsilon)$ are not the same. In calculation of $\omega(\xi, \eta)$, many assumptions, including shallow reflecting surface and nodes being placed on the desired working surface, have been made. Because of this, formulas for computing the best-fit surface RMS error are not applicable in calculation of the direct RMS error. For example, normal distances from the three nodes of the triangular facets to the best-fit surface are assumed the same. This is not true in general case if stringent surface accuracy evaluation is required. For design of a DMR with high surface accuracy, exact analytical formulas for computing the direct RMS error are needed.

Equation (48) can be directly used to calculate the direct RMS error if μ is obtained. To obtain μ for a typical triangular facet, a local coordinate system (τ, υ, μ) is defined in Figure 12, where the origin is at one of the facet nodes; the τ-axis is in the direction from (τ_1, υ_1) to (τ_2, υ_2); the υ-axis is normal to the τ-axis, lying within the facet plane; and the μ-axis is normal to the facet plane. The equation of the facet plane in the global coordinate system (x, y, z) is

$$a_p x + b_p y + c_p z + d_p = 0, \tag{49}$$

which can be obtained from coordinates of the three nodes, namely, (x_1, y_1, z_1), (x_2, y_2, z_2), and (x_3, y_3, z_3). Here for convenience, it is assumed that the node (x_1, y_1, z_1) is the origin of the local coordinate system (τ, υ, μ). In the global coordinate system, let the unit vectors of the τ-, υ-, and μ-axes be e_1, e_2, and e_3, respectively. These unit vectors are given by

$$\begin{aligned} e_1 &= \frac{\left[x_2 - x_1\ y_2 - y_1\ z_2 - z_1\right]^T}{\sqrt{(x_2 - x_1)^2 + (y_2 - y_1)^2 + (z_2 - z_1)^2}}, \\ e_3 &= \frac{1}{\sqrt{a_p^2 + b_p^2 + c_p^2}}\left[a_p\ b_p\ c_p\right]^T, \\ e_2 &= \frac{e_1 \times e_3}{|e_1 \times e_3|}. \end{aligned} \tag{50}$$

Denote the unit vectors of the global coordinate system xyz as ${e_1}'$, ${e_2}'$, and ${e_3}'$, which are expressed by

$${e_1}' = \begin{Bmatrix} 1 \\ 0 \\ 0 \end{Bmatrix}, \quad {e_2}' = \begin{Bmatrix} 0 \\ 1 \\ 0 \end{Bmatrix}, \quad {e_3}' = \begin{Bmatrix} 0 \\ 0 \\ 1 \end{Bmatrix}. \tag{51}$$

The coordinate transformation matrix E from the local coordinate system (τ, υ, μ) to the global coordinated system (x, y, z) is given as

$$E = \begin{bmatrix} E_{11} & E_{12} & E_{13} \\ E_{21} & E_{22} & E_{23} \\ E_{31} & E_{32} & E_{33} \end{bmatrix} = \begin{bmatrix} e_1^T {e_1}' & e_1^T {e_2}' & e_1^T {e_3}' \\ e_2^T {e_1}' & e_2^T {e_2}' & e_2^T {e_3}' \\ e_3^T {e_1}' & e_3^T {e_2}' & e_3^T {e_3}' \end{bmatrix}. \tag{52}$$

The global and local coordinates are related by

$$\begin{Bmatrix} \tau \\ \upsilon \\ \mu \end{Bmatrix} = E \begin{Bmatrix} x - x_1 \\ y - y_1 \\ z - z_1 \end{Bmatrix}. \tag{53}$$

Because E is an orthogonal matrix,

$$\begin{Bmatrix} x \\ y \\ z \end{Bmatrix} = E^{-1} \begin{Bmatrix} \tau \\ \upsilon \\ \mu \end{Bmatrix} + \begin{Bmatrix} x_1 \\ y_1 \\ z_1 \end{Bmatrix} = E^T \begin{Bmatrix} \tau \\ \upsilon \\ \mu \end{Bmatrix} + \begin{Bmatrix} x_1 \\ y_1 \\ z_1 \end{Bmatrix}. \tag{54}$$

It follows that the global coordinates can be expressed by

$$\begin{aligned} x &= E_{11}\tau + E_{21}\upsilon + E_{31}\mu + x_1, \\ y &= E_{12}\tau + E_{22}\upsilon + E_{32}\mu + y_1, \\ z &= E_{13}\tau + E_{23}\upsilon + E_{33}\mu + z_1. \end{aligned} \tag{55}$$

Recall that the equation of the desired parabolic working surface is

$$z - H = -\frac{1}{4F}\left(x^2 + y^2\right). \tag{56}$$

Substitute Equation (55) into Equation (56) and rearrange the resulting equation with respect to μ to obtain

$$a_1\mu^2 + a_2\mu + a_3 = 0, \tag{57}$$

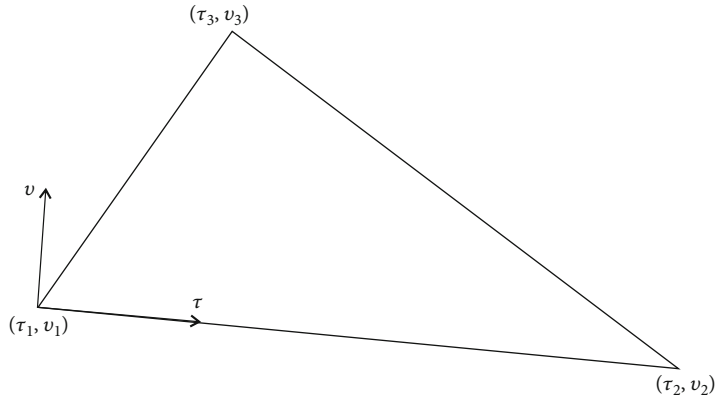

Figure 12: Local coordinate of a triangular facet for calculation of direct RMS error.

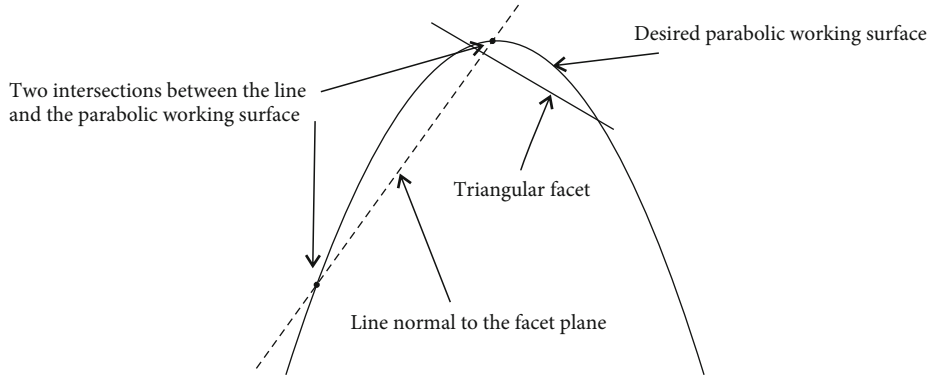

Figure 13: Two intersections between the line normal to the facet plane and the desired parabolic working surface.

with

$$\begin{aligned} a_1 &= \left(E_{31}^2 + E_{32}^2\right)\frac{1}{4F}, \\ a_2 &= E_{33} + E_{31}(x_1 + E_{11}\tau + E_{21}\upsilon)\frac{1}{2F} + E_{32}(y_1 + E_{12}\tau + E_{22}\upsilon)\frac{1}{2F}, \\ a_3 &= -H + z_1 + E_{13}\tau + E_{23}\upsilon + (x_1 + E_{11}\tau + E_{21}\upsilon)^2\frac{1}{4F} + (y_1 + E_{12}\tau + E_{22}\upsilon)^2\frac{1}{4F}. \end{aligned} \tag{58}$$

According to Equation (57), μ is a function of τ and υ, namely, $\mu = \mu(\tau, \upsilon)$. For a point (τ^*, υ^*) on the facet, $\mu(\tau^*, \upsilon^*)$ is the normal distance from the point on the facet to the parabola as described by Equation (56). Solution of Equation (57) gives

$$\mu(\tau, \upsilon) = \frac{-a_2 \pm \sqrt{a_2{}^2 - 4a_1a_3}}{2a_1}. \tag{59}$$

As shown in Figure 13, for a line that is normal to the facet plane and passes through one point on the facet, there are two intersections between the line and the parabola. For calculation of the direct RMS error, only the intersection with smaller distance from the point on the facet represents the deviation of the point from the desired working surface. Thus, out of the two roots given by Equation (59), only the one with smaller absolute value is the true solution. With such selected μ, the direct RMS error can be computed by Equations (47) and (48).

Note that the double integral in Equation (47) can also be computed numerically by applying the coordinate transformation technique introduced in Equations (49)–(59). This calculation is efficient especially when number of facets of a reflecting surface is large.

In this section, the nodal deviation RMS error, the best-fit surface RMS error, and the direct RMS error for surface accuracy evaluation of a generated mesh geometry are reviewed. The reviewed RMS calculation methods are compared in Table 1 in terms of computational efficiency and working requirements.

5. Effective Region RMS Error

During in-orbit mission of a large DMR, only central portion of the reflecting surface is being used for signal transmission since accuracy of boundary layers of the reflector is usually low. This portion of a DMR is called effective region. It is desired in design of a DMR to obtain a large effective region area. However, many DMR designs can only deliver a reflecting surface either with high surface accuracy and small effective region area, or with low surface accuracy and large effective region area. Therefore, calculation of RMS error also calls for consideration of the effective region area.

Table 1: Comparison of RMS error calculation methods for surface accuracy evaluation of a mesh geometry.

	Nodal deviation RMS error $\delta_{\text{rms-n}}$	Facet gravity center deviation RMS error $\delta_{\text{rms-gc}}$	Best-fit surface RMS error $\delta_{\text{rms-bf}}$	Direct RMS error $\delta_{\text{rms-d}}$
Computational efficiency	High	High	Low	Low
Nodes placed on the working surface	Not allowed	Required	Required	Not required
Nodes placed off the working surface	Required	Not allowed	Not allowed	Not required
Shallow working surface	Not required	Not required	Required	Not required

For convenience of analysis and design, working surface of a DMR can be viewed as a cluster of cocentered facet layers, as shown Figure 14, where each layer is a ring of facets. The layers are assigned index numbers starting from the center of the working surface, with the first layer consisting of the center of the reflector and the last layer being the one connected to the boundary. Accordingly, a layer of a smaller index number is closer to the center of the working surface than a layer of a larger index number.

A definition of effective region of a DMR was carried out by Yuan et al. [37]. In this definition, the effective region was considered as a portion of its working surface that meets the surface accuracy requirement for signal transmission. For a smooth working surface (either parabolic or spherical), due to the vertical directions of tension tie forces, the slope of a point on the surface that is near the boundary is larger than that of a point which is relatively away from the boundary. Because of this, for an almost uniform distribution of cable member tensions, a layer of a smaller index number has shorter member lengths than a layer of a larger index number [6]. This yields smaller RMS errors for the inner layers of a reflector. Thus, the layers of a working surface can be divided into two types: (i) the inner layers, which are closer to the center of the working surface and meet the surface accuracy requirement, and (ii) the outer layers, which are near the boundary of the working surface and do not satisfy the surface accuracy requirement. Obviously, the effective region of a DMR is formed by all the inner layers.

Assume that the working surface of a designed DMR has n_r facet layers. Let the RMS error of the k-th layer be $\delta_{\text{rms,k}}$, $k = 1, 2, \cdots, n_r$, which can be easily computed [38]. Assume that the reflector working surface has k_{er} inner layers. According to the above discussion, the effective region of the DMR is formed by the first k_{er} layers of the working surface. In other words, $\delta_{\text{rms,k}} \le \delta_{\text{rms}}$ for $1 \le k \le k_{\text{er}}$ and $\delta_{\text{rms,k}} > \delta_{\text{rms}}$ for $k_{\text{er}} + 1 \le k \le n_r$, where δ_{rms} is the required surface error upper bound given in Equation (5).

One objective in design of a DMR is to assure enough effective region area for operation. For a reflector, which can be either a center-feed parabolic reflector or an offset-feed parabolic reflector, its effective region can be calculated by $S_e = \sum_{k=1}^{k_{er}} S_k$ where S_k is the surface area of the k-th layer. The RMS error $\delta_{\text{rms-er}}$ of the effective region can be evaluated either by the outmost inner layer:

$$\delta_{\text{rms-er}} = \frac{\delta_{\text{rms},k_{er}}}{\beta}, \tag{60}$$

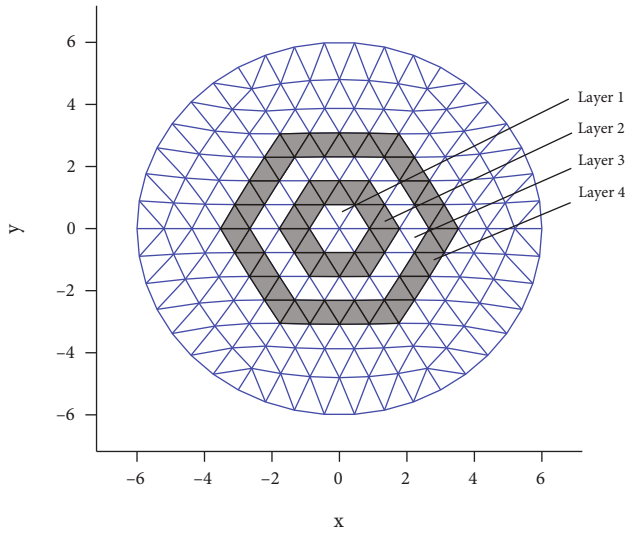

Figure 14: Layers of a mesh geometry of a DMR.

or by a mean value:

$$\delta_{\text{rms-er}} = \frac{1}{S_e \beta} \sum_{k=1}^{k_{er}} S_k \delta_{\text{rms},k}, \tag{61}$$

where

$$\beta = \frac{S_e}{S}, \tag{62}$$

with S being the area of the whole aperture of the reflector. Note that for a reflector without a clear aperture rim, for example, some reflectors are hexagonal with only six nodes being attached to a supporting structure [15], S in Equation (62) is the area of all mesh facets that are used for reflecting signals.

6. Numerical Examples

In this work, several methods of RMS error calculation for large DMRs have been reviewed. For a clearly comparison, the nodal deviation RMS errors, the best-fit surface RMS errors, and the direct RMS errors of three mesh geometries (a two-facet mesh geometry, a center-feed parabolic DMR, and an offset-feed parabolic DMR) are calculated, respectively. Advantages and limitations of the reviewed methods of RMS error calculation shall be presented by examples in this section.

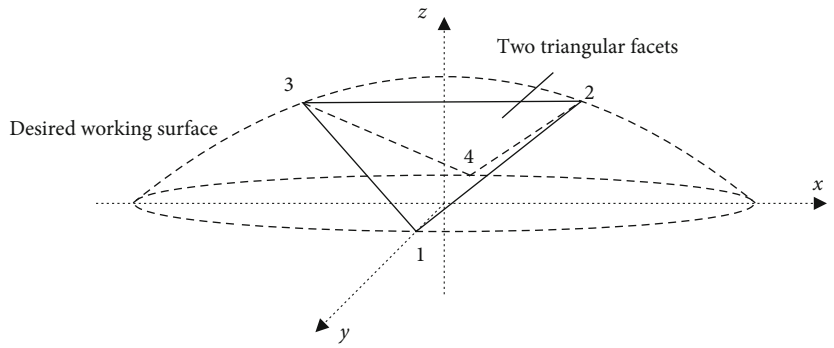

Figure 15: Two triangular facets with nodes being placed on the desired working surface.

6.1. A Two-Facet Mesh Geometry

6.1.1. Calculation of the Nodal Deviation RMS Error. A two-facet mesh geometry and a desired working surface are shown in Figure 15. Recall the two assumptions (shallow desired working surface and placement of nodes on the desired working surface) made in the best-fit RMS error calculation; the desired working surface in this example is a shallow center feed parabola with focal length F being 10 meters and aperture diameter D being 4 meters. Equation of the desired working surface is

$$z - 0.1 = -\frac{1}{40}\left(x^2 + y^2\right). \tag{63}$$

The four nodes that form the two triangular facets are placed on the desired working surface, with coordinates given as

$$\begin{aligned} (x_1, y_1, z_1) &= (0, -2, 0), \\ (x_2, y_2, z_2) &= (1, 0, 0.075), \\ (x_3, y_3, z_3) &= (-1, 0, 0.075), \\ (x_4, y_4, z_4) &= (0, 2, 0). \end{aligned} \tag{64}$$

Thus, the gravity center of the two facets are

$$\begin{aligned} \left(x_{c,1}, y_{c,1}, z_{c,1}\right) &= (0, -0.6667, 0.05), \\ \left(x_{c,2}, y_{c,2}, z_{c,2}\right) &= (0, 0.6667, 0.05). \end{aligned} \tag{65}$$

For the nodal deviation RMS error calculated in Equation (19), calculation is trivial with $\delta_{\text{rms-n}} = 0$, because all nodes of the mesh geometry are on the desired working surface. Calculation in Equation (20) is given as

$$\delta_{\text{rms-gc}} = \left(\frac{\sum_{t=1}^{n} S'_t \left(Z'_t - Z'_{g_t} \right)^2}{\sum_{t=1}^{n} S'_t} \right)^{1/2} = 0.0389, \tag{66}$$

with

$$\begin{aligned} S'_1 &= 2, \\ S'_2 &= 2, \\ Z'_1 &= 0.0889, \\ Z'_2 &= 0.0889, \\ Z'_{g_1} &= 0.05, \\ Z'_{g_2} &= 0.05. \end{aligned} \tag{67}$$

6.1.2. Calculation of the Best-Fit Surface RMS Error. The best-fit surface RMS error is obtained by properly determining a best-fit surface of a mesh geometry through an iterative process that is usually solved by a numerical optimization algorithm [34]. To show application of the technique, calculation of the best-fit surface RMS error in one iteration is given in details. In this iteration, focal length F' of the effective surface and the vertices distance h between the effective surface and the desired working surface are assumed as 9.9 meters and 0.01 meter, respectively.

The first step is to define two local coordinate systems (ξ, η) for the two triangular facets and obtain local coordinates for nodes of the two facets as

$$\begin{aligned} \xi_{1,1} &= 0, \\ \xi_{1,2} &= 2.0014, \\ \xi_{1,3} &= 0, \\ \xi_{2,1} &= 0, \\ \xi_{2,2} &= 0, \\ \xi_{2,3} &= 2.0014, \\ \eta_{1,1} &= 0, \\ \eta_{1,2} &= -1, \\ \eta_{1,3} &= -2, \\ \eta_{2,1} &= 0, \\ \eta_{2,2} &= 2, \\ \eta_{2,3} &= 1. \end{aligned} \tag{68}$$

Table 2: Comparison of different RMS error calculation methods (mm).

	Nodal deviation RMS error $\delta_{\text{rms-n}}$	Facet gravity center deviation RMS error $\delta_{\text{rms-gc}}$	Best-fit surface RMS error $\delta_{\text{rms-bf}}$	Direct RMS error $\delta_{\text{rms-d}}$
Mesh geometry with two facets	0	38.9	7.7	30.2

Areas S of the two facets are

$$S_1 = S_2 = 2.0014. \tag{69}$$

ϕ_1 and ϕ_2 are calculated as

$$\phi_1 = \phi_2 = \iint_S \omega^2 d\xi d\eta = 8.6921 \times 10^{-4}. \tag{70}$$

The RMS error of this effective surface is

$$\delta_{\text{rms-eff}} = \sqrt{\frac{1}{S_{\text{mesh}}} \sum_i \phi_i} = 0.0208. \tag{71}$$

According to the definition of the best-fit surface RMS error, in a numerical optimization algorithm, $\delta_{\text{rms-eff}}$ is calculated in each iteration with F' and h being adjusted until the smallest value of $\delta_{\text{rms-eff}}$ is found. This value is the best-fit RMS error $\delta_{\text{rms-bf}}$. After minimized by the numerical optimization algorithm, the best-fit RMS error is obtained as

$$\delta_{\text{rms-bf}} = 0.0077, \tag{72}$$

with the corresponding F_{bf} and h_{bf} being 10 meters and 0.0292 meter. Thus, equation of the best-fit surface is

$$z - 0.0708 = -\frac{1}{40}\left(x^2 + y^2\right). \tag{73}$$

6.1.3. Calculation of the Direct RMS Error. For direct RMS error calculation, nodal coordinates of the two facets under local coordinate system (τ, υ) are

$$\begin{aligned}
&\tau_{1,1} = 0\\
&\tau_{1,2} = 2.2373\\
&\tau_{1,3} = 0\\
&\tau_{2,1} = 0,\\
&\tau_{2,2} = 2,\\
&\tau_{2,3} = 1,\\
&\upsilon_{1,1} = 0,\\
&\upsilon_{1,2} = 1.3434,\\
&\upsilon_{1,3} = 1.7891,\\
&\upsilon_{2,1} = 0,\\
&\upsilon_{2,2} = 0,\\
&\upsilon_{2,3} = -2.0014.
\end{aligned} \tag{74}$$

Due the simplicity of this example, φ for the two facets can be directly obtained as

$$\varphi_1 = \varphi_2 = \iint_{S_1} \mu_1^2 d\tau d\upsilon = 1.8193 \times 10^{-3}. \tag{75}$$

The direct RMS error is then calculated as

$$\delta_{\text{rms-d}} = \sqrt{\frac{1}{S_{\text{mesh}}} \sum_i \varphi_i} = 0.0302. \tag{76}$$

For comparison, the RMS errors calculated by the three methods reviewed are listed in Table 2.

6.2. A Center-Feed Mesh Reflector and an Offset-Feed Mesh Reflector. In this section, the reviewed methods of RMS error calculation shall be applied to a parabolic center-feed mesh reflector and a parabolic offset-feed mesh reflector both with 127 nodes. The aperture diameter D of the center-feed reflector is 12 meters, with the focal ratio (F/D) being 0.5. F is the focal length of the center-feed reflector. The aperture diameter D_p of the parent parabola of the offset-feed reflector is 12 meters, with the focal ratio (F_p/D_p) being 0.33. F_p is the focal length of the parent parabola of the offset-feed reflector. The offset distance is 1 meter. Technique of boundary nodes reduction introduced in Ref. [6] is applied to topology design of both reflectors. Form findings of these reflectors are done by the fixed nodal position method introduced in Ref. [28]. For simplicity, all nodes are placed on the desired working surfaces. Top views of these two reflectors that show topology designs and effective region areas are given in Figure 16.

The nodal deviation RMS error $\delta_{\text{rms-n}}$, the facet gravity center deviation RMS error $\delta_{\text{rms-gc}}$, the best-fit surface RMS error $\delta_{\text{rms-bf}}$, the direct RMS error $\delta_{\text{rms-d}}$, and the effective region RMS error $\delta_{\text{rms-d}}$ of this mesh reflector are listed in Table 3. From observation of Table 3, RMS errors vary significantly in different calculation methods. Methods that only consider nodal deviation have limitation for stringent surface accuracy analysis because it fails to consider geometric difference between the facet planes and the curved desired working surface. The best-fit surface RMS error, while being used in many cases, measures deviation of a mesh geometry from its best-fit surface, not the desired working surface. This is an accurate evaluation only for shallow reflectors with nodes all being placed on the desired working surface. When a reflector is deep or nodes are placed off the desired working surface, the best-fit surface RMS error is not an appropriate measurement. Since the best-fit surface so generated is different from the desired working surface, the location of focal point of the reflector also changes. So the best-fit surface RMS error does not applied to a DMR with fixed feed source. The direct RMS

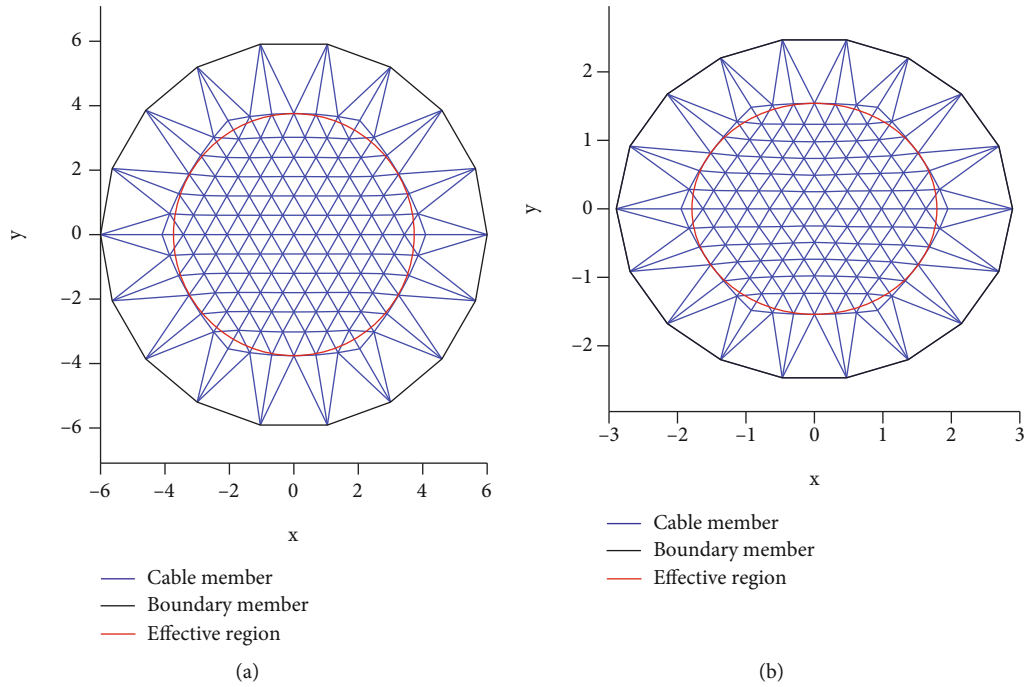

Figure 16: Top view of the two mesh reflectors with 127 nodes: (a) the center-feed mesh reflector and (b) the offset-feed mesh reflector.

Table 3: Comparison of different RMS error calculation methods (mm).

	Nodal deviation RMS error δ_{rms-n}	Facet gravity center deviation RMS error δ_{rms-gc}	Best-fit surface RMS error δ_{rms-bf}	Direct RMS error δ_{rms-d}	Effective region RMS error δ_{rms-er}
Center-feed mesh reflector	0	7.08	1.40	4.24	10.22
Offset-feed mesh reflector	0	2.41	0.44	1.26	3.50

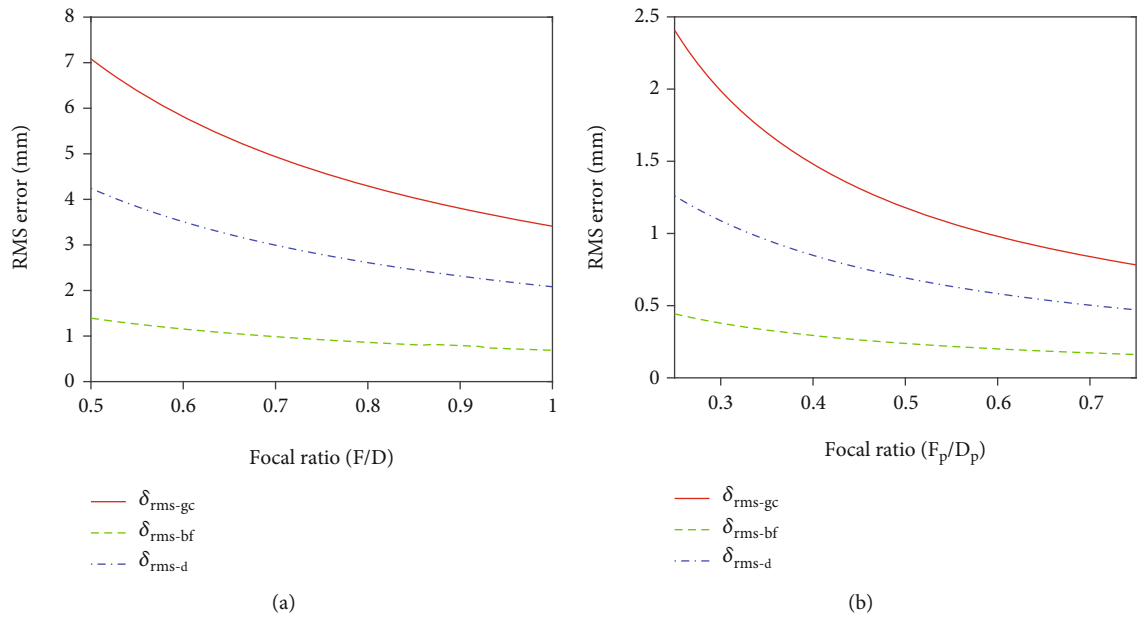

Figure 17: Comparison of RMS errors as the focal ratio increases for (a) the center-feed mesh reflector and (b) the offset-feed mesh reflector.

error evaluates deviation of a mesh geometry directly from the desired working surface. It is extremely useful in evaluating a reflector with high surface accuracy requirement. It is applicable to both shallow and deep reflectors, while allowing nodes being placed both on and off the desired working surface. It can also be observed from Table 3 that the δ_{rms-er}

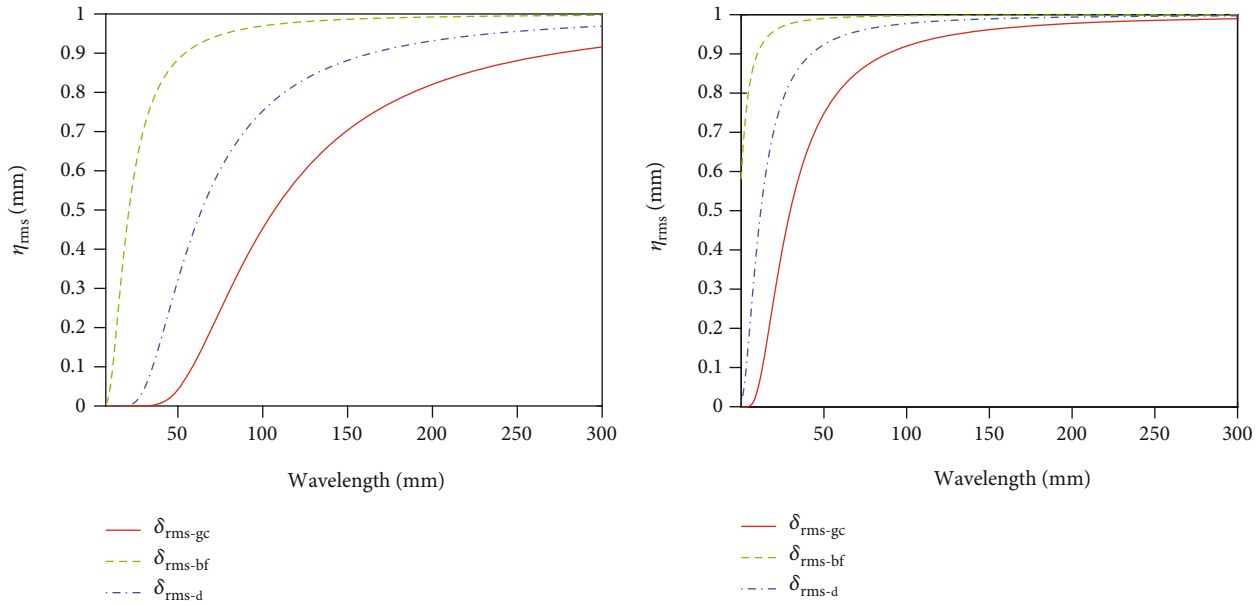

FIGURE 18: Comparison of reflector gain efficiency factor η_{rms} obtained by the three RMS error calculation methods, δ_{rms-gc}, δ_{rms-bf}, and δ_{rms-d} for (a) the center-feed mesh reflector and (b) the offset-feed mesh reflector.

is not always consistent with other definitions of RMS errors, since the effective region area is also included in the surface accuracy evaluation. For a reflector with smaller effective region area, δ_{rms-er} can still be large even when the RMS error of facets within the effective region is small.

In addition, the simulation results show that that the RMS errors of the offset-feed mesh reflector are much smaller than those of the center-feed mesh reflector. This is because an offset-feed mesh reflector is cut from a parent sphere or parabola. Thus, it is usually shallower than a center-feed reflector with a similar aperture diameter. As seen in many reflector designs, a shallow DMR can achieve a much higher surface accuracy than a deep one.

The comparison of the three RMS error calculation methods, δ_{rms-gc}, δ_{rms-bf}, and δ_{rms-d}, under different focal ratio are presented in Figure 17. As seen in the simulation results, all the three RMS errors decrease as the focal ration of the reflector increases, because a shallow DMR with high focal ratio can achieve a much higher surface accuracy than a deep one with low focal ratio. This property is successfully captured by all the three methods in comparison.

The comparison of the reflector gain efficiency factor η_{rms} in Equation (6) under the three RMS error calculation methods, δ_{rms-gc}, δ_{rms-bf}, and δ_{rms-d} within a wavelength range of 7.5-300 mm are plotted in Figure 18. As seen in Figure 18, differences among the reflector gain/loss estimations by the three methods of RMS error calculation are significant. Meanwhile, the reflector gain efficiency factor η_{rms} varies for different wavelengths. Note that Equation (6) is only for rough estimation of RMS error impact on the reflector gain. Accurate reflector gain evaluation requires a detailed radiofrequency analysis, which can be performed by a software for radiofrequency pattern calculation.

7. Conclusions

Methods of root-mean-square error calculation for large deployable mesh reflectors are reviewed. The main results from this investigation are summarized as follows.

(i) Concept of reflector gain and effective surface error (half path length error) are given. The reflector gain is a factor to measure the reflector performance

(ii) Approaches to RMS error prediction or estimation in preliminary design of large deployable mesh reflectors are shown. The predicted RMS error can be used as a guidance in reflector design, mainly to determine the maximum allowable member length. Influences of mesh saddling, thermal loads, and member length imperfection are considered in these estimations

(iii) Methods of RMS error calculation for generated mesh geometry of large deployable mesh reflectors are presented. The nodal deviation RMS error is easy to implement but fails to include geometric difference between facet planes and the desired working surface. The best-fit surface RMS error evaluates deviation of a mesh geometry from its best-fit surface. This method requires shallow reflector and nodes being placed on the desired working surface. Therefore, the best-fit surface RMS error is not applicable to mesh reflectors with stringent surface accuracy requirement. In addition, the best-fit surface RMS error cannot be used to evaluate surface accuracy for a mesh geometry with nodes being placed off the desired working surface. The direct RMS error calculates deviation of a mesh geometry

directly from the desired working surface. It is applicable to both shallow and deep reflecting surfaces. It also allows reflector nodes to be placed off the desired working surface. For complicated mesh geometry with many facets, numerical methods may be required in calculating the double integral of normal distance between the facets to the desired working surface over the facet area

(iv) Concept of effective region is introduced. An adjusted measurement of surface accuracy is suggested when the concept of effective region is involved. This measurement has two evaluation factors, the effective region area and the RMS error of facets within the effective region

(v) RMS errors of a mesh geometry with two triangular facets, a center-feed mesh reflector, and an offset-feed mesh reflector are calculated by the RMS error calculation methods reviewed. Results in these demonstrative examples show that RMS errors may vary significantly if calculated by different methods

(vi) The effective region RMS error is also used in measuring surface accuracy for a center-feed mesh reflector and an offset-feed mesh reflector. Numerical results show importance and necessity of considering the area of effective region in surface accuracy evaluation of large deployable mesh reflectors

Conflicts of Interest

The author declares no conflicts of interest.

Acknowledgments

The author acknowledges support from the US NSF (National Science Foundation) through grant 2104237.

References

[1] P. K. Agrawal, M. S. Anderson, and M. F. Card, "Preliminary design of large reflectors with flat facets," *IEEE Transactions on Antennas and Propagation*, vol. 29, no. 4, pp. 688–694, 1981.

[2] R. Nie, B. He, and L. Zhang, "Deployment dynamics modeling and analysis for mesh reflector antennas considering the motion feasibility," *Nonlinear Dynamics*, vol. 91, no. 1, pp. 549–564, 2018.

[3] Y. Tang, T. Li, and X. Ma, "Pillow distortion analysis for a space mesh reflector antenna," *AIAA Journal*, vol. 55, no. 9, pp. 3206–3213, 2017.

[4] S. Yuan, B. Yang, and H. Fang, "Enhancement of large deployable mesh reflectors by the self-standing truss with hard-points," in *In: AIAA Scitech 2019 Forum*, Session: Spacecraft Antennas, and Other Optical Apertures, p. 752, San Diego, California, 2019.

[5] J. M. Hedgepeth, "Accuracy potentials for large space antenna reflectors with passive structure," *Journal of Spacecraft and Rockets*, vol. 19, no. 3, pp. 211–217, 1982.

[6] H. Shi, S. Yuan, and B. Yang, "New methodology of surface mesh geometry design for deployable mesh reflectors," *Journal of Spacecraft and Rockets*, vol. 55, no. 2, pp. 266–281, 2018.

[7] J. Ruze, "Antenna tolerance theory—a review," *Proceedings of the IEEE*, vol. 54, no. 4, pp. 633–640, 1966.

[8] H. Tanaka, "Surface error estimation and correction of a space antenna based on antenna gainanalyses," *Acta Astronautica*, vol. 68, no. 7-8, pp. 1062–1069, 2011.

[9] R. Spencer, "A least square analysis of the effect of phase errors on antenna gain, Air Force Cambridge Research Laboratories," *Ref. E*, vol. 5025, p. 1949, 1949.

[10] M. Zarghamee, "On antenna tolerance theory," *IEEE Transactions on Antennas and Propagation*, vol. 15, no. 6, pp. 777–781, 1967.

[11] C. Jenkins, J. Wilkes, and D. Marker, "Improved surface accuracy of precision membrane reflectors through adaptive rim control," in *In: 39th AIAA/ASME/ASCE/AHS/ASC Structures, Structural Dynamics, and Materials Conference and Exhibit*, p. 1983, Long Beach,CA,U.S.A., 1998.

[12] A. Miyasaka, M. Homma, A. Tsujigata, K. Nakamura, K. Yamada, and A. Meguro, "Design and ground verification of large deployable reflector," in *In: 19th AIAA Applied Aerodynamics Conference*, p. 1480, Anaheim, CA, U.S.A., 2001.

[13] G. Tibert, *Deployable Tensegrity Structures for Space Applications[Ph.D. thesis]*, KTH, Stockholm, Sweden, 2002.

[14] M. Thomson, "AstroMesh deployable reflectors for ku and ka band commercial satellites," in *In: 20th AIAA International Communication Satellite Systems Conference and Exhibit*, p. 2032, Montreal, Quebec, Canada, 2002.

[15] A. Tibert and S. Pellegrino, "Deployable tensegrity reflectors for small satellites," *Journal of Spacecraft and Rockets*, vol. 39, no. 5, pp. 701–709, 2002.

[16] Y. Tang, T. Li, Z. Wang, and H. Deng, "Surface accuracy analysis of large deployable antennas," *Acta Astronautica*, vol. 104, no. 1, pp. 125–133, 2014.

[17] R. X. Meyer, "Precision of mesh-type reflectors for large spaceborne antennas," *Journal of Spacecraft and Rockets*, vol. 22, no. 1, pp. 80–84, 1985.

[18] W. Fichter, "Reduction of root-mean-square error in faceted space antennas," *AIAA Journal*, vol. 22, no. 11, pp. 1679–1684, 1984.

[19] J. M. Hedgepeth, *Accuracy Potentials for Large Space Antenna Structures*, Astro Research Corporation Carpinteria, California, United States, 1980.

[20] J. M. Hedgepeth, "Influence of fabrication tolerances on the surface accuracy of largeantenna structures," *AIAA Journal*, vol. 20, no. 5, pp. 680–686, 1982.

[21] K. Miura and K. Tanizawa, "Tension truss antenna—concept, reality and future," in *In: IUTAM-IASS Symposium on Deployable Structures: Theory and Applications*, pp. 291–300, Springer, Cambridge, UK, 2000.

[22] W. H. Greene, "Effects of random member length errors on the accuracy and internal loads of truss antennas," *Journal of Spacecraft and Rockets*, vol. 22, no. 5, pp. 554–559, 1985.

[23] Y. Zong, N. Hu, B. Duan, G. Yang, H. Cao, and W. Xu, "Manufacturing error sensitivity analysis and optimal design method of cable-network antenna structures," *Acta Astronautica*, vol. 120, pp. 182–191, 2016.

[24] H. Shi, B. Yang, M. Thomson, and H. Fang, "Coupled elastic-thermal dynamics of deployable mesh reflectors," in *In: 52nd*

AIAA/ASME/ASCE/AHS/ASC Structures, Structural Dynamics and Materials Conference, p. 2001, Denver, Colorado, 2011.

[25] M. Mobrem, "Methods of analyzing surface accuracy of large antenna structures due to manufacturing tolerances," in *In: 44th AIAA/ASME/ASCE/AHS/ASC Structures, Structural Dynamics, and Materials Conference*, AIAA, p. 1453, Norfolk, Virginia, 2003.

[26] R. Nie, B. He, L. Zhang, and Y. Fang, "Deployment analysis for space cable net structures with varying topologies and parameters," *Aerospace Science and Technology*, vol. 68, pp. 1–10, 2017.

[27] R. Nie, B. He, D. H. Hodges, and X. Ma, "Form finding and design optimization of cable network structures with flexible frames," *Computers & Structures*, vol. 220, pp. 81–91, 2019.

[28] S. Yuan and B. Yang, "The fixed nodal position method for form finding of high-precision lightweight truss structures," *International Journal of Solids and Structures*, vol. 161, pp. 82–95, 2019.

[29] S. Yuan, B. Yang, and H. Fang, "Improvement of surface accuracy for large deployable mesh reflectors," in *In: AIAA/AAS Astrodynamics Specialist Conference*, AIAA, p. 5571, Long Beach, California, 2016.

[30] H. Deng, T. Li, Z. Wang, and X. Ma, "Pretension design of space mesh reflector antennas based on projection principle," *Journal of Aerospace Engineering*, vol. 28, article 04014142, 2014.

[31] T. Li, Y. Tang, and T. Zhang, "Surface adjustment method for cable net structures considering measurement uncertainties," *Aerospace Science and Technology*, vol. 59, pp. 52–56, 2016.

[32] S. Morterolle, B. Maurin, J. Quirant, and C. Dupuy, "Numerical form-finding of geotensoid tension truss for mesh reflector," *Acta Astronautica*, vol. 76, pp. 154–163, 2012.

[33] W. Rusch and P. Potter, *Analysis of reflector antennas*, Academic Press, 111 Fifth Avenue, New York, NY 10003 & Berkeley Square House, London, WIX 6BA, 2013.

[34] J. Nocedal and S. Wright, *Numerical Optimization*, Springer Science & Business Media, 233 Spring Street, New York, NY 10013, 2006.

[35] S. Yuan and B. Yang, "Design and optimization of tension distribution for space deployable mesh reflectors," in *In: 26th AAS/AIAA Space Flight Mechanics Meeting*, pp. 765–776, Univelt Escondido, CA, 2016.

[36] S. Yuan, B. Yang, and H. Fang, "Direct root-mean-square error for surface accuracy evaluation of large deployable mesh reflectors," in *In: AIAA SciTech 2020 Forum*, p. 935, Orlando, Florida, 2020.

[37] S. Yuan, B. Yang, and H. Fang, "Self-standing truss with hard-point-enhanced large deployable mesh reflectors," *AIAA Journal*, vol. 57, no. 11, pp. 5014–5026, 2019.

[38] S. Yuan, B. Yang, and H. Fang, "The projecting surface method for improvement of surface accuracy of large deployable mesh reflectors," *Acta Astronautica*, vol. 151, pp. 678–690, 2018.

Hindawi
International Journal of Aerospace Engineering
Volume 2022, Article ID 9600677, 12 pages
https://doi.org/10.1155/2022/9600677

Research Article

A Novel Microscopic Modeling Scheme for the Shape Memory Polymer Composites with respect to the Ambient Temperature

Yang Li,[1] Junjie Ye,[2] Lu Liu,[2] Baoquan Shi,[2] and Yumin He[3]

[1]*Xi'an Institute of Space Radio Technology, Xi'an 710100, China*
[2]*Research Center for Applied Mechanics, Key Laboratory of Ministry of Education for Electronic Equipment Structure Design, Xidian University, Xi'an 710071, China*
[3]*College of Mechanical and Electrical Engineering, Xi'an University of Architecture and Technology, Xi'an 710055, China*

Correspondence should be addressed to Junjie Ye; ronkey6000@sina.com

Received 10 March 2022; Revised 18 April 2022; Accepted 27 June 2022; Published 22 July 2022

Academic Editor: Chuang Liu

This paper is aimed at studying the effective mechanical property of shape memory polymer composites (SMPC) reinforced with natural short fibers. To this end, a novel modeling scheme was presented. The SMPC was firstly equivalent to the composite laminates, and the natural short fibers are also subtly equivalent to the ellipsoidal inclusions distributed in the matrix materials periodically. Moreover, a represented volume element along laminate thickness can be easily chosen, and its elastic constants are accurately acquired by employing a proper microscopic mechanical model. Herein, the high-fidelity generalized method of cells, which represents a good ability in predicting the effective mechanical behaviors of composites, was used. On this basis, the classic laminate theory was improved to suitable for describing the elastic constants and failure strength the SMPC with respect to ambient temperature. Numerical results show a good consistency to the experimental data. Moreover, a higher ambient temperature tends to sharply decrease their final failure strength. It is also revealed that the presented modeling method shows a great potential in calculating the effectively mechanical property of the natural short fiber-reinforced composites.

1. Introduction

Due to its unique molecular structure and good performances, including light weight, low cost, and high strain recovery rate, shape memory polymer (SMP) exhibits a widespread prospect in medical, energy, and electronic communications [1, 2]. It is reported by Leng et al. [3] that the maximum strain of the SMP reach to 600%. However, its low stiffness and recovery stress seriously limited its application in some extent. To overcome the flaws mentioned above, some reinforced phases, such as carbon fibers, carbon nanotubes, and nanoparticle, were presented to be mixed with the SMP to form the shape memory polymer composites (SMPC) [4]. Due to its intrinsic characteristic of the slow unfolding, the SMPC have been widely prepared as some deployable components in the satellite equipment, such as hinge and truss structure [5]. According to a statistical result by Castet and Saleh [6], the failure of solar wing during the deployment procedure is accounting for 17% of the total failure events, which results in a final failure of the satellite. To maximum guarantee the safe operation of the satellite equipment, it is critical to grasp the effective mechanical property of the SMPC with respect to the ambient temperature.

A large number of experimental tests have been executed on the standard specimen or structure of the SMPC to acquire its mechanical [7–9], electrical [10, 11], and shape memory performances [12]. The recovery capable of the SMPC under various loads was investigated by Basit et al. [13], and it exhibits a good potential in diverse applications. Le and Goo [14] executed on a folding and deployment test of the SMPC hinge at -10°C to investigate its shape recoverability and revealed that its deployment performance is closely dependent on ambient temperature. To reveal the temperature influences, an infrared camera and thermocouples were employed to observe the temperature distribution. By using a series of experimental methods, Wang et al. [15] studied the thermodynamic and shape memory properties of the SMPC. Moreover, its fracture interface was investigated

by scanning electron microscopy. It is indicated that a good mechanical property can be acquired when fiber mass fraction is equal to 8%. Dao et al. [16, 17] measured the moment and blocking force of the SMPC hinge by employing a pulley-mass system. The test method provides a guideline for evaluating its mechanical performances. Annin et al. [18] investigated the deformation and damage of the SMPC during the bending and torsion. Moreover, the fiber off-axis angle influences on the formation process was also revealed. Lelieveld et al. [19] executed on the thermomechanical tests to investigate the actuation characteristics of the SMPC. Kim et al. [20] explored the recovery and physical properties by using the experimental tests on the strength and thermal conductivity.

In recent years, a large number of theoretical methods [21] have been presented to investigate elastic constants, nonlinear deformation, and failure characteristic of the SMPC. With an analogy way with thermomechanical responses at macroscale, Wang et al. [22] presented a chain model to optimize the chain system of the SMPC. It is revealed that the shape memory property is improved by increasing the cross link density. Arvanitakis [23] presented a constitutive level-set model to capture its mechanical behaviors under the thermomechanical cycle loading. Sun et al. and Gu et al. [24, 25] presented a multiscale strategy and established the thermoviscoelastic constitutive equation to investigate the buckling critical stress under the finite deformation, and the numerical results lay a solid foundation for its application and design. Bergman and Yang [26] proposed a macroscopic model combining a nonlinear geometric model with a temperature-dependent constitutive equation to investigate the shape fixation process. Li et al. [27] established a three dimension model by employing the ABAQUS to study the vibration mode and natural frequency of the large spatial deployable structure. The modal test results show a good consistency with the simulation results. Based on the homogenization scheme, Song et al. [28] presented a constitutive model for the SMPC subjected to the thermomechanical load. The experimental tests were executed on the standard specimens for a comparison.

For the SMPC, the mechanical property is closely dependent on its microscopic feature, including inclusion arrangement, interfacial bonding, and inclusion morphology. It is hardly for a macroscopic model to reveal the microscopic characteristic influences. A comprehensive investigation with full consideration of the microscopic factors influence has been executed by some researchers. By choosing a cylindrical representative volume element (RVE), Khalili et al. [29] evaluated the interface property influences on mechanical behaviors of the SMPC. Liu and Jiang [30] presented a novel hierarchical micromechanic method to study the microstructural feature influences on the thermal conducting behavior of the SMPC. However, few studies refer to random inclusions in the matrix materials. The main objective of this paper is to focus on investigating the effective mechanical property of the SMP reinforced with natural short fibers. To this end, an effective modeling scheme based on the microscopic constitutive equation was presented. The outline was summarized as follows: Section 2 presented the modeling scheme and microscopic modeling process of the SMP reinforced with natural short fibers. To validate the effectiveness of the presented method, experimental data and numerical results were both introduced for a comparison in Section 3. On this basis, a series of simulation analysis were executed to fully study the failure strength of the SMPC with respect to ambient temperature in Section 4. Conclusions are shown in Section 5.

2. Modeling Process of the SMPC

2.1. The Equivalent Procedure of the SMPC. For the shape memory polymer composites, short fibers always present obvious random characteristic due to the limitation of the preparation technology as shown in Figure 1(a). In the coordinate system x_1-x_2-x_3, the short fiber direction can be accurately determined with respect to the fiber angles of θ and γ as shown in Figure 1(b).

It is reported by Cai et al. [31, 32] that the random short fibers exhibit an obvious directionality and closely dependent on resin flow direction. To simplify the microscopic modeling procedure, the random short fibers are always considered to be periodically distributed in matrix materials according to the homogenization theory as shown in Figure 2(a). According to the statistical results derived from the microscopic morphology, the random short fibers are equivalently represented by the ellipsoidal model. In addition, the fiber direction and density along thickness direction represent obvious differences. In details, few fibers can be found in the upper and lower edges, and the short fiber density in the center location is much higher. Therefore, the equivalent structure of the SMPC can be considered as the composite laminate (Figure 2(b)), whose upper and lower edges consist of pure polymer, while other regions can be treated as serials of unidirectional (UD) laminas. To sum up, the SMPC are accurately discretized as ten UD laminas, and eight of them are reinforced with ellipsoidal fibers. It should be noted that the elastic modulus of the natural fiber composites along x_1-direciton is identical to the equivalent composites.

2.2. Numerical Modeling Process. It is assumed that the SMPC is equivalent to the composite laminates, which consist of serials of the UD laminas mentioned above. The equivalent ellipsoidal inclusions are assumed to be periodically distributed in the SMP. The simplified numerical procedure for the SMPC can be summarized as follows: (1) a proper RVE in each lamina can be easily selected along the thickness direction as shown in Figure 2(c). On this basis, the effective modulus of each lamina can be obtained by employing an effective microscopic mechanical model. (2) The SMPC consists of a series of unidirectional laminas. Therefore, the effective elastic modulus and mechanical property of the SMPC can be acquired by employing the classic laminate theory. (3) The numerical results by the presented method and experimental data are both employed for a comparison. On this basis, the failure strength of the SMPC with respect to ambient temperature is investigated by implanted the failure criterion.

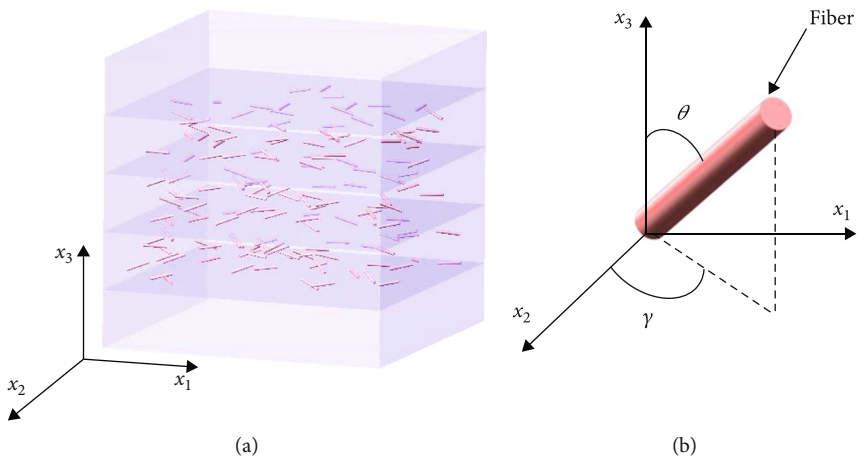

Figure 1: Three-dimension image of the SMPC. (a) SMPC reinforced with short fibers. (b) Short fiber direction.

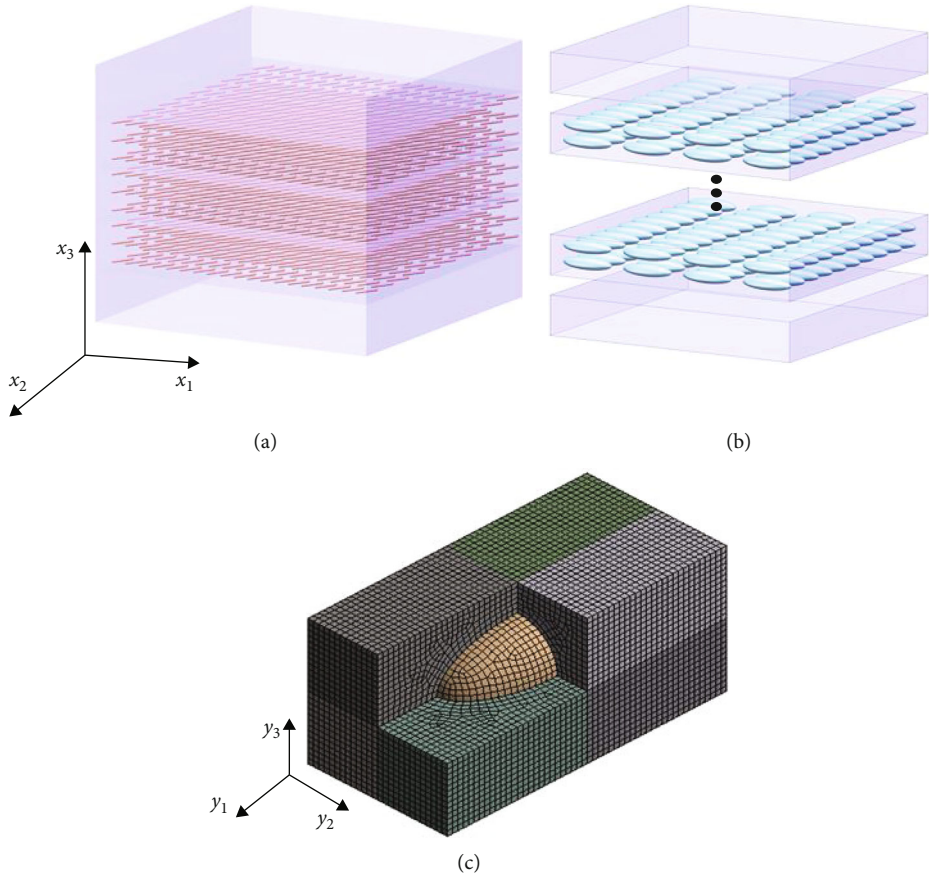

Figure 2: Simplified modeling procedure of the SMPC reinforced with natural short fibers. (a) The effective 3D equivalent structure. (b) SMPC treated as the composite laminated reinforced with the periodic ellipsoidal inclusion. (c) The RVE discretized by serials of hexahedral subcells.

2.2.1. Microscopic Constitutive Relation. By employing a microscopic mechanical theory, such as Eshelby equivalent inclusion theory [33], Mori-Tanaka method [34], self-consistent model, and generalized self-consistent model [35], the elastic constants of the composites can be acquired. However, they limit to analyze some inclusions with special geometric shape. It is hardly for the microscopic theories mentioned above to reveal the relation between geometric shape and inclusion distribution influences on the effective modulus. In recent years, the high-fidelity generalized method of cells (HFGMC) represented a good ability to investigate nonlinear deformation [36] and failure modes [37] of the composites under a coupled multifield environment. Ye et al. [38] presented a multiscale modeling framework by combining with the finite element method (FEM) to reveal the failure mechanism of the composites from

microscopic damage to macroscopic fracture. Herein, the HFGMC is employed to calculate the effective modulus of the RVE reinforced with a spheroidal inclusion. During the numerical modeling process, the RVE as shown in Figure 2(c) is discretized as $N_\alpha \times N_\beta \times N_\gamma$ subcells. It should be noted that the parameters N_α, N_β, and N_γ indicate the discretized subcell number along y_1-, y_2-, and y_3-direction, respectively. The subscripts $\alpha = 1, 2, \cdots, N_\alpha$, $\beta = 1, 2, \cdots, N_\beta$, and $\gamma = 1, 2, \cdots, N_\gamma$ indicate the numbered subcell. The second-order subcell displacement component $u_i^{(\alpha\beta\gamma)}$ in the RVE is expressed as the function of the fluctuating average displacements $W_{i(000)}^{(\alpha\beta\gamma)}$ and the higher-order displacement components $W_{i(lmn)}^{(\alpha\beta\gamma)}$, that is,

$$\begin{aligned} u_i^{(\alpha\beta\gamma)} = {} & \bar{\varepsilon}_{ij} x_j + W_{i(000)}^{(\alpha\beta\gamma)} + \bar{y}_1^{(\alpha)} W_{i(000)}^{(\alpha\beta\gamma)} + \bar{y}_2^{(\beta)} W_{i(010)}^{(\alpha\beta\gamma)} \\ & + \bar{y}_3^{(\gamma)} W_{i(001)}^{(\alpha\beta\gamma)} + \frac{1}{2}\left[3\bar{y}_1^{(\alpha)2} - \frac{d_\alpha^2}{4}\right] W_{i(200)}^{(\alpha\beta\gamma)} \\ & + \frac{1}{2}\left[3\bar{y}_2^{(\beta)2} - \frac{h_\beta^2}{4}\right] W_{i(020)}^{(\alpha\beta\gamma)} + \frac{1}{2}\left[3\bar{y}_3^{(\gamma)2} - \frac{l_\gamma^2}{4}\right] W_{i(002)}^{(\alpha\beta\gamma)}, \end{aligned} \tag{1}$$

where d_α, h_β, and l_γ denote the subcell dimension along y_1-, y_2-, and y_3-direction (Figure 2(c)), respectively.

With full consideration of the displacement continuity condition between the adjacent subcells, the relation between the subcell strain components $\varepsilon_{ij}^{(\alpha\beta\gamma)}$ and average strains $\bar{\varepsilon}_{ij}$ can be expressed as follows [36, 39]:

$$\sum_{\alpha=1}^{N_\alpha} d_\alpha \varepsilon_{11}^{(\alpha\beta\gamma)} = d\bar{\varepsilon}_{11} \quad \left(\beta = 1,\cdots,N_\beta, \gamma = 1,\cdots,N_\gamma\right), \tag{2}$$

$$\sum_{\beta=1}^{N_\beta} h_\beta \varepsilon_{22}^{(\alpha\beta\gamma)} = h\bar{\varepsilon}_{22} \quad \left(\alpha = 1,\cdots,N_\alpha, \gamma = 1,\cdots,N_\gamma\right), \tag{3}$$

$$\sum_{\gamma=1}^{N_\gamma} l_\gamma \varepsilon_{33}^{(\alpha\beta\gamma)} = l\bar{\varepsilon}_{33} \quad \left(\alpha = 1,\cdots,N_\alpha, \beta = 1,\cdots,N_\beta\right), \tag{4}$$

$$\sum_{\beta=1}^{N_\beta}\sum_{\gamma=1}^{N_\gamma} h_\beta l_\gamma \varepsilon_{23}^{(\alpha\beta\gamma)} = hl\bar{\varepsilon}_{23} \quad (\alpha = 1,\cdots,N_\alpha), \tag{5}$$

$$\sum_{\alpha=1}^{N_\alpha}\sum_{\gamma=1}^{N_\gamma} d_\alpha l_\gamma \varepsilon_{13}^{(\alpha\beta\gamma)} = dl\bar{\varepsilon}_{13} \quad \left(\beta = 1,\cdots,N_\beta\right), \tag{6}$$

$$\sum_{\alpha=1}^{N_\alpha}\sum_{\beta=1}^{N_\beta} d_\alpha h_\beta \varepsilon_{12}^{(\alpha\beta\gamma)} = dh\bar{\varepsilon}_{12} \quad \left(\gamma = 1,\cdots,N_\gamma\right), \tag{7}$$

where the symbols d, h, and l denote the dimension of the RVE.

Similarly, the normal stress continuity between the adjacent subcells are written as:

$$\sigma_{11}^{(1\beta\gamma)} = \sigma_{11}^{(2\beta\gamma)} = \cdots = \sigma_{11}^{(N_\alpha\beta\gamma)} = T_{11}^{(\beta\gamma)} \quad \left(\beta = 1,\cdots,N_\beta, \gamma = 1,\cdots,N_\gamma\right), \tag{8}$$

$$\sigma_{22}^{(\alpha 1\gamma)} = \sigma_{22}^{(\alpha 2\gamma)} = \cdots = \sigma_{22}^{\left(\alpha N_\beta\gamma\right)} = T_{22}^{(\alpha\gamma)} \quad \left(\beta = 1,\cdots,N_\beta, \gamma = 1,\cdots,N_\gamma\right), \tag{9}$$

$$\sigma_{33}^{(\alpha\beta 1)} = \sigma_{33}^{(\alpha\beta 2)} = \cdots = \sigma_{33}^{\left(\alpha\beta N_\gamma\right)} = T_{33}^{(\alpha\beta)} \quad \left(\alpha = 1,\cdots,N_\alpha, \beta = 1,\cdots,N_\beta\right), \tag{10}$$

where $\sigma_{ii}^{(\alpha\beta\gamma)} (i = 1, 2, 3)$ indicates subcell stress components, which can be simplified as the function of $T_{ii}^{(**)}$.

With respect to the axial symmetry characteristic, that is, $\sigma_{ij}^{(\alpha\beta\gamma)} = \sigma_{ji}^{(\alpha\beta\gamma)} (i, j = 1, 2, 3 \text{ and } i \neq j)$, the sub-cell shear stress components in the αth row are expressed:

$$\sigma_{23}^{(\alpha 1\gamma)} = \sigma_{23}^{(\alpha 2\gamma)} = \cdots = \sigma_{23}^{\left(\alpha N_\beta\gamma\right)} \quad (\alpha = 1,\cdots,N_\alpha), \tag{11}$$

$$\sigma_{32}^{(\alpha\beta 1)} = \sigma_{32}^{(\alpha\beta 2)} = \cdots = \sigma_{32}^{\left(\alpha\beta N_\gamma\right)} \quad (\alpha = 1,\cdots,N_\alpha). \tag{12}$$

In the αth row, the shear stresses $\sigma_{23}^{(\alpha\beta\gamma)}$ can be simplified as follows:

$$\sigma_{23}^{(\alpha\beta\gamma)} = \sigma_{23}^{(\alpha\beta\gamma)} = \cdots = T_{23}^{(\alpha)} \quad (\alpha = 1,\cdots,N_\alpha). \tag{13}$$

Similarly, the shear stress components $\sigma_{13}^{(\alpha\beta\gamma)}$ and $\sigma_{13}^{(\alpha\beta\gamma)}$ can be simplified as follows:

$$\sigma_{13}^{(\alpha\beta\gamma)} = \sigma_{13}^{(\alpha\beta\gamma)} = \cdots = T_{13}^{(\beta)} \left(\beta = 1,\cdots,N_\beta\right), \tag{14}$$

$$\sigma_{12}^{(\alpha\beta\gamma)} = \sigma_{12}^{(\alpha\beta\gamma)} = \cdots = T_{12}^{(\gamma)} \left(\gamma = 1,\cdots,N_\gamma\right). \tag{15}$$

It is revealed that the matrix materials always represented inelastic deformation. Moreover, the thermal residual stress can be easily discerned due to the mismatch of thermal expansion coefficients between the inclusion and matrix materials. Therefore, the average subcell strain components $\bar{\varepsilon}^{(\alpha\beta\gamma)}$ in the RVE are written as the function of the subcell stress $\bar{\sigma}^{(\alpha\beta\gamma)}$, that is,

$$\bar{\varepsilon}^{(\alpha\beta\gamma)} = S^{(\alpha\beta\gamma)} \bar{\sigma}^{(\alpha\beta\gamma)} + \bar{\varepsilon}^{p(\alpha\beta\gamma)} + \alpha^{(\alpha\beta\gamma)} \Delta T, \tag{16}$$

where $\bar{\varepsilon}^{(\alpha\beta\gamma)}$ and $S^{(\alpha\beta\gamma)}$ represent the subcell strain and flexibility matrix, respectively. $\bar{\varepsilon}^{p(\alpha\beta\gamma)}$ and $\alpha^{(\alpha\beta\gamma)}$ are the subcell inelastic strain and thermal expansion coefficient. ΔT is the ambient temperature variation.

In Equation (16), the subcell thermal residual stress is determined by the temperature variation and thermal expansion coefficients of the constituent materials. Inelastic subcell strain $\bar{\varepsilon}^{p(\alpha\beta\gamma)}$ can be calculated according to the loading step size. It is indicated that the subcell average strain $\bar{\varepsilon}^{(\alpha\beta\gamma)}$ can be effectively calculated once the subcell averaged

stress $\bar{\sigma}^{(\alpha\beta\gamma)}$ is determined. From Equations (8)–(10) and Equations (13)–(15), the subcell normal stress and shear stress components are solved.

Substituting Equations (8)–(10) and Equations (13)–(15) into Equation (16), the subcell average strain components $\bar{\varepsilon}^{(\alpha\beta\gamma)}$ are obtained. Combining with the displacement continuity condition in Equations (2)–(7), the subcell stresses $T_{ij}^{(*)}$ can be written as matrix form, that is,

$$\begin{bmatrix} T_{11}^{(\beta\gamma)} \\ T_{22}^{(\alpha\gamma)} \\ T_{33}^{(\alpha\beta)} \\ T_{23}^{(\alpha)} \\ T_{13}^{(\beta)} \\ T_{12}^{(\gamma)} \end{bmatrix} = \mathbf{C} \begin{bmatrix} \bar{\varepsilon}_{11} \\ \bar{\varepsilon}_{22} \\ \bar{\varepsilon}_{33} \\ \bar{\varepsilon}_{23} \\ \bar{\varepsilon}_{13} \\ \bar{\varepsilon}_{12} \end{bmatrix} + \begin{bmatrix} \Theta_{11}^{(\beta\gamma)} \\ \Theta_{22}^{(\alpha\gamma)} \\ \Theta_{33}^{(\alpha\beta)} \\ \Theta_{23}^{(\alpha)} \\ \Theta_{13}^{(\beta)} \\ \Theta_{12}^{(\gamma)} \end{bmatrix} + \begin{bmatrix} \Gamma_{11}^{(\beta\gamma)} \\ \Gamma_{22}^{(\alpha\gamma)} \\ \Gamma_{33}^{(\alpha\beta)} \\ \Gamma_{23}^{(\alpha)} \\ \Gamma_{13}^{(\beta)} \\ \Gamma_{12}^{(\gamma)} \end{bmatrix} \Delta T, \tag{17}$$

where $\bar{\varepsilon}_{ij}$ and $\Theta_{ij}^{(**)}$ indicate the macroscopic average strain and inelastic stress components. $\Gamma_{ij}^{(**)}$ denotes the thermal expansion coefficients of the constituent materials. The symbol $\mathbf{C}$ is the stiffness matrix, which consists of subcell dimension.

Once subcell stress components in Equation (17) is obtained, the macroscopic average stress $\bar{\boldsymbol{\sigma}}$ can be easily solved according to the homogenization theory, given by,

$$\bar{\boldsymbol{\sigma}} = \frac{1}{dhl} \sum_{\alpha=1}^{N_\alpha} \sum_{\beta=1}^{N_\beta} \sum_{\gamma=1}^{N_\gamma} d_\alpha h_\beta l_\gamma \boldsymbol{\sigma}^{(\alpha\beta\gamma)}. \tag{18}$$

Substituting Equation (17) into Equation (18), the macroscopic average stress is written as the function of macroscopic average strain $\bar{\boldsymbol{\varepsilon}}$ and inelastic strain $\bar{\boldsymbol{\varepsilon}}^I$, that is,

$$\bar{\boldsymbol{\sigma}} = \mathbf{C}^* \left(\bar{\boldsymbol{\varepsilon}} - \bar{\boldsymbol{\varepsilon}}^{\mathbf{I}} - \boldsymbol{\alpha}^* \Delta T \right), \tag{19}$$

where $\mathbf{C}^*$ is the stiffness matrix of the composites.

2.2.2. Microscopic Constitutive Relation. Herein, the SMPC is considered to be composed of some UD laminas. Once the elastic modulus and mechanical behavior of each UD lamina are determined, the overall property of the SMPC can be obtained by employing the classic laminate theory [40, 41]. For each UD lamina, the stress-strain relation in the global coordinate system $x_1 - x_2$ with respect to inelastic strain $\bar{\varepsilon}_i^I$ and thermal strain is improved as follows:

$$\begin{bmatrix} \sigma_x \\ \sigma_y \\ \tau_{xy} \end{bmatrix} = \begin{bmatrix} \bar{Q}_{11}^k & \bar{Q}_{12}^k & \bar{Q}_{16}^k \\ \bar{Q}_{12}^k & \bar{Q}_{22}^k & \bar{Q}_{26}^k \\ \bar{Q}_{16}^k & \bar{Q}_{26}^k & \bar{Q}_{66}^k \end{bmatrix} \begin{bmatrix} \varepsilon_x^0 \\ \varepsilon_y^0 \\ \gamma_{xy}^0 \end{bmatrix} + z \begin{bmatrix} k_x \\ k_y \\ k_{xy} \end{bmatrix} - \begin{bmatrix} \varepsilon_x^I \\ \varepsilon_y^I \\ \gamma_{xy}^I \end{bmatrix} - \Delta T \begin{bmatrix} \alpha_x^k \\ \varepsilon_y^k \\ \alpha_y^k \end{bmatrix}, \tag{20}$$

where σ_x, σ_y, and τ_{xy} indicate the stress components in the global coordinate system. ε_x^0, ε_y^0, and γ_{xy}^0 are the midplane strain components in the composite laminates. z and $\bar{Q}_{ij}^k$ are the thickness and stiffness matrix of the laminate. k_x, k_y, and k_{xy} are related to the partial differentiation of displacement to the global coordinate.

The total thickness of composite laminates is consider as the sum of each UD lamina, that is,

$$H = \sum_{k=1}^{N} (z_k - z_{k-1}), \tag{21}$$

where the symbol N is the laminate number.

The internal force components N_x, N_y, and N_{xy} as well as the internal force moments M_x, M_y, and M_{xy} in each lamina can be acquired by executing on an integral operation along the thickness, that is,

$$\begin{aligned} \begin{bmatrix} N_x \\ N_y \\ N_{xy} \end{bmatrix} = \sum_{k=1}^{N} \begin{bmatrix} \bar{Q}_{11}^k & \bar{Q}_{12}^k & \bar{Q}_{16}^k \\ \bar{Q}_{12}^k & \bar{Q}_{22}^k & \bar{Q}_{26}^k \\ \bar{Q}_{16}^k & \bar{Q}_{26}^k & \bar{Q}_{66}^k \end{bmatrix} \Bigg\{ & \int_{z_{k-1}}^{z_k} \begin{bmatrix} \varepsilon_x^0 \\ \varepsilon_y^0 \\ \gamma_{xy}^0 \end{bmatrix} dz \\ & + \int_{z_{k-1}}^{z_k} z \begin{bmatrix} k_x \\ k_y \\ k_{xy} \end{bmatrix} dz - \int_{z_{k-1}}^{z_k} \begin{bmatrix} \varepsilon_x^I \\ \varepsilon_y^I \\ \gamma_{xy}^I \end{bmatrix} dz \\ & - \int_{z_{k-1}}^{k} \Delta T \begin{bmatrix} \alpha_x^k \\ \varepsilon_y^k \\ \alpha_y^k \end{bmatrix} dz \Bigg\}, \end{aligned} \tag{22}$$

$$\begin{aligned} \begin{bmatrix} M_x \\ M_y \\ M_{xy} \end{bmatrix} = \sum_{k=1}^{N} \begin{bmatrix} \bar{Q}_{11}^k & \bar{Q}_{12}^k & \bar{Q}_{16}^k \\ \bar{Q}_{12}^k & \bar{Q}_{22}^k & \bar{Q}_{26}^k \\ \bar{Q}_{16}^k & \bar{Q}_{26}^k & \bar{Q}_{66}^k \end{bmatrix} \Bigg\{ & \int_{z_{k-1}}^{z_k} z \begin{bmatrix} \varepsilon_x^0 \\ \varepsilon_y^0 \\ \gamma_{xy}^0 \end{bmatrix} dz \\ & + \int_{z_{k-1}}^{z_k} z^2 \begin{bmatrix} k_x \\ k_y \\ k_{xy} \end{bmatrix} dz - \int_{z_{k-1}}^{z_k} z \begin{bmatrix} \varepsilon_x^I \\ \varepsilon_y^I \\ \gamma_{xy}^I \end{bmatrix} dz \\ & - \int_{z_{k-1}}^{k} \Delta T z \begin{bmatrix} \alpha_x^k \\ \varepsilon_y^k \\ \alpha_y^k \end{bmatrix} dz \Bigg\}, \end{aligned} \tag{23}$$

where k_x and k_y are the bend deflection rates. k_{xy} is the distorting rate in the midplane.

It can be found that the internal strain, midplane bend deflection, and distorting rates are unrelated to the laminate

thickness. Equations (22) and (23) can be further simplified. The constitutive relation of the composite laminates with respect to inelastic strain and thermal strain components can be written as:

$$\begin{bmatrix} N_x + N_x^I + N_x^T \\ N_y + N_y^I + N_y^T \\ N_{xy} + N_{xy}^I + N_{xy}^T \\ M_x + M_x^I + M_x^T \\ M_y + M_y^I + M_y^T \\ M_{xy} + M_{xy}^I + M_{xy}^T \end{bmatrix} = \begin{bmatrix} \mathbf{A}\,\mathbf{B} \\ \mathbf{B}\,\mathbf{D} \end{bmatrix} \begin{bmatrix} \varepsilon_x^0 \\ \varepsilon_y^0 \\ \gamma_{xy}^0 \\ k_x \\ k_y \\ k_{xy} \end{bmatrix}, \tag{24}$$

where the symbol **A** indicates the in-plane stiffness matrix. **B** and **D** are the coupling stiffness and bending stiffness matrices. The superscripts I and T are related to the inelastic and thermal components.

3. Model Validation

The studied SMPC is prepared with T-700SC short carbon fibers and trans-1, 4-polyisoprene (TPI) matrix. The average length and diameter of the carbon fiber are 2 mm and 7 μm, respectively. To verify the proposed method, the next two procedures are executed: (1) the ellipsoid fibers are assumed to be periodically distributed in the cubic matrix to equivalently replace the SMPC reinforced with natural short fibers. On this basis, a RVE with the ellipsoid inclusion can be easily selected, which can be easily discretized by the hexahedral subcells as shown in Figure 2(c). Moreover, its elastic modulus is calculated by the HFGMC and the FEM for a comparison. (2) A novel modeling procedure is proposed to acquire effective property of the SMPC with respect to ambient temperature, and the numerical results are compared with the experimental data. The constituent material parameters of the T700SC inclusion and TPI matrix at room temperature, including elastic modulus and Poisson's ratio, are shown in Table 1.

3.1. A Comparison between Numerical Methods. To validate effectiveness of the microscopic mechanical theory, a sphere inclusion whose center coincides with the cubic RVE is considered. Figure 3 indicates the elastic modulus of the composites with respect to fiber volume fraction (FVF). For a comparison, numerical results by the FEM are also indicated in the figure when the FVFs are 0.2 and 0.3. It should be pointed out that the identical subcell number $30 \times 30 \times 30$ are used to discretize the RVE during the numerical modeling. It can be easily found that the numerical results by the 3D HFGMC exhibit a good consistency with the FEM. In addition, it can be easily discerned that the elastic modulus exhibit an exponential growth with the variation of the FVF. In details, elastic modulus is 87.7 MPa when the FVF $= 0.2$ is considered, while the elastic modulus approximate to 478.8 MPa and 793.2 MPa when the FVF are 0.48 and 0.5, respectively.

Table 1: Constituent material parameters.

Constituent materials	Elastic modulus (MPa)	Poisson's ratio
T-700SC	230×10^3	0.307
TPI	54.2	0.35

To further investigate the inclusion shape influences on the elastic modulus, axial length of the ellipsoid inclusion is investigated. Herein, the RVE dimension of $d : h : l = 2 : 1 : 1$ and the FVF $= 0.2$ are considered in the example. The parameters d, h, and l denote the dimension of the RVE along y_1-, y_2-, and y_3-direction as shown in Figure 2(c), respectively. It can be easily found from Figure 4 that longitudinal and transverse modulus represented a nonlinear variation with respect to axial length ratio of the ellipsoid inclusion. Moreover, transverse modulus exhibits a sharp decrease with an increase of the axial length ratio. In details, the transverse modulus is approximate to 105.1 MPa when the ellipsoid inclusion dimension $d_s : h_s : l_s = 1.2 : 1 : 1$ is determined. It should be pointed out that the parameters d_s, h_s, and l_s denote the ellipsoid fiber dimension. However, the transverse modulus is equal to 85.1 MPa when the ellipsoid inclusion dimension $d_s : h_s : l_s = 2.6 : 1 : 1$ is considered. However, the longitudinal modulus is 81.3 MPa when the ellipsoid inclusion dimension $d_s : h_s : l_s = 1.2 : 1 : 1$ is considered.

3.2. A Comparison with the Experimental Data. It is reported by Cai et al. [31, 32] (2021, 2022) that the FVF long thickness exhibits an obvious difference. In other words, the fiber distributed in the UD lamina close to the laminate surface is relative fewer. Therefore, it is critical to determine the FVF in each UD lamina, which can be found in Table 2. Herein, the FVF of the SMPC from 5% to 9% are considered in the example. The SMPC is further divided into 10 UD laminas, and the FVF in the surface UD laminas is different. Herein, the symbol "#" indicates the lamina number along thickness direction as shown in Figure 2(b). In addition, the ellipsoid fiber content should also be determined. According to the experimental data at room temperature, the ellipsoid fiber dimension in the 5% SMPC is determined by $d_s : h_s : l_s = 2.6 : 1 : 1$. Elastic modulus at an elevated temperature is also considered in the example. Herein, it should be noted that the elastic modulus of matrix materials is temperature-dependent, whose material parameters are provided by Zeng et al. [42, 43]. It should be noted that Poisson's ratio of the constituent materials is considered to be temperature-independent. In other words, this parameter of the constituent materials is a constant without respect to the ambient temperature influence during the numerical calculation. With respect to the raised ambient temperature, a sharp decrease of the elastic modulus for the SMPC is easily discerned as shown in Figure 5. This is attributed to the decreased modulus of matrix materials. Moreover, numerical results represent a good consistency to the experimental data. Overall, numerical results by the presented method exhibit a higher accuracy than the method proposed by Zeng et al. [42]. In details, an approximate results between the

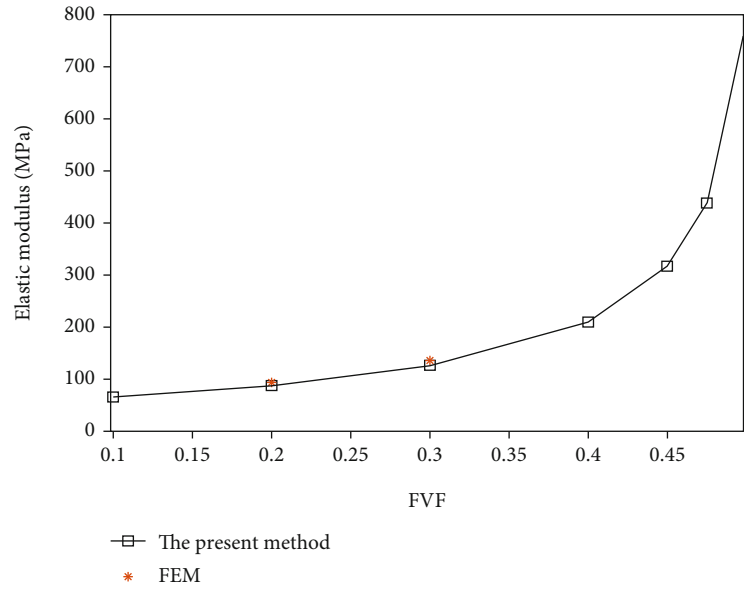

Figure 3: A comparison of elastic modulus E_{11} between the HFGMC and the FEM.

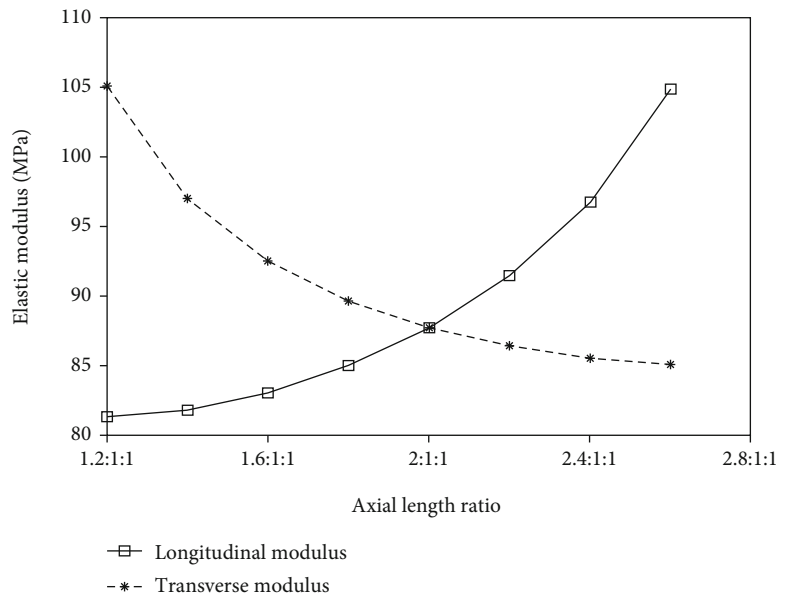

Figure 4: Elastic modulus investigation with respect to axial length ratio of the ellipsoid inclusion.

Table 2: FVF in each lamina.

FVF of the composites	1#	2#	3#	4#	5#	6#	7#	8#	9#	10#
5%	1%	6%	6%	6%	6%	6%	6%	6%	6%	1%
7%	3%	8%	8%	8%	8%	8%	8%	8%	8%	3%
9%	5%	10%	10%	10%	10%	10%	10%	10%	10%	5%

present method and the Zeng's method can be found at 301 K. The maximum error can be found when the ambient temperature is equal to 334 K, and the present method exhibits a much higher accuracy than the method proposed by Zeng et al.

Similarly, procedures are also executed on the 7% and 9% SMPC to determine the ellipsoid fiber dimension at room temperature, and elastic modulus with respect to ambient temperature is also investigated as shown in Figures 6–7. The ellipsoid inclusion dimension are $d_s : h_s$

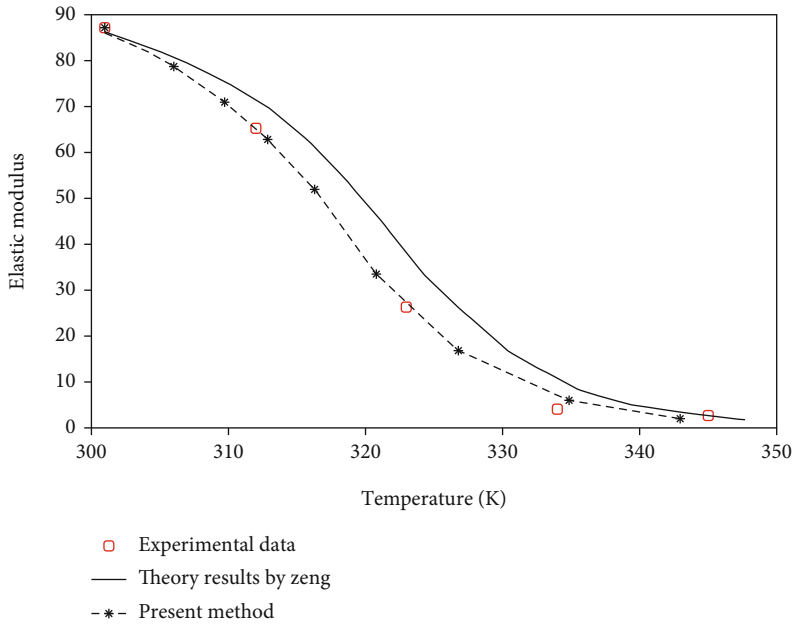

Figure 5: A comparison of elastic modulus with respect to ambient temperature when the FVF = 5%.

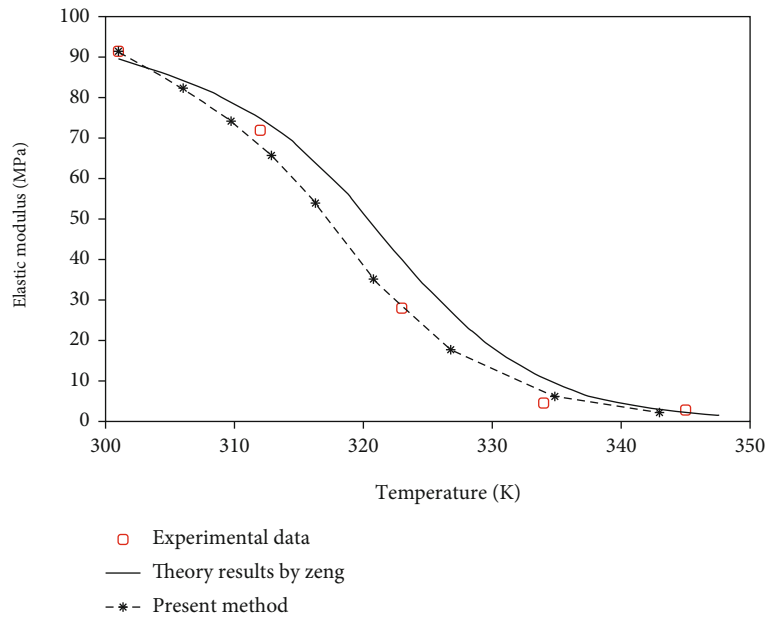

Figure 6: A comparison of elastic modulus with respect to ambient temperature when the FVF = 7%.

: $l_s = 2.4 : 1 : 1$ and $d_s : h_s : l_s = 2.1 : 1 : 1$, respectively. Combing with the FVF = 5%, an obvious difference of the inclusion dimension can be found. A sharp decrease of elastic modulus can be found when a higher ambient temperature is considered. Compared with experimental data, it is revealed that numerical results provided by the present method exhibit a higher accuracy than the theoretical method provided by Zeng et al. [42]. Combined with the numerical results as shown in Figures 4–6, it can be concluded that the FVF will contribute to an increase of the elastic modulus. In details, the elastic modulus is approximate to 86.99 MPa at the room temperature when the FVF = 5%. While the elastic moduli increase to 91.12 MPa and 93.32 MPa when the FVF is 7% and 9%, respectively.

4. Failure Strength Investigations

It is critical for researchers to grasp the failure property of the SMPC in service to maximum their usage life. However, the failure characteristic are closely dependent on many factors, including the FVF, fiber arrangement, and constituent material property. In addition, the service environment also plays an important role in the mechanical property. For instance, the SMPC are exposed to a high temperature

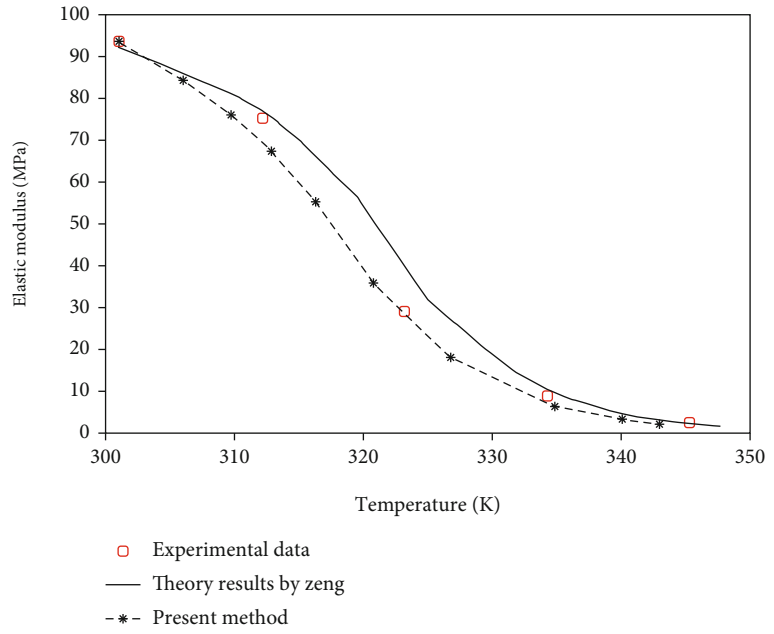

Figure 7: A comparison of elastic modulus with respect to ambient temperature when the FVF = 9%.

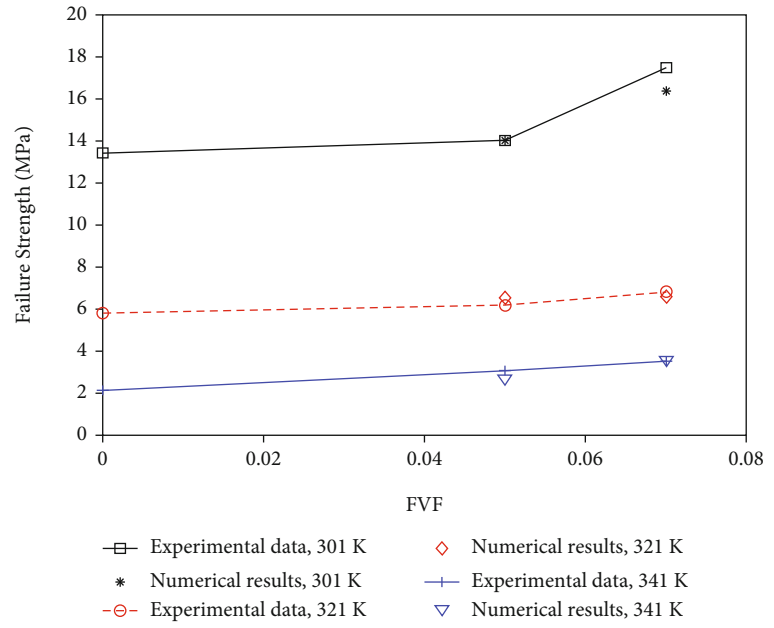

Figure 8: Investigations of the failure strength with respect to the FVF variations at different ambient temperatures.

condition, which may seriously reduce the failure strength. To fully grasp ambient variation influences, the failure strength at the room temperature and the elevated temperatures 321 K and 341 K are considered. To further valuate the failure strength of the SMPC with respect to the FVF variations, the SMP mixed with 5% and 7% natural short fibers are also investigated. It should be noted that the discretize mode of the composite laminate and inclusion shape in the matrix materials are identical with the study in Section 3. Moreover, the inelastic deformation derived from the matrix materials and thermal residual stress derived from the preparation process are both ignored.

Figure 8 indicates the failure strength of the SMPC with respect to the FVF variations at three ambient temperatures, that is, 301 K, 321 K, and 341 K. Herein, the failure property of the constituent materials at different ambient temperatures are derived from the study by Guo et al. [43]. The fiber longitudinal and transversal failure strengths are 4900 MPa and 80 MPa, respectively. During the prediction of the final failure strength, the maximum stress criterion [44] is employed. It should be pointed out that the failure strength of matrix is temperature-dependent, while the fiber strength always equal to a constant in evaluating the final failure strength at different ambient temperatures. For a further

validation, experimental data and numerical results of the failure strength are both indicated. In general, a good consistency between numerical results and experimental data can be found in the figure, and the increased short fibers tend to improve the failure strength of the SMPC in some extent. This is attributed to a higher failure strength of the natural fibers. The maximum error 6.34% can be found under the 301 K when the FVF = 0.07 is considered. In addition, an elevated temperature tends to sharply decrease the final failure strength of the SMPC. In details, the failure strength is approximate to 16.39 MPa when the ambient temperature 301 K is considered. However, the failure strengths decreased to 6.61 MPa and 3.59 MPa when the ambient temperatures 321 K and 341 K are considered. This is attribute to a huge reduction of the elastic modulus with an increase of the ambient temperature. In other words, the lower elastic modulus of the constituent materials sharply decrease the stiffness behavior of the SMPC. Naturally, their failure strength is reduced to some extent.

5. Conclusions

In this study, mechanical behaviors of the SMPC reinforced with natural short fibers were investigated by the presented constitutive model. The SMPC represents a huge deformation in service, and the improved laminate theory is suitable to describing its deformation and inclusion fraction influences on the SMPC. Numerical results of the elastic constants show a good consistency with the experimental data, which demonstrated the improved constitutive model. The conclusions are summarized as follows:

(1) The SMPC reinforced with natural short fibers can be considered as the composite laminates, which are composed of the UD laminas with ellipsoid inclusion, whose inclusion dimension can be easily determined according to the experimental data at room temperature

(2) The present method exhibits a good accuracy in investigating elastic modulus, which represents a sharp decrease with respect to an elevate temperature. For the 5% SMPC, the ellipsoid fiber dimension $d_s : h_s : l_s = 2.6 : 1 : 1$ represents a good consistency with experimental data. When the SMPC with 7% and 9% short fibers are considered, the ellipsoid inclusion dimensions are $d_s : h_s : l_s = 2.4 : 1 : 1$ and $d_s : h_s : l_s = 2.1 : 1 : 1$, respectively

(3) The final failure strength of the SMPC can be effectively acquired by the proposed ellipsoidal inclusion model, and a higher ambient temperature results in a sharp decrease of their failure strength

The investigations in this article provide a new rapid evaluation method in predicting the mechanical property of natural short fiber composites, while the proposed method limits to a small FVF. A higher FVF gives rise to a negative influence on the failure strength, which may be attributed to the variation of interfacial property.

Data Availability

The raw/processed data required to reproduce these findings cannot be shared at this time due to technical or time limitations.

Conflicts of Interest

The authors declare that they have no known competing financial interests or personal relationships that could have appeared to influence the work reported in this paper.

Authors' Contributions

Yang Li is responsible for writing—original draft and methodology; Junjie Ye for writing—original draft, methodology, and supervision; Lu Liu for validation, visualization, and software; Baoquan Shi for methodology, writing—review and editing, and supervision; and Yumin He for validation and visualization.

Acknowledgments

This work was supported by the National Natural Science Foundation of China, China (nos. 52175112 and 51675397); the National Natural Science Foundation of Shaanxi Province, China (no. 2018JM5029); and the Fundamental Research Funds for the Central Universities (JB210421).

References

[1] E. Yarali, A. Taheri, and M. A. Baghani, "A comprehensive review on thermomechanical constitutive models for shape memory polymers," *Journal of Intelligent Material Systems and Structures*, vol. 31, no. 10, pp. 1243–1283, 2020.

[2] S. Basak and A. Bandyopadhyay, "Solvent responsive shape memory polymers-evolution, current status, and future outlook," *Macromolecular Chemistry and Physics*, vol. 222, no. 19, article 2100195, 2021.

[3] J. S. Leng, X. Lan, Y. J. Liu, and S. du, "Shape-memory polymers and their composites: stimulus methods and applications," *Progress in Materials Science*, vol. 56, no. 7, pp. 1077–1135, 2011.

[4] P. Mather, X. Luo, and I. Rousseau, "Shape memory polymer research," *Annual Review of Materials Research*, vol. 39, no. 1, pp. 445–471, 2009.

[5] L. Xia, H. Gao, W. Bi, W. Fu, G. Qiu, and Z. Xin, "Shape memory behavior of carbon black-reinforced trans-1,4-polyisoprene and low-density polyethylene composites," *Polymers*, vol. 11, no. 5, 2019.

[6] J. F. Castet and J. H. Saleh, "Satellite and satellite subsystems reliability: statistical data analysis and modeling," *Reliability Engineering and System Safety*, vol. 94, no. 11, pp. 1718–1728, 2009.

[7] E. R. Abrahamson, M. S. Lake, N. A. Munshi, and K. Gall, "Shape memory mechanics of an elastic memory composite resin," *Journal of Intelligent Material Systems and Structures*, vol. 14, no. 10, pp. 623–632, 2003.

[8] J. Sun, Y. Y. Liu, and J. S. Leng, "Mechanical properties of shape memory polymer composites enhanced by elastic fibers

and their application in variable stiffness morphing skins," *Journal of Intelligent Material Systems and Structures*, vol. 26, no. 15, pp. 2020–2027, 2014.

[9] Y. An, J. Kim, N. S. Goo et al., "Preparation and analysis of the deployment behavior of shape memory polymer composite antennas," *Composites Research*, vol. 31, no. 6, pp. 347–354, 2018.

[10] M. S. Murugan, S. Rao, and G. N. Dayananda, "Actuation of shape memory polymer composites triggered by electrical resistive heating," *Journal of Intelligent Material Systems and Structures*, vol. 28, no. 17, pp. 2363–2371, 2017.

[11] L. Xia, X. Liu, and Z. Huang, "Study of electro-induced shape-memory Eucommia ulmoides rubber composites reinforced with conductive carbon blacks," *Express Polymer Letters*, vol. 15, no. 7, pp. 600–611, 2021.

[12] K. Yu, Y. J. Liu, and J. S. Leng, "Conductive shape memory polymer composite incorporated with hybrid fillers: electrical, mechanical, and shape memory properties," *Journal of Intelligent Material Systems and Structures*, vol. 22, no. 4, pp. 369–379, 2011.

[13] A. Basit, G. L'Hostis, and B. Durand, "The recovery properties under load of shape memory polymer composite material," *Materials Science and Engineering Technology*, vol. 50, no. 12, pp. 1555–1559, 2020.

[14] V. L. Le and N. S. Goo, "Deployment performance of shape memory polymer composite hinges at low temperature," *Journal of Intelligent Material Systems and Structures*, vol. 30, no. 17, pp. 2625–2638, 2019.

[15] Z. Q. Wang, J. B. Liu, J. M. Guo, X. Sun, and L. Xu, "The study of thermal, mechanical and shape memory properties of chopped carbon fiber-reinforced TPI shape memory polymer composites," *Polymers*, vol. 9, no. 11, pp. 594–604, 2017.

[16] T. D. Dao, N. S. Goo, and W. R. Yu, "Blocking force measurement of shape memory polymer composite hinges for space deployable structures," *Journal of Intelligent Material Systems and Structures*, vol. 29, no. 18, pp. 3667–3678, 2018.

[17] T. D. Dao, N. S. Goo, and W. R. Yu, "Design, fabrication, and bending test of shape memory polymer composite hinges for space deployable structures," *Journal of Intelligent Material Systems and Structures*, vol. 29, no. 8, pp. 1560–1574, 2017.

[18] B. D. Annin, E. V. Karpov, and A. Y. Larichkin, "Influence of anisotropy on the deformation of a polymer composite with shape memory," *Mechanics of Solids*, vol. 55, no. 6, pp. 761–766, 2020.

[19] C. Lelieveld, K. Jansen, and P. Teuffel, "Mechanical characterization of a shape morphing smart composite with embedded shape memory alloys in a shape memory polymer matrix," *Journal of Intelligent Material Systems and Structures*, vol. 27, no. 15, pp. 2038–2048, 2016.

[20] M. Kim, S. Jang, S. Choi, J. Yang, J. Kim, and D. Choi, "Analysis of shape memory behavior and mechanical properties of shape memory polymer composites using thermal conductive fillers," *Micromachines*, vol. 12, no. 9, article 1107, 2021.

[21] X. Z. Xin, L. W. Liu, Y. J. Liu, and J. Leng, "Mechanical models, structures, and applications of shape-memory polymers and their composites," *Acta Mechanica Solida Sinica*, vol. 32, no. 5, pp. 535–565, 2019.

[22] Z. Q. Wang, M. Z. Chang, F. Y. Kong, and K. Yun, "Optimization of thermo-mechanical properties of shape memory polymer composites based on a network model," *Chemical Engineering Science*, vol. 207, pp. 1017–1029, 2019.

[23] A. I. Arvanitakis, "A constitutive level-set model for shape memory polymers and shape memory polymeric composites," *Archive of Applied Mechanics*, vol. 89, no. 9, pp. 1939–1951, 2019.

[24] J. P. Gu, H. Y. Sun, H. Zeng, and Z. Cai, "Modeling the thermomechanical behavior of carbon fiber-reinforced shape memory polymer composites under the finite deformation," *Journal of Intelligent Material Systems and Structures*, vol. 31, no. 4, pp. 503–514, 2020.

[25] H. Y. Sun, J. P. Gu, Y. Tang, and Z. M. Xie, "Multi-scale analysis of thermo-mechanical properties of 2.5d angle-interlock woven shape memory polymer composites," *Journal of Mechanics*, vol. 35, no. 4, pp. 475–486, 2019.

[26] D. Bergman and B. Yang, "An analytical shape memory polymer composite beam model for space applications," *International Journal of Structural Stability and Dynamics*, vol. 16, no. 2, article 1450093, 2016.

[27] F. Li, L. Liu, X. Lan et al., "Modal analyses of deployable truss structures based on shape memory polymer composites," *International Journal of Applied Mechanics*, vol. 8, no. 7, article 1640009, 2017.

[28] J. J. Song, Q. Chen, and H. E. Naguib, "Constitutive modeling and experimental validation of the thermo-mechanical response of a shape memory composite containing shape memory alloy fibers and shape memory polymer matrix," *Journal of Intelligent Material Systems and Structures*, vol. 27, no. 5, pp. 625–641, 2016.

[29] S. M. R. Khalili, A. Saeedi, and E. Fakhimi, "Evaluation of the effective mechanical properties of shape memory wires/epoxy composites using representative volume element," *Journal of Composite Materials*, vol. 50, no. 13, pp. 1761–1770, 2016.

[30] N. Liu and L. L. Jiang, "Effect of microstructural features on the thermal conducting behavior of carbon nanofiber-reinforced styrene-based shape memory polymer composites," *Journal of Intelligent Material Systems and Structures*, vol. 31, no. 14, pp. 1716–1730, 2020.

[31] H. Cai, J. Ye, J. Shi et al., "A new two-step modeling strategy of the randomly distributed short fibers in composites with respective to primary voids," *Composite Science and Technology*, vol. 218, article 109122, 2022.

[32] H. Cai, J. J. Ye, J. W. Y. W. Wang et al., "An effective micro-scale approach for determining the anisotropy of polymer composites reinforced with randomly distributed short fibers," *Composite Structures*, vol. 240, article 112087, 2020.

[33] S. Lurie, D. Volkov-Bogorodsky, and E. Aifantis, "Eshelby's inclusion problem in the gradient theory of elasticity: applications to composite materials," *International Journal of Engineering Science*, vol. 49, no. 12, pp. 1517–1525, 2011.

[34] M. Katouzian and S. Vlase, "Mori-Tanaka formalism-based method used to estimate the viscoelastic parameters of laminated composites dagger," *Polymers*, vol. 12, no. 11, article 2481, 2020.

[35] R. B. Yang, Y. M. Lee, Y. C. Shiah, and T. W. Tsai, "On the generalized self-consistent model for the effective thermal conductivity of composites reinforced by multi-layered orthotropic fibers," *International Communications in Heat and Mass Transfer*, vol. 49, pp. 55–59, 2013.

[36] J. Aboudi, S. M. Arnold, and B. A. Bednarcyk, *Micromechanics Software*, Elsevier Science Pub. Ltd, Amsterdam, Netherlands, 2013.

[37] J. J. Ye, Y. W. Wang, Z. W. Li et al., "Failure analysis of fiber-reinforced composites subjected to coupled thermo-mechanical loading," *Composite Structures*, vol. 235, article 111756, 2020.

[38] J. J. Ye, C. C. Chu, H. Cai et al., "A multi-scale model for studying failure mechanisms of composite wind turbine blades," *Composite Structures*, vol. 212, pp. 220–229, 2019.

[39] J. Aboudi and M. Ryvkin, "The effect of localized damage on the behavior of composites with periodic microstructure," *International Journal of Engineering Science*, vol. 52, pp. 41–55, 2012.

[40] G. L. Shen, G. K. Hu, and B. Liu, *Mechanics of Composite Materials*, Tsinghua University Press, China, 2013.

[41] Z. Zhai, *Multiscale Modeling Based on Generalized Cell of Method and Its Application in Composite Structural Health Monitoring, [Ph.D. Thesis]*, Xi'an Jiaotong University, China, 2014.

[42] H. Zeng, J. Leng, J. Gu, and H. Sun, "Modeling the thermomechanical behaviors of short fiber reinforced shape memory polymer composites," *International Journal of Mechanical Sciences*, vol. 166, article 105212, 2020.

[43] J. Guo, Z. Wang, L. Tong, H. Lv, and W. Liang, "Shape memory and thermo-mechanical properties of shape memory polymer/carbon fiber composites," *Composites: Part A*, vol. 76, pp. 162–171, 2015.

[44] Y. Wang, *Mechanics and Structural Design of Composite Materials*, East China University of science and technology Press, Shanghai, 2012.

Hindawi
International Journal of Aerospace Engineering
Volume 2022, Article ID 2038932, 11 pages
https://doi.org/10.1155/2022/2038932

Research Article

Deployment Impact Experiment and Dynamic Analysis of Modular Truss Antenna

Shikun Zheng,[1,2] Tuanjie Li,[1] Jiang Zhao,[2] Xiaofei Ma,[2] Jialong Zhu,[2] Zhirong Huang,[2] and Yingyi Lang[1]

[1]*School of Mechano-Electronic Engineering, Xidian University, Xi'an 710071, China*
[2]*Xi'an Institute of Space Radio Technology, Xi'an 710100, China*

Correspondence should be addressed to Tuanjie Li; tjli@mail.xidian.edu.cn

Received 1 April 2022; Revised 15 June 2022; Accepted 21 June 2022; Published 8 July 2022

Academic Editor: Paolo Gasbarri

The deployment of a modular truss antenna reflector is relied on the driven energy of the springs between the components of the structure. The deployment process is characterized by fast speed and large impact. In order to study the impact characteristics of antenna deployment on the boundary, the deployment dynamic analysis of a modular truss antenna reflector is carried out. The deployment impact experiment is performed to obtain the impact forces of the reflector on the boundary. The dynamic model of the modular truss reflector is modified according to the experiment results. The dynamic analysis of a satellite with an arm and a modular truss reflector is conducted by using the modified reflector model. The dynamic behavior of the satellite in orbit during the modular truss antenna reflector deployment is predicted.

1. Introduction

In recent years, in order to meet the increasing demands of satellite communication, navigation, and earth observation, more and more large deployable antenna reflectors have been developed and applied in satellite engineering. When the satellite is in the launch stage, this kind of antenna is placed in the rocket fairing in a folded state. After the satellite being launched into space, it is gradually expanded to the working state through the deployment function of the antenna itself. Large deployable antennas usually include solid surface deployable antenna, cable-net deployable antenna, and inflatable deployable antenna [1]. Among them, the cable-net deployable antenna composed of a support structure, and a metal mesh is the most widely used one. Common cable-net deployable antennas include umbrella-type antenna [2], modular truss antenna [3], wrap-rib antenna [4], and hoop modular truss antenna [5–7]. Among them, the modular truss deployable antenna is widely used in various satellites due to its high storage ratio, large structural stiffness, and good stability.

The modular truss deployable antenna reflector structure was first proposed by National Aeronautics and Space Administration (NASA) in 1968 [8]. By changing the size and number of modules, it can adapt to the needs of different calibers. The basic unit that makes up the modular truss deployable antenna includes tetrahedron, quadrangular pyramid, hexagonal column, and hexagonal platform. So far, the modular truss deployable antenna with tetrahedron as the basic unit is the most widely used. For example, the 5.2 m diameter PETA truss antenna is developed by General Dynamics Corporation (GDC) [9]. The 7 m diameter truss deployable antenna reflector developed by Johnson Space Center (JSC) was successfully applied to the "Kondor" spacecraft [10]. And Jet Propulsion Laboratory (JPL) in the United States has studied a modular truss deployable antenna based on shape memory composite deployment hinge for large aperture and high surface accuracy antenna [11]. Among foreign researches, Russia has the most extensive research and application of modular truss deployable antennas. The tetrahedral modular truss deployable antenna developed by Russian Space Agency has been successfully applied to spacecraft such as "Nature," "Soyuz" spacecraft, and "Mir" space station since 1985. The application of truss

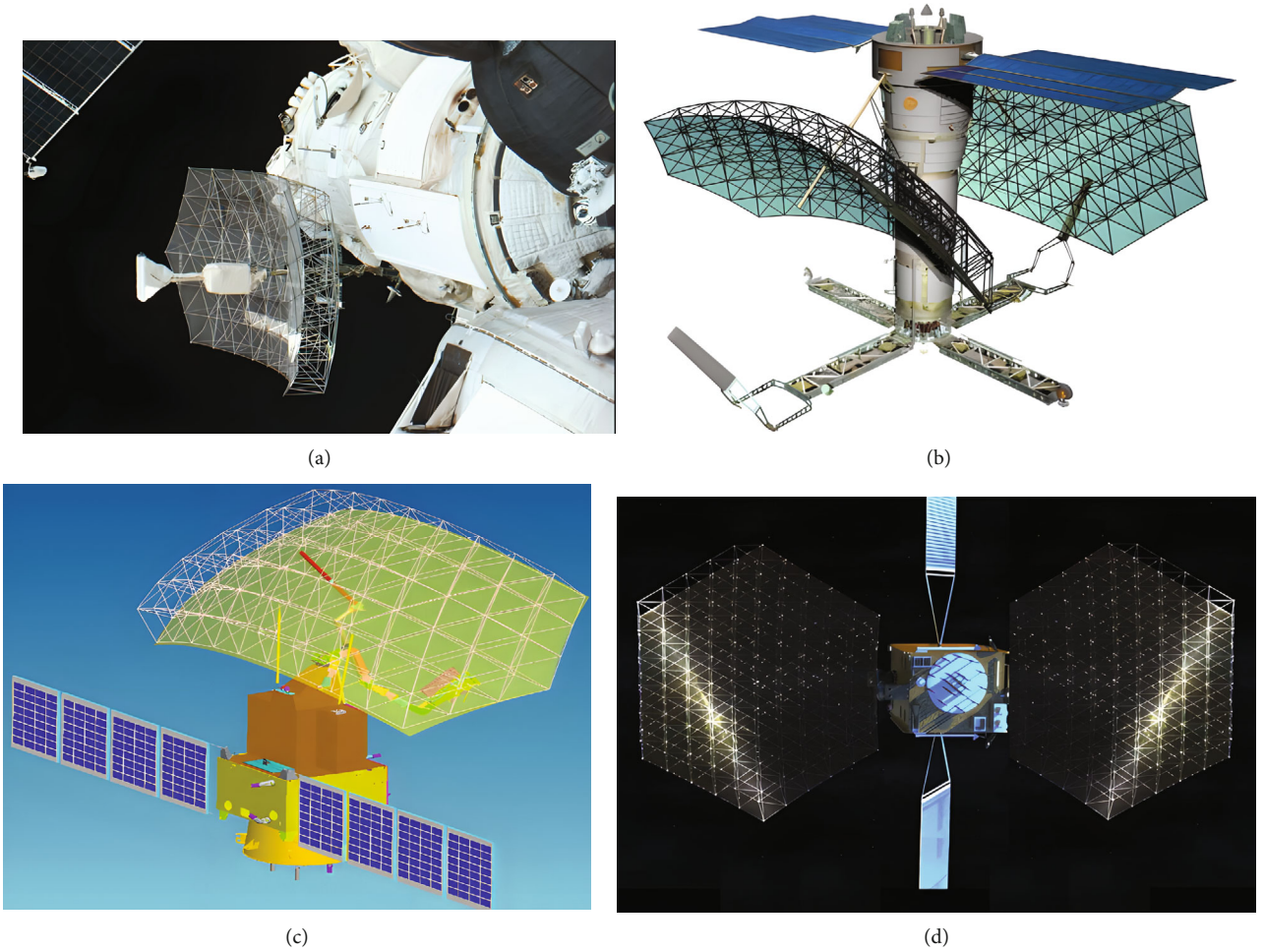

(a) (b) (c) (d)

Figure 1: Applications of modular truss antenna. (a) "Mir" space station. (b) Pion satellite. (c) Environmental disaster reduction satellite. (d) BeiDou navigation satellite.

antenna in various countries is shown in Figure 1. The SAR antenna of the "Mir" space station adopts a 6 m × 2.8 m modular truss antenna, as shown in Figure 1(a). The Pion satellite launched by Russia in June 2021 uses a modular truss antenna with a diameter of 12 m × 4 m, as shown in Figure 1(b). At the same time, domestic research on modular truss deployable antenna has also been carried out; meanwhile, offset feed and normal feed modular truss antennas have been developed one after another, which have been applied to BeiDou navigation, environmental disaster reduction, satellite communication, and other fields. The antenna diameter ranges from 6 m to 9 m, and the working frequency band covers the UHF ~ S frequency band, as shown in Figures 1(c) and 1(d).

Usually in the design process of the tetrahedral modular truss antenna, the designer is concerned about the structural rigidity and structural strength, and the shape distortion error of the reflecting surface is concerned by designers [12–15]. There are relatively few related literatures on deployment dynamics of truss antenna. Wang et al. [16, 17] created a dynamics model of tetrahedral element by using commercial software ADAMS and carried out simulation and experimental research on its deployment process. At the same time, they analyzed the deployment process of a tetrahedral modular truss antenna reflector under zero gravity and no boundary conditions and studied the force of the rod during the deployment process of the reflector. Guan and Liu [18] tested the deployment process of a kind of tetrahedral modular truss antenna and proposed a control method to reduce the impact load but did not conduct the on-orbit impact analysis. Huang et al. [19] analyzed the impact force of a kind of offset-fed modular truss antenna but did not study the satellite motion law during the deployment of the reflector. However, the above research did not consider the influence of reflector deployment on the boundary.

Considering that tetrahedral truss antenna has the characteristics of fast deployment and large impact, the deployment of the antenna reflector will inevitably have a significant impact on the satellite attitude. Therefore, in this paper, the dynamic characteristics of a class of normal feed tetrahedral modular truss deployable antennas are studied, and the dynamic simulation and experimental verification of the impact characteristics of the reflector expansion on the boundary are carried out, respectively. The reflector dynamics model was modified by the experimental data, and the on-orbit dynamics behavior of the reflector-deployment arm-satellite combination during the reflector deployment was predicted by dynamic simulation.

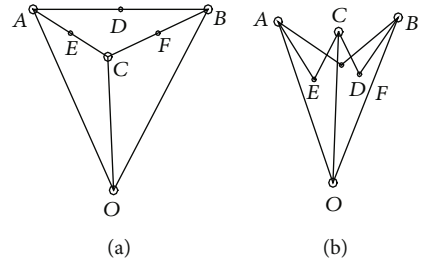

Figure 2: The principle of tetrahedral element expansion. (a) Folded state. (b) Expanded state.

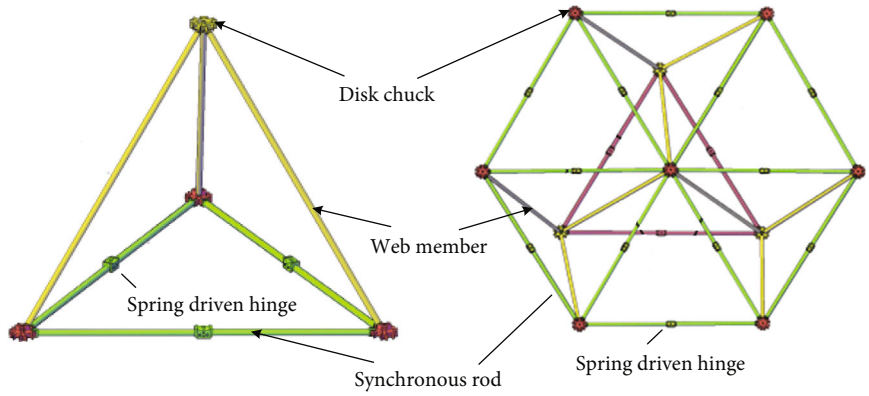

Figure 3: Tetrahedral element and its geometric extension structure.

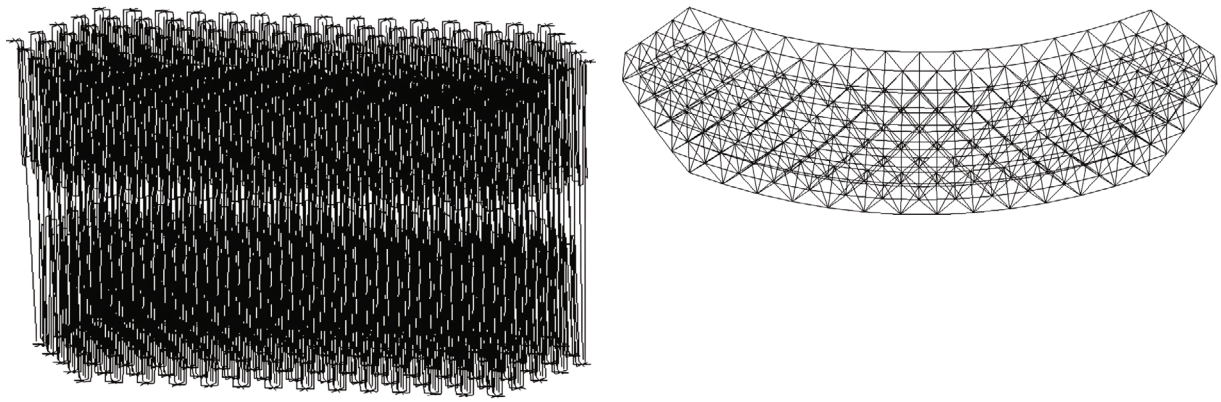

Figure 4: A tetrahedral truss antenna reflector. (a) Folded state. (b) Expanded state.

2. Tetrahedral Modular Truss Antenna Reflector

The tetrahedral modular truss antenna is assembled by a series of tetrahedral elements, as shown in Figure 2. Each tetrahedral element contains six rods and four nodes. The three rods AB, AC, and BC on the bottom edge constitute the upper and lower chords of antenna truss, and the three edges OA, OB, and OC are the web members connecting the upper and lower chords. The nodes in the middle of the three chords are designed with folding/deploying function, so that the chord has deployable characteristics.

Figure 3 shows the composition structure of the tetrahedral truss element. The tetrahedral element can be conveniently expanded to form a larger scale truss structure.

According to the above theory, the required reflector truss structures of different diameters can be obtained by means of topology expansion using this principle. Figure 4 shows a normal feed tetrahedral modular truss antenna reflector.

As shown Figure 4, the drive nodes in the middle of the reflector's chords store energy during the folding process. When the reflector is unlocked, the drive node releases energy, which drives both the upper and lower chords to

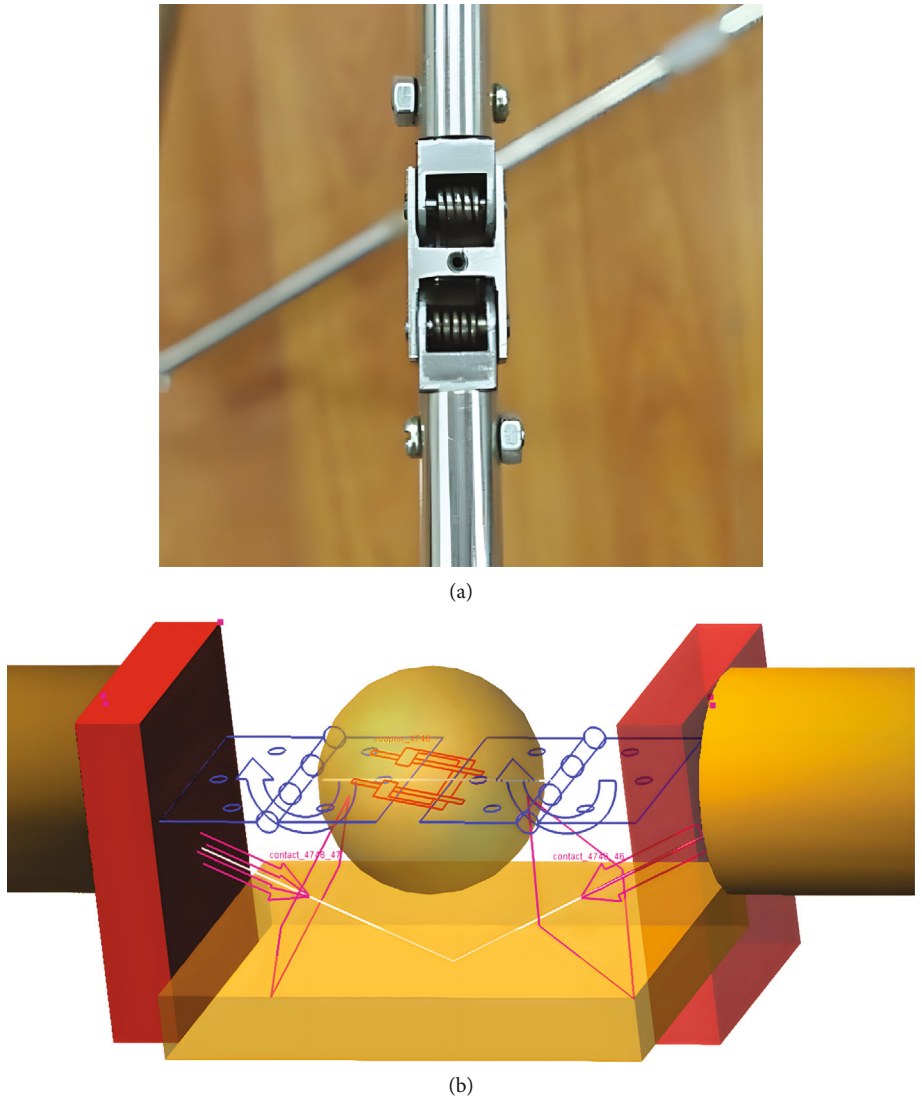

(a)

(b)

Figure 5: Synchronous hinge products and models. (a) Synchronous hinge products. (b) Synchronous hinge models.

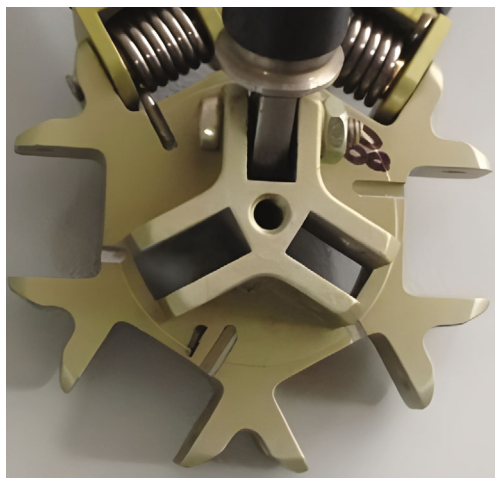

Figure 6: Connection between disk and web.

expand outwards, and the web members rotates outwards around the designated rotation pair. Finally, the antenna reflector is expanded to form a certain surface under the action of the elastic strain energy from the torsion spring. This kind of instantaneous expanding antenna drove by torsion spring will inevitably produce strong impact collision during the deployment process. In order to accurately predict the impact of reflector deployment on other satellite components, the dynamic analysis of antenna reflector deployment is needed.

The dynamic model is established by using the commercial software ADAMS. The components of the reflector are considered as rigid bodies. The Revolute Joint is used to model the connection between the synchronous rod and the synchronous hinge. Synchronous hinge products and models are shown in Figure 5. In order to simulate the synchronous motions of the adjacent folding rods, the Coupler Joint is added for two adjacent Revolute Joints between the folding rods and the hinge housing, so that the rotations between the two folding rods and hinge can be synchronous.

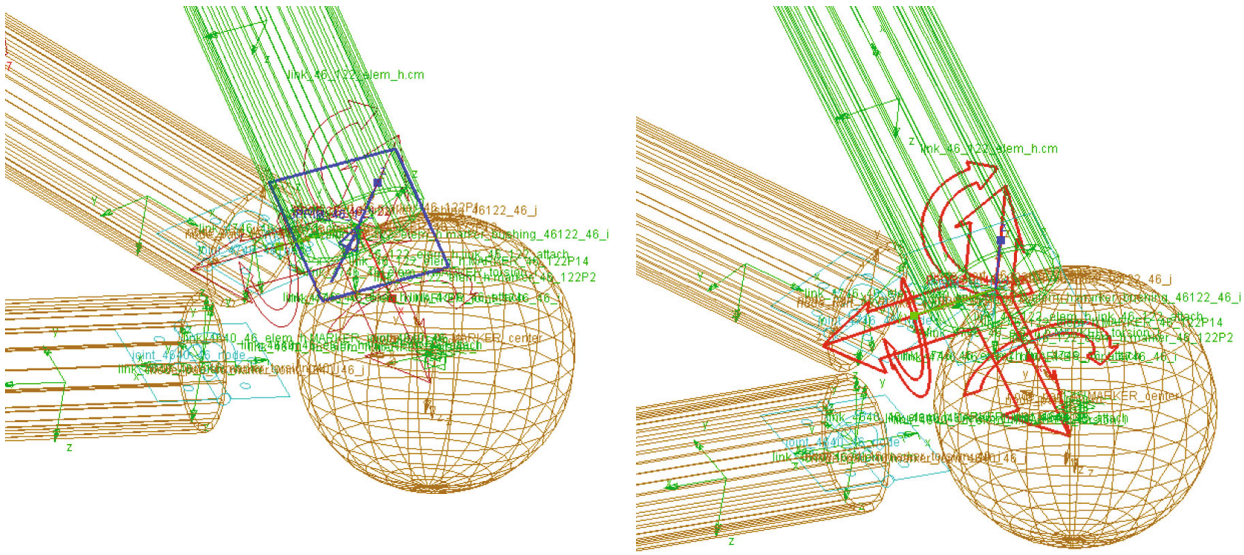

(a) (b)

Figure 7: Modeling of connection between disk and web. (a) Inline Primitive Joint. (b) BISTOP force function.

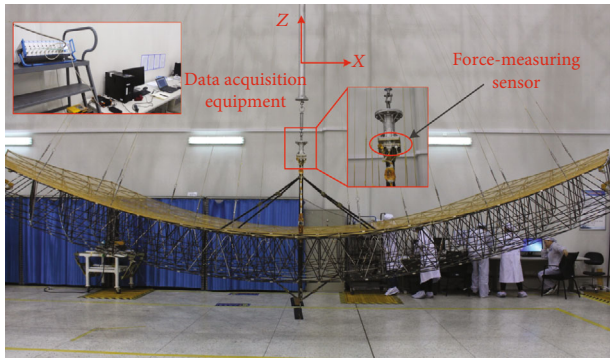

Figure 8: The impact test of reflector deployment.

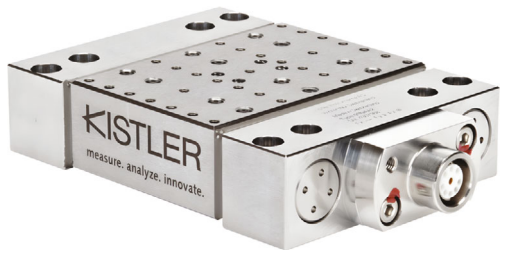

Figure 9: Kistler 9119AA2 force sensor.

The contact between the folding rod and the hinge is also created, and then the deployment state can be maintained when the reflector is unfolded completely.

In order to avoid the overconstraints of the dynamic model of the reflector, the busing force is used as the flexible connection to model the connection between the disk and the synchronous rod. The stiffness coefficient of the bushing force in the rotational direction between the disk and the folding rod is set to zero, and the stiffness coefficients the other directions are set as large numbers.

As shown in Figure 6, there is a clearance between the disk and the web. In order to model the clearance accurately, the combination of the Inline Primitive Joint and the BISTOP force function in the ADAMS are used to model the connection of the disk and the web, as shown in Figure 7.

3. Ground Deployment Simulation and Experiment

In this paper, the deployment process of a normal feed tetrahedral modular truss antenna reflector under gravity unloading environment is studied as shown in Figure 8. The ground deployable experiment device of antenna reflector is designed, and the unloading plate is fixed on the unloading truss. In order to eliminate the influence of gravity, the unloading system including the cables, and the spring balances is used to connect the reflector unloading point and unloading plate lifting point, respectively. The unloading system can not only realize the gravity unloading of the reflector but also resist the external vibrations in the experiment.

Using the Kistler 9119AA2 compact multicomponent dynamometer as shown in Figure 9 as the force sensor, the compact six components can be measured. The Dewesoft data acquisition system is used for the data acquisition. The force sensor is installed at the connection between the reflector component and the external component to measure the impact force of the reflector deployment on the boundary. The force sensor experiment status is shown in Figure 8.

The method described in the previous section is used to establish the reflector dynamics model and carry out the dynamics simulation of the reflector deployment process. The reflector deployment process obtained from the dynamics simulation calculation is shown in Figure 10.

Considering that the reflector is symmetrical about XZ plane and YZ plane, the impact of its deployable process on the outside is mainly reflected in the Z direction. The

(a)

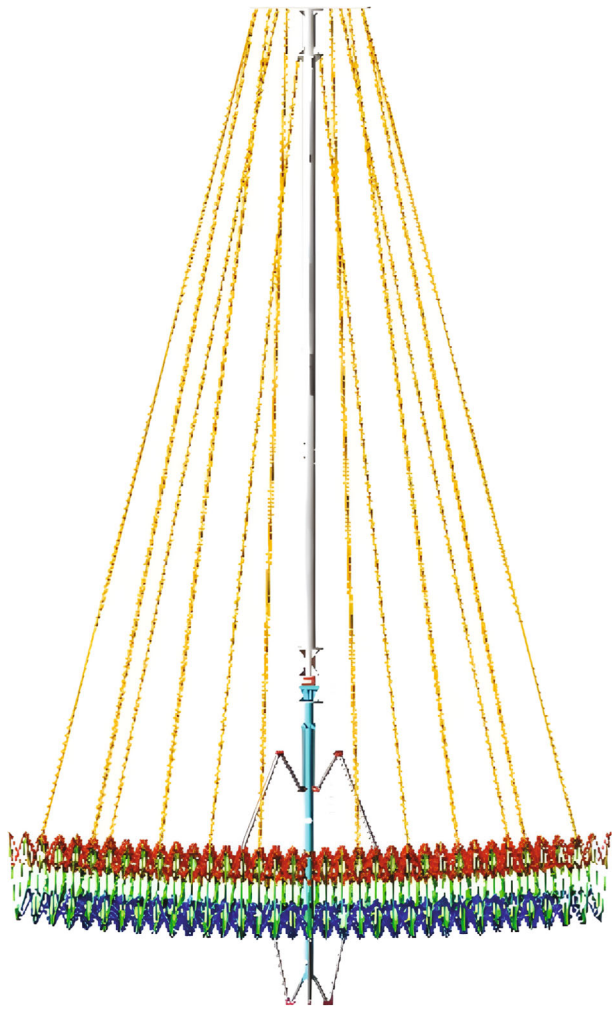

(b)

Figure 10: Continued.

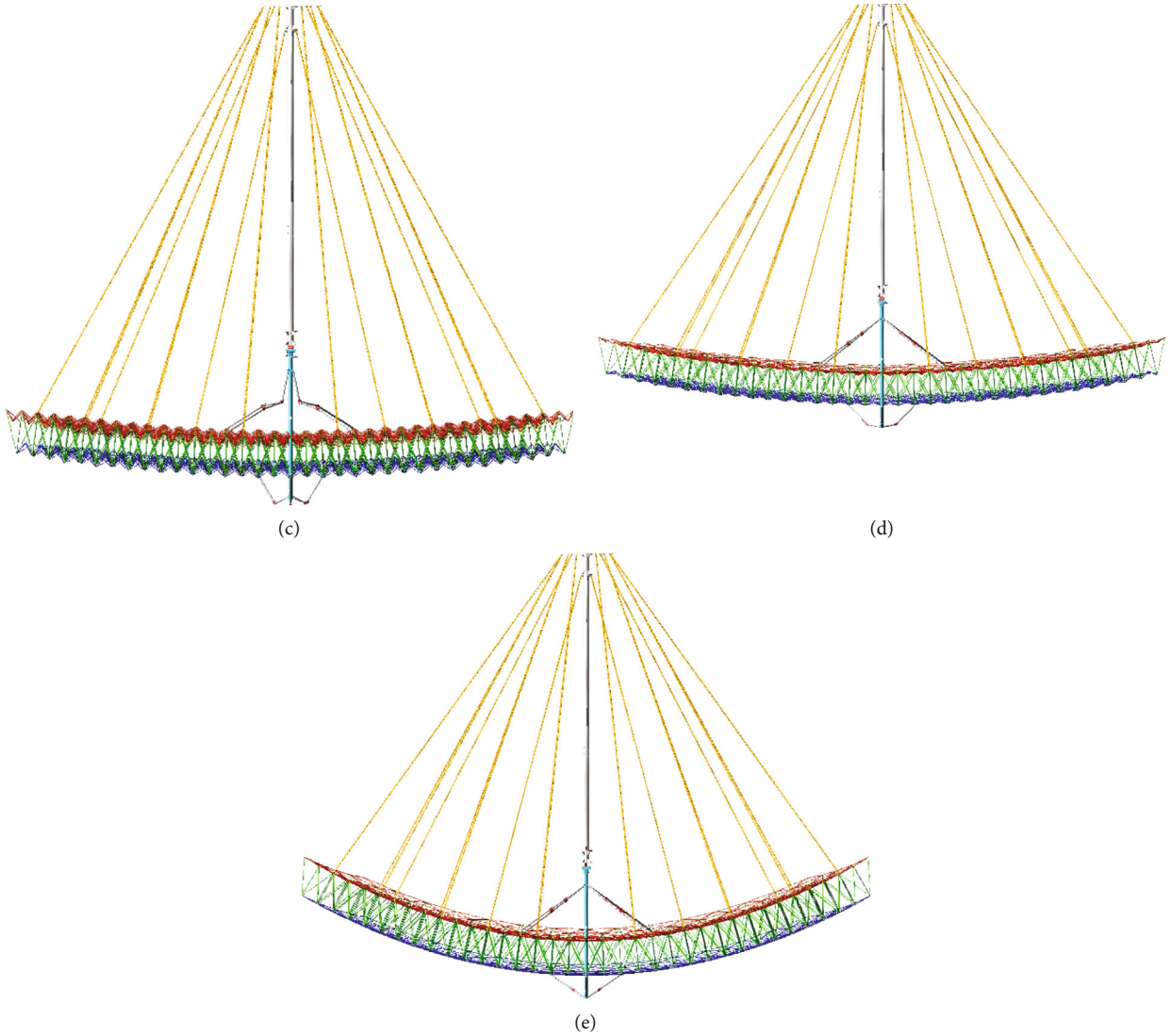

Figure 10: The simulation of reflector deployment process. (a) Deployed process 1. (b) Deployed process 2. (c) Deployed process 3. (d) Deployed process 4. (e) Deployed process 5.

parameters of the dynamic model are modified according to the impact force Fz measured by the force sensor.

The modified parameters of the dynamic model include the clearance of web and disk, damping coefficient, static friction coefficient, and dynamic friction coefficient. Taking the difference between the impact force measured by experiment and the impact force of dynamic simulation as the objective function J, the following optimization model is established:

$$\begin{aligned} &\text{find} && \Delta x = [x_1 x_2 x_3 x_4], \\ &\min && J = F_m - F_s(x_1, x_2, x_3, x_4), \\ &s.t. && x_{\text{imin}} < x_{\text{i}} < x_{\text{imax}}, i = 1, 2, 3, 4, \end{aligned} \tag{1}$$

in which x_1 is the clearance between web and disk, x_2 is the damping coefficient, x_3 is the static friction coefficient, x_4 is the dynamic friction coefficient, F_s is the impact force obtained by dynamic simulation, and F_m is the impact force measured by experiment. First, input a set of parameters to be corrected for dynamic simulation and make the difference between the impact force measured by the experiment and the impact force obtained by the dynamic simulation to obtain the function value of the objective function J. Then, the value of the objective function is minimized by adjusting the parameter $x_i (i = 1, 2, 3, 4)$ to be corrected, and the model parameters should be controlled within a reasonable range when modifying the model parameters. The group of correction parameters that minimizes the objective function value is the corrected model parameters.

The modified model parameters are as follows: the clearance between web and disk is 1 mm, the damping coefficient of the flexible connection between the disk and the bar is 5.0, the dynamic friction coefficient is 0.2, and the static friction coefficient is 0.4. After model modification, the impact force comparison between the simulation results and the ground test results is shown in Table 1.

Table 1: The comparison between the simulation and test results.

No.	Parameters		Test results	Simulation results
1	Peak impact force during deployment (amplitude)	$Fx\|N$	55.2	2.43
2		$Fy\|N$	79.1	53
3		$Fz\|N$	491.2	513.8

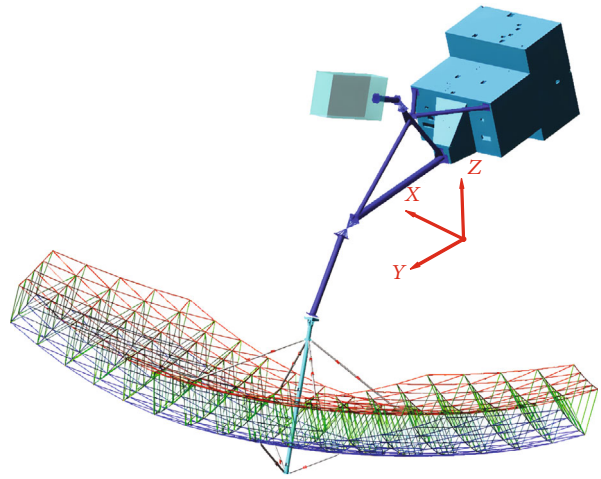

Figure 11: The schematic diagram of normal feed truss antenna satellite.

Both simulation and test results show that the impact force in the Z direction is significantly greater than that in the other two directions, which is consistent with expectations. Moreover, the maximum impact force calculated by the simulation is basically equal to the maximum impact force Fz measured by the ground test, and the error is about $(513.8 - 491.2)/491.2 = 4.6\%$. The reflector is symmetrical with respect to the Plane YOZ, so that the simulation result Fx is close to 0. And the reflector is quasisymmetrical with respect to the plane XOZ, so that the Fy is larger than Fx, but much smaller than Fz. But to the assembly errors of the unloading system in the experiment, the test results of Fx and Fy are larger than the simulation results. Since the size of the reflector in the X direction is significantly larger than the size in the Y direction, Fx is more significantly affected by the assembly errors.

4. Impact Dynamics Analysis on Orbit

In order to analyze the impact characteristics of reflector deployable on orbit, a rigid-flexible coupling dynamic model is established for a small satellite of CAST2000 platform as shown in Figure 11, which includes reflector, deployment arm, and satellite platform. The solar wing and satellite are merged into a satellite platform. The weight of the satellite platform is 750 kg, and the moments of inertia around the center of mass X, Y, and Z axes are $2.2 \times 10^3 Nm^2$, $1.4 \times 10^3 Nm^2$, and $2.5 \times 10^3 Nm^2$, respectively. The weight of antenna reflector, feed, and deployment arm is 75 kg, 65 kg, and 43 kg, respectively.

The reflector is modeled by the modified dynamic model. The feed and the satellite are considered as rigid bodies, and the arms connecting the satellite, the feed, and the reflector are considered as flexible bodies by using the modal synthesis method, which is treated by importing the modal neutral files generated by the finite element analysis software in the ADAMS model in this paper.

For the above dynamics model, the deployment dynamics simulation of the reflector under gravity-free condition is studied. And the displacement curve of the satellite centroid is shown in Figure 12(a).

It can be seen from Figure 12(a) that with the deployment of the antenna reflector, the centroid position of the satellite moves in a small range. Because the reflector deployment is basically symmetric with respect to the YZ plane, there is almost no position change of the satellite centroid along the X direction. So, the deployment has little influence on the displacement change of the centroid in the X direction. The curves of velocity and acceleration are shown in Figure 12(b) and (c).

Figures 12(d)–12(f) , respectively, show the curve of satellite attitude angle, attitude angular velocity, and attitude angular acceleration changing with time. It can be seen from Figure 12(d) that the on-orbit deployment of antenna reflector has a great influence on rolling angle and a small influence on attitude angles in the other two directions. In the early stage of reflector deployment, the rolling angle increases to 1.1°. With the rapid deployment of antenna reflector, the rolling angle decreases rapidly. The change of rolling angle reaches a stable stage during a period of oscillation.

The attitude angular velocity of the satellite shows that the deployment of antenna reflector has the greatest influence on the rolling angle. The attitude angular velocity

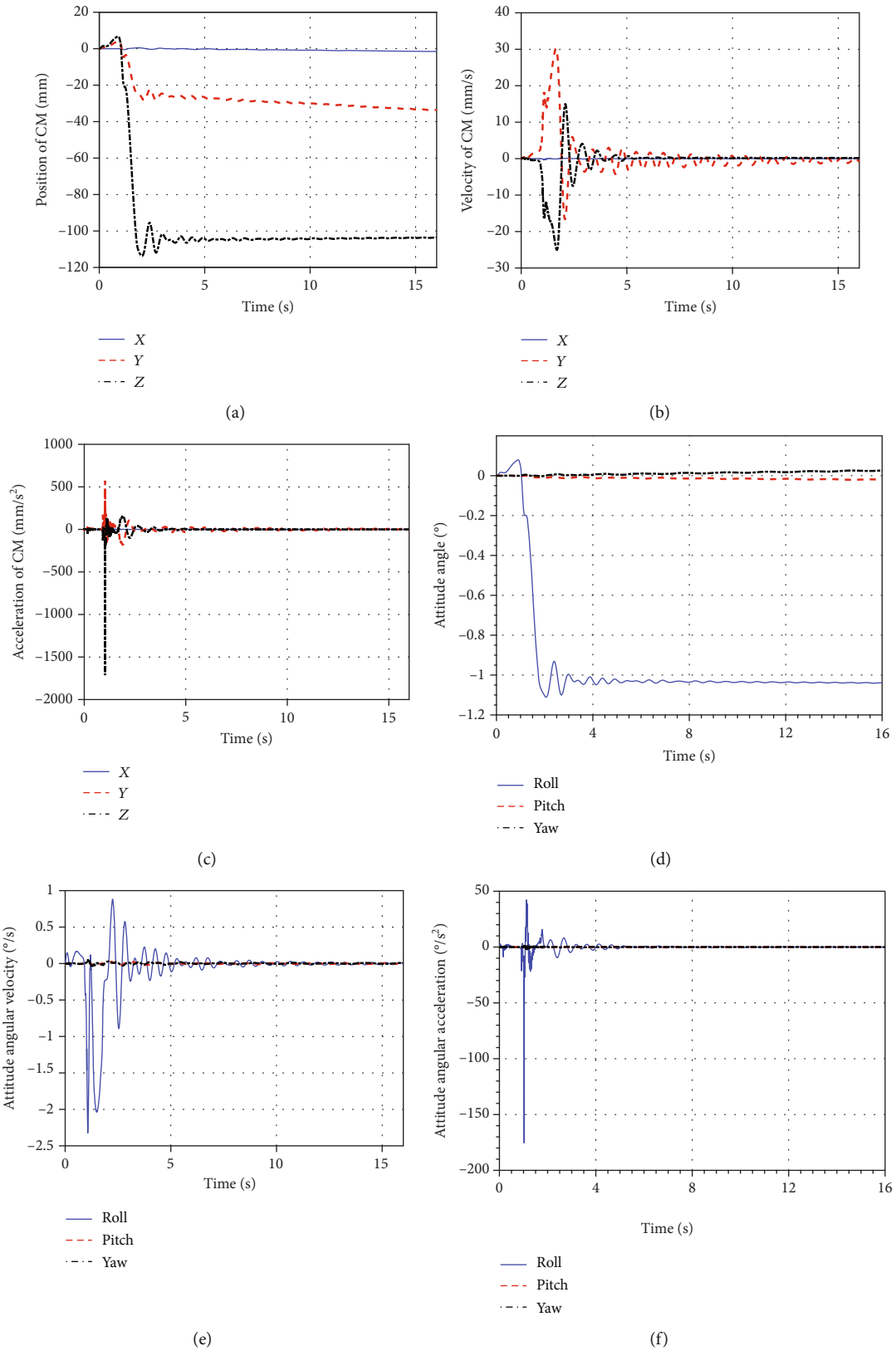

Figure 12: Simulation results of the system on orbit. (a) The displacement curve of the satellite centroid. (b) The velocity curve of the satellite centroid. (c) The acceleration curve of the satellite centroid. (d) The attitude angle of the satellite. (e) The attitude angular velocity of the satellite. (f) The attitude angular acceleration of the satellite.

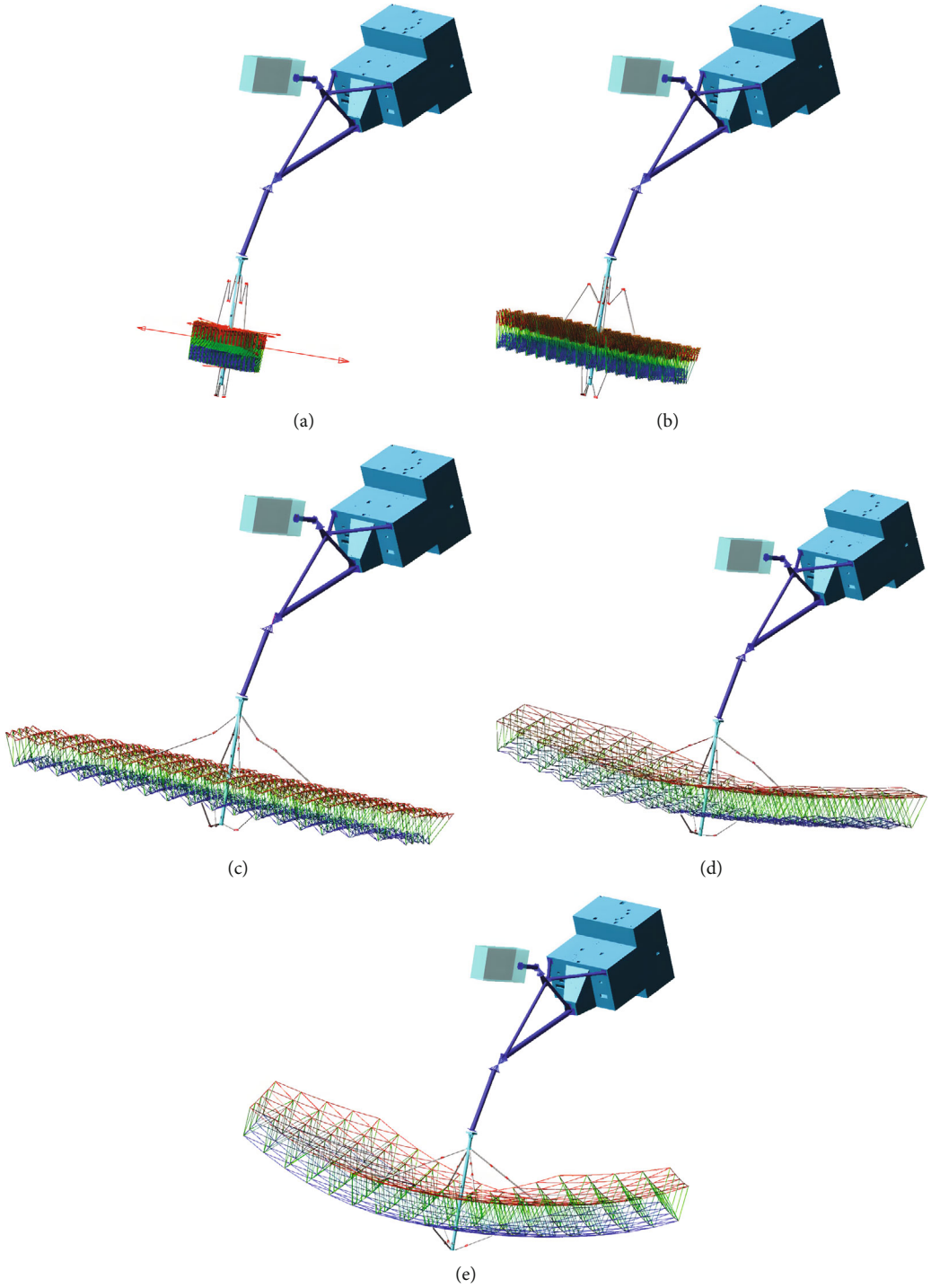

Figure 13: The deployment process of normal feed truss antenna satellite. (a) Deployed process 1. (b) Deployed process 2. (c) Deployed process 3. (d) Deployed process 4. (e) Deployed process 5.

shows a trend of oscillation attenuation and gradually decayed to close to zero over time. When the satellite is completely stable, the satellite-antenna reflector will keep uniform rotation without the external disturbance. The deployment process of normal feed truss antenna satellite obtained from the dynamics simulation calculation is shown in Figure 13.

5. Conclusion

In this paper, a multibody dynamic model of a tetrahedral framed deployable antenna reflector is established. In order to optimize the accuracy of the dynamic model, dynamic simulation and experimental research were carried out for the ground deployment test of the frame antenna reflector,

and the impact force on the boundary of the reflector deployment under ground conditions was obtained. The reflector dynamics simulation model is modified by minimizing the objective function. With the revised reflector dynamics simulation model, we can predict the impact of the antenna deployment on the satellite platform in the on-orbit state. In order to predict the impact of the antenna deployment on the satellite platform, the dynamic analysis of the spacecraft on-orbit deployment including the satellite platform, deployment arm, feed, and reflector was carried out. In the change law of angular velocity and angular acceleration, the results show the following:

(1) By comparing the impact force of the experiment and the simulation experiment, the correction parameters of the dynamic simulation are determined

(2) Since the reflector expansion is basically symmetrical with respect to the YZ plane, the expansion has little effect on the displacement change of the centroid in the X direction

(3) The deployment of the antenna reflector has the greatest influence on the roll angle. As time goes by, the attitude angular velocity exhibits a trend of oscillation attenuation and gradually attenuates to close to zero

Based on the research results of this paper, it can provide a reference for the attitude adjustment of the frame antenna reflector in the deployment process. Make the satellite attitude adjustment process smoother and more stable. The model can be further modified and optimized according to the expansion of the on-orbit antenna.

Data Availability

Data is available on request.

Conflicts of Interest

The authors declare that they have no conflicts of interest.

References

[1] G. Tibert, *Deployable tensegrity structure for space applications*, Royal Institute of Technology Department of Mechanics, Sweden, 2002, Doctoral Thesis.

[2] J. A. Moses, "FLTSATCOM thermal test and flight experience," in *AIAA 26th Thermophysics conference*, vol. 24-26, Honolulu, 1991.

[3] W. A. Imbriale, G. Steven, and B. Luigi, *Space Antenna Handbook*, John Wiley & Sons, 2012.

[4] A. G. Roederer and Y. Rahmat-Samii, "Unfurlable satellite antennas: a review," *Annales des Telecommunications*, vol. 44, no. 9-10, pp. 475–488, 1989.

[5] M. D. Stegman, "SMAP antenna feed radome: design, development and test," in *2011 Aerospace Conference*, pp. 1–14, Big Sky, MT, USA, 2011.

[6] K. J. Fu, Z. H. Zhao, G. Ren et al., "From multiscale modeling to design of synchronization mechanisms in mesh antennas," *Acta Astronautica*, vol. 159, pp. 156–165, 2019.

[7] F. Angeletti, P. Iannelli, P. Gasbarri, and M. Sabatini, "End-to-end design of a robust attitude control and vibration suppression system for large space smart structures," *Acta Astronautica*, vol. 187, pp. 416–428, 2021.

[8] J. A. Fager and E. C. Hamilton, "Large erectable antenna for space application final report," 1969, Report, No. GDC-DCL69-003.

[9] NASA Center for Aerospace Information, *Requirements, Design and Development of Large Space Antenna Structures*, Nasa STI/Recon Technical Report N, Virginia, 1980.

[10] A. S. Chebotarev, V. A. Panteleev, N. M. Feyzulla, E. M. Mitrofanov, and A. N. Plastikov, "Truss-type deployable reflector antenna systems for synthetic aperture radar mounted on a small spacecraft," in *2014 24th International Crimean Conference Microwave & Telecommunication Technology*, pp. 521-522, Sevastopol, Ukraine, 2014.

[11] H. Fang, L. Shook, J. Lin, J. Pearson, and J. Moore, "A large and high radio frequency deployable reflector," in *AIAA 3rd AIAA/ASME/ASCE/AHS/ASC structures, Structural Dynamics and Materials Conference*, Honolulu, Hawaiia, 2012.

[12] J. M. Hedgepeth, "Influence of fabrication tolerances on the surface accuracy of largeantenna structures," *AIAA Journal*, vol. 20, no. 5, pp. 680–686, 1982.

[13] S. L. Padula, H. M. Adelman, M. C. Bailey, and R. T. Haftka, "Integrated structural electromagnetic shape control of large space anatenna reflectors," *AIAA Journal*, vol. 27, no. 6, pp. 814–819, 1989.

[14] R. A. Burdisso and R. T. Haftka, "Statistical analysis of static shape control in space structures," *AIAA Journal*, vol. 28, no. 8, pp. 1504–1508, 1990.

[15] W. H. Greene and R. T. Haftka, "Reducing distortion and internal forces in truss structures by member exchanges," *AIAA Journal*, vol. 28, no. 9, pp. 1655–1662, 1990.

[16] X. K. Wang, B. Cai, H. F. Fang, and X. F. Ma, "Deployment analysis of a deployable truss structure," in *International Conference on Computer Information Systems and Industrial Applications (CISIA 2015)*, Atlantis Press, 2015.

[17] X. Wang, Y. Wang, H. Fang, P. Huang, and Z. Chen, "Deployment dynamic analysis of a tetrahedral truss reflector," in *2nd AIAA Spacecraft Structures Conference*, pp. 5–9, Kissimmee, Florida, 2015.

[18] F. L. Guan and L. Liu, "Deployment control and test of deployable tetrahedral truss antenna," *Journal of Engineering Design*, vol. 17, no. 5, pp. 381–387, 2010, (in Chinese).

[19] Z. Huang, Y. Song, S. Zheng, J. Zhu, and X. Wang, "Deployment impact analysis of the offset-fed truss reflector," *Journal of Xidian University*, vol. 43, no. 1, pp. 110–115, 2016, (in Chinese).

Hindawi
International Journal of Aerospace Engineering
Volume 2022, Article ID 8063786, 8 pages
https://doi.org/10.1155/2022/8063786

Research Article

Application of Stewart Platform in the Low-Frequency Vibration Characteristic Test of Space Truss Deployable Antenna on Satellite

Hui Wang, Jiang Zhao, Yonggang Xue, Zhirong Huang, Shikun Zheng, and Xiaofei Ma

China Academy of Space Technology (Xi'an), Xi'an, China

Correspondence should be addressed to Hui Wang; wangh23@cast504.com

Received 13 April 2022; Revised 20 May 2022; Accepted 17 June 2022; Published 4 July 2022

Academic Editor: Adel Ghenaiet

The space truss deployable antenna has low natural frequency, multi-closed-loop, and multiredundant structure characteristics, which is a kind of flexible antenna. It is hard to obtain the vibration characteristics under low frequency by finite element analysis or conventional shaking table test. To verify the structure characteristics of the antenna in the folded state below 2 Hz, a low-frequency vibration system is established based on the 6-DOF Stewart platform. Rotation matrix analysis method was adopted to obtain the platform's velocity and acceleration characteristics. Then, a low-frequency vibration test was carried out on the platform. The results show that the natural frequency of the antenna is 1.51 Hz and the maximum dynamic displacement is 140.6 mm, which provides a certain foundation for the further development of the space truss antenna.

1. Introduction

The space truss deployable antenna is a large-scale mesh deployable truss structure with high storage ratio and large deployment stiffness. The main structure is composed of multiple tetrahedral frame elements with energy storage springs. These basic tetrahedral retraction and deployment elements share nodes, and the retraction movement is associated to form a multi-closed-loop and multiredundant space structure [1–3]. The antenna is folded and fixed before launch, and the expansion is realized by a spring driving on the orbit to form a paraboloid. The antenna has good strength, stiffness, and high deployment reliability [4, 5]. It can flexibly construct the truss system by changing the number of basic truss elements or adopting different connection methods. Due to the stiffness characteristics of the structure and the freedom of the configurable truss structure, many research institutions have carried out relevant technical research at present [6–9].

Due to the limitation of rocket payload space, the large aperture antenna needs to be folded. The antenna must be able to withstand the vibration from the rocket or itself without damage during launch. The general method is to use the finite element analysis method or shaking table test to simulate the real vibration environment during transportation [10].

The truss antenna contains a large number of rods, ropes, and hinges, and its dynamic model is complex, which brings great challenges to the finite element solution [11]. At the same time, to reduce the weight of the antenna, the lightweight carbon fiber composite is usually used as the rod material, which will inevitably reduce the strength of the rod and make the flexibility of the antenna more obvious. The fundamental frequency of the antenna in the folded state is usually below 2 Hz. Therefore, the vibration test of the truss antenna puts forward higher requirements for the working frequency and output load of the shaking table.

Limited by the current low-frequency shaking table technology, the frequency range of the small shaking table is 2 ~ 10 kHz and that of the large shaking table is 5 ~ 2 kHz. Therefore, it is difficult to realize the low-frequency vibration assessment [12]. The Stewart platform is a spatial 6-

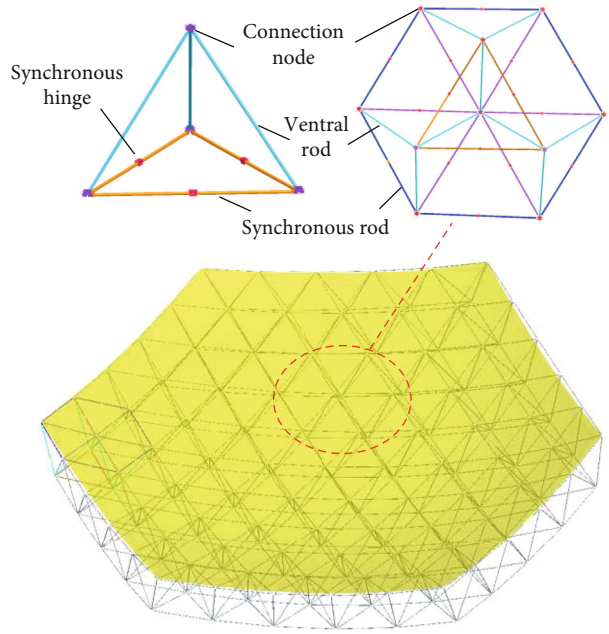

Figure 1: Frame units with tetrahedral element.

DOF parallel mechanism. By controlling the independent movement of six telescopic cylinders, it can simulate various attitude responses of the spacecraft during space flight, especially the low-frequency vibration during launch. It has become an important simulation test device for dynamic reliability research of aerospace equipment [13, 14].

In this paper, a low-frequency vibration characteristic test platform suitable for the space truss antenna is built based on Stewart platform, and relevant low-frequency tests are carried out to obtain the fundamental frequency and dynamic displacement in the stowed state, which provide a certain foundation for the further development of the space truss antenna.

2. Antenna's Structure Characteristics

The antenna is composed of reflector, truss, and a metal mesh. The reflector truss is composed of several frame units. Each unit adopts a tetrahedral element, which is composed of web members, folding rods, connection nodes, and torsion springs, as shown in Figure 1.

The three folding rods can be folded symmetrically around the middle, and the middle of each folding rod is provided with a hinge, which contains a spring. When the tetrahedron is folded, the spring element of the folding rod stores energy and acts as the driving force of the tetrahedron unit when it is deployed. The deployable state and fold state of the antenna are illustrated in Figure 2.

3. Kinematics Analysis of Stewart Platform

3.1. 6-DOF Stewart Platform. The 6-DOF Stewart parallel platform is mainly composed of the load platform, base platform, and six driving cylinders. Each driving cylinder is connected to the load platform and base platform, respectively,

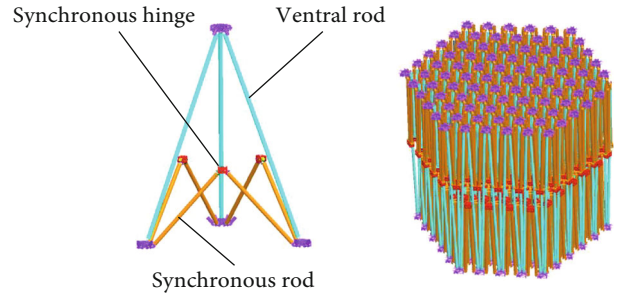

Figure 2: Fold state of the antenna.

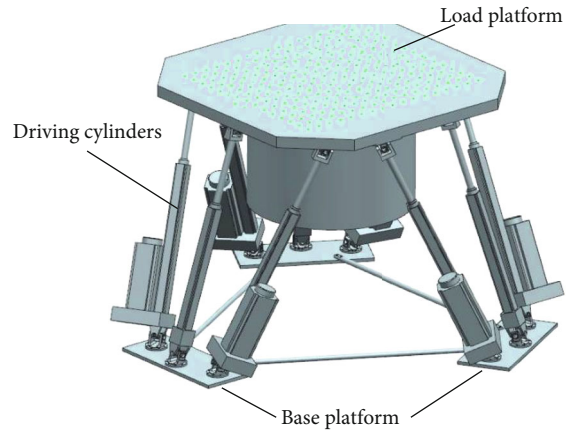

Figure 3: 6-DOF Stewart parallel platform.

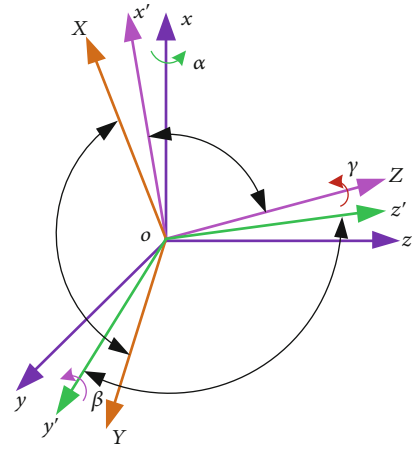

Figure 4: Cardan angle coordinate system schematic diagram.

by a hinge. According to different hinge modes, it can be divided into ball joint S-P-S (sphere joint-prismatic joint-sphere joint) type and universal joint U-P-S (universal joint-prismatic joint-sphere joint) type.

The working platform includes an upper platform, lower platform, load mounting plate, upper and lower connecting hinges, servo actuator, auxiliary cylinder, and base, as shown in Figure 3. The servo actuator is composed of an electric cylinder and motor. The servo actuator receives the control signal and works on the platform to make the upper platform realize longitudinal, heel, yaw, lifting, transverse, and

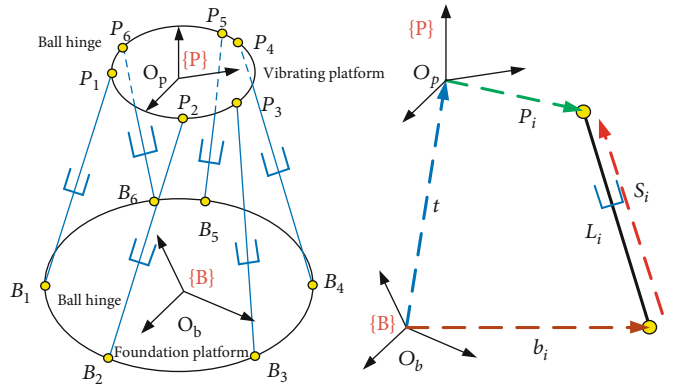

Figure 5: Coordinate system of Stewart platform.

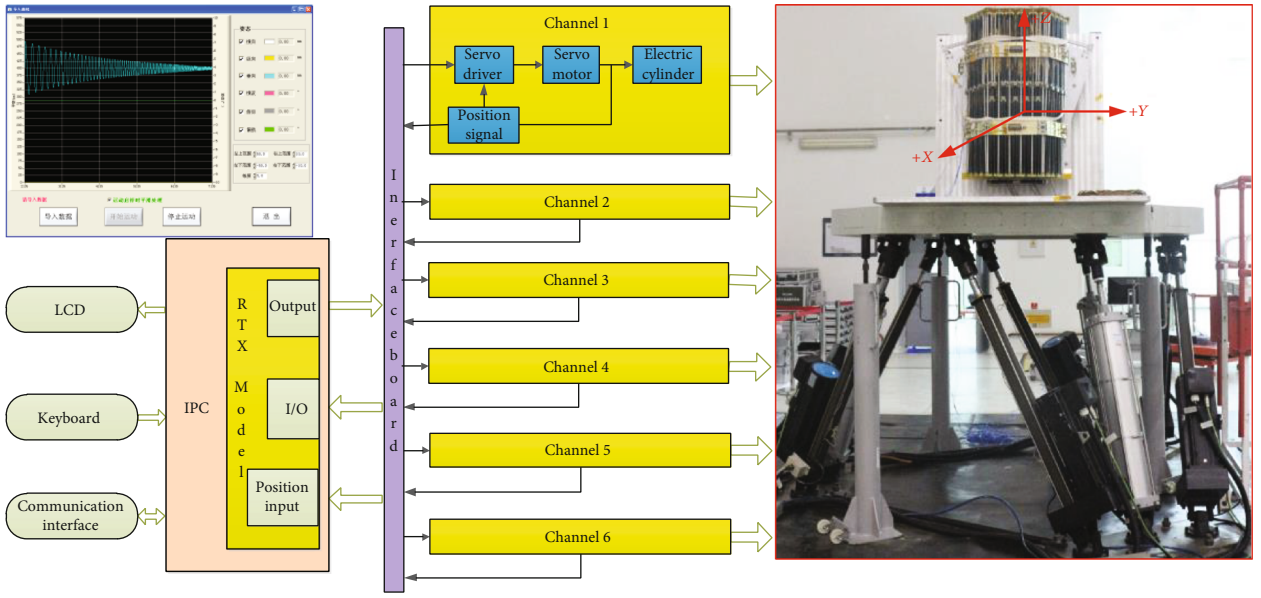

Figure 6: Experimental schematic diagram of Stewart platform.

lateral movement and drive the load to realize the simulated motion.

3.2. Rotation Matrix Method. The attitude description of Stewart platform generally adopts the multirigid body rotation coordinate method [15]. In this paper, the Cardan angular coordinate is adopted based on the Cartesian coordinate system, and three coordinate axes are selected in a certain order for three consecutive rotations.

The Cardan angular coordinates are shown in Figure 4. The coordinate system $o-xyz$ first rotates the angle α around the x-axis counterclockwise to $o-xy'z'$, then rotates the angle β around the y' axis to $o-x'y'Z$, and finally rotates the angle γ around the Z-axis to the position of the coordinate system $o-XYZ$. Each rotation relationship can be described by a matrix. From the coordinate system $o-xyz$ to the coordinate system $o-xy'z'$, the point P can be expressed as (y,z) in the coordinate system $o-XYZ$ and (y',z') in the coordinate system $o-xy'z'$. The relationship is expressed by the following equation.

$$y' = Y\cos\gamma - Z\sin\gamma, \tag{1}$$

$$z' = Y\sin\gamma + Z\cos\gamma. \tag{2}$$

In matrix form,

$$\begin{bmatrix} x \\ y \\ z \end{bmatrix} = \begin{bmatrix} 1 & 0 & 0 \\ 0 & \cos\alpha & -\sin\alpha \\ 0 & \sin\beta & \cos\alpha \end{bmatrix} \begin{bmatrix} x \\ y' \\ z' \end{bmatrix}. \tag{3}$$

Similarly,

$$\begin{bmatrix} x \\ y' \\ z' \end{bmatrix} = \begin{bmatrix} \cos\beta & 0 & \sin\beta \\ 0 & 1 & 0 \\ -\sin\beta & 0 & \cos\beta \end{bmatrix} \begin{bmatrix} x' \\ y' \\ Z \end{bmatrix}, \tag{4}$$

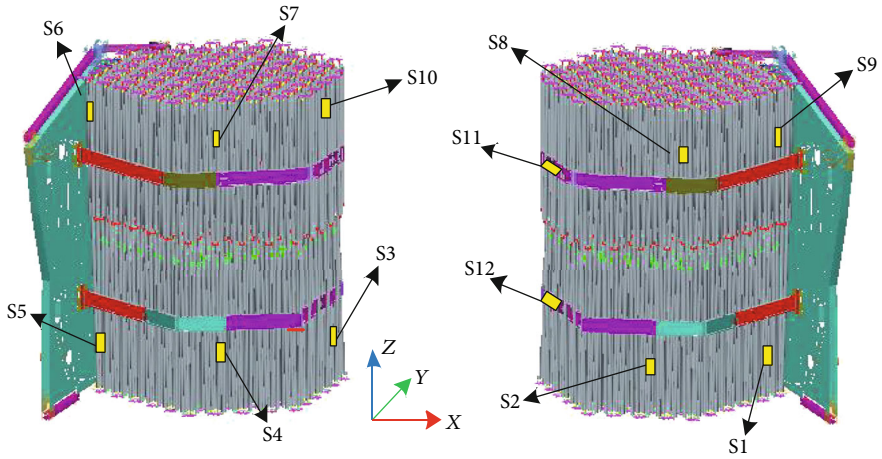

Figure 7: Measuring points on the antenna.

$$\begin{bmatrix} x' \\ y' \\ Z \end{bmatrix} = \begin{bmatrix} \cos\gamma & -\sin\gamma & 0 \\ \sin\gamma & \cos\gamma & 0 \\ 0 & 0 & 1 \end{bmatrix} \begin{bmatrix} X \\ Y \\ Z \end{bmatrix}. \quad (5)$$

Therefore,

$$\begin{bmatrix} x \\ Y \\ Z \end{bmatrix} = \begin{bmatrix} c\beta c\gamma & -c\beta s\gamma & s\beta \\ c\alpha s\gamma + s\alpha s\beta c\gamma & c\alpha c\gamma - s\alpha s\beta s\gamma & -s\alpha c\beta \\ s\alpha s\gamma - c\alpha s\beta c\gamma & s\alpha c\gamma + c\alpha d\beta d\gamma & c\alpha c\beta \end{bmatrix} \begin{bmatrix} X \\ Y \\ Z \end{bmatrix}, \quad (6)$$

where c represents cos () and s represents sin ().

Therefore, the vector between the coordinate system $o - XYZ$ and the coordinate system $o - xyz$ can be converted by the direction cosine matrix R, which can be expressed as

$$R = \begin{bmatrix} c\beta c\gamma & -c\beta s\gamma & s\beta \\ c\alpha s\gamma + s\alpha s\beta c\gamma & c\alpha c\gamma - s\alpha s\beta s\gamma & -s\alpha c\beta \\ s\alpha s\gamma - c\alpha s\beta c\gamma & s\alpha c\gamma + c\alpha d\beta d\gamma & c\alpha c\beta \end{bmatrix}. \quad (7)$$

3.3. Inverse Kinematics of Stewart Platform. To accurately control the position and attitude of Stewart platform, the six cylinders' length needs to be solved according to the predetermined position and attitude of the upper load platform, namely, three linear coordinate parameters (x, y, z) and three rotational coordinate parameters (α, β, γ).

Two reference points O_p and O_b, which are associated with the load platform and base platform, are selected to establish the Cartesian coordinate systems $\{P\}$ and $\{B\}$, respectively. The coordinate system $\{B\}$ is considered fixed, in which other coordinates can be represented expediently.

The vector from the origin point O_b of the coordinate system $\{B\}$ to the origin point O_p of the coordinate system $\{P\}$ can be represented as t, where $t = (x, y, z)$. The Cardan angle between $\{P\}$ and $\{B\}$ is θ, where $\theta = (\alpha, \beta, \gamma)$.

Table 1: Input conditions for low-frequency vibration test.

Direction	Frequency (Hz)	Magnitude
Z	0.4 ~ 1.8	0.04~0.45 g
	1.8 ~ 6	0.45 g
	6 ~ 8	0.45~0.65 g
X	0.4 ~ 2.1	0.1 ~ 0.33 g
	2.1 ~ 8 Hz	0.33 g
Y	0.8 ~ 5	0.2 g
Scanning rate	0.05 Hz/s	

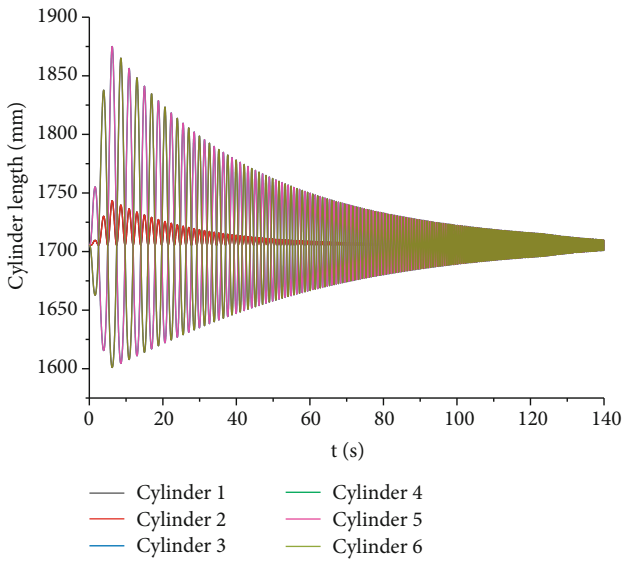

Figure 8: Motion curves of the six cylinders during the test in the X -direction.

It is assumed that the vector from O_p to the connection point between the load platform and each electric cylinder is P_i, the vector from O_b to the connection point between the base platform and each cylinder is b_i, and the vector of the connection points at both ends of the six cylinders is S_i,

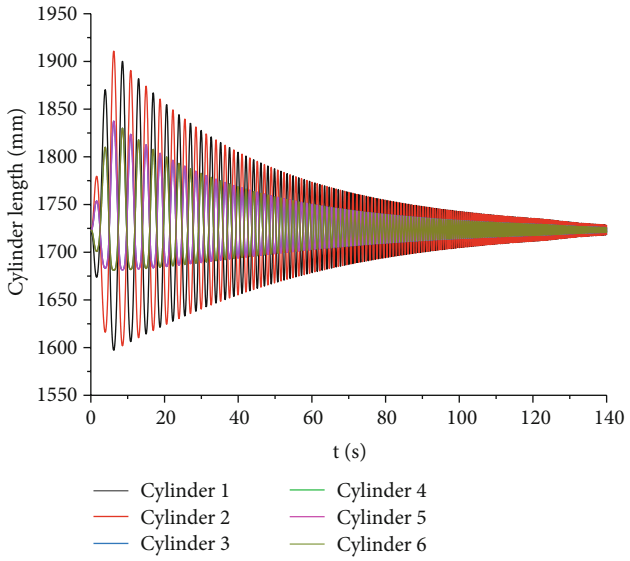

Figure 9: Motion curves of the six cylinders during the test in the Y -direction.

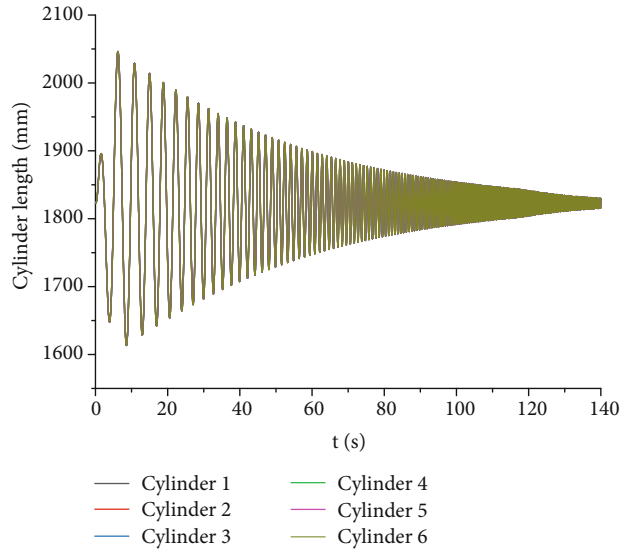

Figure 10: Motion curves of the six cylinders during the test in the Z-direction.

and the relation between the vectors above can be illustrated in Figure 5.

Then, the following formula can be obtained:

$$S_i = Rp_i + t - b_i, \tag{8}$$

where R is the rotating cosine matrix ($i = 1, 2, 3, 4, 5, 6$).

The length of electric cylinder is

$$L_i = \|S_i\| = \frac{(Rp_i + t - b_i)}{\|Rp_i + t - b_i\|} L_i = \|S_i\|. \tag{9}$$

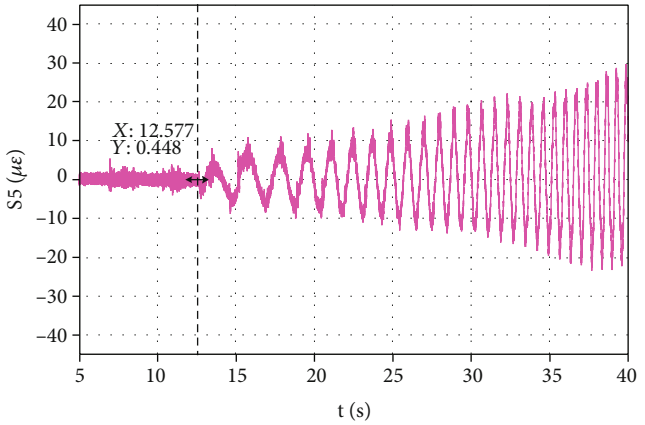

Figure 11: Response curve of point S5 in X-direction vibration.

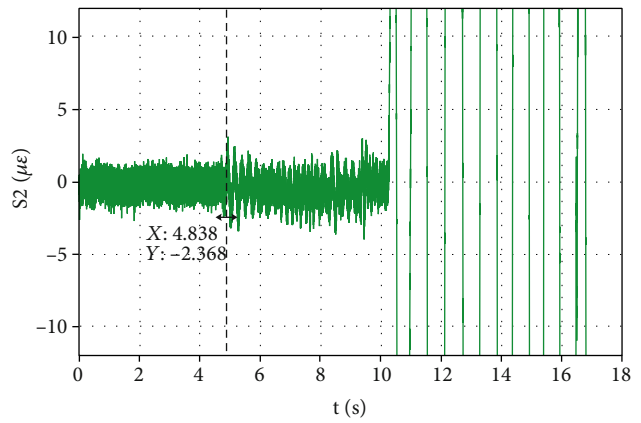

Figure 12: Response curve of point S2 in Y-direction vibration.

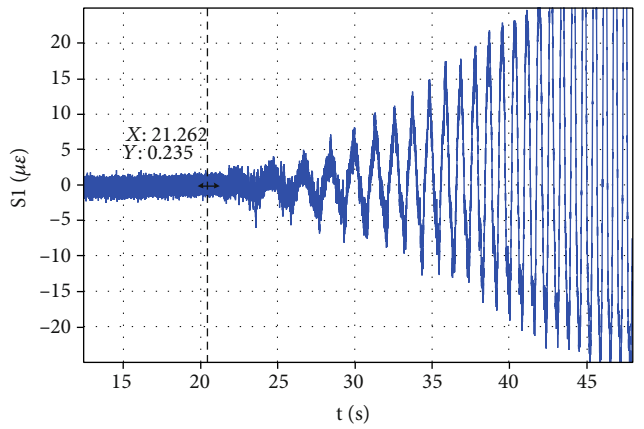

Figure 13: Response curve of point S1 in Z-direction vibration.

And the unit vector of S_i is

$$s_i = \frac{S_i}{\|S_i\|}. \tag{10}$$

The formula above establishes the relationship between the pose of the load platform and the cylinder, that is, the inverse kinematics of Stewart platform.

Table 2: Test result of each measuring point in X-direction.

Measuring point	X-direction Amplitude ($\mu\varepsilon$)		Time (s) Initial time	First peak time	Initial frequency (Hz)	Fundamental frequency (Hz)
S1	-50	42.9		91		
S2	-79.8	29.7		92.7		
S3	-104.1	54.6		74.8		
S4	-89	51		82		
S5	-82.3	86		80.3		
S6	-276	40	12.6	90	0.4	4.02
S7	-134	87		86		
S8	-75	137		100		
S9	-22	41		91.9		
S10	-157	344		85		
S11	-27	85		91.9		
S12	-29	46		92.6		
Dynamic displacement				dx: -8.2 ~ 8.75 mm; dy: -4.1 ~ 4.3 mm; dz: -61.8 ~ 64.3 mm		

Table 3: Test result of each measuring point in Y-direction.

Measuring point	Y-direction Amplitude ($\mu\varepsilon$)		Time (s) Initial time	First peak time	Initial frequency (Hz)	Fundamental frequency (Hz)
S1	-68.4	119		22.2		
S2	-46	20		22.9		
S3	-120	16		22.2		
S4	-110	22		22.9		
S5	-64	123		20.1		
S6	-179	102	9.8	21.3	0.8	1.51
S7	-439	38		24.0		
S8	-374	195		24.0		
S9	-9.6	148		23.3		
S10	-12	268		22.9		
S11	-9.6	40		22.2		
S12	-33.5	59		22.2		
Dynamic displacement				dx: -1.73~12.37 mm; dy: -140.6 ~ 117.1 mm; dz: -6.76~3.67 mm		

The Jacobian matrix is related to the cylinder extension velocity S_i and the velocity vector $\dot{\chi}$, and the attitude of the load platform is a function of $(x, y, z, \alpha, \beta, \gamma)$, then,

$$\begin{aligned} \omega &= \dot{\theta}, \\ v &= \dot{t}, \\ \dot{\chi} &= \left(v^T \omega^T\right)^T, \\ q_i &= R p_i. \end{aligned} \tag{11}$$

The sliding speed of each cylinder is

$$\dot{S}_i = s_i(v + \omega \times q_i) = \left(s_i^T (q_i \times s_i)^T\right) \begin{pmatrix} v \\ \omega \end{pmatrix} = J\dot{\chi}. \tag{12}$$

Then, the Jacobian matrix is

$$J = \left(s_i^T (q_i \times s_i)^T\right). \tag{13}$$

4. Low-Frequency Vibration Test

A low-frequency vibration test system based on 6-DOF Stewart platform is established as shown in Figure 6. In the system, the main function of the electrical control part is to receive the command data output by the control system and transmit it to the servo driver. The signal is amplified to control the motor movement, which will drive the electric cylinder to realize various postures of the platform.

In the test, the truss antenna is installed on the platform, and the vibration load acts on the platform along three mutually orthogonal directions, respectively. The measuring points on the structure are showed in Figure 7.

Table 4: Test result of each measuring point in Z-direction.

Measuring point	Z-direction Amplitude ($\mu\varepsilon$)		Time (s) Initial time	First peak time	Initial frequency (Hz)	Fundamental frequency (Hz)
S1	-29.7	33.5	21.31	87.4	0.4	4.02
S2	-45.7	42.6		110.6		
S3	-45.4	83.2		94.4		
S4	-129.4	161.7		88.4		
S5	-48.4	78.7		95.3		
S6	-365.1	255.7		93.7		
S7	-167	276.9		94.0		
S8	-298.2	98.8		93.6		
S9	-39.3	33.8		93.9		
S10	-109.7	215.9		93.8		
S11	-21.8	23.4		94.0		
S12	-47.2	17.3		93.9		
Dynamic displacement	dx: -8.7 ~ 9.25 mm; dy: -4.6 ~ 4.6 mm; dz: -62.4 ~ 65.1 mm					

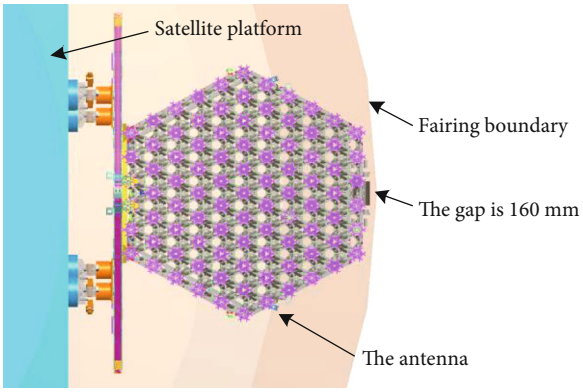

Figure 14: Installation status of antenna in the fairing.

The test conditions are determined as shown in Table 1. Moreover, a constant frequency vibration test was carried out at 1.5 Hz with 0.2 g load according to the actual needs.

Figures 8–10 show the motion curves of the six cylinders during the vibration test.

The following figures (Figures 11–13) show the response curve in each direction during the vibration, and the tables (Tables 2–4) give the maximum strain and dynamic displacement response and fundamental frequency information of the above main measuring points. The fundamental frequency information is obtained by time conversion, and the dynamic displacement is obtained by high-speed photogrammetry system, and the measurement accuracy is better than 0.1 mm.

According to the test results, the response in X-direction and Z-direction of the truss antenna is coupled, and the fundamental frequency is 4.02 Hz, while the fundamental frequency in Y-direction is the lowest, which is 1.51 Hz as shown in Figure 3 and Table 4. The maximum dynamic displacement of the antenna is 140.6 mm. Figure 14 shows the gap between the antenna and the fairing in a certain application, which is much greater than the dynamic displacement.

5. Conclusion

The truss deployable antenna has the remarkable characteristics of low fundamental frequency and flexible nonlinearity, which makes it difficult to use the conventional shaking table to investigate the vibration characteristics in the low frequency band. In this paper, a low-frequency test system based on 6-DOF Stewart parallel platform is established, and the structural characteristics of the antenna in the stowed state below 2 Hz are analyzed. It shows that the lowest fundamental frequency is 1.51 Hz in Y-direction and the dynamic displacement is 140.6 mm. The results are of great value to the further engineering application of the antenna.

Data Availability

The data that support the findings of this study are available from China Academy of Space Technology (Xi'an). Restrictions apply to the availability of these data, which were used under license for this study. Data are available from the authors with the permission of our constitution.

Conflicts of Interest

The authors declare that they have no conflicts of interest.

Acknowledgments

This work was supported by the National Natural Science Foundation of China (NNSFC) under Grant No. 11290154 and No. U1537213.

References

[1] X. Y. Chen and F. L. Guan, "A large deployable hexapod paraboloid antenna," *Journal of Astronautics*, vol. 22, no. 1, pp. 75–78, 2001.

[2] Z. R. Huang, Y. P. Song, and S. K. Zheng, "Analysis of configuration design and deployable coordination of offset—fed

truss reflector," *Mechanical Science and Technology for Aerospace Engineering*, vol. 11, pp. 1791–1796, 2016.

[3] R. Q. Liu, D. K. Tian, Z. Q. Deng, H. W. Guo, and Z. J. Liu, "Kinematics modeling and driving spring design of truss structure for deployable truss antenna," *Advanced Materials Research*, vol. 457, pp. 1337–1341, 2012.

[4] Z. H. Qi, J. H. Chang, and G. Wang, "Analysis and control of deployment process for hoop truss deployable antenna," *Journal of Astronautics*, vol. 35, no. 1, pp. 61–68, 2014.

[5] M. Akira, I. Hironori, and T. Akio, "Study on ground verification for large deployable modular structures," *Journal of Spacecraft & Rockets*, vol. 43, no. 4, pp. 780–787, 2006.

[6] J. W. Guo, Y. S. Zhao, X. D. Xun, and Y. J. Li, "Design and analysis of truss deployable antenna mechanism based on a novel symmetric hexagonal profile division method," *Chinese Journal of Aeronautics.*, vol. 34, no. 8, pp. 87–100, 2021.

[7] M. L. Zhao and F. L. Guan, "Kinematic analysis deployable toroidal spatial truss structures for large mesh antenna," *Journal Of The International Association For Shell And Spatial Structures*, vol. 46, no. 3, pp. 195–204, 2005.

[8] J. A. Fager, "Large space erectable antenna stiffness requirements," *Journal of Spacecraft & Rockets*, vol. 17, no. 2, pp. 86–93, 2015.

[9] Z. R. Huang, S. K. Zheng, J. L. Zhu, and C. Guo-Ding, "Design optimization of expansion driven components for the HJ-1-C satellite," *Journal of Radars*, vol. 3, no. 3, pp. 282–287, 2014.

[10] X. S. Jin, "The environmental testing of spacecrafes and its developing trends," *Spacecraft Environment Engineering*, vol. 19, pp. 12–18, 2002.

[11] F. Hu, Y. P. Song, S. K. Zheng, Z. Huang, and J. Zhu, "Advances and trends in space truss deployable antenna," *Journal of Astronautics*, vol. 39, no. 2, pp. 111–120, 2018.

[12] L. Liu, *Design and Development on Linear Vibratior with Low-Frequency of Aerospace Products Testing [M.S. thesis]*, Harbin Institute of Technology, Harbin, China, 2015.

[13] A. Preumont, M. Horodinca, I. Romanescu et al., "A six-axis single-stage active vibration isolator based on Stewart platform," *Journal of Sound and Vibration*, vol. 300, no. 3-5, pp. 644–661, 2007.

[14] D. Kamesh, R. Pandiyan, and A. Ghosal, "Modeling, design and analysis of low frequency platform for attenuating micro-vibration in spacecraft," *Journal of Sound and Vibration*, vol. 329, no. 17, pp. 3431–3450, 2010.

[15] C. Qian, E. Jia-qiang, L. Ming, D. Yuan-wang, and Z. Mao, "Vibration analysis of the dynamic model of Stewart platform with six degrees of freedom," *Journal of Hunan University (Natural Sciences)*, vol. 43, no. 2, pp. p36–p42, 2016.

Hindawi
International Journal of Aerospace Engineering
Volume 2022, Article ID 2164485, 13 pages
https://doi.org/10.1155/2022/2164485

Research Article

Thermal-Structural Analysis of the Support Structure for a Modular Space Deployable Antenna

Lu Jin,[1] **Feiyang Zhang**,[1] **Dake Tian**,[2] **Qinghe Wang**,[1] **and Quanyu Cao**[1]

[1]*School of Civil Engineering, Shenyang Jianzhu University, Shenyang 110168, China*
[2]*School of Mechanical Engineering, Shenyang Jianzhu University, Shenyang 110168, China*

Correspondence should be addressed to Dake Tian; tiandake@sjzu.edu.cn

Received 10 February 2022; Revised 18 April 2022; Accepted 21 April 2022; Published 3 June 2022

Academic Editor: Tuanjie Li

A modular space deployable antenna has the advantages of extensibility, adaptability, and versatility, which is an ideal structure to meet the development trend of large aperture, high precision, and light weight for the deployable antenna in the future. To date, there are few reports on the temperature response of a modular deployable antenna in the thermal alternating environment in orbit. The aim of this study is at investigating the influence of a modular deployable antenna support structure on the surface accuracy and stability under the space thermal alternating environment. For this purpose, the thermal-structure analysis of the deployable antenna support structure was carried out by ANSYS APDL finite-element software. Using the transient temperature field obtained by thermal analysis as the boundary condition, the coupling law of stress development and thermal deformation of the support chord and cable caused by the antenna structure constraint position and other parameters is analyzed. In a uniform thermal field, the thermal stress of cables in the central module of the structure is the highest and that of the chord components in the same-circle modules is essentially the same. The thermally stress of the upper chords increases progressively toward the outer module, whereas that of cables decreases in the same direction. The thermal deformation at the upper-layer centroid of the structure can reach about 15 mm, so the influence on the accuracy of the antenna cannot be ignored. When the splicing vertical rod of adjacent modules in the outermost of the support structure is taken as the constraint connecting with the extension arm, the thermal deformation of the structure is minimum. The heat-insulating composite coating should be adopted on the surface of the antenna structure to reduce the thermal deformation and improve the adaptability. The thermal-structural analysis model proposed in this study could accurately estimate the behaviour of thermal deformation for the modular space deployable antenna, but the further coupling condition of the nonuniform temperature field could still be conducted. The results can provide a reference for the basic theory and engineering application of thermal-structural analysis for extralarge-aperture modular deployable antennas in the future.

1. Introduction

The deployable antenna plays an important role in the transmission and acquisition of information in the aerospace and defence fields. This new type of space deployable structure is the product of the rapid development of aerospace science and technology over the past two to three decades [1, 2]. Deployable antennas have already been widely applied in various fields, including space communications, military reconnaissance, earth observation, and satellite navigation [3–6]. Given the increasing demand for a precise satellite service in deep space exploration, the thermal response of the deployable antenna support structure to the harsh space environment has become important considerably. As a satellite moves in an orbit, the support structure of a deployable antenna is subject to thermodynamic issues induced by solar radiation, such as vibration and the resulting stress and deformation [7–9]. Especially for large-aperture modular deployable antenna, these problems occur most commonly when the antenna passes through the Earth's shadow.

Thermally induced vibrations were first theoretically predicted by Boley [10], who also established a basis for vibration parameter determination. In the decades that followed, the subject of thermally induced structural response attracted

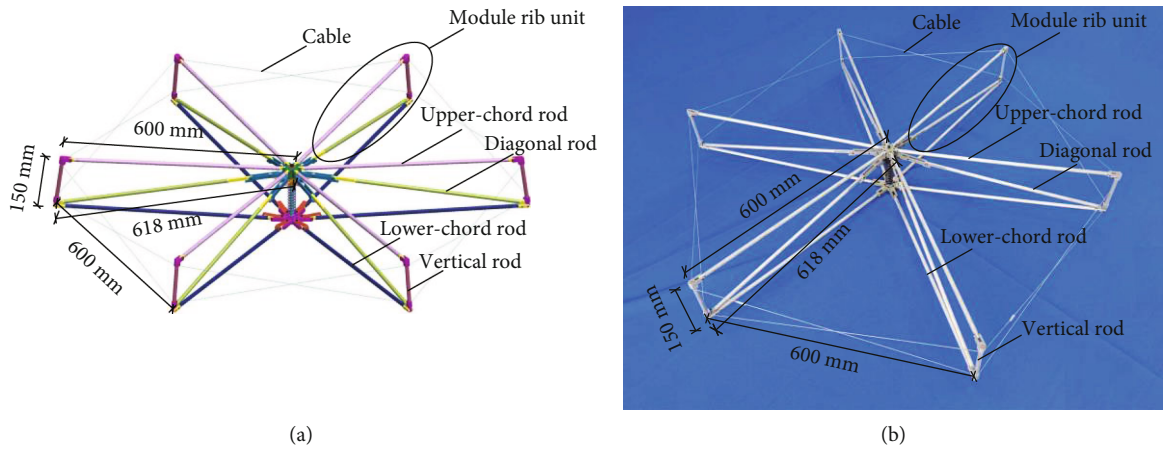

Figure 1: A single module. (a) The three-dimensional prototype. (b) The single-module prototype.

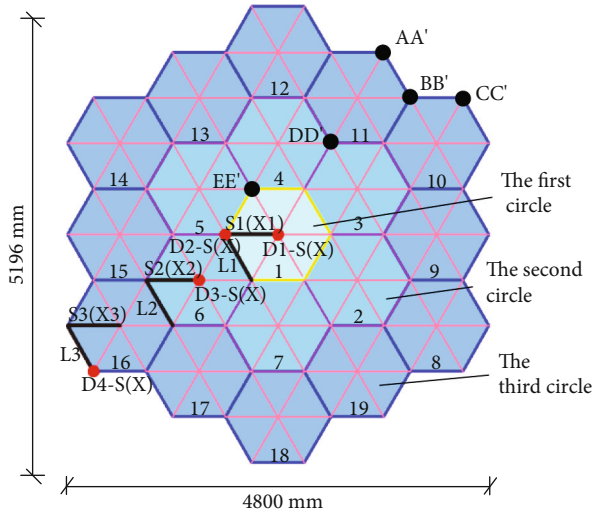

Figure 2: Module arrangement with the marked points and rods.

attention from scholars and researchers worldwide. For example, by analyzing bending vibrations of the Hubble Space Telescope solar arrays, Thornton and Kim [11] determined the coupling between the dynamic response of the structure and transient temperature field and the basis is established for determining the stability of bending vibrations. Namburu and Tamma [12] reported that there are significant differences between the dynamic response of deployable members under the action of general linear thermal effects and those under nonlinear thermal effects. Johnston and Thornton [13] examined spacecraft attitude disturbances resulting from thermally induced deformations of flexible appendages and determined that the attitude response of the system is related to the ratio of the thermal and structural response times of flexible appendages. Zhang [14] conducted temperature field analysis, thermal stress analysis, and structural deformation simulation analysis for a deployable parabolic antenna with a 5 m diameter. Ding and Xue [15] used the Fourier-finite-element method to simulate the thermal response of aerospace structures with thin-walled tubular components in the transient temperature field and thereby provided an effective method for analyzing the transient temperature field and thermal deformation of the complex aerospace structure. Rodriguez et al. [16] developed the thermocryogenic technology for the thermocryogenic system of the tropospheric emission spectrometer, and this in turn maximised the overall performance of the instrument. Fan et al. [17] studied the thermal-dynamic coupling of the in-orbit structure with flexible appendages using a modified Lagrange-finite-element method. Liu et al. [18] conducted a study on thermally induced vibrations of a deployable rib antenna using the finite-element method and showed that thermal vibrations affect the surface accuracy of the antenna structure. Abbas et al. [19] developed a three-dimensional rectangular plate element with variable thicknesses for panels of re-entry vehicles, which is exposed to a severe thermal environment under a supersonic flow condition. Sun [20] simulated and analyzed the structural strength and dynamic properties of a deployable spiral antenna in the extreme thermal environment of space and thereby provided a guiding reference for the antenna structure design. Yun and Yuan [21] conducted thermal-structural analysis of a deployable hoop antenna, and it is demonstrated that when passing through the Earth's shadow in orbit, the antenna structure is subjected to significant overall structural deformation in a nonuniform temperature field. Wu et al. [22] conducted thermal-structural analysis of a deployable hoop antenna and determined that the temperature field significantly impacts an antenna's surface tension and shape accuracy. In summary, the thermal-structural coupling response of large-aperture space deployable antenna structures cannot be neglected because it considerably impacts the vibration and deformation of the antenna surface [23, 24].

Furthermore, large aperture, high precision, and light weight have become the trend of antenna development. The modular space deployable antenna studied in this paper is a new kind of space structure with great development potential and value, which meets the development trend of large aperture and high precision of the antenna. Based on the topological theory, the modular element can meet the development trend and requirements of 100-meter aperture of the antenna in the future. For the extralarge-aperture antenna, dense rods and shadow occlusion of extralarge-aperture mesh are

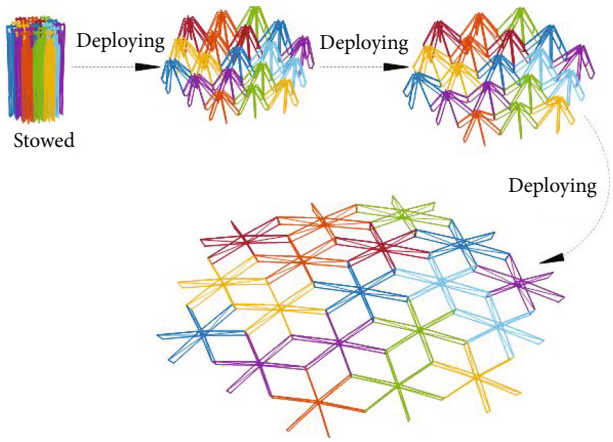

Figure 3: The deployment process of 3-circle 19-module antenna support structure (without cables).

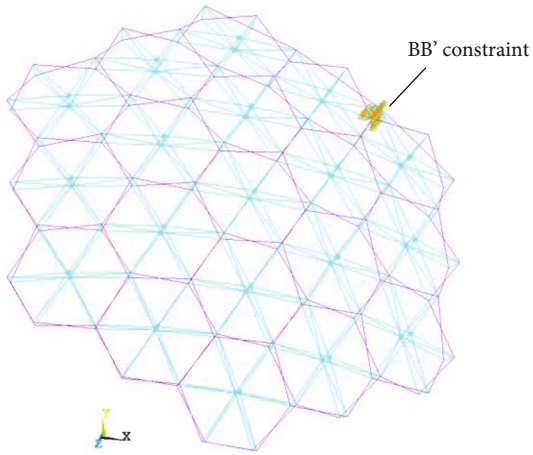

Figure 4: FEM of the modular deployable antenna.

Table 1: Thermophysical parameters of antenna materials.

Material property	Aluminum alloy	Steel cable
Elastic modulus: E (GPa)	70	150
Poisson ratio: μ	0.31	0.3
Density: ρ (kg/m^3)	2840	7850
Thermal conductivity: k (W/m/K)	195	49.8
Specific heat capacity: c (J/kg)	924	465
Thermal expansion coefficient: α (K^{-1})	2.2×10^{-5}	1.2×10^{-5}
Emissivity: ε	0.6	0.26
Radiation absorptivity: ε_1	0.9	0.9

obvious. The thermal-induced deformation and thermal-induced vibration pose more significant threat to the performance of the antenna in orbit. It will also restrict its future application. However, there is a paucity of analytical studies in this area and only fewer cases have been applied in orbit.

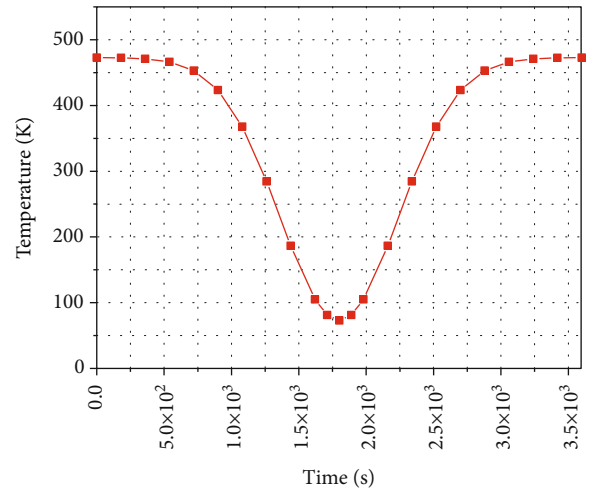

Figure 5: Temperature distribution of the transient temperature field.

In this study, thermal-structural analysis of a modular space deployable antenna in the transient thermal field is analyzed, whose basic configuration is composed of 19 hexagonal modules with a diameter of 5 meters. Furthermore, the thermally induced stress of different rod and cable elements of the support structure and the deformation of the key points include the centroid point and the farthest point away from structural constraint is considered. The trends of thermally induced overall deformation are compared for different constraint positions of the antenna structure to provide a basis for selecting the safest and most optimal design for the support structure for the modular space deployable antenna. In addition, the research results can provide a reference for the basic theory and engineering application of thermal-structural analysis for extralarge-aperture modular deployable antennas in the future.

2. Finite-Element Model and Validation

2.1. Structure of the Modular Deployable Antenna. The antenna structure is a support back frame after the deployment and locking of the space deployable antenna, which is composed of a plurality of hexagonal modules arranged topologically according to the accuracy of the antenna network [25, 26]. Firstly, a rib unit is composed of upper chord and lower chord rods, a diagonal web rod, and a vertical rod and the length of the upper and lower chord rods is 600 mm, the length of the diagonal web rod is 618 mm, and the length of the vertical rod is 150 mm; then, a single-hexagon module with a side length of 600 mm is composed of six rib units and a cable (Figure 1). Figure 1(a) is the three-dimensional prototype of a single module, and Figure 1(b) is the single-module prototype.

The single-module topology forms a 3-circle 19-module antenna structure with a size of 4800 mm × 5196 mm (Figure 2). The topological positions, number of circles, and marking points of each module are shown in Figure 2.

Table 2: Statistical analysis of thermal stress and deformations.

Time (s)	Maximum deformation (mm)	Deformation at the upper centroid (mm)	Maximum stress of chord rod (MPa)	Maximum stress of cable (MPa)	Maximum stress of constraint (MPa)
1	32.05	13.15	50.67	47.94	3.94
180	32.00	13.12	50.56	47.83	3.93
360	31.75	13.02	50.17	47.46	3.9
540	30.90	12.66	48.81	46.18	3.8
720	28.54	11.71	45.12	42.7	3.51
900	23.25	9.53	36.76	34.79	2.85
1080	13.37	5.48	21.13	20.01	1.63
1260	−1.51	−0.62	−2.38	−2.26	−0.18
1440	−18.97	−7.74	−29.94	−28.42	−2.30
1620	−33.02	−13.45	−52.90	−50.30	−4.05
1710	−37.44	−15.26	−59.53	−56.54	−4.56
1800	−39.02	−15.91	−61.92	−58.84	−4.72
1915	−37.44	−14.77	−59.53	−56.54	−4.56
1980	−33.02	−13.45	−52.90	−50.30	−4.05
2160	−18.97	−7.74	−29.94	−28.42	−2.30
2340	−1.51	−0.62	−2.38	−226	−0.18
2520	13.37	5.48	21.13	20.01	1.63
2700	23.25	9.53	36.76	34.79	2.85
2880	28.54	11.71	45.12	42.7	3.51
3060	30.90	12.66	48.81	46.18	3.8
3240	31.75	13.02	50.17	47.46	3.9
3420	32.00	13.12	50.56	47.83	3.93
3600	32.05	13.15	50.67	47.94	3.94

As shown in Figure 2, there is 1 module in the first circle and there are 6 and 12 modules in the second and third circles, respectively. AA′, BB′, CC′, DD′, and EE′ represent the position of splicing vertical rods, S1 represents the no. 1 upper chord, X1 represents the no. 1 lower chord, L1 represents the no. 1 cable, and D1-S and D1-X represent the no. 1 point of the upper layer and lower layer, respectively.

Figure 3 shows the expansion process of a 3-circle 19-module support structure from a folded state to a deployed state. After expansion, its total size is 4800 mm × 5196 mm, in which the upper chord forms an inner concave surface and the lower chord forms an outer convex surface. The model is based on the principle prototype in the previous work. The geometry size of the antenna structure is 1 : 1 restored, and the appearance design of the deployable antenna is basically consistent with the actual structure. The main structure of the principle prototype is made of aluminum alloy, and the theoretical and experimental research on the unfolding function, unfolding characteristics, unfolding accuracy, and dynamics characteristics has been completed. In the model of Figure 3, all rod members of the structure are 2A12 aluminum alloy hollow round rods, the vertical rod outer diameter is 12 mm, and the inner diameter is 10 mm. The outer diameter of the upper and lower chords and inclined rods is 10 mm and the inner diameter is 8 mm. The cable is a steel wire cable whose diameter is 1 mm.

2.2. Model Establishment. APDL was used to build the finite-element model of the modular deployable antenna as shown in Figure 4. In the thermal stress analysis, the displacement and rotation angles of the vertical rod BB′ connecting two outermost modules are constrained because this component is connected to the deployment arm of the satellite antenna. After deployment, the overall stability of the support structure is maintained via tension cables and rigidly connected rods; the cable applied 200 N preload. The thermophysical parameters of the antenna materials are shown in Table 1.

3. Transient Thermal Analysis

3.1. Theoretical Basis of Temperature Field Analysis. The temperature field is closely related to the geometry of the structure. Based on the principle of heat transfer theory, the governing differential equation of heat conduction of the three-dimensional object can be written as [27]

$$\frac{\partial}{\partial x}\left(k_x \frac{\partial T}{\partial x}\right) + \frac{\partial}{\partial y}\left(k_y \frac{\partial T}{\partial y}\right) + \frac{\partial}{\partial z}\left(k_z \frac{\partial T}{\partial z}\right) = \rho c \frac{\partial T}{\partial t}, \quad (1)$$

where k_x, k_y, and k_z are the coefficients of thermal conductivity of rod elements in x, y, and z directions in space; ρ denotes the density of the material; c denotes the specific heat capacity of the material.

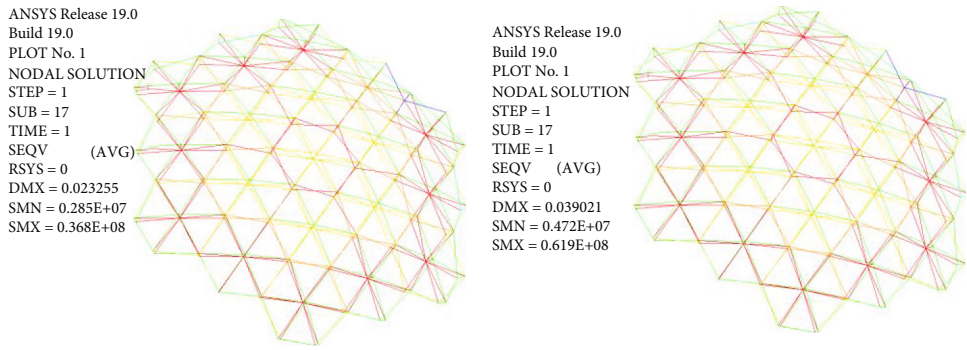

(a) (b)

Figure 6: Thermal stress distribution. (a) $t_1 = 900$ s. (b) $t_2 = 1800$ s.

The radiation boundary condition is assumed as follows:

$$-\left(k_x \frac{\partial T}{\partial x} n_x + k_y \frac{\partial T}{\partial y} n_y + k_z \frac{\partial T}{\partial z} n_z\right) = aXT^4 - Tq_r.. \quad (2)$$

The initial condition is as follows:

$$T(x, y, z)_{t=0} = T_0, \quad (3)$$

where n_x, n_y, and n_z are the direction cosines of the outer normal of rod elements in three directions, a denotes the Stefan Boltzmann constant ($5.67 \times 10^{-8}\text{W/m}^2/\text{K}^4$), X denotes the coefficient of blackness, T denotes the structure of temperature, q_r denotes the radiant heat flow density per unit area, and T_0 denotes the initial temperature of structure.

According to the Galerkin method, it can be deduced in formulas (1)–(3) as follows:

$$[C]^e \frac{\partial}{\partial t}\{T(t)\}^e + ([K_k]^e + [K_r]^e)\{T(t)\}^e = \{F_r\}^e, \quad (4)$$

where $[C]^e$ denotes the heat capacity matrix of the structural element, $[K_k]^e$ denotes the heat transfer matrix of the structural element, $[K_r]^e$ denotes the thermal radiation matrix of the structural element, and $\{F_r\}^e$ denotes the thermal load vector of the structural element.

Then, the temperature field calculation equation of the structure at t moment can be obtained:

$$\left(\frac{[C]}{\Delta t} + [K_k + K_r]\right)\{T(t)\}_t = \{F_r\} + \frac{[C]}{\Delta t}\{T(t)\}_{t-\Delta t}, \quad (5)$$

where Δt denotes the time step.

Basing on the abovementioned temperature field solution and the working environment in orbit, the calculation of the thermal analysis model of the antenna structure is simplified and assumed, so that the thermal analysis and the thermal-structural coupling analysis are more suitable for the practical engineering application of the antenna in orbit.

To simplify the thermal-structural analysis, the following basic assumptions are adopted:

(a) The antenna enters and leaves the Earth's shadow area for 1 h, i.e., 3600 s

(b) The temperature change of the antenna structure in the radiant during 3600 s is within the range 73.15 K~473.15 K

(c) The effect of shadow occlusion is not considered so that each element of the antenna support structure receives the same amount of radiation in each period

The fit curve of the temperature change during the time when the antenna moves in and out the Earth's shadow is used to obtain the temperature change function as follows:

$$T(t) = T_0 - T_S \times e^{-0.5\times((t-t_c)/\tau)^2}, \quad (6)$$

where T_S denotes the magnitude of temperature change, t_c denotes the experience time of entering the shadow area fully, $t_c = 1800$ s, τ denotes the characteristic time for thermal response, and $\tau = 440.2$ s [28].

3.2. Thermal Analysis. Based on the aforementioned assumptions, in the thermal analysis of the antenna structure using APDL, LINK33 is used to simulate the temperature element of chord rods and cables and MASS71 is used to simulate concentrated mass components. Figure 5 shows the temperature distribution curve of the deployable antenna obtained using the FEM simulation in the transient temperature field. When the metal mesh surface of the antenna is not considered, the shadow occlusion effect is not obvious. Therefore, the shadow occlusion is not considered in the thermal analysis for the support structure in this paper and the temperature field distribution of the whole antenna structure is uniform at each moment and the temperature of each rod of the whole antenna structure is the same. For example, at $t_1 = 900$ s and $t_2 = 1800$, the overall temperatures of the structure are 423.517 K and 73.168 K, respectively.

It can be seen in Figure 5 that the temperature decreases slowly when the antenna begins to pass through the Earth's

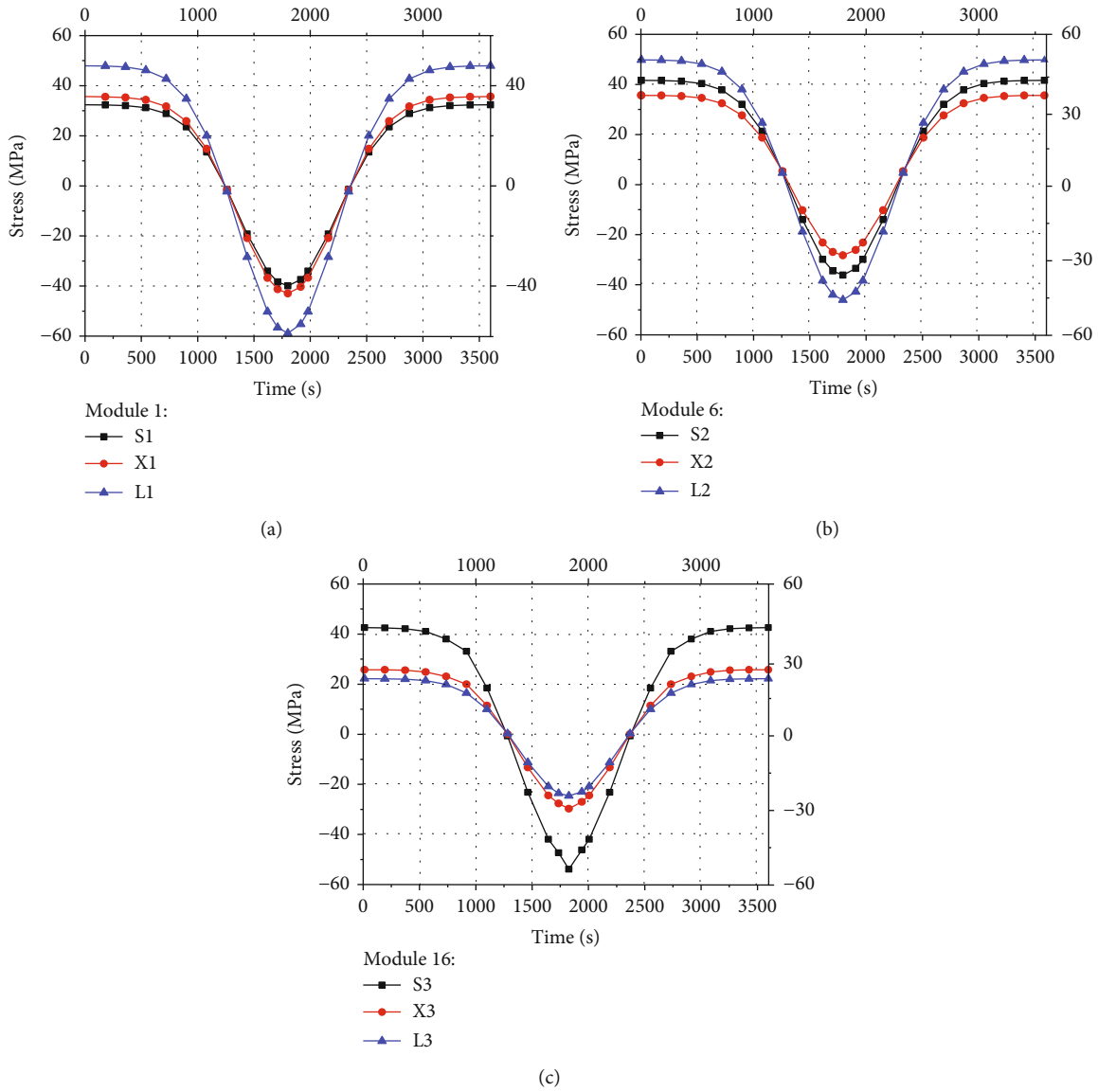

Figure 7: The thermal stress distribution of different rods in the same module. (a) Module 1. (b) Module 6. (c) Module 16.

shadow at 0~900 s. After the antenna has entered the shadow area completely, the temperature decreases rapidly. At 1800 s, the antenna structure begins to come out of the shadow area, the temperature of each chord changed contrary to the process of entering the shadow area. Finally, the antenna structure returns to its original temperature at 3600 s. The thermal analysis results are used as the basis for the thermal-structural analysis.

4. Thermal-Structural Analysis of the Antenna Structure

4.1. Model Overview. The ANASY finite-element analysis software is used to analyze the thermal-structural model of the modular support structure including the stress development and development-time history in the transient temperature field. The transient temperature field obtained in Section 3.2 is used as the temperature boundary conditions for the thermal-structural analysis of the antenna, and the temperature elements (LINK33) are converted into structural elements (LINK180). When the antenna is deployed in the orbit, one vertical rod is attached to the deployment boom of the satellite antenna. In Figure 4, the vertical rod BB' is used as the fulcrum of the expansion where the modular structure begins to unfold. Hence, its rotational angle and displacement in the x, y, and z directions are constrained. It is assumed that the thermal expansion coefficient of the structural elements does not change with the change in the temperature field, i.e., the stress and displacement of the antenna structure at 273.15 K are equivalent to 0. The thermophysical properties of the structural elements are listed in Table 1.

4.2. Thermal Stress Analysis. Indirect thermal stress analysis was carried out, and the obtained transient temperature field was applied to the structural stress analysis as the basic load. The maximum thermal stress variation of the components

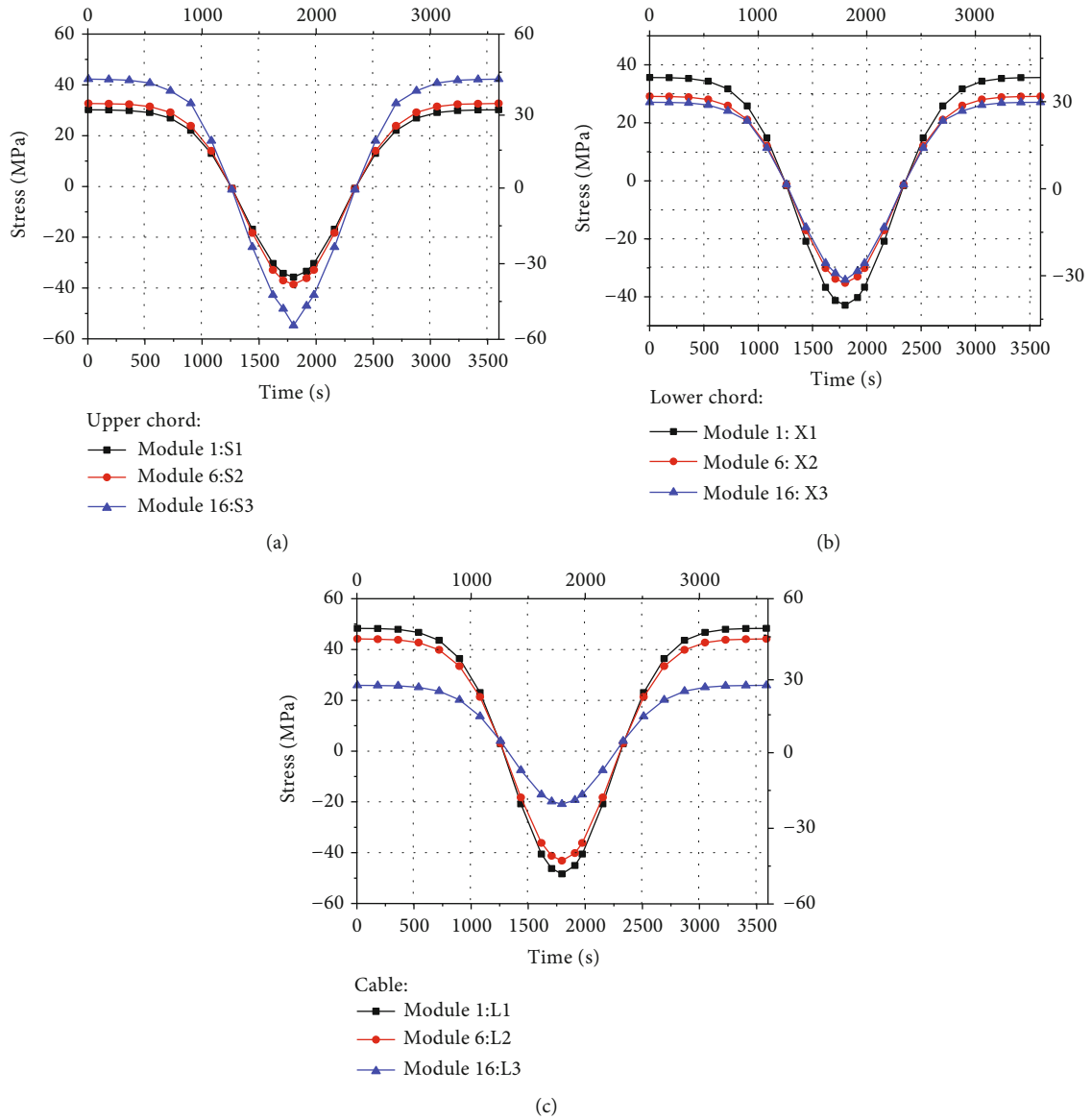

Figure 8: Thermal stress distribution of the rods in different modules. (a) Upper chord. (b) Lower chord. (c) Cable.

and the deformation trend of the centroid and edge of structure were obtained, and the statistics were shown in Table 2. It can be seen in Table 2 that the maximum normal stress of the chord at each time occurs at the 12th module and the minimum stress occurs at the vertical rod BB′. The maximum stress of the cable occurs at the first module of the structure. The maximum cumulative deformation of the antenna occurs at the point D4-X where it is the farthest point away from the constraint BB′, and the deformation is within the range of 32.05 mm~−39.02 mm. The deformation at the upper centroid point D1-S is within the range of 13.15 mm~−15.91 mm. So, it is gained that the effect of thermal deformation of the structural centroid on the antenna surface accuracy cannot be ignored.

The deformation and stress changes of the structure are consistent with the transient temperature field curve. At both 1 s and 3600 s moment, the maximum normal stress of the chord is 50.67 MPa and that of the cable is 47.94 MPa. In the meantime, the maximum deformation at D4-X is 32.05 mm. The deformation and stress of the antenna structure are very small at 1260 s and 2340 s, and the temperature is 293.15 K. At 1800 s, the maximum negative stress of the chord rod in the 12th module is −61.92 MPa and that of cable L1 in the central module is −58.84 MPa and the cold shrinkage deformation is −39.02 mm at this moment. However, compared to other rods, the thermal stress of the vertical rod at constraint BB′ is negligible. At each time, the maximum stress of the chord in the 12th module is about 5.23% greater than the average stress of the cable in the central module, indicating that the chord is subjected to greater stress than the cable in the transient temperature field.

Next, the transient temperature field at $t_1 = 900$ s and $t_2 = 1800$ s is used to analyze the thermally induced stress in different modules and the deformation of the antenna structure.

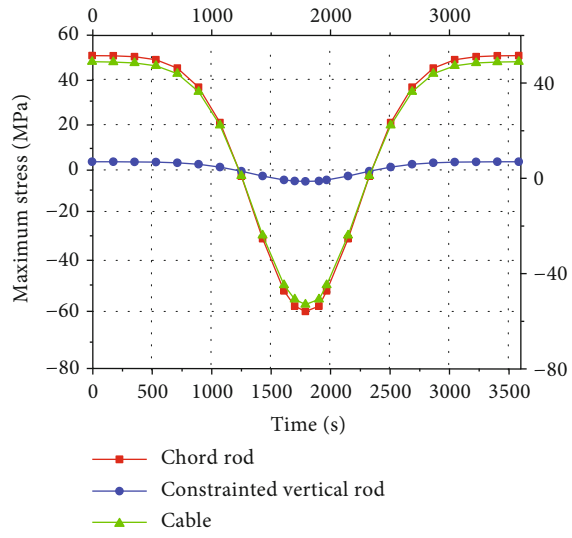

Figure 9: Time history of the maximum thermal stress.

Figure 6 shows the thermal stress distribution of each module of the antenna structure. It can be seen in Figure 6 that the stress distribution trend of the support structure is basically the same at each moment. In the central module, the cable stress is the largest, followed by the lower chord stress, and the upper chord stress is the least. In the second-circle module, the 6th module is taken as an example, the cable stress is the largest, followed by the upper chord stress, and the lower chord stress is the least. In the 16th module of the third circle, the stress of the upper chord is the largest, that of the lower chord is smaller, and the cable stress is the least. In addition, with the increase of circle, the stress of chord rod increases and the cable stress decreases gradually.

In order to further explain the stress development of structural component rods, the upper chord, lower chord, and cable stress of the 1st, 6th, and 16th modules were extracted and compared. Figure 7 shows the thermal stress distribution of the different component rods in the same module, and that of the same component in the different modules is shown in Figure 8.

In Figure 7, the thermal stress of upper chord S1 in the first module is 8.87% smaller than that of lower chord X1. In the 6th module that belongs to the second circle, the stress of upper chord S2 exceeds that of lower chord X2 by 17.3%. The cable thermal stress is the biggest in the 1st and 6th modules, the thermal stress of chord S1 is smaller than that of lower chord X1, and upper chord S2 in the 6th module is bigger than lower chord X2. In the 16th module, the thermal stress of cable L3 is the smallest and the maximum stress of upper chord S3 is bigger than that of L3 about 52.27%.

Figure 8 shows the comparison of the same component's thermal stress in the 1st, 6thm and 16th modules of the antenna structure, and the thermal stress of upper chord S1 decreases by 7.72% and 33.22% compared with that of upper chord S2 and S3, while the thermal stress of lower chord X1 increases by 22.43% and 24.97% compared with that of X2 and X3, respectively. The thermal stress of cable L3 is 46.58% and 51.42% lower than that of cable L2 and L1. Additionally, it was determined that the stress of the upper chord components increases gradually with each circle modules, whereas the stress of the cables gradually decreases.

The time history of the maximum thermal stress in the different components is shown in Figure 9. It is evident that the lowest of stress occurs in the constrained vertical rod at any moment. Moreover, the maximum stress trends for different components are consistent with the transient temperature field. Specifically, when the antenna structure begins to pass through the Earth's shadow at about $t_1 = 900$ s, its thermal stress decreases by approximately 27.45%. The maximum negative stress occurs at $t_2 = 1800$ s; at this moment, the antenna is passing through the Earth's shadow. After 1800 s, the thermal stress begins to increase again and mirrors the decreasing temperature trend before $t_2 = 1800$ s until the antenna has passed the shadow area completely.

The deformation curves of the key positions such as the vertical rod BB′, the centroid point D1-S(X), and the farthest point D4-S(X) from the constraint are shown in Figure 10. It can be seen that during the time from 0 s to 1260 s and 2360 s to 3600 s, the structure is in the thermal expansion and elongation stage, and in the middle period from 1260 s to 2360 s, the structure has cold contraction deformations. There is almost no deformation at the restraint vertical rod BB′. The deformation trend at the positions D4-S(X) and D1-S(X) is consistent with the time. The deformations of the upper and lower key points are not different significantly, and the accumulated deformation at D4-X is the largest. The deformation at the upper centroid point D1-S varies in the range 13.15 mm~−15.91 mm, where it is the most important factor affecting the accuracy of the antenna surface. Therefore, the influence of centroid point deformation on the accuracy of the antenna surface should be further studied.

The overall deformation of the structure at typical moment $t_1 = 900$ s and $t_2 = 1800$ s is shown in Figure 11. It is obvious that the further point away from the constraint, the greater the total cumulative deformation of the structure at this point and the maximum deformation of the antenna structure occurs at point D4-S(X) which is farthest from the constraint.

The aforementioned analysis shows that the antenna structure undergoes thermal expansion and contraction in the transient temperature field. In the first module, the stress in the upper chord and lower chord rods does not significantly change because of the action of the tension cables. However, in the second-circle and third-circle modules, the upper chord components expand and contract more than the lower chord because the cables inside the parabolic support structure undergo higher tension due to temperature variations in the transient temperature field. Consequently, the thermal stress in the upper chord components is higher. The highest thermal stress occurs in the third-circle modules. Therefore, the deformations of the farthest point from the constraint and the centroid point of structure cannot be ignored.

4.3. Thermal Analysis of Structures with Different Constraints. This section elucidates the effect of the

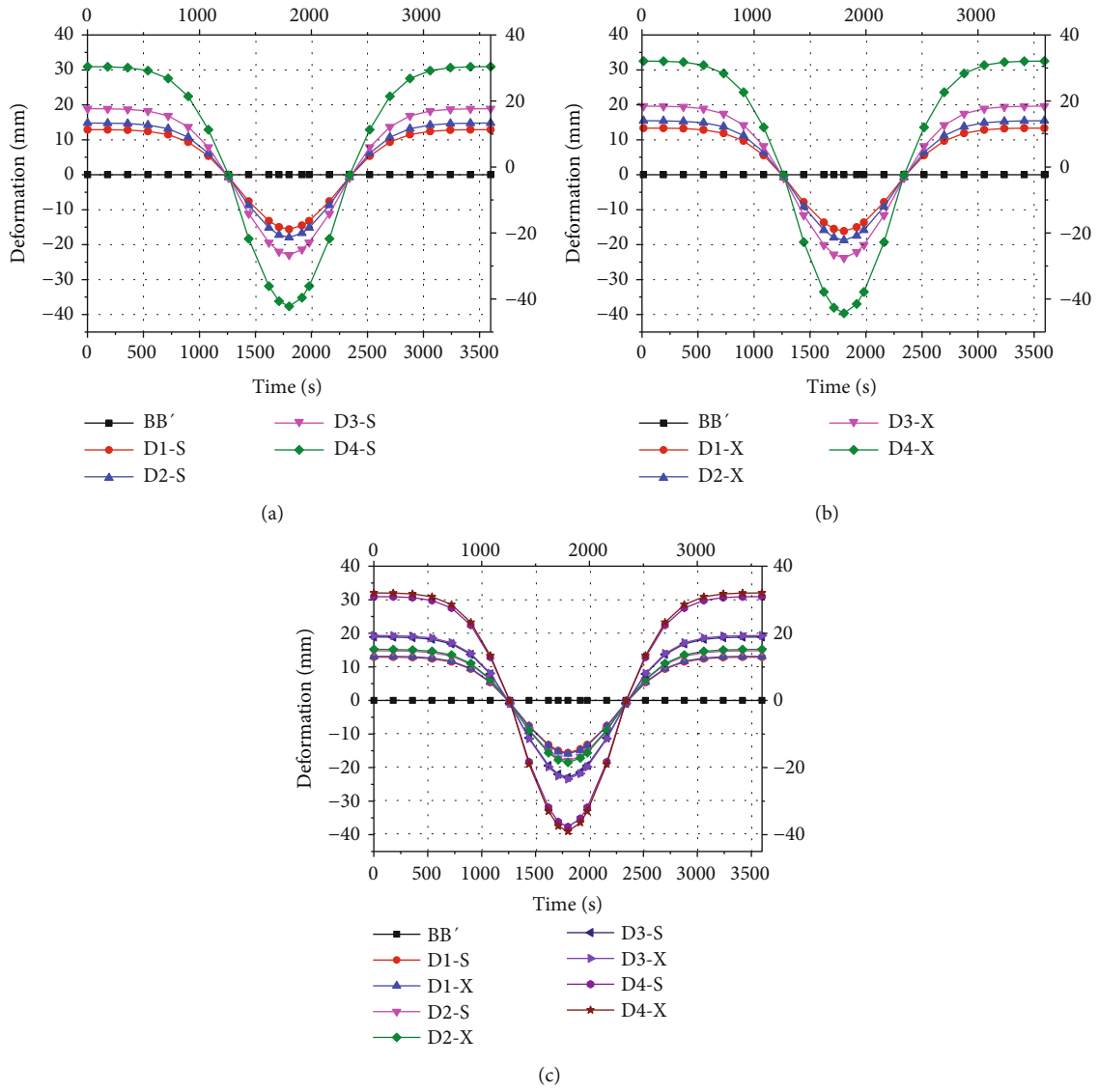

Figure 10: Time history deformation curve at key points of antenna structure. (a) The upper rods. (b) The lower rods. (c) The upper and lower rods.

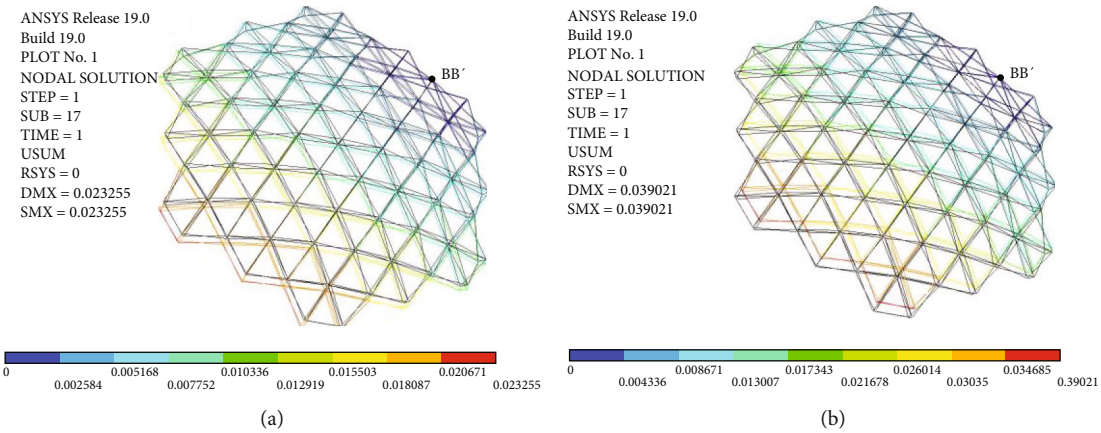

Figure 11: Overall deformation of the antenna structure. (a) $t_1 = 900$ s. (b) $t_2 = 1800$ s.

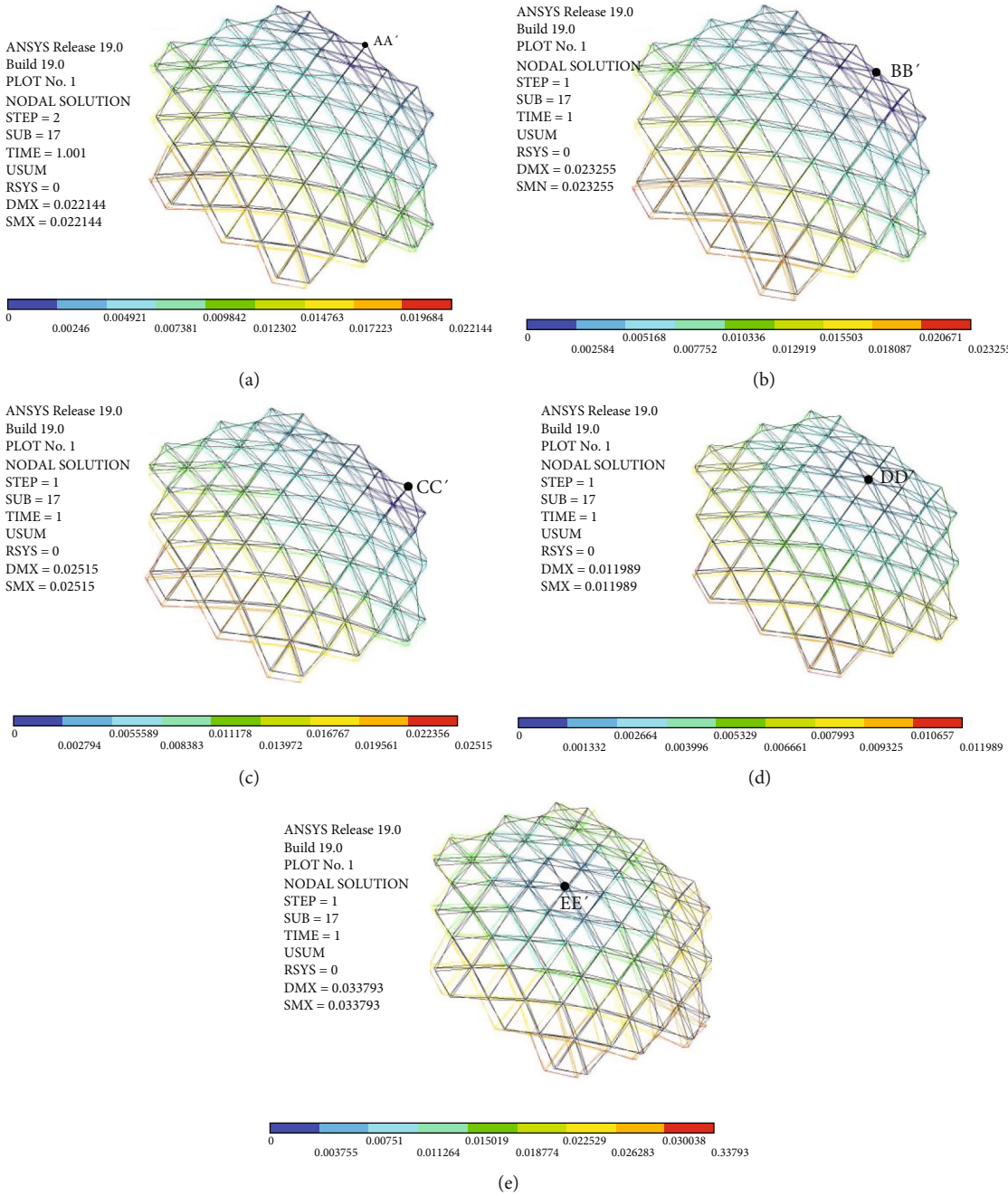

Figure 12: Overall deformation of structures with different constraints. (a) The constraint at AA′. (b) The constraint at BB′. (c) The constraint at CC′. (d) The constraint at DD′. (e) The constraint at EE′.

constraint position on the centroid D1-S(X) deformation of the antenna in the transient alternating temperature field. The vertical rods AA′, BB′, CC′, DD′, and EE′ of the structure are assumed to be the fulcrums of antenna expansion, separately. When the constraint is set at the abovementioned five vertical rods separately, the overall deformation of the antenna support structure at $t_1 = 900$ s is shown in Figure 12.

According to the application status of the antenna structure, the outermost vertical rod is the preferred position of the expansion fulcrum. When the constraint position of the antenna structure is required to be at AA′, BB′, and CC′ separately, the overall deformation of the structure constrained at the vertical rod CC′ is the largest and that of structure constrained at BB′ is slightly smaller and the structure constrained at AA′ deformation is minimum. Although the deformation in the case constrained at AA′ is smaller than that of the case at BB′ slightly and the vertical rod at BB′ has stronger stiffness because it is located at the splicing of two adjacent modules, so, the vertical rod BB′ is more conducive to being the fulcrum of antenna structure expansion, as shown in Figure 12(b).

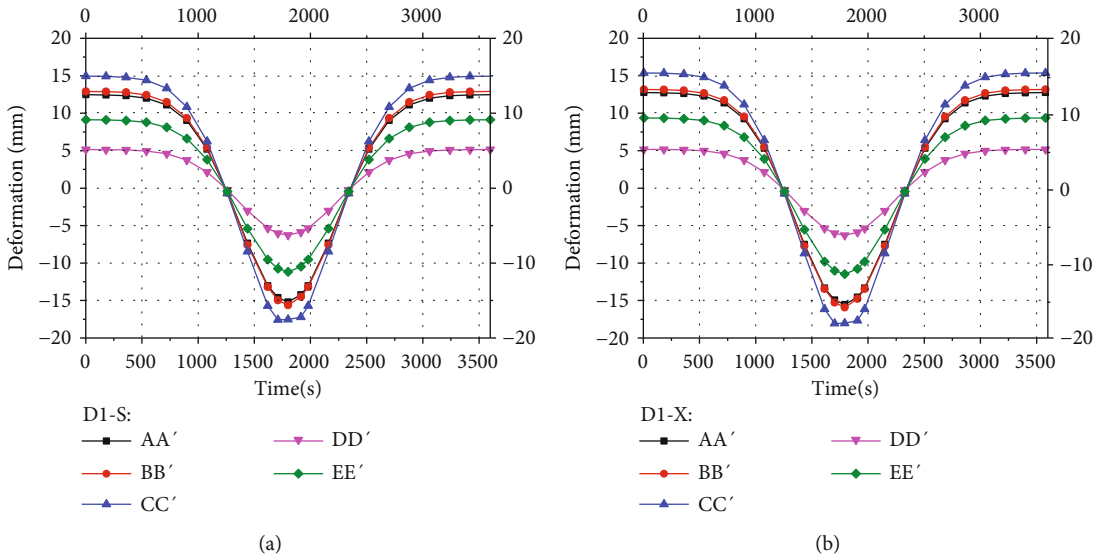

Figure 13: Thermal deformation curves of the centroid at different constraints. (a) Deformation of centroid D1-S. (b) Deformation of centroid D1-X.

If it is possible that the middle vertical rod, such as DD′ and EE′, inside the antenna is used to be the expansion fulcrum, the overall deformation of the structure constrained at DD′ is smaller than that at EE′. Moreover, because there is a large torsion ratio for the structure constrained at the EE′ vertical rod, so, it is better to choose the DD′ vertical rod as the middle expansion fulcrum of the antenna structure; see Figure 12(d).

The deformation development of the centroid D1-S(X) at different constraints with the temperature history is shown in Figure 13. Comparing between Figure 13(a) and Figure 13(b), the deformation trends of upper centroid D1-S and lower centroid D1-X are consistent with changes in temperature under working conditions at different constraints. The maximum difference of deformation between D1-S and D1-X is 3.33% under condition at constraint BB′, and the total average difference is 2.04%, indicating that there is little difference between D1-S and D1-X at each constraint.

The deformation amplitude of centroid D1-S of the upper layer structure constrained at AA′ is 12.47 mm~ −15.20 mm, and at any moment, the deformation is the smallest in the case of the edge constraint. Compared with the constraint at the CC′ vertical rod, its deformation is reduced by 17.42% and the total average deformation is reduced by 16.3%. Compared with the constraint BB′ case, the deformation decreases by about 3.44% and the average deformation decreases by about 3.02%. The D1-S deformation is within the range of 5.15 mm~−6.27 mm in the case constrained at DD′, and the deformation is the smallest under all working conditions. Compared with the constraint EE′ case, the maximum deformation of D1-S is reduced by 43.95% and the average reduction is about 43.66%. Compared with the constraint AA′ case, the deformation of D1-S is reduced by 56.71% and the total average reduction is 56.94%.

Based on the aforementioned results, when the expansion fulcrum of the antenna is set at the outermost vertical rod of the structure, it is suggested that the structure constraint should be applied at the splicing vertical rod of two outermost adjacent modules; the comprehensive performance of the structure is optimal in this case, such as BB′ as shown in Figure 2. When the fulcrum can also be located in the middle of the antenna, it is suggested that the constraint of the support structure should be selected at the splicing vertical rod of the adjacent modules in the second circle, such as DD′ in Figure 2. The constrained vertical rod serves as the connection between the antenna structure and the satellite boom. No matter where is the constraint, the range of thermal deformation due to the transient temperature field should be limited. It can reduce the adverse effect of thermal deformation on the surface accuracy of the modular deployable antenna.

5. Conclusions

In this study, the thermal analysis and thermal-structural analysis of the modular space-deployable antenna support structure under the action of the alternating temperature field are carried out and the thermal stress and deformation development law of each component in the antenna are obtained. The influence trend of the constraint position on the structure central and overall deformations is studied. Finally, the optimal constraint position of the antenna is suggested. The main conclusions of this study are as follows.

(1) During the thermal analysis of the antenna structure, the temperature of each component element is assumed as in accordance with the transient temperature field and the overall temperature changes slowly when the antenna enters and exits the Earth's shadow area. Furthermore, the temperature drops significantly in the shadow area completely

(2) The transient temperature field obtained via structural thermal analysis can provide boundary conditions for the thermal-structural analysis. The thermal stress and deformation time history of the antenna structure are essentially consistent with the trend of the transient temperature field

(3) In same circle module, the thermal stress in upper chord rods is higher than that in lower chord rods and it progressively increases toward the outer edge of the antenna structure. When the thermal exchange amplitude of the deployable antenna structure is large, the accumulated deformation at the centroid of the upper structure can reach up to 15 mm and the influence on the mesh accuracy of the antenna structure cannot be ignored

(4) It is recommended to select the splicing vertical rod of adjacent modules in the outermost or the second circle as the constraint position of the antenna structure. The constrained vertical rod connects the antenna to the satellite boom, where it is also the expansion fulcrum of the antenna, and both the overall and central deformations of the structure will be limited to the allowable values in any case

(5) It is suggested that the thermal protection measures such as ZS-1 high-temperature-resistant thermal insulation coating should be adopted on the surface of the antenna support structure to increase the adaptability of the antenna in the extreme space environment. Using the abovementioned measures, the adverse influence of temperature alternation on the antenna deformation and the mesh surface accuracy can be reduced

This study presented preliminary work on thermal-structural analysis of the support structure for the modular space-deployable antenna under a uniform temperature field, and more complicated models considering rigid-flexible coupling and shadow occlusion could be used in the future to achieve more conclusions.

Data Availability

All data generated or analyzed during this study are included within the article.

Conflicts of Interest

The authors declare that there is no conflict of interest regarding the publication of this paper.

Acknowledgments

This research was supported by the key program of the National Natural Science Foundation of China (Grant no. 51835002), the China Postdoctoral Science Foundation (Grant no. 2019M661126), and the Foundation of Liaoning Education Department (Grant no. LJKZ0563). These supports are gratefully acknowledged by the authors.

References

[1] F. Hu, Y. Song, Z. Huang, L. Yichen, M. Xiaofei, and L. Wan, "Design optimization of modular configuration for deployable truss antenna reflector," *China Space Science and Technology*, vol. 42, no. 1, pp. 1–8, 2021.

[2] D. Tian, H. Gao, L. Jin et al., "Research status and prospect of modular space deployable and foldable mechanism," *China Space Science and Technology*, vol. 41, no. 4, pp. 16–31, 2021.

[3] Y. Ding, W. Shen, J. Li, Z. Cheng, J. Jin, and J. Sun, "Research on Trusted Full-Proxy Homomorphic Transmission Mechanism for Satellite Communication," *Chinese Space Science and Technology*, vol. 40, no. 4, p. 84, 2020.

[4] H. L. Qian, J. Zhong, and F. Fan, "Analysis on non-uniform temperature field due to sunshine for the antenna structure of Shanghai 65-meter-aperture radio telescope," *China Civil Engineering Journal*, vol. 43, no. 3, pp. 39–46, 2014.

[5] J. Wu, Z. H. Zhao, and G. X. Ren, "Dynamic analysis of space structure deployment with transient thermal load," *Advanced Materials Research*, vol. 1673, pp. 803–807, 2012.

[6] X. F. Ma, Y. Li, and Y. Xiao, "Development and tendency of large space deployable antenna reflector," *Space Electronic Technology*, vol. 15, no. 2, pp. 16–26, 2018.

[7] Z. Shen, Q. Tian, X. Liu, and G. Hu, "Thermally induced vibrations of flexible beams using absolute nodal coordinate formulation," *Aerospace Science and Technology*, vol. 29, no. 1, 2013.

[8] L. J. Cheng and D. M. Xue, "Thermal-dynamic analysis of large scale space structures by FEM," *Journal of Tsinghua University (Science and Technology)*, vol. 21, no. 5, 2004.

[9] Z. H. Chen, *Research on Synthesis of Shaped Reflector and Thermal Analysis of Antenna In-Orbit*, Zhejiang University, 2009.

[10] B. A. Boley, "Approximate analyses of thermally induced vibrations of beams and plates," *Journal of Applied Mechanics*, vol. 39, no. 1, pp. 212–216, 1972.

[11] E. A. Thornton and Y. A. Kim, "Thermally induced bending vibrations of a flexible rolled-up solar array," *Journal of Spacecraft and Rockets*, vol. 30, no. 4, pp. 438–448, 1993.

[12] R. Namburu and K. Tamma, "Thermally-induced structural dynamic response of flexural configurations influenced by linear/non-linear thermal effects," in *32nd Structures, Structural Dynamics, and Materials Conference*, U.S.A., 1991.

[13] J. D. Johnston and E. A. Thornton, "Thermally induced attitude dynamics of a spacecraft with a flexible appendage," *Journal of Guidance Control and Dynamics*, vol. 21, no. 4, pp. 581–587, 1998.

[14] S. J. Zhang, *Design and Thermal Analysis of Spatial Deployable Truss Structures*, Zhejiang University, 2001.

[15] Y. Ding and D. M. Xue, "Finite element analysis of transient temperature field and thermal deformation of space thin-walled circular tube under radiation heat transfer," *Journal of Astronautics*, vol. 23, no. 5, pp. 49–56, 2002.

[16] J. I. Rodriguez, A. Na-Nakornpanom, and J. G. Rivera, "On-orbit thermal performance of the TES instrument-three years in space," *SAE International Journal of Aerospace*, vol. 1, no. 1, pp. 364–375, 2009.

[17] L. J. Fan, J. Duan, Z. H. Xiang, D. M. Xue, and Z. Z. Cen, "Nonlinear finite element analysis of thermal-dynamics coupling system of large flexible spatial structures," *Journal of Astronautics*, vol. 30, no. 1, pp. 299–304, 2009.

[18] J. Liu, M. B. Zhu, and G. Cao, "Numerical analysis of thermal vibration of space borne deployable antenna," *China Space Science and Technology*, vol. 31, no. 2, pp. 53–57, 2011.

[19] L. K. Abbas, X. Rui, and P. Marzocca, "Aerothermoelastic analysis of panel flutter based on the absolute nodal coordinate formulation," *Multibody System Dyna-mics*, vol. 33, no. 2, pp. 163–178, 2015.

[20] Y. T. Sun, "Structure design and analysis of a space-borne antenna," *Electro-Mechanical Engineering*, vol. 34, no. 3, pp. 31–34, 2018.

[21] H. L. Yun and P. F. Yuan, "Thermal-structural analysis of hoop deployable antenna in real orbital environment," *Mechanical Science and Technology for Aerospace Engineering*, vol. 38, no. 10, pp. 1612–1618, 2019.

[22] C. K. Wu, B. Y. He, and P. F. Yuan, "Thermal-structural analysis of hoop deployable antenna with metal hinges," *Chinese Journal of Engineering Design*, vol. 27, no. 3, pp. 349–356, 2020.

[23] S. Corpino, M. Caldera, F. Nichele, M. Masoero, and N. Viola, "Thermal design and analysis of a nanosatellite in low earth orbit," *ActaAstronautica*, vol. 115, pp. 247–261, 2015.

[24] P. Yeonkyu, K. Geuknam, and P. Sangyoung, "Novel structure and thermal design and analysis for cubesats in formation flying," *Aerospace*, vol. 8, no. 6, p. 150, 2021.

[25] R. Q. Liu, D. K. Tian, Z. Q. Deng, and H. W. Guo, "Modal analysis of truss structure for deployable truss antenna with multi module," *Transactions of Beijing Institute of Technology*, vol. 31, no. 6, pp. 685–690, 2011.

[26] D. K. Tian, *Design and Experimental Research on Truss Structure for Modular Space Deployable Antenna*, Harbin Institute of Technology Press, 2012.

[27] X. An and G. Feng, "Thermally induced vibration of the main mast of the space station's solar arrays," *Structure and Environment Engineering*, vol. 32, no. 3, 2005.

[28] G. G. Yang, M. B. Zhu, P. Y. Lian, F. Gao, and Y. L. Zong, "Thermal induced coupling-dynamic analysis of a deployable satellite antenna system," *Journal of Vibration and Shock*, vol. 33, no. 24, pp. 173–178, 2014.

Hindawi
International Journal of Aerospace Engineering
Volume 2022, Article ID 3590103, 9 pages
https://doi.org/10.1155/2022/3590103

Research Article

Surface Adjustment Method Based on Fuzzy Theory for Cable Net Structures under Multi-Uncertainties

Tuanjie Li,[1] **Li Yan**,[2] **Zhiyang Shi**,[1] **Zijie Zeng**,[1] **and Yaqiong Tang**[1]

[1]*School of Mechano-Electronic Engineering, Xidian University, P.O. Box 188, Xi'an 710071, China*
[2]*Aerospace System Engineering Shanghai, Shanghai 201109, China*

Correspondence should be addressed to Tuanjie Li; tjli@mail.xidian.edu.cn

Received 27 April 2022; Revised 8 May 2022; Accepted 12 May 2022; Published 25 May 2022

Academic Editor: Fangzhou Fu

Because of manufacturing errors, measuring errors, and unpredictable service environment, the cable net structure to be further adjusted is in an uncertainty state. In this paper, the uncertain factors including elastic deformation, thermal deformation, and measurement uncertainties are considered as fuzzy variables, which are equivalent into fuzzy tensions to simplify calculation. A fuzzy force density method is developed for accuracy analysis of the cable net structures under multi-uncertainties, and an optimization model is developed for surface adjustment. The above method is applied to numerical model adjustment of circular truss cable net structure. The results show that the adjusted surface accuracy is significantly enhanced and its fuzziness is concentrated compared with the initial surface accuracy, which verify the validity of the proposed method.

1. Introduction

Cable net structures have been widely applied to space deployable reflector antennas such as the AstroMesh antenna, the TerreStar antenna, the antenna of JAXA Engineering Test Satellite, and the SkyTerra antenna [1–5]. High-accuracy surface is a prerequisite for ensuring the electrical performance of the antennas. However, limited by manufacturing and assembling technology, artificial surface adjustment is an essential and tiresome step to improve the surface accuracy, which has been revealed very sensitive to manufacturing errors and environmental changes [6–8].

There have been many researchers that have done a lot to improve the efficiency of adjustment strategies. Hiroaki and Natori [9] proposed a shape control method based on the concept of self-equilibrated stresses to improve the control efficient. Du et al. [10] presented a shape adjustment procedure based on optimization and then converted the procedure into a sequential quadratic programming problem to make it more easily. Niu et al. [11] established an optimal adjustment model that an influence coefficient matrix was treated as one target. The above adjustment methods regarding the current configuration of the cable net structure can be accurately obtained. Actually, because of the limitation of measurement accuracy and changeable environment, there must be some uncertain factors such as nodal positions, cable pretensions, material parameters, and environmental temperature [12, 13]. Under the influence of these uncertain factors, how does the surface accuracy of the cable net structure change and how to ensure the surface accuracy in a reliable range becomes particularly important.

Nowadays, the methods for dealing with uncertainty can be divided into three categories including the probability theory [14–16], the fuzzy algorithm [17], and the interval method [18]. The probability theory is a helpful tool in modeling situations where the primary source of uncertainty is randomness [19, 20]. But sometimes, we argue that uncertainty takes other forms; instead of asking whether something is true, we ask how much of it is true and how much a certain property is exhibited in a particular instance. In our previous work [21], an interval force density was proposed and an optimization adjustment model was established for the surface adjustment of cable net structures. However, it is found that only mean and marginal cases can be obtained by the interval method and probability

distribution functions need to be further studied. Probability method needs to study the probability distribution of uncertain variables based on a large number of statistical data, while fuzzy algorithm can study uncertainty model by membership function which can be estimated by experience. In order to improve the efficiency of cable net structure adjustment considering uncertainty in engineering, it is necessary to study how to apply fuzzy algorithm to adjustment. Thus, this paper proposes a fuzzy force density method to deal with the surface adjustment problem of the cable net structures under multi-uncertainties. The paper has a guiding significance for the adjustment of cable net structure considering uncertainty in the case of few samples in engineering.

2. Brief Summary of the Fuzzy Set Theory

Define a fuzzy subset of U as function A: $U \longrightarrow [0, 1]$, that is, a characteristic function from U into interval $[0, 1]$. The value $A(u)$ is called the membership of point u in the fuzzy set U or the degree to which point u belongs to set A.

$$^{\lambda}A = \{u | A(u) \geq \lambda, u \in U\}, \tag{1}$$

where $^{\lambda}A$ is called the λ-cut of the fuzzy set A, $\lambda \in [0, 1]$.

If the lower bound $u^l(\lambda)$ and upper bound $u^u(\lambda)$ are given, the fuzzy number A can be obtained by summing all λ-cut sets as

$$^{\lambda}A = \left\{ \left[u^l(\lambda), u^u(\lambda) \right], \lambda \in [0, 1] \right\}. \tag{2}$$

Defining $\tilde{x}$ as a fuzzy variable and its fuzzy number as $A(\lambda)$, $\tilde{x}$ can be described by

$$\tilde{x} = \tilde{x}(\lambda, \delta) = x^c(\lambda) + x^r(\lambda)\delta, \tag{3}$$

where $x^c(\lambda)$ and $x^r(\lambda)$ are the midvalue and the amplitude of $\tilde{x}$, respectively, and where

$$\begin{aligned} x^c(\lambda) &= \frac{x^u(\lambda) + x^l(\lambda)}{2}, \\ x^r(\lambda) &= \frac{x^u(\lambda) - x^l(\lambda)}{2}. \end{aligned} \tag{4}$$

Then, the fuzzy variable $\tilde{x}$ can be described by the interval variables λ and δ, where $\lambda \in [0, 1]$ and $\delta \in [-1, 1]$. When the cut level λ is given, the fuzzy variable $\tilde{x}$ becomes an interval variable. Therefore, the operation of the fuzzy variable $\tilde{x}(\lambda, \delta)$ can be discretized into the operation of interval variables.

3. Mathematical Models for Fuzzy Cable Net Structures

Cable net structures inevitably suffer from multiple sources of uncertainty in the process of manufacture, assembly, and on-orbit service. Limited by our ability to get information, parameters of the structures like nodal positions, cable pretensions, material parameters, and environmental temperatures must be uncertain. Thus, we use some fuzzy variables to describe these uncertainties. In order to reveal the influence of these uncertainties on the surface accuracy of the cable net structures, the mathematic models are firstly established based on the force density method and the fuzzy theory in this section.

3.1. Equivalent Fuzzy Cable Tensions for a Cable Net Structure under Multi-Uncertainties. For the cable net structure whose geometric forms are given, the sources of uncertainty can be divided into three categories: elastic deformation uncertainty, thermal deformation uncertainty, and measurement uncertainty [21], among which the uncertainties which would cause cable tension changes can be equivalent into a total fuzzy tension to simplify calculation.

According to Hooke's Law, elastic property of a cable can be expressed by the following equation.

$$\varepsilon = \frac{F}{EA} = \frac{L - L_0}{L_0}, \tag{5}$$

where ε is the cable strain, F is the cable tension, E is the elastic modulus, A is the cross-sectional area, L is the stretched length, and L_0 is the unstretched length.

3.1.1. Uncertainty of Elastic Deformation. Because of multi-uncertainties, the axial tension, the elastic modulus, and the cross-sectional area are fuzzy variables. Thus, the above equation can be rewritten as

$$\tilde{\varepsilon} = \frac{F + \Delta\tilde{F}_E(\lambda, \delta)}{\tilde{E}(\lambda, \delta)\tilde{A}(\lambda, \delta)} = \frac{L - \tilde{L}_0(\lambda, \delta)}{\tilde{L}_0(\lambda, \delta)}, \tag{6}$$

where $\tilde{\varepsilon}$ is the fuzzy strain; $\tilde{E}$ is the fuzzy elastic modulus; $\tilde{A}$ is the fuzzy cross-sectional area; $\tilde{L}_0$ is the fuzzy unstretched length; $\Delta\tilde{F}_E(\lambda, \delta)$ is the fuzziness of the cable tension caused by uncertainty of elastic deformation; see below.

$$\Delta\tilde{F}_E(\lambda, \delta) = \frac{L - \tilde{L}_0(\lambda, \delta)}{\tilde{L}_0(\lambda, \delta)} \tilde{E}(\lambda, \delta)\tilde{A}(\lambda, \delta) - F. \tag{7}$$

According to the fuzzy set theory, the above equation can be rewritten as

$$\begin{aligned} \Delta\tilde{F}_E(\lambda, \delta) = {} & \frac{L - [l_0^c(\lambda) + l_0^r(\lambda)\delta]}{l_0^c(\lambda) + l_0^r(\lambda)\delta} [E^c(\lambda) + E^r(\lambda)\delta] \\ & \cdot [(A^c(\lambda) + A^r(\lambda)\delta)] - F, \end{aligned} \tag{8}$$

where l_0^c and l_0^r are the midvalue and the amplitude of the unstretched length; E^c and E^r are the midvalue and the amplitude of the elastic modulus; A^c and A^r are the midvalue and the amplitude of the cross-sectional area.

3.1.2. Uncertainty of Thermal Deformation. According to the thermoelasticity theory, the thermal strain ε_T of a cable is

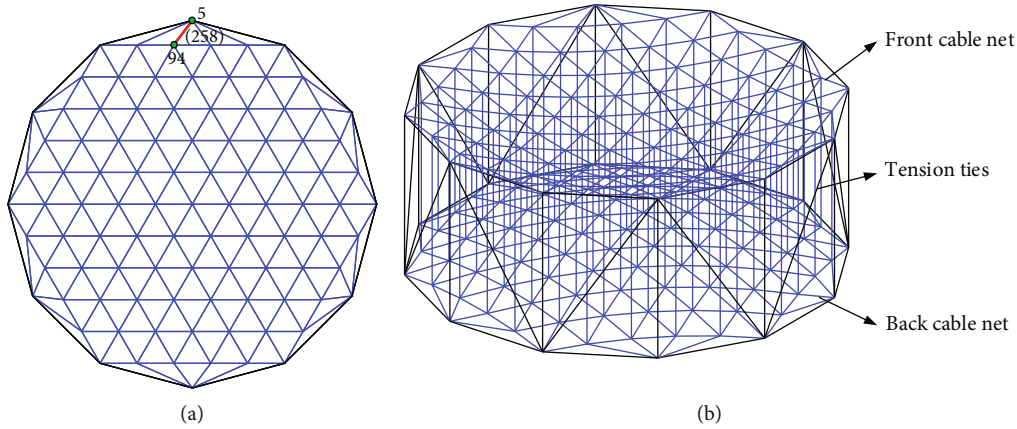

Figure 1: Circular truss cable net structure: (a) top view; (b) side view.

Table 1: Geometric parameters of the cable net structure.

Items	Value
Diameter of aperture	7 m
Focal lengths of front and back cable net	4 m
Piecewise number	5
Cable radius	1 mm
Elastic modulus of cables	20 GPa
Coefficient of thermal expansion	2×10^{-7}

directly proportional to the temperature difference ΔT, specifically as follows.

$$\varepsilon_T = \alpha \Delta T, \tag{9}$$

where α is the coefficient of thermal expansion.

The tension uncertainty caused by thermal deformation can be equivalent to

$$\Delta \tilde{F}_T = EA\alpha \Delta T. \tag{10}$$

Considering the uncertainties of the temperature difference, the coefficient of thermal expansion, the elastic modulus, and the cross-sectional area, the uncertainty of the tension caused by the thermal deformation can be obtained as

$$\Delta \tilde{F}_{\Delta T}(\lambda, \delta) = \tilde{E}(\lambda, \delta)\tilde{A}(\lambda, \delta)\tilde{\alpha}(\lambda, \delta)\Delta \tilde{T}(\lambda, \delta), \tag{11}$$

where $\Delta \tilde{F}_{\Delta T}$ is the fuzziness of the cable tension caused by the uncertainty of the temperature difference; $\tilde{\alpha}$ is the fuzzy coefficient of thermal expansion; $\Delta \tilde{T}$ is the fuzzy temperature difference.

According to the fuzzy set theory, the above equation can be rewritten as

$$\begin{aligned} \Delta \tilde{F}_{\Delta T}(\lambda, \delta) = {} & [E^c(\lambda) + E^r(\lambda)\delta][A^c(\lambda) + A^r(\lambda)\delta] \\ & \cdot [\alpha^c(\lambda) + \alpha^r(\lambda)\delta][\Delta T^c(\lambda) + \Delta T^r(\lambda)\delta], \end{aligned} \tag{12}$$

where α^c and α^r are the midvalue and the amplitude of the coefficient of thermal expansion, respectively; ΔT^c and ΔT^r are the midvalue and the amplitude of the temperature difference.

3.1.3. Uncertainty of Tension Measurement. There will be some uncertainties when applying and measuring cable tensions. Defining the fuzzy tension caused by manufacture and measure as $\Delta \tilde{F}_M$, the following equation can be obtained.

$$\Delta \tilde{F}_M(\lambda, \delta) = \Delta F_M^c(\lambda) + \Delta F_M^r(\lambda)\delta, \tag{13}$$

where ΔF_M^c and ΔF_M^r are the midvalue and the amplitude of the fuzzy tension caused by manufacture and measure.

3.1.4. Equivalent Fuzzy Tension. Combining Equations (8), (12), and (13), the equivalent fuzzy tension can be obtained as

$$\tilde{F}_{\text{total}}(\lambda, \delta) = F + \Delta \tilde{F}_E(\lambda, \delta) + \Delta \tilde{F}_T(\lambda, \delta) + \Delta \tilde{F}_M(\lambda, \delta), \tag{14}$$

where $F\sim_{\text{total}}$ is the equivalent fuzzy tension.

3.2. Surface Accuracy Analysis for a Fuzzy Cable Net Structure. For an arbitrary node j connected by some cables, the force balance equations can be obtained as

$$\begin{cases} \sum\limits_{j \in S_j}^{S_j} \tilde{F}_{ij} \dfrac{\tilde{x}_j - \tilde{x}_i}{\tilde{L}_{ij}} = 0, \\ \sum\limits_{j \in S_j}^{S_j} \tilde{F}_{ij} \dfrac{\tilde{y}_j - \tilde{y}_i}{\tilde{L}_{ij}} = 0, \\ \sum\limits_{j \in S_j}^{S_j} \tilde{F}_{ij} \dfrac{\tilde{z}_j - \tilde{z}_i}{\tilde{L}_{ij}} = 0, \end{cases} \tag{15}$$

where $\tilde{F}_{ij}$ denotes the fuzzy tension of the cable connected to nodes i and j; $(\tilde{x}_i, \tilde{y}_i, \tilde{z}_i)$ is the fuzzy coordinates of node i; S_j

Table 2: Fuzzy parameters of the cable net structure.

Item	L_0(mm)		T(°C)		E(Pa)		A(mm^2)		F(N)		$\alpha(10^{-7}/°C)$	
	a_L	σ_L	a_T	σ_T	a_E	σ_E	a_A	σ_A	a_F	σ_F	a_α	σ_α
Value	L_0	0.1%	0	10	2×10^{10}	1%	π	0.01	F	0.1	2	0.01

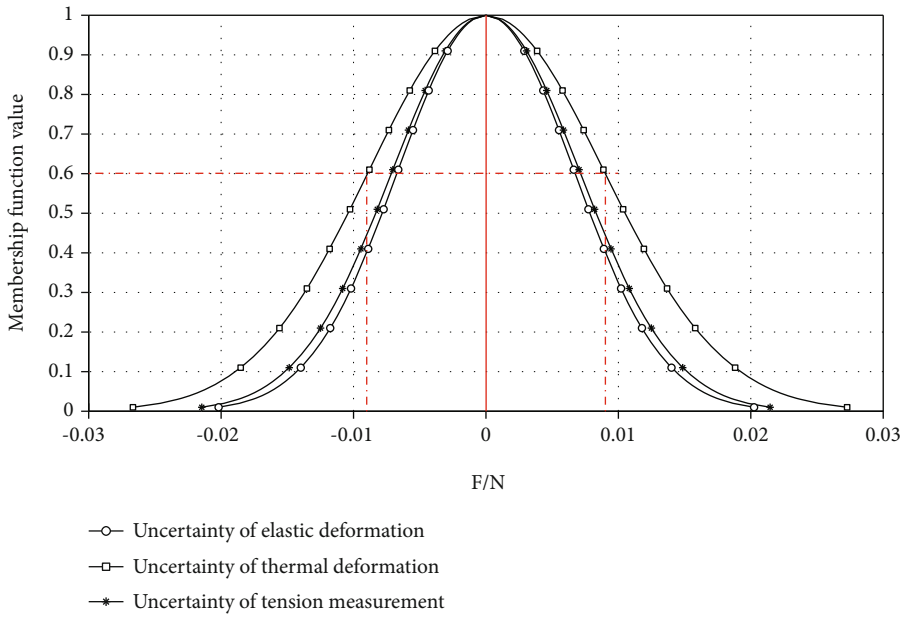

Figure 2: The distribution of the membership functions for three equivalent fuzzy tensions.

is the set of all cables connected to node j; $\tilde{L}_{ij}$ is the fuzzy length of the cable connected to nodes i and j.

According to Section 3.1, the fuzzy tension $\tilde{F}_{ij}$ can be obtained by Equation (14).

$$\tilde{F}_{ij}(\lambda,\delta) = F_{ij} + \Delta\tilde{F}_{ij,E}(\lambda,\delta) + \Delta\tilde{F}_{ij,T}(\lambda,\delta) + \Delta\tilde{F}_{ij,M}(\lambda,\delta). \tag{16}$$

In order to consider the effects of geometric and tension uncertainties simultaneously, a fuzzy force density is introduced as follows.

$$\tilde{q}_{ij}(\lambda,\delta) = \frac{\tilde{F}_{ij}(\lambda,\delta)}{\tilde{L}_{ij}(\lambda,\delta)}. \tag{17}$$

Referring to the force density method [8], the static equilibrium equations can be obtained as follows.

$$\begin{cases} \mathbf{C}_s^{\mathrm{T}}\tilde{\mathbf{Q}}\mathbf{C}_s\tilde{\boldsymbol{x}}(\lambda,\delta) = \mathbf{0}, \\ \mathbf{C}_s^{\mathrm{T}}\tilde{\mathbf{Q}}\mathbf{C}_s\tilde{\boldsymbol{y}}(\lambda,\delta) = \mathbf{0}, \\ \mathbf{C}_s^{\mathrm{T}}\tilde{\mathbf{Q}}\mathbf{C}_s\tilde{\boldsymbol{z}}(\lambda,\delta) = \mathbf{0}, \end{cases} \tag{18}$$

where $\tilde{\mathbf{Q}}$ is a diagonal matrix containing fuzzy force densities; $\mathbf{C}_s$ is the incidence matrix of the cable net structure; $\tilde{\boldsymbol{x}}(\lambda,\delta)$ is a column vector of x-coordinates; $\tilde{\boldsymbol{y}}(\lambda,\delta)$ is a column vector of y-coordinates; $\tilde{\boldsymbol{z}}(\lambda,\delta)$ is a column vector of z-coordinates. If some nodal coordinates are given, e.g., these nodes are attached to a foundation, $\mathbf{C}_s$ can be partitioned as

$$\mathbf{C}_s = [\mathbf{C}_u\ \mathbf{C}_f], \tag{19}$$

where the restrained nodes have been put at the end of the numbering sequence. Equation (18) can be rewritten as

$$\begin{aligned} \tilde{\boldsymbol{x}}_u(\lambda_{x_u},\delta) &= -\left(\mathbf{C}_u^{\mathrm{T}}\tilde{\mathbf{Q}}\mathbf{C}_u\right)^{-1}\mathbf{C}_u^{\mathrm{T}}\tilde{\mathbf{Q}}\mathbf{C}_f\tilde{\boldsymbol{x}}_f(\lambda,\delta), \\ \tilde{\boldsymbol{y}}_u\left(\lambda_{y_u},\delta\right) &= -\left(\mathbf{C}_u^{\mathrm{T}}\tilde{\mathbf{Q}}\mathbf{C}_u\right)^{-1}\mathbf{C}_u^{\mathrm{T}}\tilde{\mathbf{Q}}\mathbf{C}_f\tilde{\boldsymbol{y}}_f(\lambda,\delta), \\ \tilde{\boldsymbol{z}}_u\left(\lambda_{z_u},\delta\right) &= -\left(\mathbf{C}_u^{\mathrm{T}}\tilde{\mathbf{Q}}\mathbf{C}_u\right)^{-1}\mathbf{C}_u^{\mathrm{T}}\tilde{\mathbf{Q}}\mathbf{C}_f\tilde{\boldsymbol{z}}_f(\lambda,\delta), \end{aligned} \tag{20}$$

where $\tilde{\boldsymbol{x}}_u$, $\tilde{\boldsymbol{y}}_u$, and $\tilde{\boldsymbol{z}}_u$ are the column vectors of unknown x-, y-, and z-coordinates; $\tilde{\boldsymbol{x}}_f$, $\tilde{\boldsymbol{y}}_f$, and $\tilde{\boldsymbol{z}}_f$ are the column vectors of the given x-, y-, and z-coordinates, respectively.

Taking the ideal coordinates $\{\boldsymbol{x}_0, \boldsymbol{y}_0, \boldsymbol{z}_0\}$ as a reference, the fuzzy root-mean-square error (RMS), which can be used to evaluate the structure accuracy, can be obtained as follows.

$$\tilde{\omega}_{\mathrm{rms}}(\lambda,\delta) = \sqrt{\frac{\left(\|\tilde{\boldsymbol{x}}_u - \boldsymbol{x}_0\|_2^2 + \|\tilde{\boldsymbol{y}}_u - \boldsymbol{y}_0\|_2^2 + \|\tilde{\boldsymbol{z}}_u - \boldsymbol{z}_0\|_2^2\right)}{N_u}}, \tag{21}$$

where N_u is the number of the nodes with unknown coordinates.

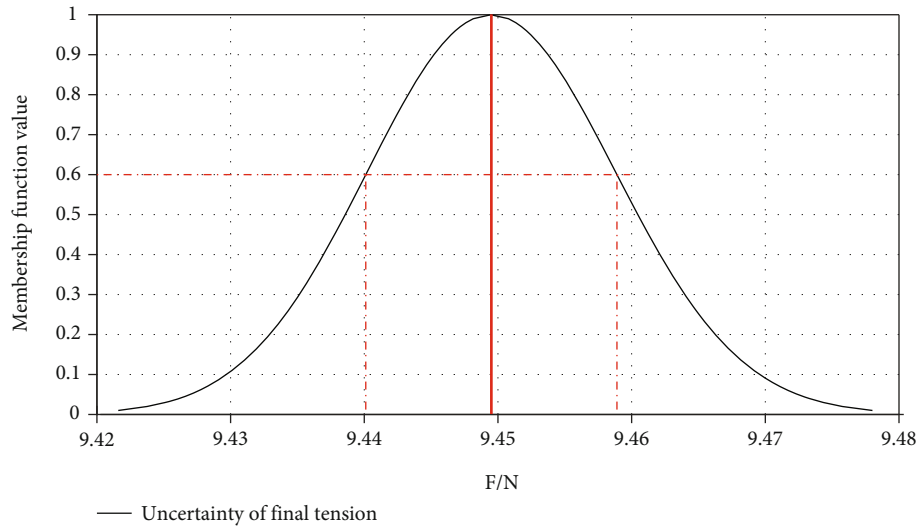

Figure 3: The distribution of the membership functions for the total equivalent fuzzy tension.

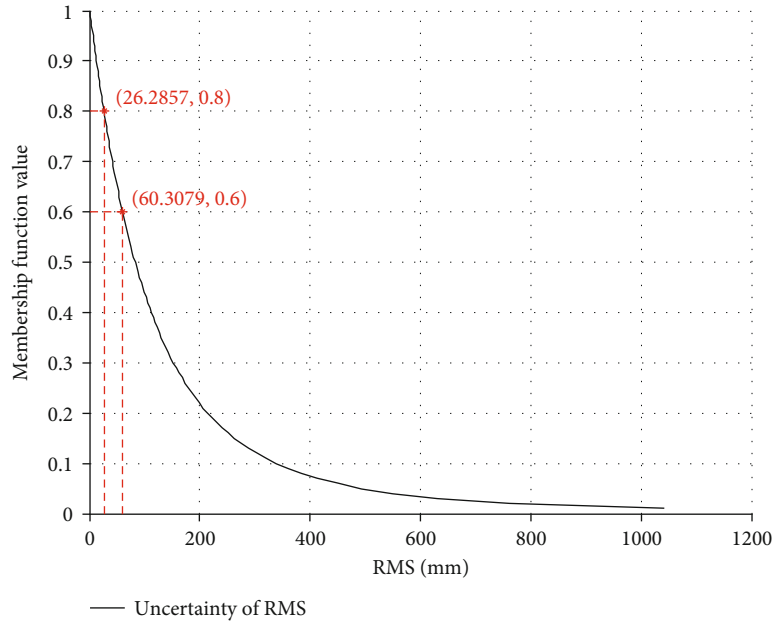

Figure 4: Distribution of the membership function for RMS.

4. Optimization Model for Adjustment of a Cable Net Structure under Multi-Uncertainties

The force density of an adjustable cable connected to nodes i and j can be modified as

$$\tilde{q}_{ij} = \frac{\tilde{F}_{ij}}{\tilde{L}_{ij} - a_{ij}}, \tag{22}$$

where a_{ij} is the adjustment amount of the cable.

Substituting Equation (22) into Equation (20), the cable net structure after adjustment can be obtained and the surface accuracy can be then calculated by Equation (21). Base on this, we establish the following optimization model, which can be solved by the advance and retreat algorithm [21], for the adjustment of the cable net structure under multi-uncertainties:

$$\begin{aligned} &\text{Find} \quad \{a_{ij}\} \\ &\min \quad \text{mean}(\tilde{w}_{\text{rms}}) \\ &\text{s.t.} \quad \text{Equation (20)} \\ &g_1^{ij} = a_0 - |a_{ij}| \le 0 \\ &g_2^{ij} = \frac{\tilde{F}_{ij}}{\tilde{L}_{ij} - a_{ij}} > 0 \end{aligned} \tag{23}$$

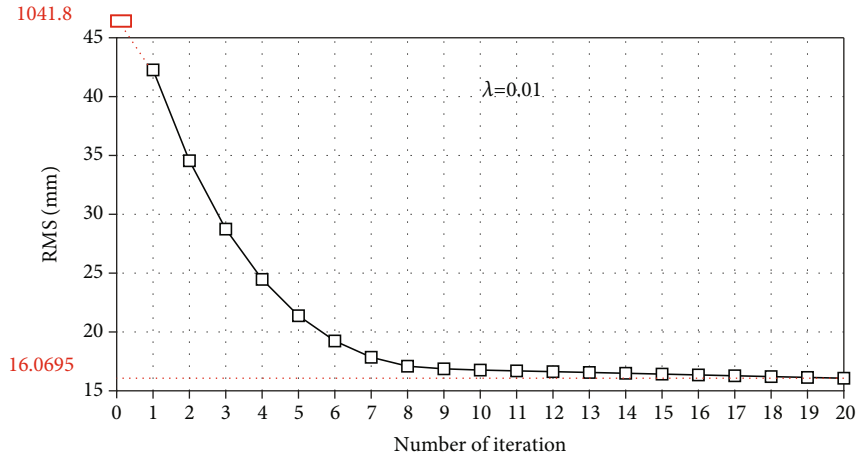

(a)

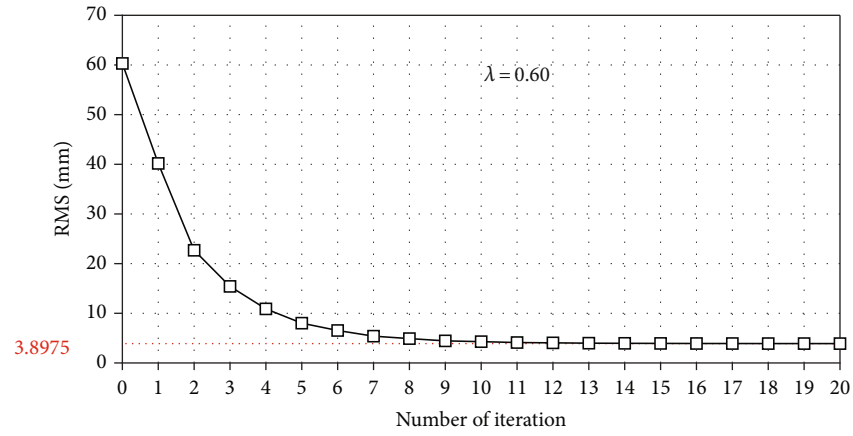

(b)

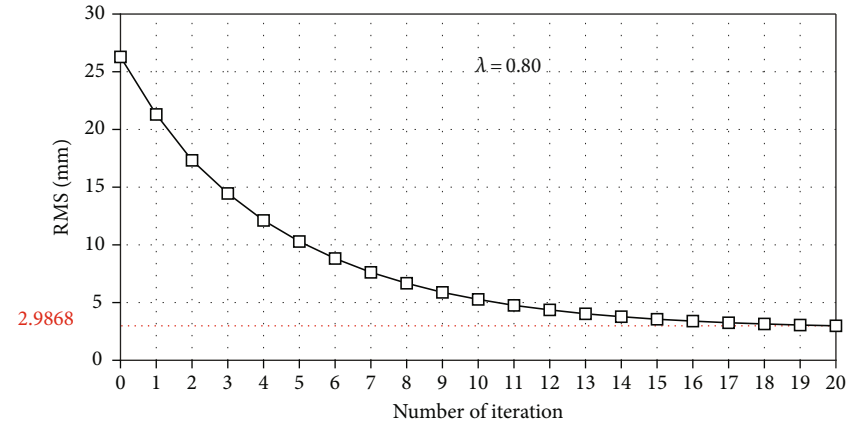

(c)

Figure 5: Continued.

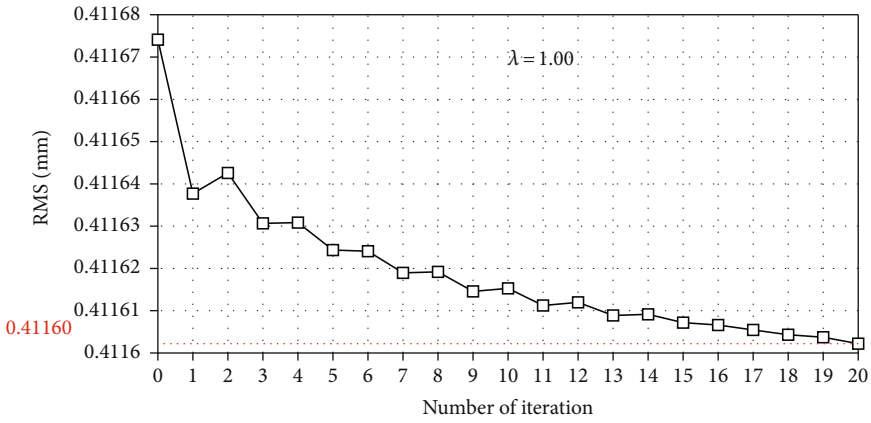

(d)

Figure 5: RMS iterative process under different cut levels: (a) $\lambda = 0.01$; (b) $\lambda = 0.60$; (c) $\lambda = 0.80$; (d) $\lambda = 1.00$.

where $\{a_{ij}\}$ is the set of adjustment amount containing all adjustable cables; mean$(\tilde{w}_{\text{rms}})$ is the mean value of the fuzzy RMS; a_0 is the minimum adjustment length; g_1^{ij} denotes an inequality constraint that the a_{ij} cannot be smaller than the minimum adjustment amount a_0 which is dependent on the engineering practice; and g_2^{ij} denotes an inequality constraint that the force density of the cables must be positive due to the fact that the cable has no compressive rigidity.

The adjustment progress of the cable net structure under multi-uncertainties is as follows.

Step 1. Uniformly discrete the horizontal cut set λ into λ^i $(i = 1, 2, 3, \cdots)$. When $k = 0$ and horizontal cut set is equal to λ^i, solve initial node coordinates and initial cable tensions by membership function of fuzzy variables.

Step 2. Calculate adjustment amount $\{a_{ij}\}^{(k)}$ by Equation (23).

Step 3. Update fuzzy force density matrix $\tilde{\mathbf{Q}}^{(k)}$ by Equation (22). Update node coordinates and cable tensions by Equation (20). Calculate $\tilde{w}_{\text{rms}}^{(k)}$ by Equation (21).

Step 4. When $\tilde{w}_{\text{rms}}^{(k)} \le \varepsilon_{\text{ideal}}$ ($\varepsilon_{\text{ideal}}$ is a given ideal RMS), turn to Step 5; else, let $k = k + 1$ and turn to Step 2.

Step 5. Record the optimal objective function value and design variable value under level cut set λ^i. When $\lambda^i = 1$, turn to Step 6; else, let $i = i + 1$; turn to Step 1.

Step 6. The distribution of membership function of the adjusted RMS is obtained by curve fitting.

5. Numerical Example

Take a cable net structure which has been applied to the hoop truss reflectors as an example to illustrate the proposed method. As shown in Figure 1, the cable net structure is composed of a front cable net, a back cable net, and tension ties, among which the front cable net is usually used to support the wire mesh to reflect electromagnetic wave and tension ties are adjustable cables. The geometrical parameters and the material parameters of the cable net structure are shown in Table 1, and the uncertain parameters are shown in Table 2. In this example, the membership functions of the fuzzy variables obey a normal distribution of which the function can be written as

$$\mu(x) = \exp\left\{-\left(\frac{x-a}{\sigma}\right)^2\right\} \sigma > 0, \quad x \in R, \tag{24}$$

where a and σ are the mean and the standard deviation of the fuzzy variable, respectively.

5.1. Equivalent Fuzzy Cable Tensions. When the λ-level cut value is specified as 0.01, 0.02 ... 0.99, and 1.0, respectively, for the fuzzy variables, the interval value of the equivalent fuzzy cable tension $\tilde{F}_{ij}(\lambda, \delta)$ corresponding to the λ-level cut set can be obtained by Equation (16). Then, the discrete intervals can be connected and fitted to obtain the membership distribution curve of the equivalent fuzzy cable tension $\tilde{F}_{ij}$. Taking cable 258 which is connected to nodes 49 and 5 as shown Figure 1 as an example, the cores of the cable length and the cable tension are 0.6132 m and 9.4495 N, respectively. The distributions of the membership functions for the cable tensions caused by elastic deformation uncertainty $(k = 1)$, thermal deformation uncertainty $(k = 2)$, and tension measurement uncertainty $(k = 3)$ can be obtained by Equations (13), (18), and (19) and drawn in Figure 2.

It can be seen from the figure that the fuzziness of the three equivalent tensions $\tilde{F}_{ij}^k \in [-0.01, 0.01]$N $(i = 49,\ j = 5,\ k = 1, 2, 3)$ when the cut level $\lambda >= 0.6$, that is to say the membership degrees of the equivalent fuzzy tensions are greater than 0.6 when $|\tilde{F}_{ij}^k| <= 0.01$ $(i = 49,\ j = 5,\ k = 1, 2, 3)$. By Equation (23), the distribution of the membership function for the total equivalent fuzzy tension can be obtained and shown as Figure 3, from which it can be seen that $\tilde{F}_{ij} \in$

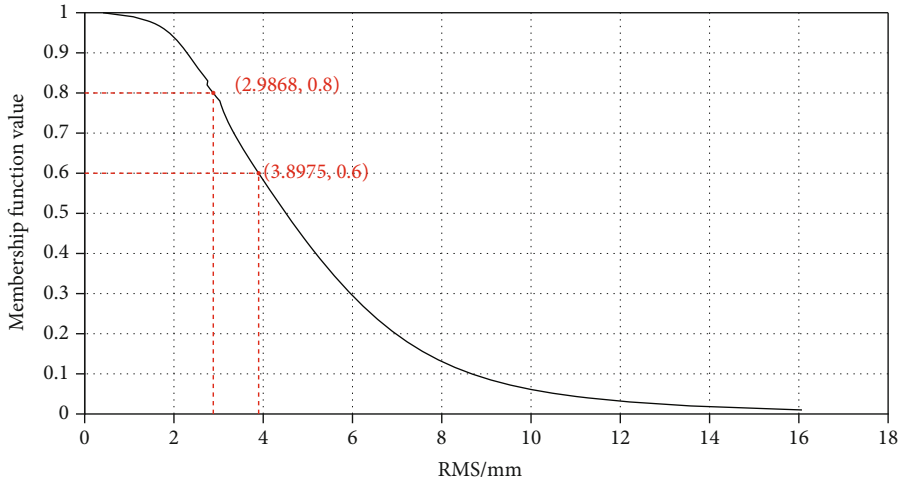

Figure 6: Distribution of RMS membership function after adjustment.

[9.44, 9.46] when the cut level is greater than 0.6 and the curve obeys the normal distribution with 9.4495 N mean and 0.0131 N standard deviation.

5.2. Surface Accuracy Analysis. Due to the measurement error, the nodal positions are also of uncertainty. It is assumed that the membership function for the nodal coordinates obeys the normal distribution with zero mean and 1 mm standard deviation. According to Equation (23), the membership function for RMS can be obtained as shown in Figure 4. The curve is an addition of multiple Gauss curves but not a single normal distribution curve. It can be seen from the figure that RMS < 60.3079 mm when the degree of the membership is greater than 0.6 and RMS < 26.2857 mm when the degree of the membership is greater than 0.8. The fuzziness of the surface accuracy is dispersed, and further adjustment should be carried out to increase the surface accuracy.

5.3. Adjusting the Cable Net Structure. To calculate the adjustment amount of the tension ties, the advance and retreat algorithm is used to solve the optimization model introduced in Section 4, and the RMS value changes in the interactive process are drawn in Figure 5 with the level cut set specified as 0.01, 0.6, 0.8, and 1.0, respectively, for example. From the iterative curves, it can be seen that the convergence speeds are fast in the first 10 steps and the RMS are rapidly decreased, but after that the convergence speed slows down; repetitive adjustment work is needed. What is more, it can be seen from Figure 5, the closer the λ-level cut value is to 1, the smaller the deviation of the RMS is. When $\lambda = 1.00$ with a small initial RMS, the coupling effect of front nodes is significant. It may occur that adjusting the tension tie can make the front nodes directly connected to it closer to the ideal position, but the nodes around tensioning tie are affected to deviate from the ideal position, thus making the adjusted RMS larger. This phenomenon makes the adjustment efficiency of advance and retreat algorithm reduced when RMS is small.

The results after 20 iterations are chosen to be the adjustment amount. After adjusting, the RMSs at different cut levels are drawn in Figure 6. It can be seen that RMS $<$ 3.8975 mm when the degree of the membership is greater than 0.6, and RMS < 2.9868 mm when the degree of the membership is greater than 0.8. Compared with the initial surface accuracy, the fuzziness of the surface accuracy is concentrated and the surface accuracy is increased.

6. Conclusion

We have developed a surface adjustment method for the cable net structures under multi-uncertainties including elastic deformation uncertainty, thermal deformation uncertainty, and measurement uncertainty.

The main contributions of this paper are presented as follows. (1) The uncertain variables are considered as the fuzzy values, membership functions, and λ-level cut sets are introduced to describe the fuzzy values. (2) The elastic deformation uncertainty, thermal deformation uncertainty, and tension measurement uncertainty are equivalent into a total equivalent fuzzy tension to simplify calculation. (3) The force density method is applied to modeling static equilibrium equations for cable net structures with fuzzy parameters. (4) An optimization model for the adjustment of cable net structures under multi-uncertainties is established.

According to the numerical example, the following conclusions can be summarized. (1) Using the advance and retreat algorithm to solve the optimization model can achieve fast convergence. (2) The adjustment efficiency of advance and retreat algorithm will be reduced when the initial RMS is small. (3) This method can be used to obtain the uncertainty distribution of the surface accuracy of cable net structure without sample only by engineering experience. (4) The fuzziness of the surface accuracy can be concentrated effectively by the proposed method.

Data Availability

The data used to support the findings of this study are available from the corresponding author upon request.

Conflicts of Interest

The authors declare that there is no conflict of interest regarding the publication of this paper.

Acknowledgments

The authors are very grateful to the references for their previous research works. This project is supported by the National Natural Science Foundation of China (Nos. 51775403 and 51905401).

References

[1] M. Mobrem, S. Kuehn, C. Spier, and E. Slimko, "Design and performance of Astromesh reflector onboard soil moisture active passive spacecraft," in *Proceedings of the IEEE Aerospace Conference*, pp. 1–10, Big Sky, MT, USA, 2012.

[2] H. W. Gang, C. Shi, M. Li, Z. Q. Deng, and R. Q. Liu, "Design and dynamic equivalent modeling of double-layer hoop deployable antenna," *International Journal of Aerospace Engineering*, vol. 2018, Article ID 9430267, 15 pages, 2018.

[3] R. Nie, B. Y. He, L. D. Zhang, and Y. G. Fang, "Deployment analysis for space cable net structures with varying topologies and parameters," *Aerospace Science and Technology*, vol. 68, pp. 1–10, 2017.

[4] J. G. Cai, Z. Ren, Y. F. Ding, X. Deng, Y. Xu, and J. Feng, "Deployment simulation of foldable origami membrane structures," *Aerospace Science and Technology*, vol. 67, pp. 343–353, 2017.

[5] G. G. Yang, D. W. Yang, Y. Q. Zhang, and J. L. Du, "Form-finding design of cable-mesh reflector antennas with minimal length configuration," *Aerospace Science and Technology*, vol. 63, pp. 9–17, 2017.

[6] Y. S. Fan, X. F. Ma, Z. J. Li, and T. J. Li, "Sensitivity analysis of surface accuracy of mesh antennas to cable length," *Applied Mechanics and Materials*, vol. 456, pp. 234–239, 2013.

[7] J. Mitsugi, T. Yasaka, and K. Miura, "Shape control of the tension truss antenna," *AIAA Journal*, vol. 28, no. 2, pp. 316–322, 1990.

[8] Y. Q. Tang and T. J. Li, "Equivalent-force density method as a shape-finding tool for cable-membrane structures," *Engineering Structures*, vol. 151, pp. 11–19, 2017.

[9] T. Hiroaki and M. C. Natori, "Surface control of cable-network structures based on concept of self-equilibrated stresses," *JSME International Journal Series C Mechanical Systems, Machine Elements and Manufacturing*, vol. 49, no. 4, pp. 1067–1072, 2006.

[10] J. L. Du, Y. L. Zong, and H. Bao, "Shape adjustment of cable mesh antennas using sequential quadratic programming," *Aerospace Science and Technology*, vol. 30, no. 1, pp. 26–32, 2013.

[11] Z. Y. Niu, X. L. Li, S. M. Wang, and Y. Li, "Shape accuracy optimization adjustment for deployable antenna reflector of space truss," *Machinery design & manufacture*, vol. 6, no. 1, pp. 123–125, 2011.

[12] T. J. Li, H. Q. Deng, Y. Q. Tang, J. Jiang, and X. F. Ma, "Accuracy analysis and form-finding design of uncertain mesh reflectors based on interval force density method," *Proceedings of the Institution of Mechanical Engineers, Part G: Journal of Aerospace Engineering*, vol. 231, no. 11, pp. 2163–2173, 2017.

[13] S. C. Yuan, B. G. Yang, and H. F. Fang, "Form-finding of large deployable mesh reflectors with elastic deformations of supporting structures," in *2018 AIAA Spacecraft Structures Conference*, Kissimmee, Florida, USA, 2018.

[14] A. Johari, A. Hooshmand Nejad, and S. Mousavi, "Probabilistic model of unsaturated slope stability considering the uncertainties of soil-water characteristic curve," *Scientia Iranica*, vol. 25, no. 4, pp. 2039–2050, 2018.

[15] A. Johari, A. R. Khodaparast, and A. A. Javadi, "An analytical approach to probabilistic modeling of liquefaction based on shear wave velocity," *Iranian Journal of Science and Technology, Transactions of Civil Engineering*, vol. 43, no. S1, pp. 263–275, 2019.

[16] A. Johari and S. Mousavi, "An analytical probabilistic analysis of slopes based on limit equilibrium methods," *Bulletin of Engineering Geology and the Environment*, vol. 78, no. 6, pp. 4333–4347, 2019.

[17] C. Soize, "A comprehensive overview of a non-parametric probabilistic approach of model uncertainties for predictive models in structural dynamics," *Journal of Sound and Vibration*, vol. 288, no. 3, pp. 623–652, 2005.

[18] J. Ma, J. J. Chen, J. G. Zhang, and T. Jiang, "Interval factor method for interval finite element analysis of truss structures," *Multidiscipline Modeling in Materials and Structures*, vol. 1, no. 4, pp. 367–376, 2005.

[19] C. W. Fei, H. Li, C. Lu, L. Han, B. Keshtegar, and O. Taylan, "Vectorial surrogate modeling method for multi-objective reliability design," *Applied Mathematical Modelling*, vol. 109, pp. 1–20, 2022.

[20] C. W. Fei, H. T. Liu, R. P. Liem, Y. Choy, and L. Han, "Hierarchical model updating strategy of complex assembled structures with uncorrelated dynamic modes," *Chinese Journal of Aeronautics*, vol. 35, no. 3, pp. 281–296, 2022.

[21] T. J. Li, Y. Q. Tang, and T. Zhang, "Surface adjustment method for cable net structures considering measurement uncertainties," *Aerospace Science and Technology*, vol. 59, pp. 52–56, 2016.

Hindawi
International Journal of Aerospace Engineering
Volume 2022, Article ID 4265384, 8 pages
https://doi.org/10.1155/2022/4265384

Research Article

Mechanics Design of Conical Spiral Structure for Flexible Coilable Antenna Array

Hairui Wang,[1,2] Yao Zhang,[1] Siyu Chen,[1] Yinji Ma,[1] Heling Wang,[3] Ying Chen,[3] and Xue Feng[1]

[1]*AML, Department of Engineering Mechanics, Center for Flexible Electronics Technology, Tsinghua University, Beijing 100084, China*
[2]*State Key Laboratory for Strength and Vibration of Mechanical Structures, Xi'an Jiaotong University, Xi'an 710049, China*
[3]*Institute of Flexible Electronics Technology of THU, Jiaxing 314000, China*

Correspondence should be addressed to Ying Chen; chenying@ifet-tsinghua.org

Received 19 March 2022; Accepted 7 April 2022; Published 24 May 2022

Academic Editor: Tuanjie Li

Limited by the effective launch capacity of a rocket, the deployable antenna is very important in the design of spaceborne antenna array. Compared to traditional deployable antenna, flexible coilable antenna array has higher surface precision and better vibration control and therefore is more suitable for high frequency communication. In order to minimize the weight of satellite and reduce cost of its launch, a design guideline to the geometry parameters of flexible coilable antenna array is crucial. Existing models cannot be directly applied to interaction and large deformation between coilable membrane and conical spiral antenna in the flexible coilable antenna array. Hence, the geometry parameters of the conical spiral structure and the thickness of the coilable membrane in the flexible coilable antenna array have not been optimized yet. In this paper, the interaction between the coilable membrane and the concial spiral antenna is analyzed in the antenna array. A concise formula is derived to predict the critical force that flattens the conical spiral antenna by a coiling scroll. Combined with a theoretical model to predict the deformation of the membrane, the model provides an important theoretical support for the lightweight design and mechanical design of flexible coilable antenna array, such as the thickness of the coilable membrane. The proposed design is validated by experiments. The above findings have potential applications in the effective reduction of antenna array weight and satellite launch costs.

1. Introduction

Antenna is an important terminal in information transmission system [1–4]. Limited by the effective launching capacity of the rocket, the existing large-scale spaceborne antenna array is usually folded to reduce the space occupied at the launching stage [5–8] and then deployed in orbit and responsible for communication transmission. For example, tensegrity-membrane and umbrella antenna have been put into use on the satellite [9–11]. Due to folding traces on the antenna surface, these folded antennas have problems such as large overall weight and poor shape accuracy [12–15]. Hence, it is difficult to apply in high-frequency communication which requires strict control of membrane deformation and vibration [16–18]. Inspired by serpentine design with low strain in two-dimensional (2D) flexible electronics [19–22], flexible coilable antenna array with 2D patch antennas can overcome the above problems [23]. However, the 2D patch antenna behaving linear polarization cannot handle the ionosphere of the atmosphere compared with 3D spiral antennas behaving circular polarization [24]. Hence, we propose a new concept of a spaceborne antenna array, i.e., a flexible coilable array with resilient spiral antennas which behave linear

polarization and has a low strain under the compression, as shown in Figure 1. This coilable array has advantages such as high shape accuracy and deployment and small impact and vibration, which has not been used on satellites at present.

When the flexible coilable antenna array is coiling, the conical spiral antenna would be compressed and combined with coilable membrane. There may be two extremely unfavorable deformation conditions at this time. When the thickness of the coilable membrane is too large, the membrane is too rigid to roll and also overweight. On the other hand, when the thickness of the membrane is too small, the membrane is too compliable to compress conical spiral antennas on the surface of the scroll. Therefore, a theoretical model is essential to determine the minimum thickness required for the coilable membrane to fully compress the conical spiral antenna and to achieve lightweight design of membrane to optimize the launching cost. However, during the coiling process, the conical spiral antenna from the outer ring to the inner ring gradually contacts the bottom surface of membrane. The conical spiral antenna has a complex, large deformation and displacement, exhibiting significant nonlinearity [25–28]. It remains challenging to model the mechanics design of conical spiral antenna for flexible coilable antenna array. The widely used close-coiled spring theory and sparse-coiled spring theory are only suitable for small deformation in the linear elastic regime [29–33]. In addition, there are some nonlinear theories in consideration of the change of the helix angle [34–37]. However, the constraint of the underlying membrane on the deformation of the spring structure is not considered, such that these models cannot be applied to the coiling process. Finite element models were adopted to obtain the deformation process of a general conical spiral antenna [38–41] but could not lead to any analytical solution or scaling law [42–44]. It is of great significance to the lightweight design and mechanical design of the flexible coilable antenna array.

This paper is arranged as follows: the coiling behavior of the flexible coilable antenna array with conical spiral antennas is studied. The deformation between the coilable membrane and the spiral antenna is deduced during the coiling process. The finite element method and the phototype are used to verify the accuracy of the theoretical derivation. This provides modeling and numerical support and theoretical guidance for the design of conical spiral antenna and the selection of membrane thickness.

2. Structural Model of the Flexible Coilable Antenna Array

Figure 1 shows a schematic diagram of flexible coilable antenna array with three-dimensional (3D) conical spiral antennas during the coiling process. The coilable antenna array is mainly composed of a feed, a flexible coilable membrane, and several conical spiral antennas. A large number of conical spiral antennas are uniformly distributed on the coilable membrane. One end of the conical spiral antenna is fixedly connected with the coilable membrane, and the other end is traction-free. The membrane is rolled up by a drive motor to compress the coilable antenna array and press it on the scroll, as shown in Figure 1(b). After the coilable antenna array enters its orbit, the coilable membrane rotates in the opposite direction and unfolds such that the antennae return to the original 3D state due to elasticity, as shown in Figure 1(d).

For ease of analyzing the mechanical behavior of the coilable antenna array, this antenna model would be simplified as coilable membrane with conical spiral antenna. During the coiling process, the straight portion of the coilable membrane (see Figure 1(d)) has rigid-body displacement in the horizontal direction without deformation. The coiled portion presses and deforms the spiral antenna. The conical spiral antenna is a tubular structure fabricated by highly elastic material. The inner cavity of the conical spiral tube (typical diameter is greater than 1 mm) is arranged with a metal wire as a radiating element (typical diameter is less than 0.2 mm). The mechanical behavior of the spiral tube is considered at this time since the metal wire is thin.

At the moment of contact, the height H of the antenna and the radius R_r of the scroll are related geometrically via (see Figure 2(a))

$$2\sin^2\frac{\alpha}{2} = \frac{H}{R_r}. \tag{1}$$

To ensure that the conical spiral antenna can be flattened rather than tipped during the coiling process, the contract angle α between the antenna and the membrane should be close to zero for a vertical pressing. Given the height of the conical spiral antenna, this requires the radius of the scroll to be sufficiently large, so that the height of the conical spiral antenna is much smaller than the radius of the scroll. Therefore, the interaction between the coilable membrane and one conical spiral antenna can be regarded as the vertical force applied by two planar membranes.

Figures 2(b) and 2(c) show the cross section of the conical spiral antenna, which define geometric parameters of the flexible coilable antenna array. Thickness of the coilable membrane is defined as b_m. R_r represents the radius of the scroll. Pitch of the conical spiral antenna is defined as t. R_n and R_1 are the upper and lower radius of the conical spiral antenna. From the biggest layer to the smallest layer for the radius of the conical spiral antenna, it numbers as 1, 2, i, and n, successively. d is the diameter of the conical spiral antenna. b is the ratio of the inner and outer diameter of the conical spiral antenna. L is the total length of the conical spiral antenna, which is equal to $n\pi(R_1 + R_n)$. The radius of the ith layer is $R_i = R_1 - i/n(R_1 - R_n)$.

3. Mechanical Behavior of Conical Spiral Antenna

For the spiral antenna to be fully flattened in the coiling process, the membrane rigidity needs to be much larger than the antenna rigidity, such that the membrane deformation is much smaller than the antenna deformation. Therefore, the mechanical behaviors of the conical spiral antenna can be analyzed without consideration of the membrane

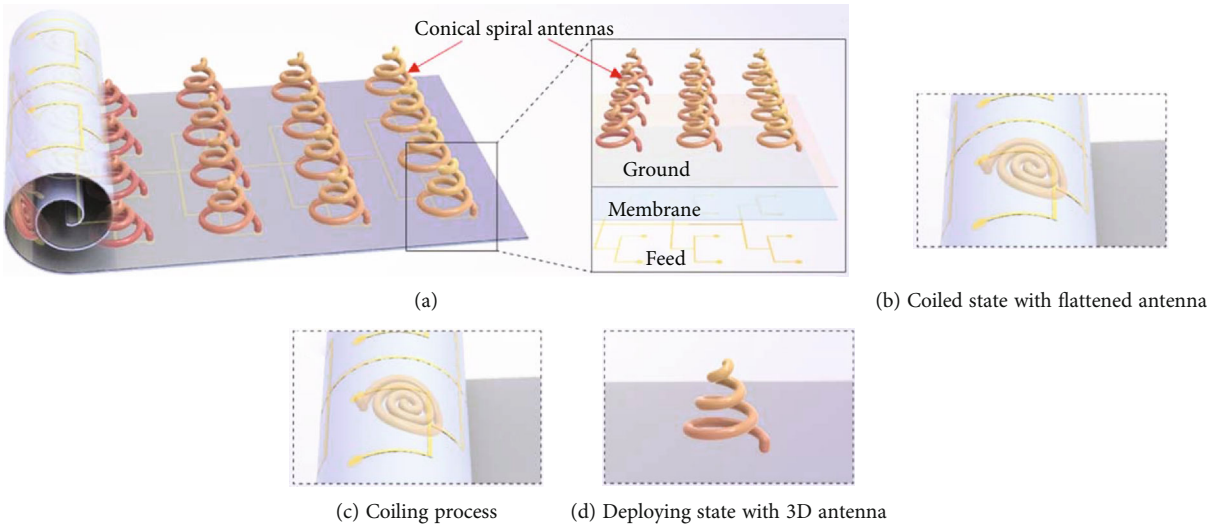

Figure 1: Schematic illustration of flexible coilable antenna array with conical spiral antenna.

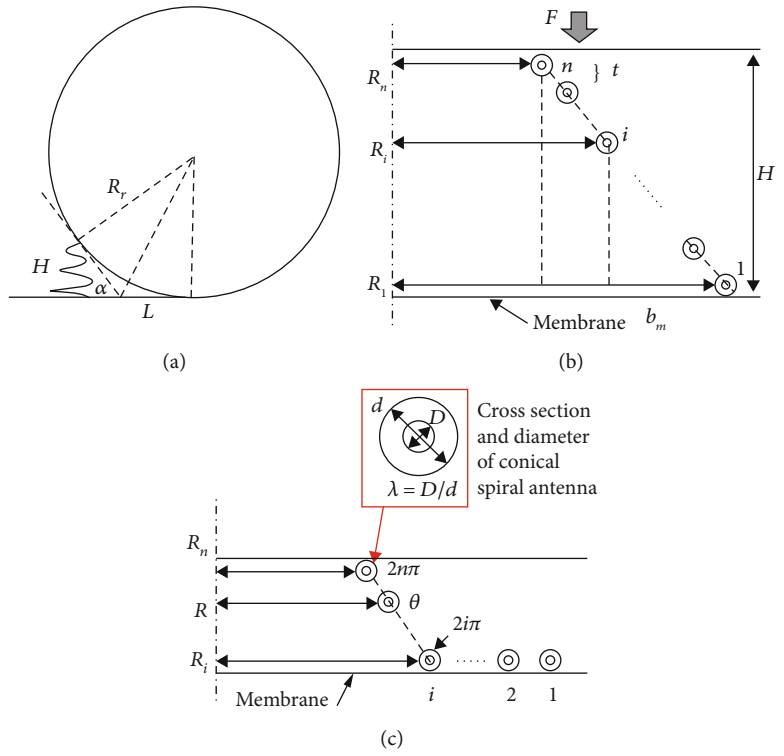

Figure 2: (a) Geometric relationship between scroll and conical spiral antenna. (b) Cross section of conical spiral antenna at the initial state. (c) Cross section of conical spiral antenna under partial compression.

deformation. The bottom end of the conical spiral antenna is fixedly connected to the bottom of coilable membrane, and the contact force F from the top membrane is applied vertically on the top end. During the compressive process, the bottom of the spiral antenna would be in contact with the coilable membrane of the antenna and no longer separate.

Because the conical spiral antenna has a small helix angle, the deformation is dominated by torsion. It is different for the force required to flatten each layer of the conical spiral antenna. Initially, for a small deformation, the displacement of the antenna at the contact position, induced by the contact force, can be obtained analytically as

$$\delta = \int_0^L \frac{F \cdot R^2}{GI_p} ds = \int_{R_n}^{R_1} \frac{2\pi F R^3 n}{GI_p(R_1 - R_n)} dR = \frac{n\pi F\left(R_1^4 - R_n^4\right)}{2GI_p(R_1 - R_n)}, \tag{2}$$

where a polar angle θ of the conical spiral antenna goes downward from the smallest to the biggest for the radius. $ds = Rd\theta = (2\pi nR/R_1 - R_n)dR$ is the derivative of the conical spiral antenna. G is the shear modulus. $I_p = \pi d^4(1 - \lambda^4)/32$

is the polar moment of inertia of the hollow circular section with respect to center of circle for the conical spiral antenna. $\lambda = D/d$ is the ratio of inside and outside diameters of the tube.

The stiffness in the ith layer for the conical spiral antenna can be expressed as $k_i = GI_p/\pi R_i^3$ based on the torsional theory with small deformation. When the force exceeds a critical value,

$$F_1 = \frac{tGI_p}{2\pi R_1^3}. \tag{3}$$

The first layer before all others of the spiral antenna is fully flattened on the membrane and no longer has displacement. At this moment, the displacement at the contact position with the membrane is t. When the pressing force further increases, the model can be regarded as a spring with outer radius R_2 replacing R_1 in the previous analysis. In general, the displacement can be obtained similarly as

$$\delta = i \cdot t + \frac{n\pi F\left(R_i^4 - R_n^4\right)}{2GI_p(R_1 - R_n)} = \frac{n}{R_1 - R_n}\left[\frac{\pi F}{2GI_p}\left(R_i^4 - R_n^4\right) + t(R_1 - R_i)\right]. \tag{4}$$

The maximum force required to flatten all layers of the conical spiral antenna is

$$F_0 = \frac{tGI_p}{2\pi R_n^3}. \tag{5}$$

Based on Equation (6), the normalized displacement $nt - \delta/nt$ can be expressed in terms of normalized force F/F_0 as

$$\left(\frac{nt - \delta}{nt}\right)\left(\frac{R_1}{R_n} - 1\right) = \frac{3}{4}\left(\frac{F_0}{F}\right)^{1/3} + \frac{F}{4F_0} - 1. \tag{6}$$

Equation (6) illustrates that the maximum compressive force is closely related to the third power of the minimum radius of the conical spiral antenna. Equation (7) gives the quantitative relationship between normalized force and displacement during compression. At the initial stage of compression, the force on the conical spiral antenna is linearly proportional to its displacement. When F approaches F_0, the normalized force increases rapidly with the normalized displacement. The stiffness of the conical spiral antenna increases during the entire compressive process.

Numerical simulation is performed to validate the above analytical model. Several 3D geometric models of the conical spiral antenna are established in different geometric parameters (G, t, d, R_1, R_n, etc.) by using a modeling software UG. The finite element model of the conical spiral antenna is established by using the commercial software ABAQUS. The upper and lower membranes are defined by analytical rigid body, as shown in Figures 2(b) and 2(c). And there is a friction between the top of the antenna and the upper membrane. The beam element is applied to the coilable antenna model. Hence, there is a complex nonlinear contact between the conical spiral antenna and the membrane in the numerical model, making it difficult to predict the maximum force. When the conical spiral is fully flattened, it has a great effect on the convergence and accuracy of the numerical results. Therefore, the corresponding force extracted as a comparison, when the normalized displacement is 60-90%. As shown in Figure 3, the force and displacement in the theoretical solution are validated by finite element analysis (FEA) without any parameter fitting, for the conical spiral antenna with polypropylene (PP) material. The baseline for the geometrical and material parameters of conical spiral antenna are $E = 890\,\text{MPa}$, $d = 1\,\text{mm}$, $\lambda = 0.2$, $R_1 = 2.5\,\text{mm}$, $R_n = 14\,\text{mm}$, $t = 4\,\text{mm}$, and $n = 5$. The parameter $(1 - \delta/nt)$ $(R_1/R_n - 1)$ has a large of range.

It can be seen that there is a high nonlinearity between the normalized force and displacement in the conical spiral antenna. It is shown that, through the numerical analysis, the changes of geometric parameters for the conical spiral antenna have no effect on the nonlinear relationship. It is proved that numerical results are highly consistent with the theoretical results. Therefore, this derived theory can be used to estimate the compressive force and displacement. In turn, it can be used for the design of conical spiral antenna structure yet.

4. Thickness of Coilable Membrane

The foregoing studies have investigated the deformation behavior of the conical spiral antenna under the force applied by two parallel membranes. Dozens of conical spiral antennas are periodically arrayed on the coilable membrane in both the circumferential and the axial directions, where the spacing between adjacent antennas is defined as w_1 and w_2, respectively. As the spacing is much smaller than the membrane size, the period force F applied by the conical spiral antenna on the rolled membrane is equivalent to a uniform pressure $P = F/w_1 \cdot w_2$ in both circumferential and axial directions. The larger the diameter of the scroll, the greater the thickness (b_m) of the membrane can be wound. The increasing thickness magnifies the rigidity of the membrane itself, and the total weight of the antenna increases at the same time. To optimize the flight cost of the spacecraft, it is necessary to determine the minimum thickness required by the coilable membrane to fully compress the antenna.

For the pressure P applied by the conical spiral antenna much smaller than the elastic modulus (E_m) of membrane, i.e., $P \ll E_m$, the induced membrane deformation (ΔR_r) is small and linearly elastic, as shown in Figure 4. The Poisson's ratio of the membrane is defined as ν_m. The stress in circumferential direction of the membrane can be obtained from force balance as

$$\sigma_\varphi = \frac{P \cdot 2\pi R_r W_m}{2 \cdot b_m W_m} = \frac{P \cdot \pi R_r}{b_m}. \tag{7}$$

Noticing that the strain in radial direction is negligible for a membrane with small thickness, the membrane deformation is

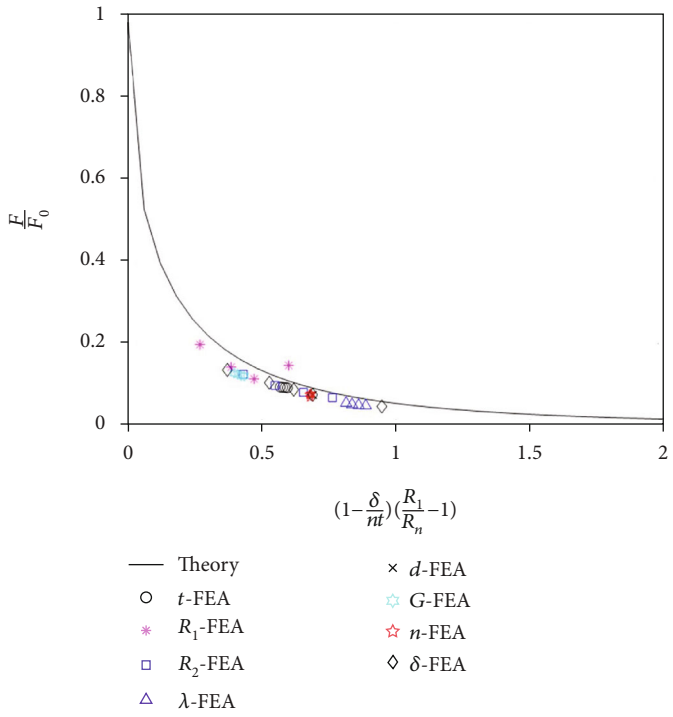

Figure 3: Theoretical and finite element analysis (FEA) results of the normalized force F/F_0 vs. normalized displacement $(1-\delta/nt)(R_1/R_2-1)$ relationship in different geometric parameters (G, t, d, R_1, R_2, n, and δ).

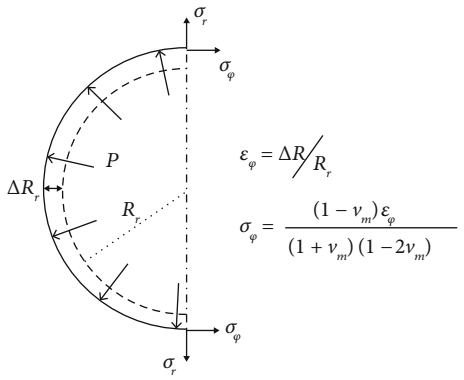

Figure 4: Schematic illustration of the membrane deformation after coiling.

$$\frac{\Delta R}{R_r} = \varepsilon_\varphi = \frac{\pi R_r P\left(1-\nu_m-2{\nu_m}^2\right)}{E_m \cdot b_m \cdot (1-\nu_m)}. \tag{8}$$

When the conical spiral antennas are fully flattened, the membrane deformation is equal to the cross-sectional diameter of the conical spiral structure, i.e., $\Delta R = d$, and a pressure applied by the membrane with thickness b_m is $E_m d b_m(1-\nu_m)/\pi R_r^2(1-\nu_m-2{\nu_m}^2)$. According to Equation (6), the pressure needs to be larger than $tGI_p/2\pi w_1 \cdot w_2 R_n^3$ for the membrane to fully flatten the antenna, i.e.,

$$\frac{E_m d b_m(1-\nu_m)}{\pi R_r^2(1-\nu_m-2{\nu_m}^2)} \geq \frac{tGI_p}{2\pi w_1 \cdot w_2 R_n^3}. \tag{9}$$

Hence, with the other parameters given, the required thickness of the membrane is

$$b_m > b_{\min} = \frac{tGI_p R_r^2\left(1-\nu_m-2{\nu_m}^2\right)}{2w_1 w_2 d E_m R_1^3(1-\nu_m)}. \tag{10}$$

The minimum thickness $b_{\min}$ of the membrane can be calculated, which is related to the geometrical and material parameters and the arrangement density of the conical spiral antenna. Taking the C-band conical spiral antenna with polymer as an example, the geometrical and material parameters of conical spiral antenna and membrane and the calculated minimum thickness $b_{\min}$ are shown in Table 1. Finally, one prototype for flexible coilable antenna array with conical spiral antennas is fabricated as shown in Figure 5. The

Table 1: Parameters of membrane and conical spiral antenna.

Antenna, membrane	ν, ν_m	t (mm)	E, E_m (MPa)	d (mm)	R_r (mm)	w_1, w_2 (mm)	R_1 (mm)	b_m (mm)
PP, PET	0.42, 0.32	4	890, 4000	1	100	40, 40	2	0.018
PI, PI	0.34, 0.34	4	4000, 4000	1	100	40, 40	2	0.087

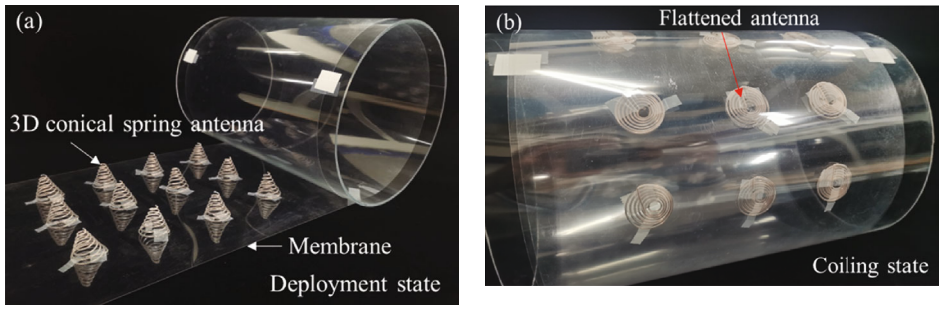

(a) (b)

Figure 5: Prototype of the fabricated flexible coilable antenna array.

thickness of the coilable membrane fabricated by polyethylene terephthalate (PET) is 0.1 mm, and the diameter of conical spiral antenna fabricated by polypropylene (PP) is 1 mm. Twelve conical spiral antennas are periodically arrayed on the coilable membrane in both the circumferential direction with 50 mm and the axial direction with 50 mm. The radius of scroll is 75 mm. Under the action of the membrane, the conical spiral antennas can be fully flattened and resiled during the coiling and outspreading processes, separately, as shown in Figure 5.

5. Conclusion

The flexible coilable antenna array with conical spiral antenna is a brand new spaceborne array. This paper investigates mechanical behavior of the flexible coilable antenna array during the coiling process. A theoretical relationship of the conical spiral antenna is given between normalized force and displacement, which exhibits a high nonlinear behavior. FEA is performed to validate the above theoretical model. Furthermore, the thickness of the coilable membrane to fully flatten the antenna can be predicted by an analytical solution about the geometrical and material parameters between the coilable membrane and the conical spiral antenna. This research provides important theoretical support for the design and fabrication of the flexible coilable antenna array with conical spiral antennas.

Data Availability

The data used to support the findings of this study are included within the article.

Conflicts of Interest

The authors declare that there are no conflicts of interest regarding the publication of this paper.

Acknowledgments

The authors gratefully acknowledge the financial supports of NSFC (Grant Nos. U20A6001, 11625207, 11921002, and 12102223) and State Key Laboratory for Strength and Vibration of Mechanical Structures (SV2021-KF-09).

References

[1] Z. Xie, R. Avila, Y. Huang, and J. A. Rogers, "Flexible and stretchable antennas for biointegrated electronics," *Advanced Materials*, vol. 32, no. 15, p. 1902767, 2020.

[2] Y. Zhang, D. C. Castro, Y. Han et al., "Battery-free, lightweight, injectable microsystem for in vivo wireless pharmacology and optogenetics," *Proceedings of the National Academy of Sciences*, vol. 116, no. 43, pp. 21427–21437, 2019.

[3] Z. Xie, B. Ji, and Q. Huo, "Mechanics design of stretchable near field communication antenna with serpentine wires," *Journal of Applied Mechanics -Transactions of the ASME*, vol. 85, no. 4, 2018.

[4] S. Kanaparthi, V. R. Sekhar, and S. Badhulika, "Flexible, eco-friendly and highly sensitive paper antenna based electromechanical sensor for wireless human motion detection and structural health monitoring," *Extreme Mechanics Letters*, vol. 9, pp. 324–330, 2016.

[5] C. Wang, Y. Wang, P. Lian et al., "Space phased array antenna developments: a perspective on structural design," *IEEE Aerospace and Electronic Systems Magazine*, vol. 35, no. 7, pp. 44–63, 2020.

[6] H. Fang, M. Lou, J. Huang, L. Hsia, and G. Kerdanyan, "Design and development of an inflatable reflectarray antenna," *IPN Progress Report*, vol. 149, pp. 1–18, 2002.

[7] H. Wang, D. Zhao, Y. Jin, M. Wang, T. Mukhopadhyay, and Z. You, "Modulation of multi-directional auxeticity in hybrid origami metamaterials," *Applied Materials Today*, vol. 20, p. 100715, 2020.

[8] H. Yang, H. Guo, Y. Wang, J. Feng, and D. Tian, "Analytical solution of the peak bending moment of an M boom for membrane deployable structures," *International Journal of Solids and Structures*, vol. 206, pp. 236–246, 2020.

[9] S. Zhang, J. Du, B. Duan, G. Yang, and Y. Ma, "Integrated structural–electromagnetic shape control of cable mesh reflector antennas," *AIAA Journal*, vol. 53, no. 5, pp. 1395–1399, 2015.

[10] P. K. C. Wang and J. C. Sarina, "Control of reflector vibrations in large spaceborne antennas by means of movable dampers," *Journal of Applied Mechanics-Transactions of the Asme*, vol. 50, no. 3, pp. 669–673, 1983.

[11] Y. Liu, F. Pan, B. Ding, Y. Zhu, K. Yang, and Y. Chen, "Multistable shape-reconfigurable metawire in 3D space," *Extreme Mechanics Letters*, vol. 50, article 101535, 2022.

[12] Y. Rahmat-Samii and R. Haupt, "Reflector antenna developments: a perspective on the past, present and future," *IEEE Antennas and Propagation Magazine*, vol. 57, no. 2, pp. 85–95, 2015.

[13] Z. M. Xia, C. G. Wang, and H. F. Tan, "Quasi-static unfolding mechanics of a creased membrane based on a finite deformation crease–beam model," *International Journal of Solids and Structures*, vol. 207, pp. 104–112, 2020.

[14] S. Yang and C. Sultan, "Deployment of foldable tensegrity-membrane systems via transition between tensegrity configurations and tensegrity-membrane configurations," *International Journal of Solids and Structures*, vol. 160, pp. 103–119, 2019.

[15] X. Wu, R. Cheng, T. H. T. Chan, G. Liu, and J. Xia, "Algorithm for rapidly predicting the worst surface accuracy of deployable mesh reflectors," *Applied Mathematical Modelling*, vol. 98, pp. 229–244, 2021.

[16] S. H. Eedala, S. Elakiyaa, R. Nethra, R. Asha, and M. Jayakumar, "Design of helical array antenna based ground terminal for satellite communication on the move," in *4th International Conference on Electronics, Communication and Aerospace Technology*, Coimbatore, India, Nov. 2020.

[17] J. Jiang, L. Zhang, N. Luo et al., "An ultra-wideband stacked spiral-helix composite antenna," in *14th European Conference on Antennas and Propagation*, Copenhagen, Denmark, March 2020.

[18] M. A. Elmansouri, J. B. Bargeron, and D. S. Filipovic, "Ultra-wideband spiral-helix antenna array," in *Antennas and Propagation Society International Symposium*, Memphis, TN, USA, July 2014.

[19] X. Meng, B. Liu, Y. Wang, T. Zhang, and J. Xiao, "Third-order polynomials model for analyzing multilayer hard/soft materials in flexible electronics," *Journal of Applied Mechanics-Transactions of the Asme*, vol. 83, no. 8, 2016.

[20] K. Sim, S. Chen, Z. Li et al., "Three-dimensional curvy electronics created using conformal additive stamp printing, Nature," *Electronics*, vol. 2, no. 10, pp. 471–479, 2019.

[21] C. Wang, S. Zhang, S. Nie, Y. Su, W. Chen, and J. Song, "Buckling of a stiff thin film on a bi-layer compliant substrate of finite thickness," *International Journal of Solids and Structures*, vol. 188-189, pp. 133–140, 2020.

[22] T. Li and Z. Suo, "Deformability of thin metal films on elastomer substrates," *International Journal of Solids and Structures*, vol. 43, no. 7-8, pp. 2351–2363, 2006.

[23] M. R. M. Hashemi, A. C. Fikes, M. Gal-Katziri et al., "A flexible phased array system with low areal mass density, Nature," *Electronics*, vol. 2, no. 5, pp. 195–205, 2019.

[24] Y. Han, K. Hu, R. Zhao et al., "Design of combined printed helical spiral antenna and helical inverted-f antenna for unmanned aerial vehicle application," *IEEE Access*, vol. 8, pp. 54115–54124, 2020.

[25] M. Wu and W. Hsu, "Modelling the static and dynamic behavior of a conical spring by considering the coil close and damping effects," *Journal of Sound and Vibration*, vol. 214, no. 1, pp. 17–28, 1998.

[26] V. Yildirim, "A parametric study on the free vibration of non-cylindrical helical springs," *Journal of Applied Mechanics-Transactions of the Asme*, vol. 65, no. 1, pp. 157–163, 1998.

[27] Y. Luxenburg and S. Givli, "The static response of axisymmetric conical shells exhibiting bistable behavior," *Journal of Applied Mechanics-Transactions of the Asme*, vol. 88, no. 11, 2021.

[28] R. Mirzaeifar, R. DesRoches, and A. Yavari, "A combined analytical, numerical, and experimental study of shape-memory-alloy helical springs," *International Journal of Solids and Structures*, vol. 48, no. 3-4, pp. 611–624, 2011.

[29] T. Iritani, A. Shozaki, B. Sheng, M. Sugimoto, T. Okazaki, and M. Aketa, "70 Prediction of the dynamic characteristics in valve train design of a diesel engine," *SAE Transactions*, vol. 111, pp. 1–7, 2002.

[30] F. C. Grant, "Energy analysis of the conical-spring oscillator," *American Journal of Physics*, vol. 54, no. 3, pp. 227–233, 1986.

[31] M. Paredes and E. Rodriguez, "Optimal design of conical springs," *Engineering with Computers*, vol. 25, no. 2, pp. 147–154, 2009.

[32] B. Zhou, Z. Wang, and S. Xue, "Mechanical model for superelastic helical spring of shape memory alloy, Journal of," *Mechanical Engineering*, vol. 55, no. 8, pp. 56–64, 2019.

[33] E. Rodriguez, M. Paredes, and M. Sartor, "Analytical behavior law for a constant pitch conical compression spring," *Journal of Mechanical Design-Transactions of the ASME*, vol. 128, no. 6, pp. 1352–1356, 2006.

[34] Y. He, G. Zou, X. Pan, F. Zhang, and W. He, "Nonlinear theory and experimental study of helical spring," *Engineering Mechanics*, vol. 14, pp. 56–61, 1994.

[35] L. Hong, H. Yunzeng, and Y. Lihong, "Nonlinear theory of conical helical spring," *Journal of Harbin Engineering University*, vol. 26, pp. 628–632, 2005.

[36] J.-S. Chen and I. S. Chen, "Deformation and vibration of a spiral spring," *International Journal of Solids and Structures*, vol. 64-65, pp. 166–175, 2015.

[37] N. V. Viet, W. Zaki, R. Umer, and Y. Xu, "Mathematical model for superelastic shape memory alloy springs with large spring index," *International Journal of Solids and Structures*, vol. 185-186, pp. 159–169, 2020.

[38] Z. Sen, C. Shaofeng, W. Huanding, and Q. Ting, "Finite element analysis of spatial curved beam in large deformation," *Journal of Southeast University*, vol. 26, pp. 591–596, 2010.

[39] T. Meilan, W. Xinwei, and Z. Yong, "An efficient finite element of spatial curved beams, Chinese Journal of," *Computational Mechanics*, vol. 1, pp. 78–82, 2005.

[40] D. F. Lalo, M. Greco, and M. Meroniuc, "Numerical modeling and experimental characterization of elastomeric pads bonded in a conical spring under multiaxial loads and pre-compression," *Mathematical Problems in Engineering*, vol. 2019, 14 pages, 2019.

[41] J. Zhang, Z. Qi, Y. Zhuo, and S. Guo, "Stiffness analysis of helix spring using exact geometric beam element," *Engineering Mechanics*, vol. 37, p. 16, 2020.

[42] K. Zhou and F. Xiao, "Contact simulation of cylindrical helical spring based on Ansys," *Mechanical Engineering & Automation*, vol. 212, pp. 60–64, 2019.

[43] X. Yuan, S. M. Won, M. Han et al., "Mechanics of encapsulated three-dimensional structures for simultaneous sensing of pressure and shear stress," *Journal of the Mechanics and Physics of Solids*, vol. 151, article 104400, 2021.

[44] S. Li, M. Han, J. A. Rogers, Y. Zhang, Y. Huang, and H. Wang, "Mechanics of buckled serpentine structures formed via mechanics-guided, deterministic three-dimensional assembly," *Journal of the Mechanics and Physics of Solids*, vol. 125, pp. 736–748, 2019.

Hindawi
International Journal of Aerospace Engineering
Volume 2022, Article ID 4676944, 11 pages
https://doi.org/10.1155/2022/4676944

Research Article

Pretension Design and Analysis of Deployable Mesh Antenna considering the Effect of Gravity

Guanlong Su, Xiaofei Ma, Yang Li, Yesen Fan, and Hui Wang

Xi'an Institute of Space Radio Technology, Xi'an 710100, China

Correspondence should be addressed to Xiaofei Ma; maxf041600@sina.com

Received 17 March 2022; Revised 13 April 2022; Accepted 13 April 2022; Published 9 May 2022

Academic Editor: Tuanjie Li

The difference between the space and the earth environment has significantly influenced the shape accuracy of the antenna reflector surface. With the increasing demand for the aperture of the antenna reflector, gravity has become one of the main factors that restrict the accuracy. In this paper, a new method for pretension design considering the effect of gravity is proposed. The design surface can be well restored to the ideal surface in orbit. Meanwhile, this method can avoid flipping antenna reflectors or extensive experiments for modification during ground adjustment. Then, the feasibility and effectiveness of the design method are validated by several numerical simulations. Moreover, the results are compared with the previous method and the differences have been discussed in detail. Finally, the effects of cable radius, cable length, and elastic modulus of the mesh reflector have been researched, respectively.

1. Introduction

The deployable mesh antennas are widely used in spatial applications due to the good stowed/deployed ratio [1], such as TerreStar antenna, Skyterra antenna, AstroMesh hoop truss antenna, and the antenna of JAXA Engineering Test Satellite. With the vigorous development of aerospace technology, the demand for large-scale space deployable antennas is becoming urgent. At the same time, more requirements emerge in the aspects such as tiny signal transmission on the ground, great capacity of information transmission, and the realization of the high resolution of remote sensing. All of these lead to the necessity of a large aperture deployable antenna with high accuracy [2]. As an indispensable component that highly affects accuracy, the cable net structure is always one of the research hot pots. The cable net structure is a family of flexible tension structures characterized by geometric solid nonlinearities. The initial stiffness and shape can be achieved by pretension design. The purpose is to find a surface close to the desired surface under specific tension loads. Therefore, the pretension distribution plays a vital role in the surface accuracy of deployable mesh reflectors.

To form a parabolic surface, the rigidity of deployable mesh reflectors is supplied by applying pretension to the cables. This process of pretension design is called form-finding [3]. Several traditional form-finding methods have been developed, such as force density, dynamic relaxation, inverse iteration, and genetic. The force density method was the most widely used and was introduced by Schek [4].

It first transforms the nonlinear equilibrium equations into linear ones with the concept of "force density." Then, the equilibrium equations are solved by numerical method to obtain the equilibrium pretension. Then, several methods have been carried out that only consider the cable net structure as in [5, 6]. Deng et al. improved the pretension design method and considered the multiple uncertainties [7–9]. Shi et al. proposed methodologies to automatically generate pseudogeodesic mesh geometries of spherical and parabolic reflector surfaces [10, 11]. The truss is treated as rigid in [12–17] when considering the rim truss. Yang et al. [18, 19] considered the elastic rim trusses and proposed an optimal method. Nie et al. also considered the flexible frames and proposed an integrated form-finding method [20–23]. Thermal effects have also been discussed. Shi et al. proposed a new methodology of mesh geometry design [24]. Tabata

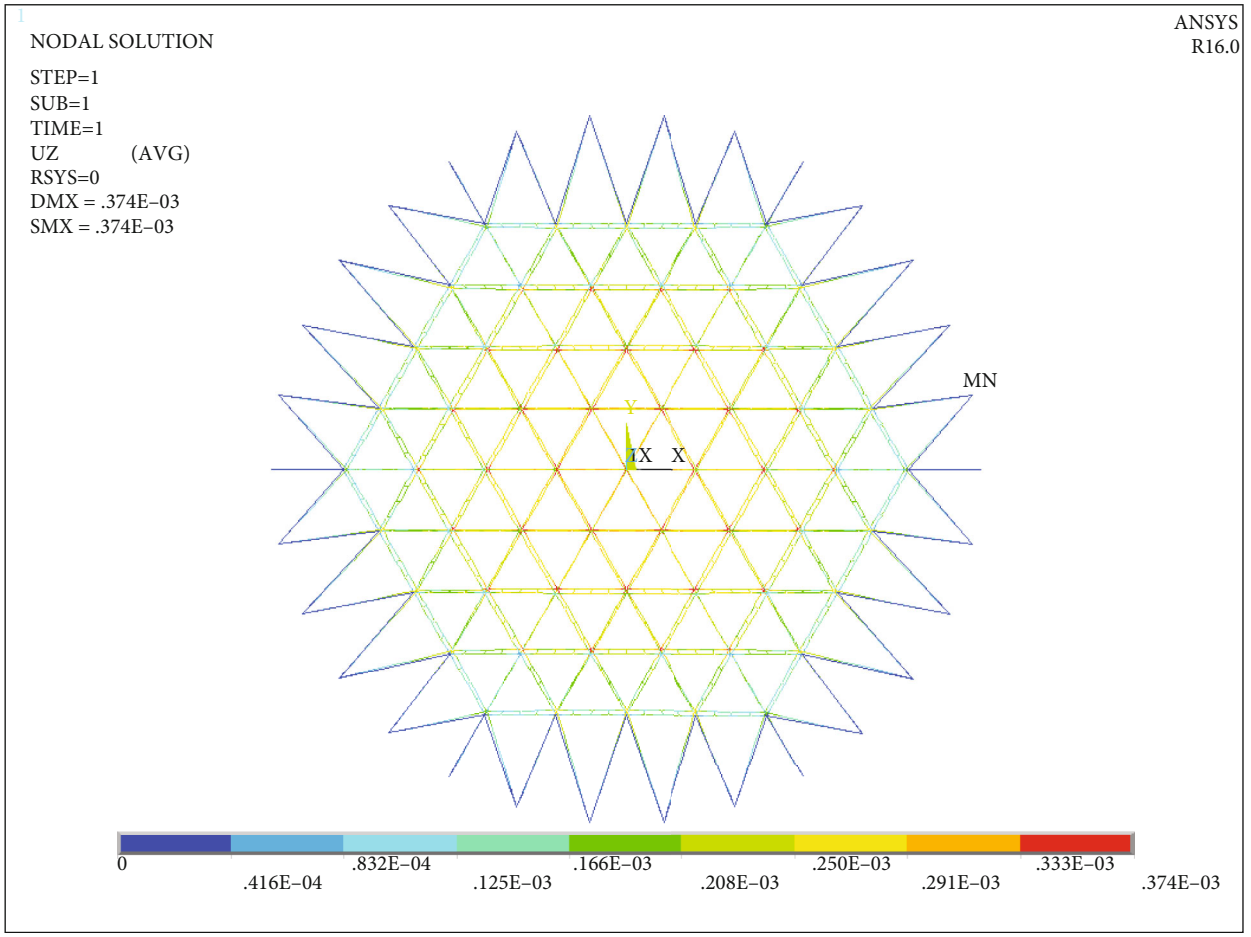

Figure 1: Nodal displacement calculated by ANSYS: subdivided finite element model.

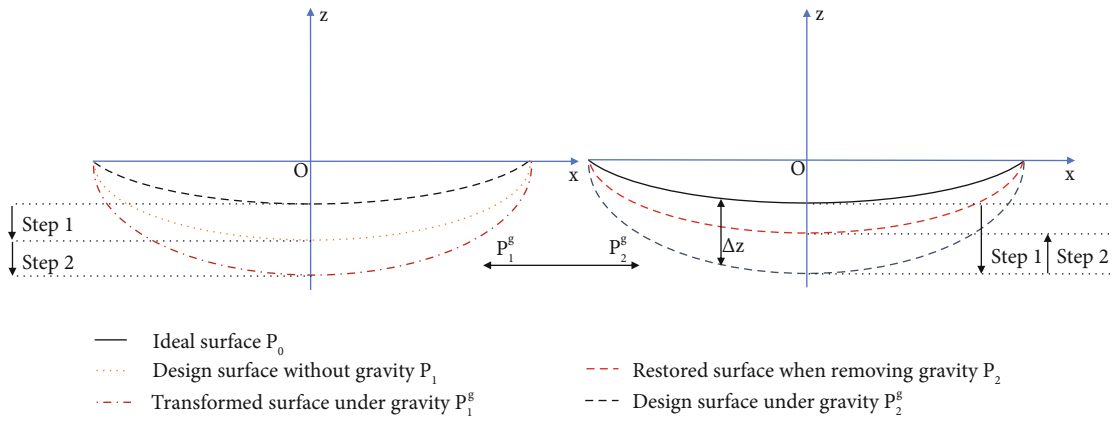

Figure 2: The comparison between two pretension design methods. (a) General method. (b) Method in this paper. The deviation between P_1^g and P_2^g increases as the antenna aperture increases.

and Natori had explored shape control concepts for mesh reflectors [25–29].

However, these existing methods are only suitable in an ideal environment. That means no gravity effect is taken into consideration. An accurate antenna reflector should be adjusted on the ground where gravity cannot be ignored. Moreover, the influence of surface accuracy resulted by gravity increases as the size of the antenna increases. Two methods are widely used in engineering to estimate the effect of gravity. The first is to flip the antenna reflector to get cup-up and cup-down surfaces by adding the two together to counteract the effect of gravity [30, 31]. This method requires a sizeable

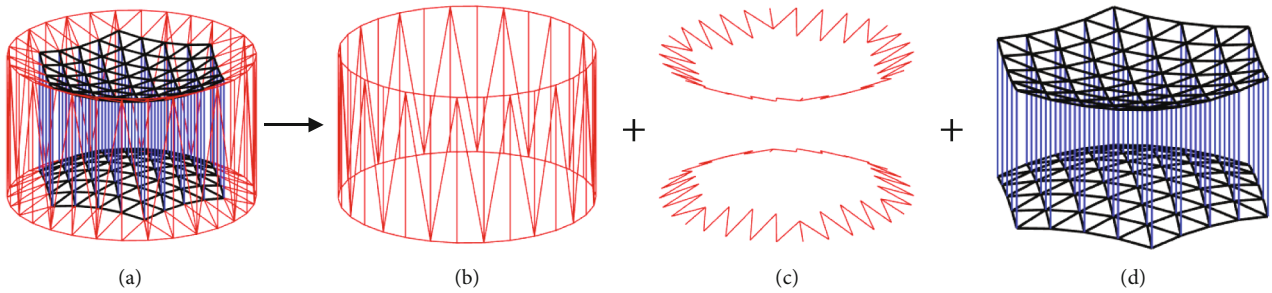

Figure 3: Composition of a mesh reflector. (a) Mesh reflector. (b) Truss. (c) Boundary cable. (d) Cable net.

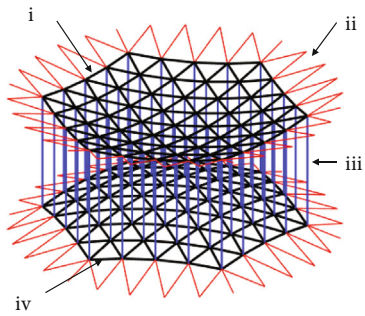

Figure 4: Schematic of a cable net structure. (a) Front cable net. (b) Boundary cables. (c) Tension tie cables. (d) Back cable net.

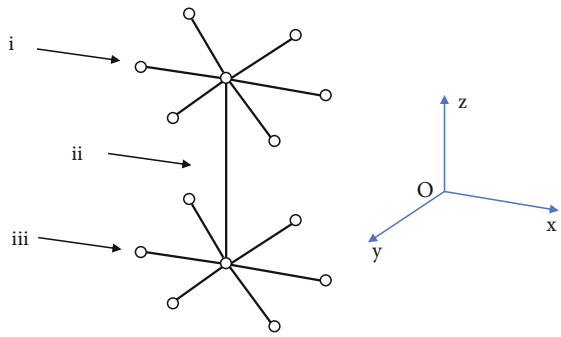

Figure 5: A cable net unit. (a) Front cable net. (b) Tension tie cable. (c) Back cable net.

experimental site and adjusting work is extremely difficult. As the antenna diameter increases, it has a significant risk to flip the antenna. Considering that the mesh antenna is a large flexible structure, flipping may cause other assembly errors or damage the antenna. The second one is based on finite element software. This method needs to combine the experimental results with the error correction method [32–34]. The critical factor is to give static loads in the form of distributed weights to the nodes of the cable net and measure the surface deformation caused by the static loads. Then, adjust the stiffness parameters to make the deformation characteristics of the mathematical model exactly match the test results. However, there are thousands of positions where static loads should be applied when the antenna aperture is large, which makes this method extremely difficult to apply in practice. Not only is there a large number of experiments, but the matching of mathematical models and experimental results is also difficult to achieve at this magnitude.

Specifically, the mesh surface is first designed according to the ideal one. Then, the deformed surface under gravity is obtained by finite element simulation. Introducing gravity into the finite element model to get the reference surface in the stage of ground adjustment is acceptable in a certain aperture range. This can be seen in Figure 1. However, when the aperture further increases, there is an obvious deviation as discussed in 4.3. Generally, model modification is necessary when considering manufacture based on the methods mentioned above. There both have insurmountable problems in the stage of ground adjustment when the aperture increases. To solve this problem, the gravity factor should be introduced in the pretension design process first. At the same time, the change of cable stiffness should also be considered in the design. There are two critical problems in this issue. The first is that the target shape of the design is no longer an ideal shape but an unknown gravitational surface. The second is whether the surface can meet the surface accuracy requirements after the gravity is removed.

The primary purpose of this paper is to propose a new method to design the pretension in the cable net structure. A new model considering gravity can be achieved to supply guidance in antenna adjustment. Generally, the pretension design considering gravity is shown in Figure 2(a), and the method in this paper is shown in Figure 2(b). The comparison of the two design methods has been discussed in detail in 3.3. The biggest difference is that the method in this paper is designed with changes in gravity and stiffness. Furthermore, the advantage of the method in this paper is that it does not require flipping the antenna or extensive experimental corrections. It should be noted that although the designed surface considering gravity can effectively guide the ground adjustment, the surface must be restored to meet the accuracy requirements after entering the orbit. This point is the most critical condition for design convergence, consistent with previous studies.

2. Composition of a Mesh Reflector

A deployed mesh reflector antenna is conceived with the concept of a tension truss, which is a light and inherently stiff structure that can be precisely and repeatedly deployed regardless of the environment. As illustrated in Figures 3 and 4, it is divided into three parts, a supporting truss, a

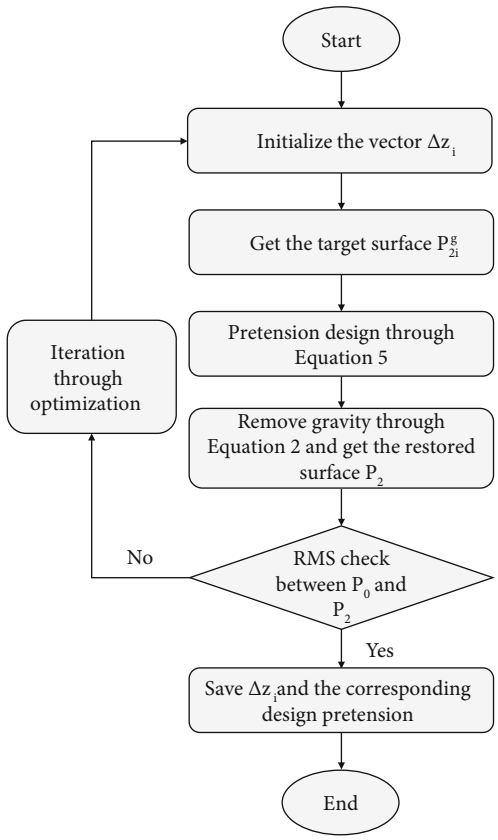

Figure 6: Algorithm of pretension optimization.

boundary cable, and a cable net reflector, including surface cables, tension tie cables, and RF reflective mesh which are sewn on the net surface. The cable net reflector and the boundary cables are named the deployable cable net structure.

3. Pretension Design Method

3.1. Mechanical Analysis of Cable. The space environment is known as a microgravity environment. Therefore, the straight-rod elements can achieve calculation accuracy that meets high efficiency in engineering requirements. According to the principle of virtual displacement, the overall stiffness matrix considering the pretensioned cable element can be divided into two parts when omitting the second-order term. They are k_E and k_G that represent the elastic stiffness matrix and geometric stiffness matrix, respectively. For a cable element in the local coordinate system, the coordinates of both ends are $(0, 0, 0)$ and $(x_j, 0, 0)$. Then, the relationship between nodal displacement and nodal force can be shown in

$$\begin{aligned} [k_E + k_G]d &= f - r, \\ r &= A_c l_c A^T \sigma - f, \\ k_E &= A_c l_c E_c \left[A^T A\right], \\ k_G &= A_c l_c \left[\sigma B^T B\right], \end{aligned} \tag{1}$$

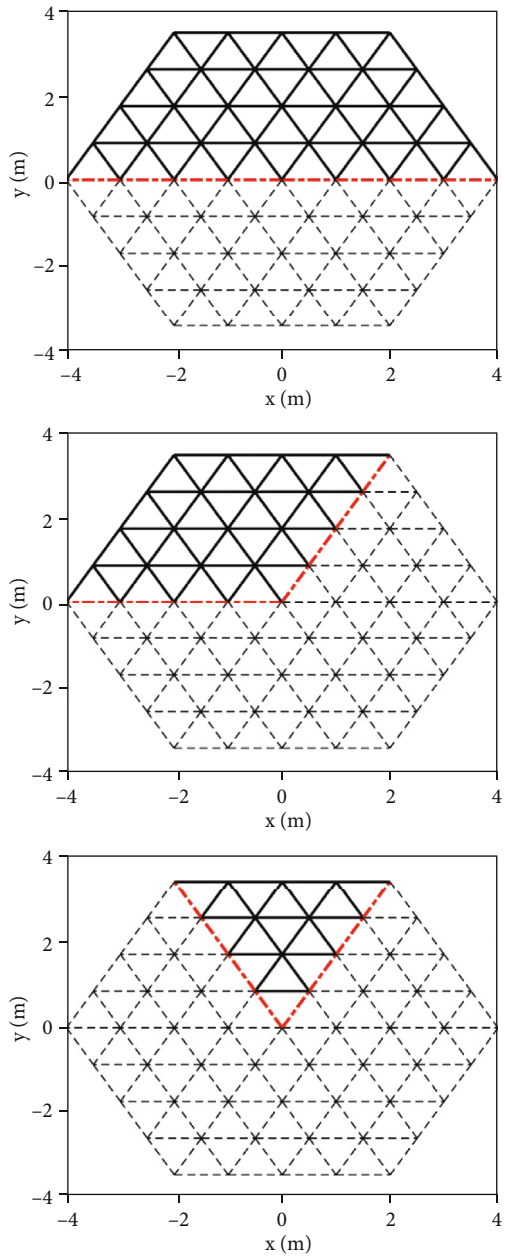

Figure 7: Characteristic structure of cable net.

where

$$\begin{aligned} A &= (b_1\, 0\, 0\, b_2\, 0\, 0), \\ B &= \begin{pmatrix} b_1 & 0 & 0 & b_2 & 0 & 0 \\ 0 & b_1 & 0 & 0 & b_2 & 0 \\ 0 & 0 & b_1 & 0 & 0 & b_2 \end{pmatrix}, \\ b_1 &= -b_2 = -\frac{1}{x_j}. \end{aligned} \tag{2}$$

And E_c, l_c, A_c, σ, f, and d indicate the elastic modulus, cable length, cross-sectional area, cable stress, external force, and nodal displacement. Then, in the overall coordinate

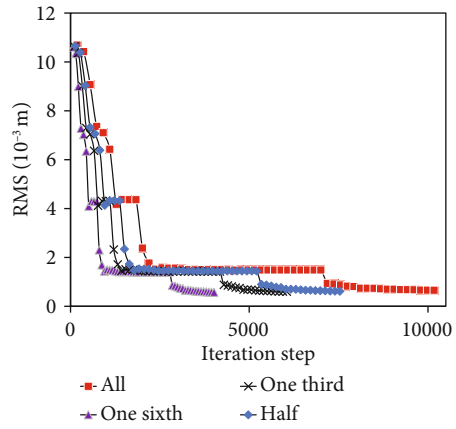

Figure 8: Iteration process of RMS error of the front cable net (interior point algorithm).

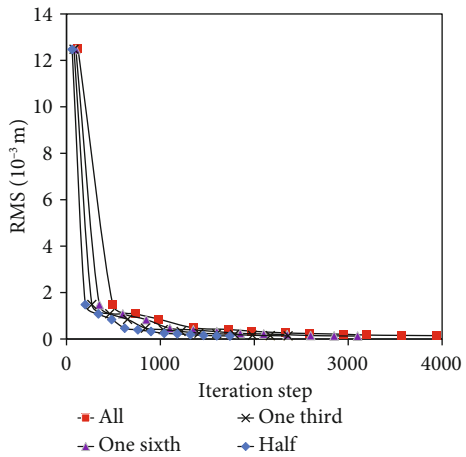

Figure 9: Iteration process of RMS error of the front cable net (quasi-Newton algorithm).

system, the above equation can be transformed by the transformation matrix to obtain the stiffness equation of the cable element.

$$[K_E + K_G]D = F - R. \tag{3}$$

By assembling the stiffness matrix equations of each cable element in the global coordinate system, the overall stiffness equation of the entire cable net structure can be obtained. When the pretensions have been designed and the external force is specific, the overall deformation of the cable net can be obtained through the stiffness equation.

3.2. Effect of Gravity. The pretension design of a cable net structure aims to determine the cable tension distribution to obtain the required reflector surface accuracy. The unit of a cable net structure is shown in Figure 5, where node i is connected to node j by a cable. The equilibrium equation of node i can be derived as follows.

$$\begin{cases} \sum_j F_{ij} \dfrac{x_i - x_j}{l_{ij}} = 0, \\ \sum_j F_{ij} \dfrac{y_i - y_j}{l_{ij}} = 0, \\ \sum_j F_{ij} \dfrac{z_i - z_j}{l_{ij}} = \sum_j G_{ij}, \end{cases} \tag{4}$$

where F_{ij}, G_{ij}, and l_{ij}, respectively, represent the tension force, the gravity, and the length of the cable between two adjacent nodes i and j of coordinates (x_i, y_i, z_i) and (x_j, y_j, z_j). It can be rewritten in the form of a matrix as follows:

$$Q_{3k\times r} F = C, \tag{5}$$

where $C = \begin{pmatrix} 0_{2k\times 1} \\ G_{k\times 1} \end{pmatrix}$.

Q is a coefficient matrix; $F = (\, F_1 \quad F_2 \quad \cdots \quad F_r \,)^T$ is the tension force vector of cables; k is the total number of free nodes; r is the total number of cables.

Since the assumption of nodes located in the required parabolic surface, the nodal locations and topology of the cable net structure can be determined. Then, the pretension design of the cable net structure can be expressed by the following optimization model:

$$\begin{cases} \text{Find} \quad F = (\, F_1 \quad F_2 \quad \cdots \quad F_r \,)^T, \\ \text{Min} \quad \text{RMS} = \sqrt{\dfrac{\sum_{j=1}^{n} \Delta S_j^2}{n}}, \\ \text{s.t.} \quad Q_{3k\times r} F = C, \\ \qquad F_i > 0 \qquad\qquad 1 \le i \le r, \end{cases} \tag{6}$$

where ΔS_j is the displacement of the jth free node in the cable net reflector, n is the total number of free nodes in the cable net reflector, and RMS is an abbreviation of the root mean square.

It should be noticed that the length of the cable changes in each iteration step after being pretensioned. In such cases, the gravity matrix also changes in each step. However, the original lengths of all cables before being pretensioned are considered unchanged.

3.3. Optimization Design Method. For a given antenna surface, the pretension can be designed through Equation (6) considering the effect of gravity. Nevertheless, the target position of the antenna reflector is unknown. Specifically, when gravity is not taken into consideration, the design surface is simply the ideal surface P_0 in orbit. However, the design surface under gravity would be deformed to P_2^g, which means that the target surface is unknown during the optimization. The difference can be illustrated in Figure 2. As gravity only works in z direction, the influences of the

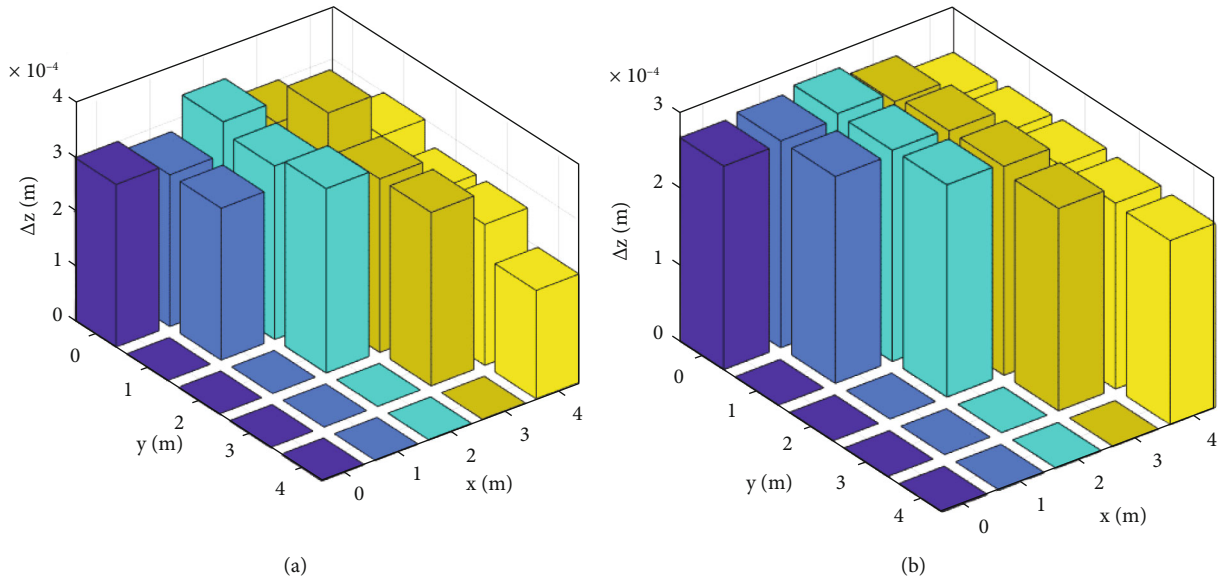

Figure 10: Surface error of front cable net considering the effect of gravity. (a) Optimization results. (b) Finite element calculation results.

coordinates in the x and y directions are ignored. There is a deviation Δz, which is unknown, between the target surface under gravity and the ideal surface. But for every certain value of Δz_i, pretension can be designed for the ith target surface. Moreover, this undergravity surface should have the ability to restore to an ideal position on orbit as required. Gravity is removed through Equation (3) after the design so that the surface would deform to a new position P_2 as shown in Figure 2. The smaller the gap between P_0 and P_2, the better it is. Obviously, all values of Δz for free nodes are negative and for boundary nodes the values are 0. The solution is to find a certain Δz with which pretension design can be solved. Then, the surface is able to recover to the ideal surface after removing the gravity. The overall algorithm is presented in the flowchart of Figure 6.

The selection of the initial values of the iteration is a critical factor in the optimization. An improper selection of the initial value will cause the result to be a local optimum instead of a global optimum. And the iteration may not converge in worst cases. To solve this problem, the values are selected by the combination of the engineering experience and the calculation results.

3.4. Improvement of Optimization. According to the above discussion, in the mathematical model of the cable net structure, each value of Δz_i is an optimization variable. In this case, even if we optimize the mathematical model to the maximum, the number of variables is still large. Taking an antenna with a diameter of 10 m as an example, the node number is 182, within the allowable range of the geometric size of the cable network. The optimization problem of this dimension not only requires a lot of computing time but also is prone to nonconvergence. Here, we need a more efficient method to reduce the number of optimization variables while ensuring the accuracy.

Fortunately, the cable net structure is a highly symmetric structure, which allows us to simplify it in different ways. According to the symmetrical form, half, one-third, and one-sixth of the cable net can be taken as a characteristic structure, as shown in Figure 7. However, the boundary of the characteristic structure is different from the original cable net. If we only use the characteristic structure for optimization, the cable stress of the nodes at the position of the red line in Figure 7 will change. When the calculation result of the characteristic structure is substituted into the cable net, there will be inevitable deformation. Although this deformation can be estimated, it will affect the stability of the optimization. The calculation time will be longer and even fail to converge, which is contrary to our original intention. In this case, we should still optimize with variables of the same dimension, but the total number of variables is reduced. That is to say, half, one-third, and one-sixth of the number of variables are used, respectively, and then, other nodes are valued according to the symmetrical relationship. Taking an antenna with a diameter of 10 m as an example, we now only set 102, 78, and 42 variables in the case of half, one-third, and one-sixth, respectively. Then, other values of Δz_i can be settled, and the dimension of Δz will still be 182. By this method, we can reduce the number of variables and do not change the boundary conditions of the cable network.

4. Results and Discussion

4.1. Pretension Design of a 10 m Mesh Reflector. A parabolic antenna with a spatial mesh reflector is shown in Figure 4. The antenna specifications are as follows:

Diameter of aperture: 10 m
Focal length of front cable net: 7.5 m
Focal length of back cable net: 7.5 m
Number of surface cables: 312 (= 156 × 2)
Number of boundary cables: 108 (= 54 × 2)
Number of tension tie cables: 61
Number of free nodes: 122 (= 61 × 2)

Table 1: Pretension distribution of the cable net.

Item	Pretension values in cables (N)		
	Maximum	Minimum	Mean
Front cable net	48.61	44.56	45.76
Back cable net	48.72	44.48	45.77
Tension tie cables	10.61	8.92	9.48

Table 2: Pretension distribution of the cable net with different aperture diameters.

Diameter of aperture (m)	Item	Pretension values in cables (N)		
		Maximum	Minimum	Mean
10	Front cable net	84.20	50.52	69.12
	Back cable net	47.56	28.04	33.52
	Tension tie cables	10.48	7.52	9.40
12	Front cable net	85.36	48.67	70.12
	Back cable net	47.12	27.44	32.48
	Tension tie cables	10.34	7.36	9.25
16	Front cable net	86.88	47.64	68.84
	Back cable net	46.88	25.44	31.92
	Tension tie cables	10.28	7.28	9.16
20	Front cable net	88.94	48.36	70.34
	Back cable net	45.24	21.68	28.48
	Tension tie cables	12.36	6.28	8.83
24	Front cable net	92.34	53.08	72.56
	Back cable net	42.76	21.56	27.44
	Tension tie cables	11.24	5.84	8.72

Height: 2 m
Type of facets: triangular
Elastic modulus of cables: 20 GPa
Radius of cables: 0.5×10^{-3} m
Density of cables: 1450 kg/m^3

First, it is important to set the initial value of Δz, which can be expressed as

$$\Delta z = \left[\Delta z_1, \Delta z_2, \cdots, \Delta z_{n_f}, \underbrace{0, 0, \cdots 0}_{n_b}\right], \quad (7)$$

where n_f and n_b represent the number of free nodes and boundary nodes, respectively. This model is simulated in different ways. Corresponding to 3.4, all free nodes, half of the free nodes, one-third of the free nodes, and one-sixth of the free nodes are used as optimization variables, respectively. All values of Δz is constrained to be negative. The tension forces of all cables are set to 40 N initially. Constrained nonlinear minimization is used to solve the problem. The iteration results of interior point algorithm and quasi-Newton algorithm are shown in Figures 8 and 9, respectively.

When using interior point algorithm, the RMS error between P_0 and P_2 of front cable net is lowered from 11.07 $\times 10^{-3}$ m to 0.66×10^{-3} m. When all free nodes are used as optimization variables, the integration step is 10711. When the characteristic structure is used to reduce the optimization variables, the integration steps are significantly reduced and the optimization results remain consistent. The results show that this method is scientific and necessary when the aperture increases.

Meanwhile, when the quasi-Newton algorithm is used, the RMS error between and of the front cable net is lowered from 12.49×10^{-3} m to 0.14×10^{-3} m. The integration step is 3936 which is much smaller than the first algorithm. The optimization result is better at the same time. Likewise, with the introduction of characteristic structures, the efficiency of optimization computations continues to increase. It can be seen from the comparison that although there are many optimization variables, the optimization results are completely acceptable in engineering. This is due to the highly symmetrical feature of the cable net structure. On the other hand, the choice of algorithm and the initial value is critical, affecting the optimization efficiency and effectively avoiding nonconvergence when the antenna aperture is continuously increased.

The surface of the front cable net considering the effect of gravity is shown in Figure 10. Only one-sixth of the model is shown in this figure. All values are negative and are taken as absolute values in the figure. The maximum nodal displacement of Δz is -0.34×10^{-3} m. Compared with the finite element calculation results, each value of Δz in the optimization results has a degree of discrimination, and the finite element calculation results are close to the same. However, the difference between the overall results is small, which shows that there is little difference between the two methods when the diameter is 10 m. The pretension distribution of the cable net structure is shown in Table 1. The design surface is basically in line with the prediction, which confirms the validity of pretension optimization. On the other hand, the forces in Table 1 show excellent uniformity that indicates a good stability in the design results. The maximum and minimum stress ratios of the front cable net and the back cable net are 1.062 and 1.096, respectively. More importantly, the surface we find has the ability to restore to the ideal surface when removing gravity. The minimum RMS between two surfaces is only 0.14×10^{-3} m which is acceptable in engineering.

In order to verify the accuracy of the calculation, a subdivided finite element model is established and distributed

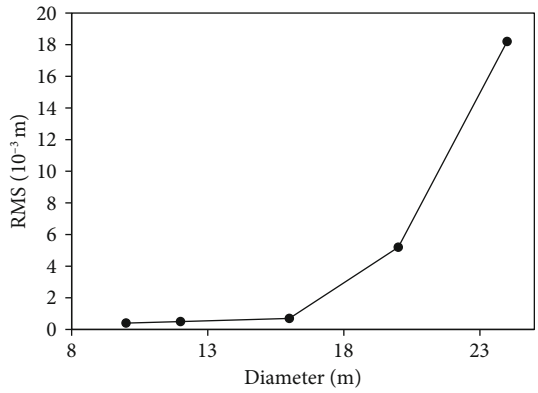

Figure 11: Deviation between P_1^g and P_2^g.

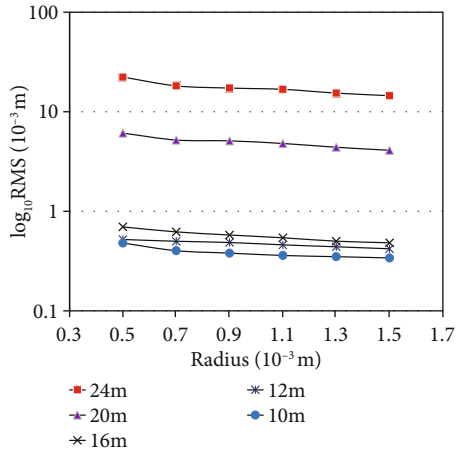

Figure 12: Effect of the cable radius.

gravity is applied on the model. In the subdivision model, multisegment elements are used to simulate the catenary cable. The subdivided model is verified by ANSYS as shown in Figure 1 in the manuscript. The maximum nodal deviation caused by gravity between the subdivided model and theoretical method in this paper is $0.37 \times 10^{-3} - 0.28 \times 10^{-3} = 0.09 \times 10^{-3}$ m, which meets the requirement (less than 0.1×10^{-3} m at least).

4.2. Pretension Design with Reflective Mesh. Taking into account the needs of large-aperture antennas in engineering applications, the algorithm is used to simulate antennas of different apertures with the influence of RF reflective mesh ($5 \times 10 - 2\,\text{kg/m}^3$), and the results are shown in Table 2.

This method can still effectively carry out the pretensioning design when considering the reflective metal mesh. The optimization method has specific stability when the antenna aperture is continuously increased. There is no failure to converge. When only considering the cable mesh structure, the pretension values of the front and back cable meshes are the same. However, after considering the RF reflective mesh, the stress on the front mesh surface increases significantly, resulting from the gravity of the RF reflective mesh directly acting on the front mesh surface. At the same time, the uniformity of pretension decreases clearly, which is closely related to the boundary of the cable net structure. On the other hand, although the pretension values of the tension cable and the back net do not change much, they also become nonuniform.

4.3. Deviation between P_1^g and P_2^g. Generally, the ideal shape P_0 is taken as the target shape during the pretension design of the antenna reflection surface. And some methods are used to iteratively calculate it to accomplish the pretension design and form-finding work. The shape obtained at this time can be called P_1, and the validity of the design is verified by comparing the RMS value of P_1 and P_0. When considering the effect of gravity, a gravity load is applied to P_1 surface to obtain P_1^g. In fact, this method is not accurate enough due to simplification. Here, the designed surface in ideal condition under gravity P_1^g and the designed surface considering gravity P_2^g are compared. It can be seen in Figure 11 that when the antenna diameter is between 10 m and 16 m, the RMS deviation of the two surfaces is minimal, only increasing from 0.402×10^{-3} m to 0.697×10^{-3} m. However, when the aperture is further increased, the deviation of the two surfaces increases sharply, and the deviation has reached 18.2×10^{-3} m when the diameter is 24 m. This also confirms that it is impossible to obtain an accurate ground surface only by loading the gravity on the design surface that does not consider gravity. This is also why the surface cannot be directly used to complete the ground adjustment in engineering. At the same time, the deviation of the two surfaces is in the form of the exponential distribution, which is related to the structure and stiffness of the cable net. When the diameter of the antenna is small, gravity is not a significant factor, but when the diameter of the antenna increases continuously, the gravity has a significant influence on the precision of the pretension and the surface.

4.4. Effect of Cable Radius. From the previous discussion, it can be concluded that when the antenna aperture is large, there is a big difference between whether gravity is considered in the pretension design stage. A natural question as whether this is caused by other factors arises. The antenna reflector mainly comprises cables, so the cable length, cable radius, and elastic modulus are all critical parameters. Firstly, the research is carried out with the radius of the cable as a variable, as shown in Figure 12.

It can be seen from the figure that when the cable radius changes, the overall RMS value shows a downward trend. When the cable radius increases, the gravity of the cable net structure increases, but the gravity of the RF reflective mesh does not change. It can be concluded that when the stiffness of the cable net structure increases, the effect of coupling with the RF reflective mesh will be weakened. However, this weakening does not make the two surfaces P_1^g and P_2^g consistent. That is to say, when the diameter of the antenna is large, changing the radius of the cable slightly impacts the surface accuracy. This may be because the gravity of the RF reflective mesh far exceeds that of the cable mesh.

4.5. Effect of Cable Length. The cable length in the cable net structure directly determines the fineness of the

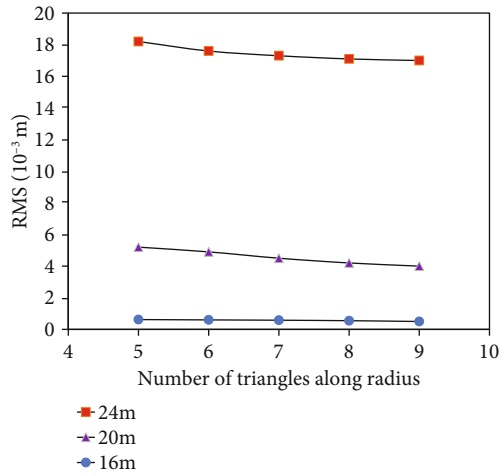

Figure 13: Effect of the cable length.

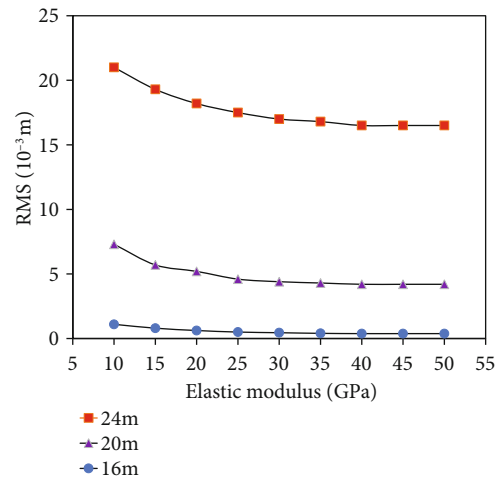

Figure 14: Effect of the elastic modulus.

mathematical model. The smaller the cable length, the more triangle segments along the radial direction. To make antennas of different diameters comparable, the number of segments in the radius triangle is used as an independent variable, and the number of segments is inversely proportional to the length of the cable. The results are shown in Figure 13. The RMS value decreases with the decrease of the cable length. Thanks to the refinement of the model, which leads to the smaller calculation error. However, generally the values tend to be stable within a certain range. This shows that the deviation between the surfaces P_1^g and P_2^g is not due to geometric errors. It also shows that when the diameter of the antenna is large, gravity greatly influences the surface accuracy.

4.6. Effect of Elastic Modulus. The elastic modulus of the cable directly affects the stiffness. When the elastic modulus increases, the effect of gravity becomes smaller and smaller. The data in Figure 14 illustrate the same conclusion. However, as the elastic modulus increases to a specific value, the value of RMS no longer decreases but tends to remain unchanged. This also shows that the two surfaces P_1^g and P_2^g are different. That implies the necessity to consider gravity in the pretension design.

5. Conclusions

A novel pretension design method considering the effect of gravity is proposed. Compared with previous methods, it can avoid flipping the antenna or excessive experiments in the stage of ground adjustment in engineering. At the same time, the method can ensure that the antenna can restore to the surface that meets the accuracy requirements after entering the orbit. Furthermore, with the increase of the antenna aperture, the method shows specific stability and does not fail to converge.

Considering that there are too many optimization variables in this optimization method, the characteristic structure is selected according to the symmetry of the cable net structure. Although the dimensions of the variables in the iterations remain unchanged, reducing the variables still effectively reduces the number of iterations. Two algorithms are used for the calculation, and the results show that the initial values according to engineering experience and calculation results are valid in the optimization.

Numerical simulations of cable net antennas with diameters ranging from 10 m to 24 m are carried out. After introducing the gravity of the RF reflective mesh, an excellent pretension distribution can still be obtained. Two surfaces are compared. When the antenna diameter is not large, the difference between the two is minimal. As the antenna aperture increases, the RMS values of the two increase exponentially. Then, the effects of cable radius, length, and elastic modulus are analysed. When the cable radius increases, the deviation of the two surfaces will decrease slightly. The same phenomenon occurs when the elastic modulus increases. However, the deviation tends to remain unchanged when the elastic modulus increases to a certain extent. When the length of the cable is changed, which will refine the model, the deviation of the two surfaces will decrease but always remain within a specific range.

In general, when the diameter of the antenna increases, the influence of gravity becomes increasingly significant. Therefore, the method proposed here can effectively estimate the ground surface of the antenna. At the same time, the flipping and experimental correction of the antenna are avoided. This is of great significance to surface adjustment in engineering. In future work, the comparison of experimental data is needed to verify the proposed method's effectiveness better.

Data Availability

The data used to support the findings of this study are available from the first author upon request.

Conflicts of Interest

The authors declare that there is no conflict of interest regarding the publication of this paper.

Acknowledgments

This work is supported by previous research in the 20th International Symposium on Distributed Computing and Applications for Business, Engineering and Science [35]. We thank all the authors for their research.

References

[1] T. J. Li, "Deployment analysis and control of deployable space antenna," *Aerospace Science and Technology*, vol. 18, no. 1, pp. 42–47, 2012.

[2] X. F. Ma, Y. P. Song, and T. J. Li, "Mesh reflector antennas: form finding analysis review," in *54th AIAA/ASME/ASCE/AHS/ASC Structures, Structural Dynamics and Materials Conference*, Boston, Massachusetts, 2013.

[3] T. J. Li, J. Jiang, H. Q. Deng, Z. C. Lin, and Z. W. Wang, "Form-finding methods for deployable mesh reflector antennas," *Chinese Journal of Aeronautics*, vol. 26, no. 5, pp. 1276–1282, 2013.

[4] H. J. Schek, "The force density method for form finding and computation of general networks," *Computer Methods in Applied Mechanics and Engineering*, vol. 3, no. 1, pp. 115–134, 1974.

[5] A. G. Tibert, "Optimal design of tension truss antennas," in *44th AIAA/ASME/ASCE/AHS/ASC structures, structural dynamics and materials conference*, Norfolk, Virginia, 2003.

[6] B. Yang, H. Shi, M. Thomson, and H. Fang, "Optimal design of initial surface profile of deployable mesh reflectors via static modeling and quadratic programming," in *50th AIAA/ASME/ASCE/AHS/ASC structures, structural dynamics and materials conference*, Palm Springs, California, 2009.

[7] H. Q. Deng, T. J. Li, and Z. W. Wang, "Design of geodesic cable net for space deployable mesh reflectors," *Acta Astronautica*, vol. 119, pp. 13–21, 2016.

[8] H. Q. Deng, T. J. Li, Z. W. Wang, and X. Ma, "Pretension design of space mesh reflector antennas based on projection principle," *Jounral of Aerospace Engineering*, vol. 28, no. 6, article 04014142, 2015.

[9] H. Q. Deng, T. J. Li, and Z. W. Wang, "Pretension design for space deployable mesh reflectors under multi-uncertainty," *Acta Astronautica*, vol. 115, pp. 270–276, 2015.

[10] H. Shi, B. Yang, and H. Fang, "Offset-feed surface mesh generation for design of space deployable mesh reflectors," in *54th AIAA/ASME/ASCE/AHS/ASC Structures, Structural Dynamics, and Materials Conference*, Boston, Massachusetts, 2013.

[11] H. Shi, B. Yang, M. Thomson, and H. Fang, "Automatic surface mesh generation fordesign of space deployable mesh reflectors," in *53rd AIAA/ASME/ASCE/AHS/ASC Structures, Structural Dynamics, and Materials Conference*, Honolulu, Hawaii, 2012.

[12] G. Yang, D. Yang, Y. Zhang, and J. Duand, "Form-finding design of cable-mesh reflector antennas with minimal length configuration," *Aerospace Science and Technology*, vol. 63, pp. 9–17, 2017.

[13] D. Yang, G. Yang, Y. Zhang, and J. Du, "Least-squares minimization of boundary cable tension ratios for mesh reflectors," *AIAA Journal*, vol. 56, no. 2, pp. 883–888, 2018.

[14] W. Liu and D. Li, "Simple technique for form-finding and tension determining of cable-network antenna reflectors," *Journal of Spacecraft and Rockets*, vol. 50, no. 2, pp. 479–481, 2013.

[15] Y. Tang, T. Li, X. Ma, and L. Hao, "Extended nonlinear force density method for form-finding of cable-membrane structures," *Journal of Aerospace Engineering*, vol. 30, no. 3, article 04016101, 2017.

[16] D. Yang, J. Liu, Y. Zhang, and S. Zhang, "Optimal surface profile design of deployable mesh reflectors via a force density strategy," *Acta Astronautica*, vol. 130, pp. 137–146, 2017.

[17] S. Morterolle, B. Maurin, J. Quirant, and C. Dupuy, "Numerical form-finding of geotensoid tension truss for mesh reflector," *Acta Astronautica*, vol. 76, pp. 154–163, 2012.

[18] S. C. Yuan and B. E. Yang, "The fixed nodal position method for form finding of high-precision lightweight truss structures," *International Journal of Solids and Structures*, vol. 161, pp. 82–95, 2019.

[19] D. Yang, Y. Zhang, P. Li, and J. Du, "Numerical form-finding method for large mesh reflectors with elastic rim trusses," *Acta Astronautica*, vol. 147, pp. 241–250, 2018.

[20] R. Nie, B. He, L. Zhang, and Y. Fang, "Deployment analysis for space cable net structures with varying topologies and parameters," *Aerospace Science and Technology*, vol. 68, pp. 1–10, 2017.

[21] R. Nie, B. He, D. H. Hodges, and X. Ma, "Form finding and design optimization of cable network structures with flexible frames," *Computers & Structures*, vol. 220, pp. 81–91, 2019.

[22] R. Nie, B. He, D. H. Hodge, and X. Ma, "Integrated form finding method for mesh reflector antennas considering the flexible truss and hinges," *Aerospace Science and Technology*, vol. 84, pp. 926–937, 2019.

[23] R. Nie, B. He, S. Yan, and X. Ma, "Optimization design method for the cable network of mesh reflector antennas considering space thermal effects," *Aerospace Science and Technology*, vol. 94, article ???, 2019.

[24] H. Shi, S. Yuan, and B. Yang, "New methodology of surface mesh geometry design for deployable mesh reflectors," *Journal of Spacecraft and Rockets*, vol. 55, no. 2, pp. 266–281, 2018.

[25] M. Tabata and M. C. Natori, "Active shape control of a deployable space antenna reflector," *Journal of Intelligent Material Systems and Structures*, vol. 7, no. 2, pp. 235–240, 1996.

[26] A. Meguro, S. Harada, and M. Watanabe, "Key technologies for high-accuracy large mesh antenna reflectors," *Acta Astronautica*, vol. 53, no. 11, pp. 899–908, 2003.

[27] H. Tanaka, N. Shimozono, and M. C. Natori, "A design method for cable network structures considering the flexibility of supporting structures," *Transactions of the Japan Society for Aeronautical and Space Sciences*, vol. 50, no. 170, pp. 267–273, 2008.

[28] H. Tanaka and M. C. Natori, "Shape control of cable-network structures based on concept of self-equilibrated stresses," *JSME International Journal Series C Mechanical Systems, Machine Elements and Manufacturing*, vol. 49, no. 4, pp. 1067–1072, 2006.

[29] H. Tanaka, "Design optimization studies for large-scale contoured beam deployable satellite antennas," *Acta Astronautica*, vol. 58, no. 9, pp. 443–451, 2006.

[30] A. Meguro, "Development of a 15m class modular mesh deployable antenna," in *48th International Astronautical Congress*, Turin, Italy, 1997.

[31] M. Thomson, "Astromesh deployable reflectors for ku and ka band commercial satellites," in *20th AIAA International Communication Satellite Systems Conference and Exhibit*, Montreal, Quebec, Canada, 2002.

[32] M. Tabata, M. C. Natori, T. Tashima, and T. Inoue, "Adjustment procedure of a high precision deployable mesh antenna for MUSES-B spacecraft," *Journal of Intelligent Material Systems and Structures*, vol. 8, no. 9, pp. 801–809, 1997.

[33] M. C. Natori, T. Takano, and T. Noda, "Ground adjustment procedure of a deployable high accuracy mesh antenna for space VLBI mission," in *39th AIAA/ASME/ASCE/AHS/ASC Structures, Structural Dynamics, and Materials Conference and Exhibit*, Long Beach,CA,U.S.A., 1998.

[34] H. Tanaka, "Study on a calibration method for shape control parameters of a self-sensing reflector antenna equipped with surface adjustment mechanisms," *Transactions of the Japan Society for Aeronautical and Space Sciences*, vol. 57, no. 2, pp. 86–92, 2014.

[35] G. L. Su, Y. Li, Y. S. Fan, H. Li, and X. Ma, "Prestress optimal design of deployable antenna considering the effect of gravity," in *20th International Symposium on Distributed Computing and Applications for Business, Engineering and Science*, Nanning, China, 2021.